

1-1-2010

Accelerated Lattice Boltzmann Method For Colloidal Suspensions Rheology And Interface Morphology

Hassan Farhat
Wayne State University

Follow this and additional works at: http://digitalcommons.wayne.edu/oa_dissertations

Recommended Citation

Farhat, Hassan, "Accelerated Lattice Boltzmann Method For Colloidal Suspensions Rheology And Interface Morphology" (2010).
Wayne State University Dissertations. Paper 13.

This Open Access Dissertation is brought to you for free and open access by DigitalCommons@WayneState. It has been accepted for inclusion in Wayne State University Dissertations by an authorized administrator of DigitalCommons@WayneState.

**ACCELETATED LATTICE BOLTZMANN MODEL FOR COLLOIDAL SUSPENSIONS
RHEOLOGY AND INTERFACE MORPHOLOGY**

by

HASSAN FARHAT

DISSERTATION

Submitted to the Graduate School

of Wayne State University,

Detroit, Michigan

in partial fulfillment of the requirements

for the degree of

DOCTOR OF PHILOSOPHY

2010

MAJOR: MECHANICAL ENGINEERING

Approved by:

Advisor Date

Co-advisor Date

© COPYRIGHT BY

HASSAN FARHAT

2010

All Rights Reserved

DEDICATION

This work is dedicated to my wife Dr. **Therese Bu Akl**– for being a caring and supportive partner who made my life such a wonderful journey; to my daughters **Maria and Yasmine**– for their patience and love; and to my sister **Susan** and her husband **Alex** – for their kindness and support. Thank you.

ACKNOWLEDGMENTS

I would like to express my appreciation to Dr. Joon Sang Lee for the vital role he played during my PHD Studies. I deeply thank him for the trust he had in me and for promoting an environment, which encourages self motivation and a constant quest for innovation and creativity.

I would like to thank Dr. Trilochan Singh, Dr. Ming-Chia Lai, Dr. Emanuel Ayorinde and Dr. Howard Matthew for serving as my doctoral committee.

I would like to thank Dr. Yong Hyun Kim and Dr. Sasidhar kondaraju for their inputs, comments and for providing a friendly working environment.

TABLE OF CONTENTS

Dedication.....	ii
Acknowledgments.....	iii
List of Tables.....	vii
List of Figures.....	viii
Nomenclature.....	xviii
CHAPTER 1 – Introduction.....	1
1.1 Colloids.....	1
1.2 Numerical methods for colloidal studies.....	3
CHAPTER 2 – Research related studies.....	5
2.1 Lattice Boltzmann method.....	5
a. Single component LBM.....	5
b. Multi-component LBM.....	7
c. Grid refinement methods.....	14
2.2 Colloidal studies.....	18
a. Surfactant-laden droplets.....	18
b. Colloids rheology.....	22
c. Red blood cells deformability.....	23
CHAPTER 3 – Outline of the present work.....	28
3.1 Research objectives.....	28
3.2 Dissertation organization.....	29
CHAPTER 4 – Accelerated lattice Boltzmann method.....	31
4.1 Migrating multi-block schemes for the D2Q9 LBM.....	31
a. The migrating multi-block algorithms.....	31

b. Simulation results and discussion.....	38
4.2 Migrating multi-block scheme for the D3Q19 LBM.....	53
a. Modified model with density contrast.....	54
b. The migrating multi-block algorithm.....	56
c. Simulation results and discussion.....	59
4.3 Migrating multi-block for the particle-interaction-potential LBM.....	73
a. The migrating multi-block algorithm.....	73
b. Simulation results and discussion.....	74
CHAPTER 5 – Hybrid LBM for surfactant-covered droplets.....	92
5.1 Surfactants convection-diffusion equation.....	92
5.2 The hybrid LBM model.....	95
5.3 Simulation results and discussion.....	99
a. Surfactant-covered droplets in simple shear flows.....	100
b. Surfactant-covered droplets in uniaxial extensional flows.....	112
c. Buoyancy of surfactant-covered droplets in infinite medium....	117
CHAPTER 6 – Suppressing coalescence in the LBM: Colloids rheology.....	122
6.1 Suppressing coalescence in the LBM.....	122
a. Optimizing the force equation for suppressing coalescence....	125
b. Test cases.....	127
6.2 Rheology.....	131
a. Direct calculation of the relative viscosity of colloids.....	131
b. Simulation results.....	134
CHAPTER 7 – Non-uniform interfacial tension LBM for RBC modeling.....	140
7.1 The heuristic approach for surfactant-covered droplets.....	140

7.2 Simulation results and discussion.....	144
CHAPTER 8 – Conclusion and Recommendations.....	160
8.1 Conclusion.....	160
a. Migrating multi-block schemes.....	160
b. Hybrid LBM.....	161
c. Suppressing coalescence in the LBM and rheology.....	161
d. Non-uniform interfacial tension LBM for RBC modeling.....	162
8.2 Recommendations for future works.....	162
Appendix.....	164
References.....	173
Abstract.....	184
Autobiographical Statement.....	186

LIST OF TABLES

Table 4.1:	Simulation results for five different cases, U_T terminal velocity from Eq. (4.23), U_M terminal velocity from the numerical simulation.....	62
Table 4.2:	Variables and dimensionless numbers for a few shape region simulations.....	64
Table 4.3:	Comparison of the calculated mass flux and momentum flux for the fifth case from Table 4.1 at 9000 coarse time steps, with data collected from the various grid nodes which constitute the upstream grid interface.....	71
Table 4.4:	Pressure-density measurements at the vena-contracta location from the three simulations are presented below.....	78
Table 4.5:	Calculation of the mass flow rate by the analytical formula of Eq. (4.27) and directly by Eq. (4.28) for three time steps.....	82
Table 4.6:	Droplet characteristics dependence on the selection of the fluid-solid interaction constants, for a constant Bond number $B = 0.55$	90
Table 5.1:	Transient dimensionless length, percentage elongation, and reference angle of inclination measured in degrees, for the clean droplet and for the droplets with three initial values of surfactant coverage c_m at dimensionless time step $\dot{\gamma}t = 3.12$	105
Table 5.2:	Transient dimensionless length, percentage elongation, and angle of inclination measured in degrees, for three initial values of surfactant elasticity E_0 at dimensionless time step $\dot{\gamma}t = 3.12$	108
Table 5.3:	Droplet transient dimensionless length, percentage elongation and angle of inclination measured in degrees for $1 \leq Pe_s \leq 100$ at dimensionless time step $\dot{\gamma}t = 3.12$	111
Table 5.4:	Comparison of the terminal velocities from the two sets of simulations in the spherical and spherical-cap regions with their respective theoretical terminal velocities.....	121

LIST OF FIGURES

Figure 1.1:	(A) Annual US polymers production showing an exponential growth. (B) Death percentage rate in the US in 2004 due blood-related diseases.....	3
Figure 2.1:	(A) Velocity vectors for the D2Q9 and (B) for the D3Q19 lattice Boltzmann method used in this study.....	6
Figure 2.2:	Illustration of the grid interfaces between the fine and the coarse block from the proposed multi-block scheme by Yu and Shy (2002).....	18
Figure 2.3:	Two mechanisms for suppressing coalescence are presented here. (A) Surfactant concentration gradient. (B) Steric repulsion (Lyu et al., 2002).....	22
Figure 2.4:	Illustration of the domain for the simple shear flow used to calculate effective viscosity Liu and Liu (2006).....	23
Figure 2.5:	(A) Simplified representation of the blood cell as Liposome, justified by the assumption that the membrane liquefies under pressure in the microvasculature.....	25
Figure 4.1:	Illustration of the standard multi-block LBM domain as it pertains to the single component flow simulation of this work.....	32
Figure 4.2:	Illustration of the migrating multi-block LBM domain as it pertains to the multiphase flow simulation used in this paper.....	35
Figure 4.3:	Flow chart for the migrating multi-block LBM for immiscible mixtures.....	37
Figure 4.4:	Migrating multi-block LBM domain for the flow around an asymmetrically placed cylinder in a channel, with the cylinder center location expressed as a function of its radius.....	39
Figure 4.5:	Instantaneous streamlines of a 2D channel flow over an asymmetrically placed cylinder with $Re = 100$ time step 2.9×10^4 measured in coarse time units. (a) fixed multi-block in which the fine block is static having a center coinciding with the cylinder center. (b) migrating multi-block in which the fine block migrated in the direction of the flow by one coarse space unit each 5.0×10^3 coarse time steps and having its center advanced by 10 fine space units in the flow direction with respect to the cylinder center.....	40

Figure 4.6: Lift and drag coefficients for fixed and migrating multi-block cases, calculated for results taken between coarse time steps 3.7×10^4 and 4.0×10^4 . A comparison of the two cases indicates that the block migration altered the results just marginally.....41

Figure 4.7: Vertical velocity contours, and location of the fine block with respect to the cylinder at coarse time step 3.6×10^4 42

Figure 4.8: (a) Graphs for the dimensionless mass flux at coarse time step 3.5×10^4 , calculated for checking the quality of the data transfer through the grid interface between the fine block and the downstream coarse block in the migrating multi-block model. Comparison between the results of the moving fine grid interface's nodes with those collected from the fixed multi-block coarse nodes which occupy the same locations. M and F in the figure stand for moving and fixed blocks, respectively.....43

Figure 4.8: (b) Graphs for the dimensionless momentum flux at coarse time step 3.5×10^4 , calculated for checking the quality of the data transfer through the grid interface between the fine block and the downstream coarse block in the migrating multi-block model. Comparison between the results of the moving fine grid interface's nodes with those collected from the fixed multi-block coarse nodes which occupy the same locations. M and F in the figure stand for moving and fixed blocks, respectively.....44

Figure 4.9: Drop mass center normalized lateral displacement by the migrating multi-block LBM compared with the solution of Murtazavi and Tryggvason (2000) for the case with $Re_d = 10.0$, $We = 16$, $\lambda = 8$ and $\zeta = 0.125$. No further data was provided for $x/H > 13.3$ since the drop reached the end of the domain (4000×300) in the MMB model measured in fine lattice. The inset in the figure is for the phase field contours of the droplet with superimposed snap shot from different time steps.....48

Figure 4.10: Normalized fluid average horizontal velocities (a), and normalized drop mass center displacements in the flow direction (b), for both the migrating block and the standard Gunstensen model versus dimensionless time.....49

Figure 4.11: Normalized lateral trajectory of the drop mass center (a) for the migrating block and the standard LBM measured with respect to dimensionless time. Normalized lift velocity (b) for the migrating block and the standard LBM calculated with respect to the dimensionless time.....50

Figure 4.12: Deformation indexes of the drops from both the standard LBM and the migrating multi-block calculated with respect to the dimensionless time.....52

Figure 4.13: Phase field contour for five consecutive snap shots taken at different time steps and superimposed in the figure. The blue blocks are fine, and the green blocks are coarse: (a) migrating multi-block and (b) standard LBM.....52

Figure 4.14: Illustration of the 3D multi-block lattice Boltzmann method domain comprising of two coarse blocks and one fine block.....57

Figure 4.15: Illustration of the grid interface plane at the beginning or the end of the fine block, where spatial and temporal interpolation are required.....58

Figure 4.16: 3D simulation of a rising bubble in an infinite medium with $M_0 = 821$, $E_0 = 374$ and $Re = 8.10$, velocity contour in the z direction for superimposed snap shots at three different time steps (left), 3D phase field contours where the fine migrating superimposed blocks are shown in blue and the coarse blocks in green (center), 2D cut of the density contour depicting the droplet profile during the various time steps (right).....61

Figure 4.17: Terminal velocity comparison and shape change with respect to the Eotvos number for values stated in Table 4.1.....62

Figure 4.18: Shape regime map by Grace 1973 used for locating the proposed model results for the various cases presented in Table 4.2. The model shows good fit within the three shape map regions.....63

Figure 4.19: Vertical velocity contour (left), phase field contour (center), and density contour (right) for a rising bubble with a density contrast $\gamma^{-1} = 10$, $M_0 = 193$, $E_0 = 88$ and $Re = 4.2$ 65

Figure 4.20: Vertical velocity contour (Left), phase field contour (center), and density contour (right) for two trailing bubbles with a density contrast $\gamma^{-1} = 2$, $M_0 = 985$, and $E_0 = 449$ 66

Figure 4.21: Phase field contours of two trailing bubbles taken at different time steps and superimposed in the same frame (left), graph for the changing dimensionless distance between the trailing bubbles with respect to time (center), 3 D phase field contours and their respective 2D cut views of

	selective snap shots intended to show various events such as trailing, collision and coalescence of the two bubbles (left).....	67
Figure 4.22:	Dimensionless mass flux measured at the upstream grid interface (plane B in Fig 4.14) for case five from Table 4.1 at 9000 coarse time steps, data collected from the coarse nodes (top left), data collected from the overlapping fine nodes (top right), and data collected from all the fine nodes (bottom).....	69
Figure 4.23:	Dimensionless momentum flux measured at the upstream grid interface (plane B in Fig 4.14) for case five from Table 4.1 at 9000 coarse time steps; data collected from the coarse nodes (top left), data collected from the overlapping fine nodes (top right), and data collected from all the fine nodes (bottom).....	70
Figure 4.24:	Phase field contours and bubble vertical displacement versus time steps comparison between the migrating multi-block simulation and the standard model with $M_0 = 682$, $E_0 = 311$, and $Re = 7.1$	72
Figure 4.25:	Illustration of 2D multi-block LBM domain, with two coarse blocks and one fine block.....	74
Figure 4.26:	Single component multiphase fluid EOS for different values of the interaction potential constant presented by Sukop and Or (2005) (Reprinted with permission).....	75
Figure 4.27:	Simulation domain with a fine block colored with blue placed immediately behind the orifice and two coarse blocks colored with red.....	76
Figure 4.28:	Top: Instantaneous streamlines of the flow through a non-central orifice with $Re \approx 788$ and $\rho_i = 450 [mu/lu^2]$. The vena contracta location was determined as the position where the streamlines were most densely packed indicating higher velocity and lower pressure region. Bottom: Velocity contour in the horizontal direction.....	77
Figure 4.29:	Pressure-density relationship for three different initial densities (Dotted line is to guide the eye). Phase separation occurred only for the initial density $\rho_i = 360 [mu/lu^2]$ since the pressure-density intersection point fell into the unphysical negative compressibility region shown in gray color. The figure insets are for the density contours from the three cases. The top left inset is from the experimental work of Mishra and Peles (2005). (Reprinted with permission).....	79

Figure 4.30: Instantaneous streamlines for time steps 2,000, 28,000 and 56,000 with increasing input velocity. The insets show the time advancing fine block in which the calculation is performed with more iterative steps.....	80
Figure 4.31: Horizontal component of the mass flux presented at three locations and three consecutive time steps.....	81
Figure 4.32: Phase field contours for four consecutive time steps, $Re_d = 9.07$ and $B = 1.66$ The migrating fine block (in blue) moved with the droplet in (A) and (B), then the droplet moved alone in (C) and settled on the wall in (D).....	85
Figure 4.33: Dimensionless droplet height and wall contact length for various Bond numbers. The lower inset show the 3D view of the droplet shapes and the upper inset is their 2D cuts.....	86
Figure 4.34: Phase field contours for four consecutive time steps with $G_{ads}^R = -0.11$, $G_{ads}^B = 0.14$ $B = 1.11$ and $Re_d = 5.52$	87
Figure 4.35: Comparison of the dimensionless droplet height and wall contact length for various Bond numbers between the wetting and the non-wetting droplet cases. The insets are the phase field contours for the wetting droplets.....	88
Figure 5.1: Initialization of the surfactant concentration at the interface of a 3D droplet: (A) 3D domain with a central droplet, (B) 2D view of the phase field showing the interface thickness, (C) 2D view of the uniform surfactant concentration contour on the interface.....	96
Figure 5.2: Flow chart for the hybrid LBM for surfactant covered- droplets.....	99
Figure 5.3: Illustration of the LBM simulation domain with a central clean droplet under simple shear stress and the three characteristic radii used in the analysis of the results.....	101
Figure 5.4: Comparison of the proposed numerical model results with the experimental and numerical results of Cristini et al. (2002) for a clean droplet dimensionless width as a function of the dimensionless time. The viscosity ratio is $\lambda = 0.1$, and the capillary number is $Ca = 4.6$. (Reprinted with permission).....	102
Figure 5.5: Interfacial area generation for droplets in simple shear flow with respect to initial surfactant coverage presented at a dimensionless time step $\dot{\gamma}t = 1.17$ $\dot{\gamma}t = 1.17$ and capillary number $Ca = 4.6$	104

Figure 5.6: (A) 2D view of the phase field contours from the central xz plane for the contaminated droplets. (B) 3D view of the phase field contours for the contaminated droplets surrounded by a fictitious block to show the variance in their dimensions. (C) 2D xz plane view of the surfactant concentration contours. (D) 2D xz plane view of the phase field contour for a clean drop. (E) 3D view of the phase field contour for the clean drop. (F) Graph representing the transient maximum values of the dimensionless surfactant concentration relative to dimensionless times. The results are for dimensionless time step $\dot{\gamma}t = 3.12$, capillary number $Ca = 4.6$, surfactant elasticity $E_0 = 0.2$ and Péclet number $Pe_s = 10$ 106

Figure 5.7: Interfacial area generation for droplets in simple shear flow with respect to surfactant elasticity presented at a dimensionless time step $\dot{\gamma}t = 1.17$ and capillary number $Ca = 4.6$ 107

Figure 5.8: (A) 2D view of the phase field contours from the central xz plane for clean droplets. (B) 3D view of the phase field contours for the contaminated droplets.(C) 2D view of the surfactant concentration contours in the xz plane. (D) 2D view of the phase field contour for the clean droplet in the xz plane. (E) 3D phase field contour for the clean droplet. (F) The graph represents the transient minimum values of the dimensionless surfactant concentration relative to dimensionless times. The results are for dimensionless time step $\dot{\gamma}t = 3.12$, capillary number $Ca = 4.6$, surfactant coverage $c_{in} = 0.2$, and Péclet number $Pe_s = 100$ 109

Figure 5.9: Interfacial area generation for droplets in simple shear flow with respect to the surface Péclet number presented at a dimensionless time step $\dot{\gamma}t = 1.17$ and capillary number $Ca = 4.6$ 110

Figure 5.10: (A) 2D xz view of the droplets phase field contours.(B) 3D view of the droplet phase field contours. (C) 2D view of the surfactant concentration contours. (D) The graph represents the dimensionless surfactant concentration relative to a position measured on the lower droplet circumference in the direction of the major axis. The results are for dimensionless time step $\dot{\gamma}t = 3.12$, surfactant elasticity $E_0 = 0.2$, surfactant coverage $c_{in} = 0.2$ and capillary number $Ca = 4.6$ 112

Figure 5.11: Phase field contours for a central droplet in uniaxial extensional flow.....113

Figure 5.12: (A-C) 2D xz view of the surfactant concentration contours for a central droplet in uniaxial extensional flow, for three values of the surfactant coverage. (D) Graph representing the dimensionless surfactant

concentration in the xz plane as a function of the horizontal coordinate normalized by the droplet radius for $\dot{\gamma}t = 0.604$, $Ca = 0.8$, $Pe_s = 100$ and $E_0 = 0.2$. The insets in the graph are for the 3D view of the phase field contours.....114

Figure 5.13: (A-C) 2D view of the surfactant concentration contours on droplets in uniaxial extensional for a range of capillary number $0.8 \leq Ca \leq 1.2$. (D) Graph representing the values of the droplet dimensionless R_1/R_0 , the dimensionless maximum Γ_{\max}^* and minimum Γ_{\min}^* surfactant concentration, respectively at dimensionless time step $\dot{\gamma}t = 0.604$. The insets in the graph are for the 3D view phase field contours.....115

Figure 5.14: (A) 2D yz view of the surfactant concentration contours is shown for a central droplet in uniaxial extensional (B) 2D yz view of the surfactant concentration of a droplet in simple shear flows. The capillary number for the extensional flow is $Ca = 0.8$ and the dimensionless time step $\dot{\gamma}t = 0.536$. The capillary number for the shear flow is $Ca = 4.6$ and the time step is $\dot{\gamma}t = 1.95$116

Figure 5.15: (A) Dimensionless terminal velocities for clean and contaminated buoyant droplets presented in the spherical region. (B) Dimensionless vertical location of the droplet mass center for the clean and the contaminated droplets. (C) 3D phase field contours for the clean droplet, (D) 3D phase field contour for the contaminated droplet. (E) 2D xz plane view of the surfactant concentration contour for the contaminated droplet. The dimensionless time step is $t/\sqrt{d/g} = 43.3$. The simulation was executed with acceleration constant $g = 2.0 \times 10^{-5}$, Morton number $M_o = 61.7$, Eotvos number $E_o = 11.5$ and Reynolds number $Re = 0.34$ 119

Figure 5.16: (A) Dimensionless terminal velocities for clean and contaminated buoyant droplets presented in the spherical-cap region. (B) Dimensionless vertical location of the droplet mass center for the clean and the contaminated droplets. (C) 3D phase field contours for the clean droplet. (D) 3D phase field contour for the contaminated droplet. (E) 2D view of the surfactant concentration contour for the contaminated droplet. The dimensionless time step is $t/\sqrt{d/g} = 49.07$. The simulation was executed with acceleration constant $g = 2.0 \times 10^{-4}$, Morton number $M_o = 617$, Eotvos number $E_o = 115$ and Reynolds number $Re = 2.6$ 120

Figure 6.1:	Two approaching droplets in a hypothetical shear flow, with the required forces for suppressing the coalescence without altering the droplets shape.....	125
Figure 6.2:	The limiting condition for determining the dimensionless function $\lambda(\alpha)$ and its curve fit, for $c_{in}^* = 1$	126
Figure 6.3:	(A) Phase field contours for droplets in quiescent flow and $c_{in}^* = 0$ for the various dimensionless time steps $t\sigma/\mu R$. (B) Phase field contours for the droplets with $c_{in}^* = 1$ for the same time steps. (C-D) Pressure contours for the droplets with time varying interaction forces.....	128
Figure 6.4:	(A) Phase field contours from the standard LBM $c_{in}^* = 0$, in which coalescence occurs instantaneously after collision. (B) Phase field contours from the proposed model $c_{in}^* = 1$ in which the coalescence is suppressed. The horizontal velocity profile at $x/H = 0.77$ is superimposed on the phase field contours.....	130
Figure 6.5:	(A) Schematic of the 2D domain of thickness $W = 1$ used for the derivation of the effective viscosity. (B) Phase field contours for two droplets in a simple shear flow with an indication of the used boundary conditions.....	132
Figure 6.6:	Dimensionless velocity profiles for the wall's adjacent nodes for various capillary numbers at dimensionless time steps $\dot{\gamma}t = 0.39$	134
Figure 6.7:	Effective viscosity of a binary fluid suspension calculated with respect to the volume fraction of the dispersed phase by Eq. (6.11) to Eq. (6.14) and by the numerical results of the proposed model Eq. (6.9). The insets are for the phase field contours.....	137
Figure 6.8:	Effects of the capillary number on the relative viscosity of a binary mixture for two volume fractions $\phi = 0.270$ and $\phi = 0.405$, constant shear rate $\dot{\gamma} = 9.75 \times 10^{-6} [ts^{-1}]$ and variable interfacial tension at dimensionless time step $\dot{\gamma}t = 0.39$	138
Figure 6.9:	Effects of the surfactant surface coverage on the relative viscosity of a droplet based immiscible mixture. The capillary number is $Ca = 0.01$ and the dimensionless time step is $\dot{\gamma}t = 0.39$	139

Figure 7.1:	Illustration of the adjustable zonal division of the interface with regions of higher (frontal) and lower (backside) interfacial tension. The darker contours show greater surface tension parameter α from Eq. (2.16). (A) Shows homogeneous α value, (B) quarter of the interface had lower α value; (C) the interface was shared equally between high and low values of α	143
Figure 7.2:	Phase field and horizontal velocity contours for four droplets streaming in a narrow vessel with homogeneous surface tension parameter (A), and with zonal averaged non-isotropic surface tension parameter whose values were explained in Fig. 7.1 for insets (B) and (C).....	146
Figure 7.3:	Phase field contours and their respective horizontal velocity contours for surface tension parameters $1.5 \times 10^{-7} \leq \alpha_0 \leq 1.05 \times 10^{-6}$ by a step of $\delta_{\alpha_0} = 3.0 \times 10^{-7}$	147
Figure 7.4:	Droplet velocity and DI dependence on the surface tension parameter.	148
Figure 7.5:	Criteria for accepting or rejecting the gap measurement along the length of the RBC used for calculating the average width. For $\theta < 11$ degree the record is taken otherwise it is rejected.....	150
Figure 7.6:	Droplet-wall gap width comparison of the proposed model with the data generated from Secomb et al. (2001). (Glycocalyx indicates that the endothelial cell layer was considered in Secomb's model and no glycocalyx indicates otherwise).....	151
Figure 7.7:	Droplet-wall gap, DI, and length calculate with respect to the droplet velocity.....	152
Figure 7.8:	Dependence of the wall-droplet gap width on the velocity. The gap increased with increasing the velocity, and the droplet elongated while distancing itself from the wall.....	153
Figure 7.9:	Dependence of the wall-droplet gap width on the velocity. The gap increased with increasing the velocity, and the droplet elongated while distancing itself from the wall.....	154
Figure 7.10:	Left-phase field contours and horizontal velocity profile for 285x41 lattice sites and 0.17, 0.25 and 0.33 discharge hematocrit. Right-horizontal velocity profile measured at the middle of the domain.....	155
Figure 7.11:	The graph represents the dependence of the Fahraeus effect on the discharge hematocrit. Comparison of the model results with the results of Sun and Munn (2005).....	156

Figure 7.12: Phase field contours and pressure contours for six different time steps. The pressure contours show a pressure difference between regions below and above the wall-side droplets. The phase field contours show the axial migration of the near-wall droplets.....157

Figure 7.13: Graph representing the axial migration of the near-walls droplets. Normalized displacement of the droplet mass center versus the corresponding time step multiplied by the shear rate of the mid location between the wall and the center of the channel.....158

NOMENCLATURE

ξ		Macroscopic physical velocity
λ		Physical relaxation time
$f_i(\mathbf{x}, t)$		Density distribution function
$f_i^{eq}(\mathbf{x}, t)$		Equilibrium density distribution function
\mathbf{e}_i		Lattice link
\mathbf{c}_i		Lattice velocity in the i^{th} direction
δ_t		Lattice time step
τ		Lattice relaxation time
ρ		Macroscopic density
ω_i		Weighting constant
c_s		Lattice speed of sound
p		Macroscopic pressure
ν		Kinematic viscosity
\mathbf{u}		Macroscopic velocity
$R_i(\mathbf{x}, t)$		Red fluid distribution function
$B_i(\mathbf{x}, t)$		Blue fluid distribution function
$\phi(\mathbf{x})$		Source term
$\mathbf{F}(\mathbf{x})$		Macroscopic force
\mathbf{u}^*		Corrected macroscopic velocity

k	Interface curvature
k_2	Forcing term constant
ρ^N	Phase field
n_x	Interface normal component
n_y	Interface normal component
$\hat{f}_i(\mathbf{x}, t)$	Post-collision distribution function
$\hat{R}_i(\mathbf{x}, t)$	Post-segregation red fluid distribution function
$\hat{B}_i(\mathbf{x}, t)$	Post-segregation Blue fluid distribution function
β	Segregation parameter
θ_f	Polar angle of the color field
$\mathbf{G}(\mathbf{x}, t)$	Local color gradient
\mathbf{J}	Local color flux
θ_i	Polar angle of the velocity link
G	Interaction strength constant
ψ	Potential function of the density
\mathbf{u}'	Composite macroscopic velocity
σ	Various mixture contributing components
$\mathbf{F}^\sigma(\mathbf{x}, t)$	Interaction force
$G_{\sigma\sigma}$	Constant for the surface tension
$\mathbf{N}^\sigma(\mathbf{x}, t)$	Fluid-solid interaction force

G_{ads}^σConstant for the fluid-solid interaction strength
$E^\sigma(\mathbf{x}, t)$Gravitational force
mGrid ratio
$\delta_{x,c}$Coarse lattice spacing
$\delta_{x,f}$Fine lattice spacing
τ_cCoarse grid relaxation time
τ_fFine grid relaxation time
M_jSecond order derivatives of the distribution function
\hat{f}_i^fPost-collision distribution function in the fine block
\hat{f}_i^cPost-collision distribution function in the coarse block
$f_i^{c,u}(\mathbf{x}, t)$Coarse distribution function in the upstream block
$f_i^{c,d}(\mathbf{x}, t)$Coarse distribution function in the downstream block
HThe channel height
UCenterline velocity
\bar{U}Average velocity
StStrouhal number
fFrequency of separation
C_LLift coefficient
C_DDrag coefficient
F_LLift force

F_D	Drag force
ζ	Ratio of the drop radius to the channel height
We	Weber number
DI	Deformation index
Ca	Capillary number
Ga	Time gain
γ	Density ratio
γ^{-1}	Density ratio
α	Interfacial tension parameter
ρ_{sp}	Spinodal density
P_{sp}	Spinodal pressure
λ_c	Cavitations number
Q	Volume flow rate
\dot{m}	Mass flow rate
B	Bond number
Γ	Surfactant concentration
\mathbf{u}_n	Normal velocity
\mathbf{u}_s	Tangential velocity
D_s	Diffusion constant
Pe_s	Surface Péclet number
$\dot{\gamma}$	Shear rate

R_0	Un-deformed droplet radius
E_0	Surfactant elasticity
Γ_∞	Saturation surfactant concentration
σ_0	Clean droplet interfacial tension
σ_s	Contaminated interfacial tension
c_{in}	Surfactant coverage
E_o	Eotvos number
M_o	Morton number
Re	Reynolds number
U_{HR}	Hadamard-Rybszynski terminal velocity
U_{Th}	Particle terminal velocity
U_M	Numerical terminal velocity
μ	Dynamic viscosity
η	Viscosity ratio
$S(x)$	Repulsive force magnitude
c_{in}^*	Nonlinear function of the ratio of the initial surfactant coverage
\mathbf{T}	Unit tangent to the interface
μ_{eff}	Effective viscosity
μ_{rel}	Relative viscosity
ϕ	Volume fraction

η_sViscosity of the spheres
 η_0Viscosity of the ambient fluid
 Γ_fFrontal initial surfactant concentration
 Γ_bBackside initial surfactant concentration
 Γ_iInitial surfactant concentration
 H_TTube hematocrit
 H_DDischarge hematocrit

CHAPTER 1

INTRODUCTION

1.1 Colloids

Colloids are chemical mixtures with one substance dispersed into the other. Colloids are characterized by a high surface to volume ratio or surface to mass ratio. This enables their inter-particle forces to alter the gravity effects. The focus of this work is on emulsions, one type of colloids in which the continuous medium and the dispersed phase are both immiscible liquids, although the proposed model can handle with comfort other types of colloids such as foams and liquid aerosols.

The study of droplet-base immiscible mixtures is of high interest for broad range of research works in the food, medical, cosmetic, polymer, water purification and pharmaceutical industries. Macro-emulsions such as water-in-oil (W/O) or oil-in-water (O/W) are indispensable in the makeup of a great number of frequently used products. To satisfy a large and diverse market demands, polymer manufacturing industries strive constantly to supply new blends with enhanced thermal and mechanical behavior. Droplet-based microfluidic systems provide a highly controllable platform for applications such as micro-reactors, drug delivery systems and information carriers on microfluidic chips containing digital logic gates.

The control of the droplet size during the production of such systems is of extreme importance. Conventional methods such as rotor-stator or more current methods like membrane emulsification (van der Graaf, 2006) are used to control the droplet size of an emulsion during formation. The required morphology of polymer blends is dependent on the rapid establishment of the equilibrium between droplet

break up and coalescence (Sundararaj and Macosko, 1995). Microfluidic droplets have to be generated in a specific frequency and sizes in order to deliver stable and repetitive functions.

The control of the droplet size is accomplished mainly by the addition of surface acting agents (surfactants), which adhere to the droplet interface and reduce the interfacial tension. Surfactants play also an important role in suppressing coalescence of the dispersed phase, and they affect the rheology of the droplet-based immiscible mixtures as a result of the intricate interplay of the evolution of surfactant distribution, drop deformation and the bulk flow (Vlahovska and Loewenberg, 2005).

Biological fluids such as saliva, urine, blood, etc are macro-colloids by nature. One of the most interesting biological fluids is blood. Blood is a biological suspension composed of 55% plasma and 45% formed elements of which 99.5% are red blood cells (RBC), 0.13% white blood cells (WBC) and 4.9% platelets. In the capillaries the membrane of the RBC fluidizes under pressure, making it feasible to approximate the cell as a surfactant covered droplet.

Historically polymer production in the USA was characterized by an exponential growth as shown in Fig 1.1 (A) (Chemical and Engineering News, 1996). 40% of this production serves as functional materials such as cosmetics, pharmaceuticals, printing ink, paints, super-absorbers in hygienic products, etc.

Another area of relevance to this study is the investigation of biological suspensions, in particular blood and blood related diseases. In 2004 an estimated 223,000 death were due to blood diseases. 214,000 were caused by blood-clotting disorders a major contributor to acute myocardial infarction (AMI) and cerebrovascular

diseases. 9,000 were attributed to red blood cell and bleeding disorders. Blood clotting disorders were expected to cost the nation's economy an amount of 105 billion, in addition to 14 Billion Dollars due to other blood diseases in 2008 (www.nhlbi.nih.gov/about/factbook-07). Figure 1.1 (B) shows the mortality rate due to blood related diseases in 2004.

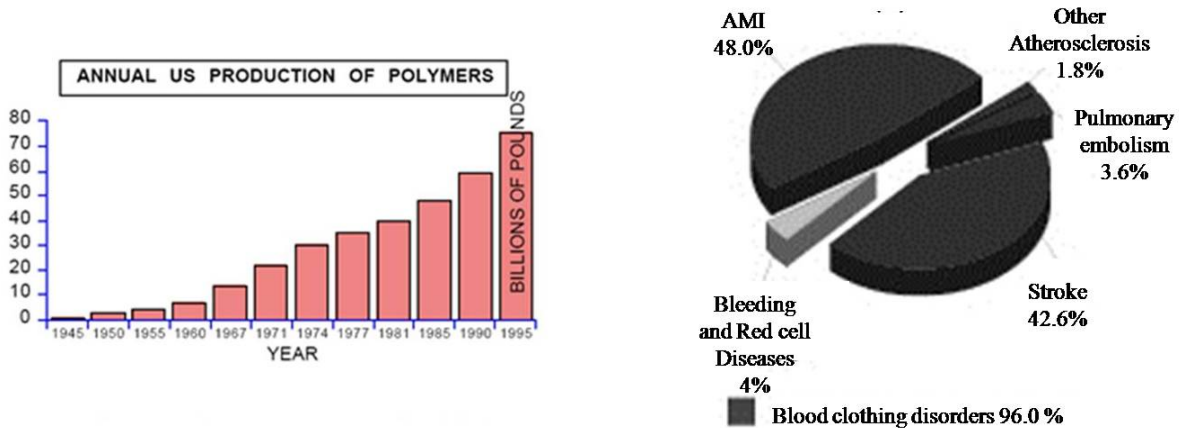


Fig 1.1 (A) Annual US polymers production showing an exponential growth. (B) Death percentage rate in the US in 2004 due to blood-related diseases.

2.1 Numerical methods for colloidal studies

The last couple decades have witnessed a considerable advancement in the computer technology which manifested itself by an exponential growth in computing powers. This made it possible to explore the full potential of an already matured branch of mathematics (numerical methods) which became a primary tool for the study of a variety of fluid problems. Colloids and biological suspensions had been the subject of investigations by a great number of numerical researchers who used large diversity of methods such as the boundary integral (Millikan et al., 1993; Li and Pozradikis, 1997; Eggleton et al., 2001; Feigl et al., 2007), the volume of fluid method (Drumright-Clarke, 2002; Drumright-Clarke and Renardy, 2004), the finite element method (Kruijt-

Stegeman et al.; 2004), the immersed boundary method (Lai et al.; 2008), the lattice Boltzmann method (LBM) (van der sman and van der Graaf, 2006). These methods were used for the study of colloids. Another methods were used for the study of blood flows, such as the immersed finite element method (Liu and Liu, 2006), the particle method (Tsubota and Yamagushi, 2006), the LBM (Dupin et al., 2003; Dupin et al. 2005; Sun and Munn, 2005) and the hybrid LBM (Dupin et al., 2007). In this work an accelerated multi-component LBM scheme with incorporated surfactants effects will be proposed and used for the study of colloids and biological fluids.

CHAPTER 2

RESEARCH RELATED STUDIES

3.1 The lattice Boltzmann method

Computational fluid dynamics (CFD) represents a powerful tool for the study of complex multi-phase and multi-component flows. Drop formation, deformation, coalescence and break-up continues to be the focus of many research works, devoted for a better understanding of microfluidic, colloids and polymers properties. Among many CFD tools, the lattice Boltzmann method (LBM) has attracted some attention during the last couple decades due to the simplicity of its algorithm, stability, and parallelism.

a. The single component LBM

The Bhatnagar-Gross-Krook (BGK) lattice Boltzmann method is an alternative computational technique used for solving a broad range of fluid problems. The isothermal, single-relaxation model is derived from the following Boltzmann kinetic equation (Yu et al. 2002):

$$\frac{df}{dt} + \xi \cdot \nabla f = -\frac{1}{\lambda}(f - f^{eq}) \quad (2.1)$$

where f is the density distribution function, ξ is the macroscopic velocity, f^{eq} is the equilibrium distribution function, and λ is the physical relaxation time. Equation (2.1) is first discretized by using a set of velocities ξ_i confined to a finite number of directions and this leads to the following equation:

$$\frac{df_i}{dt} + \xi_i \cdot \nabla f_i = -\frac{1}{\lambda}(f_i - f_i^{eq}) \quad (2.2)$$

The LBM is based on a set of equivalent Cartesian velocities. The D2Q9 BGK described here has nine velocity direction vectors (lattice links) shown in Fig 2.1 (A) with the following end points coordinates:

$$e_0(0,0); e_1(-1,1); e_2(0,1); e_3(1,1); e_4(1,0); e_5(1,-1); e_6(0,-1); e_7(-1,-1); e_8(-1,0) \quad (2.3)$$

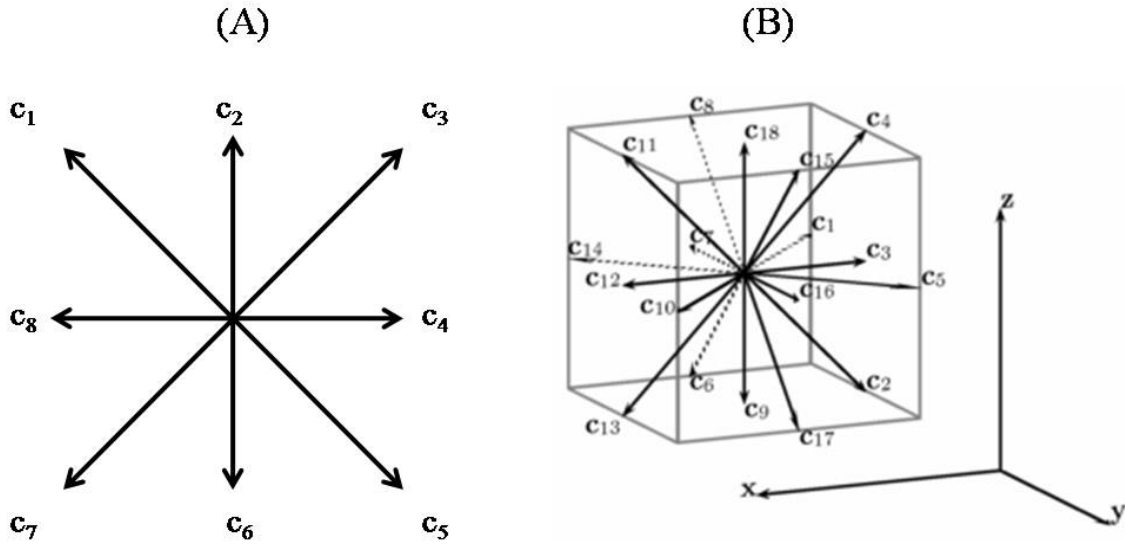


Fig 2.1 (A) Velocity vectors for the D2Q9 and (B) for the D3Q19 lattice Boltzmann method used in this study.

Figure 2.1 (B) show the lattice links for the D3Q19 model. Equation (2.2) is further discretized in the lattice space and time and this leads to the following:

$$f_i(\mathbf{x} + \mathbf{c}_i \delta_t, t + \delta_t) - f_i(\mathbf{x}, t) = -\frac{1}{\tau} [f_i(\mathbf{x}, t) - f_i^{eq}(\mathbf{x})] \quad (2.4)$$

The lattice space δ_x and the lattice time step δ_t are taken as unity and their ratio $c = \delta_x / \delta_t = 1$ is the lattice velocity. The lattice speed of sound is used for determining the fluid pressure by $p = \rho c_s^2$, and the lattice relaxation time is $\tau = \lambda / \delta_t$. The kinematic viscosity is derived from the relaxation time by the following formula:

$$\nu = (\tau - 0.5) c_s^2 \delta_t \quad (2.5)$$

The equilibrium distribution function of Eq. (2.4) is calculated as follows:

$$f_i^{eq} = \rho \omega_i \left[1 + \frac{3}{c^2} \mathbf{c}_i \cdot \mathbf{u} + \frac{9}{2c^4} (\mathbf{c}_i \cdot \mathbf{u})^2 - \frac{3}{2c^2} \mathbf{u} \cdot \mathbf{u} \right] \quad (2.6)$$

where $\mathbf{c}_i = \mathbf{e}_i / \delta_i$ is the lattice velocity in the i^{th} direction, ω_i are the weighting constants for the various lattice links:

$$\omega_i = [4/9; 1/36; 1/9; 1/36; 1/9; 1/36; 1/9; 1/36; 1/9] \quad (2.7)$$

\mathbf{u} and ρ are the macroscopic velocity and density, respectively. The macroscopic density and momentum are calculated from the distribution function as follows:

$$\rho = \sum_{i=0}^{Q-1} f_i = \sum_{i=0}^{Q-1} f_i^{eq} \quad (2.8)$$

$$\rho \mathbf{u} = \sum_{i=1}^{Q-1} \mathbf{c}_i f_i = \sum_{i=1}^{Q-1} \mathbf{c}_i f_i^{eq} \quad (2.9)$$

where Q depends on the dimension and the type of the LBM model.

Through a Chapman-Enskog expansion in the low frequency, long wavelength limits, and at low Mach number, the LBM can recover the Navier-Stokes equations to a second order accuracy if the right choice of the equilibrium distribution function is used (Chen et al., 1992; Guo et al., 2000; Latt, 2007).

b. The multi-component LBM

The most famous multi-component LBM schemes are the Gunstensen model (Gunstensen et al., 1991) and the particle-interaction-potential model (Shan and Chen, 1993; Shan and Chen, 1994). Both schemes were used in this work.

The Gunstensen model

The Gunstensen model identifies a red and a blue momentum distribution functions as $R_i(x, t)$ and $B_i(x, t)$, where x and t are the nodal position and time,

respectively. The total momentum distribution function is the sum of the two functions (Gunstensen et al. 1991):

$$f_i(\mathbf{x}, t) = R_i(\mathbf{x}, t) + B_i(\mathbf{x}, t) \quad (2.10)$$

The main difference between the two-component and the single component LBM is the modification of the collision rules in order to induce surface tension and segregate the two immiscible fluids. This is achieved by applying two-step collision rules (Gunstensen et al., 1991; Halliday et al., 2005; Halliday et al., 2006; Halliday et al., 2007, Hollis et al., 2007; Reis and Philip, 2007). The main streaming and collision function is expressed as follows:

$$f_i(\mathbf{x} + \mathbf{c}_i \delta_i, t + \delta_i) = f_i(\mathbf{x}, t) - \frac{1}{\tau} \{f_i(\mathbf{x}, t) - f_i^{eq}(\rho, \rho \mathbf{u})\} + \phi_i(\mathbf{x}) \quad (2.11)$$

where \mathbf{c}_i is the lattice velocity vector in the i^{th} direction shown in Fig. 2.1, τ is the lattice relaxation time, $\phi_i(\mathbf{x})$ is a source term used to induce an interfacial pressure step in the fluid mixture as per Lishchuk's interface method (Lishchuk et al., 2003; Lishchuk et al., 2008). The source term can also enclose a force in the flow direction, which causes fluid circulation. To define the interface between the two fluids, a phase field is described as follows (Halliday et al. 2007):

$$\rho^N(\mathbf{x}, t) = \frac{R(\mathbf{x}, t) - B(\mathbf{x}, t)}{R(\mathbf{x}, t) + B(\mathbf{x}, t)} \quad (2.12)$$

where N indicates the direction normal to the interface and the nodal red and blue densities are expressed by the following:

$$R(\mathbf{x}, t) = \sum_0^{Q-1} R_i(\mathbf{x}, t) \quad (2.13)$$

$$B(\mathbf{x}, t) = \sum_0^{Q-1} B_i(\mathbf{x}, t) \quad (2.14)$$

The two fluids can have different viscosities. This requires the use of different relaxation times in Eq. (2.5). The interface is made of a fluid mix; therefore its viscosity is determined by the following equation (Dupin et al. 2003):

$$v_{eff} = (\tau_{eff} - 0.5)c_s^2 \delta_t = \left(\frac{R}{R+B} \right) v_R + \left(\frac{B}{R+B} \right) v_B \quad (2.15)$$

Lishchuk's interface method is implemented to create a pressure step across the interface. The following surface tension force $\mathbf{F}(\mathbf{x})$ is used (Lishchuk et al. 2008):

$$\mathbf{F}(\mathbf{x}) = -\frac{1}{2} \alpha k \nabla \rho^N \quad (2.16)$$

where $\nabla \rho^N = 0$ for a constant phase field. This means that this force is only applicable on the interface. α is a surface tension parameter and k is the curvature of the interface. k is obtained from the surface gradients by solving the following equation using the finite difference method (Lishchuk et al., 2003):

$$k = n_x n_y \left(\frac{\partial n_x}{\partial y} + \frac{\partial n_y}{\partial x} \right) - n_x^2 \frac{\partial n_y}{\partial y} - n_y^2 \frac{\partial n_x}{\partial x} \quad (2.17)$$

where n_x, n_y are the x and y components of the interface normal vector $\mathbf{n} \equiv -\nabla \rho^N / |\nabla \rho^N|$. $\mathbf{F}(\mathbf{x})$ from Eq. (2.16) is used to correct the velocity by Guo's methodology (Guo et al., 2002; Dupin et al., 2003) as follows:

$$\mathbf{u}^* = \frac{1}{\rho} \left[\sum_{i=1}^{Q-1} f_i \mathbf{c}_i + \frac{1}{2} \mathbf{F}(\mathbf{x}) \right] \quad (2.18)$$

The relation between the macroscopic and a spatially varying lattice source term is by the following:

$$\phi_i(\mathbf{x}) = \omega_i \left(1 - \frac{1}{2\tau}\right) \left[3(\mathbf{c}_i - \mathbf{u}^*) + 9(\mathbf{c}_i \cdot \mathbf{u}^*)\mathbf{c}_i\right] \cdot \mathbf{F}(\mathbf{x}) \quad (2.19)$$

where \mathbf{u}^* is the corrected velocity from Eq. (2.18). For constant body force this relationship is expressed by the following equation (Halliday et al. 2007):

$$\phi_i = \omega_i \frac{1}{k_2} \mathbf{F} \cdot \mathbf{c}_i \quad (2.20)$$

where $k_2 = 1/3$ and \mathbf{F} is a constant macroscopic force such as a body force. The first collision is then applied using the corrected velocities in the calculation of the equilibrium distribution function $f^{eq}(\rho, \rho\mathbf{u})$. The second step is the segregation of the two fluids which is achieved by imposing zero diffusivity of one color into the other (Gunstensen et al., 1991). A local color gradient is identified as follows:

$$\mathbf{G}(\mathbf{x}, t) = \sum_{ij} \mathbf{c}_i \left(R_j(\mathbf{x} + \mathbf{c}_i, t) - B_j(\mathbf{x} + \mathbf{c}_i, t) \right) \quad (2.21)$$

A local color flux is calculated by the following formula:

$$\mathbf{J} = \sum_i \mathbf{c}_i \left(R_i(\mathbf{x}, t) - B_i(\mathbf{x}, t) \right) \quad (2.22)$$

The segregation step is achieved by forcing the local color flux to align with the direction of the local color gradient. Thus the colored distribution functions at the interface are redistributed such that $-\mathbf{J} \cdot \mathbf{G}$ is maximized with the following constraints:

$$\begin{aligned} \sum_i \widehat{R}_i(\mathbf{x}, t) &= R(\mathbf{x}, t) \\ \widehat{B}_i(\mathbf{x}, t) &= \widehat{f}_i(\mathbf{x}, t) - \widehat{R}_i(\mathbf{x}, t) \end{aligned} \quad (2.23)$$

where $\widehat{B}_i, \widehat{f}_i, \widehat{R}_i$ are the post-collision post-segregation blue, total, and red distribution functions respectively. The segregation can also be accomplished by a formulaic means

as described in the model of Halliday et al. (2007) in accordance with the method of D'Ortona et al. (1995):

$$\begin{aligned}\widehat{R}_i(\mathbf{x}, t + \delta_t) &= \frac{R}{R+B} \widehat{f}_i(\mathbf{x}, t + \delta_t) + \beta \frac{RB}{R+B} \omega_i \cos(\theta_f - \theta_i) |\mathbf{c}_i| \\ \widehat{B}_i(\mathbf{x}, t + \delta_t) &= \frac{B}{R+B} \widehat{f}_i(\mathbf{x}, t + \delta_t) - \beta \frac{RB}{R+B} \omega_i \cos(\theta_f - \theta_i) |\mathbf{c}_i|\end{aligned}\quad (2.24)$$

where θ_f and θ_i are the polar angle of the color field, and the angle of the velocity link respectively, β is the segregation parameter. After the segregation process the two components propagate separately as follows:

$$R_i(\mathbf{x} + \mathbf{c}_i \delta_t, t + \delta_t) = \widehat{R}_i(\mathbf{x}, t + \delta_t) \quad (2.25)$$

$$B_i(\mathbf{x} + \mathbf{c}_i \delta_t, t + \delta_t) = \widehat{B}_i(\mathbf{x}, t + \delta_t) \quad (2.26)$$

In the proposed work the Gunstensen (numerical) and D'ortona (formulaic) segregation methods were used although the numerical method produces thinner interface required for the application of the model for problems with droplets of relatively small diameter.

The Shan and Chen model

The Shan and Chen model is suitable for simulating multiphase and multi-component flows. The model uses the following interaction force between the particles of the same specie (Sukop and Thorne, 2006):

$$\mathbf{F}(\mathbf{x}, t) = -G\psi(\mathbf{x}, t) \sum_{i=0}^{Q-1} \omega_i \psi(\mathbf{x} + \mathbf{c}_i \delta_t, t) \mathbf{c}_i \quad (2.27)$$

where G is an interaction strength constant which determines the magnitude of the interaction force, and its sign imposes attraction (negative) or repulsion (positive) between the fluid particles. ψ is a potential function of the density, it must be monotonic and bounded (Shan and Chen, 1993; Shan and Chen, 1994):

$$\psi(\rho) = \psi_0 \exp(-\rho_0/\rho) \quad (2.28)$$

where ψ_0 and ρ_0 are constant used to control the potential function. The equilibrium velocity \mathbf{u}^{eq} used for the calculation of the equilibrium distribution function prior to the collision step has to be modified and the interaction force has to be imposed using the method of Buick and Greated (2000) for applying an external force into the LBM:

$$\mathbf{u}^{eq} = \mathbf{u} + \frac{\tau \mathbf{F}}{\rho} \quad (2.29)$$

where \mathbf{u} and ρ are the macroscopic velocity and density calculated by Eq. (2.8) and Eq. (2.9). With the modified equilibrium distribution function, a Chapman-Enskog expansion leads to the recovery of the isothermal Navier-Stokes equation (Shan and Chen, 2003). The pressure-density relationship is governed by the following equation of state (EOS):

$$p = \rho c_s^2 + \frac{G\psi^2(\rho)}{2} c_s^2 \quad (2.30)$$

The multi-component SC model deals with more than one fluid; therefore a composite macroscopic velocity is used to account for all the constituents of the mixture. Equation (2.8) and Eq. (2.9) are thus replaced by the following (Sukop and Thorne, 2006):

$$\rho^\sigma = \sum_{i=0}^{Q-1} f_i^\sigma = \sum_{i=0}^{Q-1} f_i^{\sigma,eq} \quad (2.31)$$

$$\mathbf{u}' = \frac{\sum_{\sigma} \frac{1}{\tau^\sigma} \sum_{i=1}^{Q-1} \mathbf{c}_i f_i^\sigma}{\sum_{\sigma} \frac{1}{\tau^\sigma} \rho^\sigma} \quad (2.32)$$

where σ refers to the various mixture contributing components, τ^σ is the individual

component relaxation time from which different fluids viscosities can be derived using Eq. (2.5).

The fluid-fluid interaction force is represented by the following equation (Martys and Chen, 1996):

$$\mathbf{F}^\sigma(\mathbf{x}, t) = -\rho^\sigma(\mathbf{x}, t) \sum_{\sigma'} G_{\sigma\sigma'} \sum_{i=0}^{Q-1} \rho^{\sigma'}(\mathbf{x} + \mathbf{c}_i \delta_t, t) \mathbf{c}_i \quad (2.33)$$

where $\mathbf{F}^\sigma(\mathbf{x}, t)$ is the interaction force exerted on component σ by the neighboring component σ' in the mixture. It is worth mentioning that the magnitude of this force, which creates a pressure jump across the fluid-fluid interface, is dependent on the constant $G_{\sigma\sigma'}$ and it determines the strength of the surface tension.

The fluid-solid interaction force exerted by each fluid component is expressed as follows (Martys and Chen, 1996):

$$\mathbf{N}^\sigma(\mathbf{x}, t) = -\rho^\sigma(\mathbf{x}, t) \sum_{i=0}^{Q-1} G_{ads}^\sigma S(\mathbf{x} + \mathbf{c}_i \delta_t) \mathbf{c}_i \quad (2.34)$$

where $S(\mathbf{x} + \mathbf{c}_i \delta_t)$ can only have a zero value for neighboring fluid node, and one for neighboring solid node respectively. G_{ads}^σ determines the interaction strength and it is positive for non-wetting fluid, and negative for wetting fluid. The force due to gravity is incorporated in the model through the following:

$$\mathbf{E}^\sigma(\mathbf{x}, t) = \rho^\sigma(\mathbf{x}, t) \mathbf{g} \quad (2.35)$$

where \mathbf{g} is the gravitational constant. The collision step is calculated by the following equation:

$$\widehat{f}_i^\sigma(\mathbf{x}, t + \delta_t) = f_i^\sigma(\mathbf{x}, t) - \frac{1}{\tau^\sigma} [f_i^\sigma(\mathbf{x}, t) - f_i^{\sigma, eq}(\rho, \rho \mathbf{u}^{\sigma, eq})] \quad (2.36)$$

where \widehat{f}_i^σ refers to post-collision distribution functions for the various fluids, and τ^σ are their corresponding relaxation times. The equilibrium functions for the constituent fluids are calculated by Eq. (2.6) using the following equilibrium velocities:

$$\mathbf{u}^{\sigma,eq} = \mathbf{u}' + \frac{\tau^\sigma (\mathbf{F}^\sigma + \mathbf{N}^\sigma + \mathbf{E}^\sigma)}{\rho^\sigma} \quad (2.37)$$

The streaming step is executed for the various fluids using the following equation:

$$f_i^\sigma(\mathbf{x} + \mathbf{c}_i \delta_t, t + \delta_t) = \widehat{f}_i^\sigma(\mathbf{x}, t + \delta_t) \quad (2.38)$$

This is followed by calculating the macroscopic observables using Eq. (2.31) and Eq. (2.32).

c. Grid refinement methods

To extend the applicability of the LBM to a variety of problems including those with turbulent flows, flows in complex geometries like porous media and special boundary shapes, several models were introduced to improve the LBM results quality, and to save computational time (Filippova and Hanel, 1998; He and Doolen, 1997; He et al., 1996; Huang et al., 2007; Imamura et al., 2005; Kandhai et al., 2000; Li et al., 2005; Lin and Lai, 2000; Liu et al., 2009; Shu et al. 2001; van der Sman, 2004; Yu and Girimaji, 2005; Yu et al., 2002). These models can be classified either by the method used: interpolation, hybrid LBM, and grid refinement, or by the nature of the grid: structured and unstructured grid.

Interpolation method was first used by He et al. (1996), who noticed that the density distribution function is continuous in the physical space; therefore it was possible to define it on non-uniform grid through interpolation. The method was further extended by Shu et al. (2001), and Li et al. (2005) who used Taylor series expansion and least square to evaluate the distribution function instead of direct interpolation.

Inamuro et al. (2005) used local time step on non-uniform grid to accelerate the solution since each grid point had its own time step based on the local advection time stability condition.

Hybrid LBM for unstructured grid combined LBM with traditional CFD tools like finite difference, finite volume, and finite element. Hybrid LBM benefited from the LBM stability, resulting from the use of the particle instead of macroscopic velocity. This guaranteed the satisfaction of the Courant-Friedrichs-Lewy (CFL) stability condition. Hybrid LBM gained also the accuracy and efficiency of the traditional CFD tools (Kandhai et al., 2000; Huang et al., 2007).

An interesting unstructured LBM model was proposed by van der Sman (2005), in which no interpolation was required, since particle velocity in this model was different for different lattice sites. This led to the elimination of the undesired numerical diffusion caused by the interpolation step.

Grid refinement methods worked by locally refining the mesh in parts of the domain characterized with complex geometry, and where higher accuracy was required. Filippova and Hanel (1998) introduced the first model which was based on passing data from the post collision distribution functions between the coarse and fine grids. The transfer of data maintained continuous viscosity and therefore Reynolds number throughout the domain. The model handled very well complex geometries by specially treating curved boundaries. Lin and Lai (2000) proposed a composite block-structured LBM in which a coarse grid covered the whole domain and only areas of interest were patched with a fine grid blocks. This method did not need time interpolation, because solutions on both grids were at the same time level. Yu et al (2002) suggested a very

efficient multi-block method in which fine and coarse grids did not overlap throughout the fine grid block, and data transfer occurred only at the interface boundary nodes. This method was later expanded to three dimensional models by Yu and Girimaji (2005).

Multiphase and multi-component flows were not as extensively studied with respect to grid refinement, as turbulent flows and near-solid boundary phenomena. The peculiarity of the multi-component flows is due to the movement and deformation of the suspended fluid. This hampers the use of preset grid refinement techniques since the area of interest is not fixed in the domain. Tolke et al (2006) proved in their Gunstensen based LBM, that the interface was distorted relative to the magnitude of the capillary forces. This was observed when they allowed the fluid interface to pass through the grid interface of different preset fixed grids. They also indicated through a mathematical model that the grid level which could be used in such cases was very restricted. Thus they resorted to the use of an adaptive grid method, in which the physical interface was always discretized on the finest grid level. Ozawa et al (2005) presented a model for multi-phase flow, with an adaptive unstructured grid. Ozawa et al (2005) used cubic interpolation with volume/area coordinates method for the streaming step and moving least-square method for the collision step. The mesh was refined based on a number density threshold using Bisection algorithm.

The grid refinement method of Yu et al (2002) will be extended in this work in what will be called the migrating multi-block scheme in order to allow its use for multiphase and multi-component flows. Yu et al (2002) proposed the following

relationships between the distribution functions of the various blocks shown in Fig 2.2.

The grid spacing ratio is expressed through the following equation:

$$m = \frac{\delta_{x,c}}{\delta_{x,f}} \quad (2.39)$$

The relationship between the relaxation times of the various blocks is expressed as follows:

$$\tau_f = \frac{1}{2} + m(\tau_c - 0.5) \quad (2.40)$$

The exchange of data between the various blocks occurs at the grid interface where fine and coarse nodes overlap through the following:

$$\widehat{f}_i^f = f_i^{eq,c} + \frac{\tau_f - 1}{m(\tau_c - 1)} [\widehat{f}_i^c - f_i^{eq,c}] \quad (2.41)$$

$$\widehat{f}_i^c = f_i^{eq,f} + m \frac{\tau_c - 1}{(\tau_f - 1)} [\widehat{f}_i^f - f_i^{eq,f}] \quad (2.42)$$

where the post-collision distribution function of the fine grid is \widehat{f}_i^f , while \widehat{f}_i^c is the post-collision distribution function of the coarse grid. A symmetrical cubic spline interpolation was used for spatial interpolation of the post-collision distribution functions on the fine block boundary.

A three-point Lagrangian formula was implemented in order to synchronize the time steps in the various blocks (Yu et al. 2002):

$$\widehat{f}_i^f(t) = \sum_{p=1}^3 [\widehat{f}_i^f(t_p) \prod_{q=1, q \neq p}^3 \frac{t - t_q}{t_p - t_q}] \quad (2.43)$$

where p, q are positive integers ranging from 1 to 3.

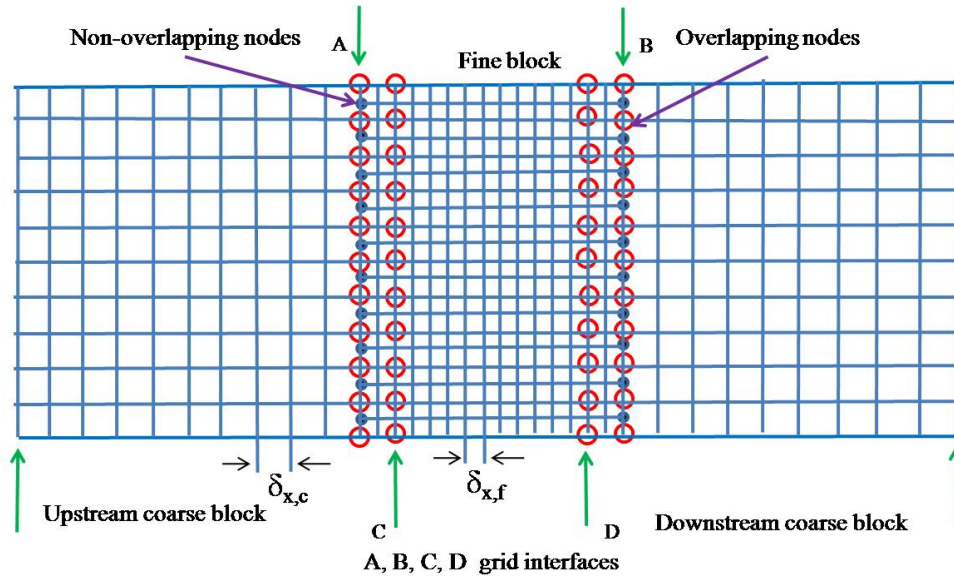


Fig 2.2 Illustration of the grid interfaces between the fine and the coarse block from the proposed multi-block scheme.

2.1 Colloidal studies

a. Surfactant-laden droplets

Surfactant-covered droplets were investigated experimentally, analytically and numerically. Sundararaj and Macosko (1995) studied the role of compatibilizers in stabilizing the morphology of some polymer blends as a result of suppressing the coalescence of the dispersed phase. Williams et al. (1997) investigated the effects of protein emulsifiers on the breakup of a single aqueous drop in shear flow, and found out that at high emulsifier concentrations the drop size was two orders of magnitude smaller than the expected size from its equilibrium interfacial tension. Lyu et al. (2002) used block copolymer to reduce the particle size in polymer blends and attributed this process to the steric repulsion which depended on the surfactant molecular weight. Hu and Lips (2003) delineated the individual effects of the dilution, the Marangoni stress and the tip stretching on surfactant covered mother drop by measuring the interfacial

tension of the subdivided generations of daughter drops. Almatroushi and Borhan (2004) examined the effect of surfactants on the buoyancy of bubbles and viscous drops in a bounded domain.

Vlahovska (2003) and Vlahovska et al. (2005) developed analytical solutions for the small perturbation of the surfactant distribution, which influenced the drop evolution in linear flows. The solutions for the system were formulated as a nonlinear matrix equation after expanding the velocity, surfactant concentration and the drop shape in spherical harmonics.

Milliken et al. (1993) studied the effect of dilute insoluble surfactant on the deformation of a drop in uniaxial extensional flow using boundary integral technique to describe the motion of the drop interface, and finite difference scheme for the mass transfer at the interface. Li and Pozridikis (1997) used similar numerical approach with a linear surfactant equation of state to study the transient deformation of spherical drop with viscosity ratio of one with respect to the matrix. Eggleton et al. (2001) studied tip streaming and drop breakup dependence on the surfactant initial coverage in linear extensional flow. Their model used boundary integral formulation for the Stokes equations, Runge-Kutta method for the interface time evolution and finite difference for the mass balance equation. Drumright-Clarke (2002) and Drumright-Clarke and Renardy (2004) used the volume of fluid method to track the interface, the projection method to solve the Navier-Stokes equations and the continuum method for the surface tension to model the effects of dilute insoluble surfactant on a drop in strong shear flow. Kruijt-Stegeman et al. (2004) used a finite element method to study the transient deformation of drops in supercritical elongational flow and the breakup of elongated

drops in quiescent medium with low surfactant coverage. The surface tension was incorporated into the finite element as a volume force. Lai et al. (2008) proposed an immersed boundary method for modeling fluid interfaces with insoluble surfactant in 2D geometries. A symmetric discretization for the surfactant concentration was employed to insure surfactant mass conservation numerically. Finally van der Graaf (2006) and van der Sman and van der Graaf (2006) used a free energy based LBM to develop a diffuse model for studying the adsorption of surfactant onto flat and drops interfaces. The model was tested briefly in 2D linear shear and uniform flow fields to show its applicability when coupled to the hydrodynamics.

The following studies (Lyu et al., 2002; Jeon and Makosco, 2003; Milliken et al., 1992; Hu and Lips, 2003; Cheng et al., 2005; Sundaraj and Makosco, 1995; Kleshchsnok and Lang, 2007) provide a good understanding of the physical interaction and deformation of droplets during their formation and breakup. The following facts are selected due to their relevance to the subject of this work:

- Surfactants reduce the surface tension and therefore enhance the deformability of the droplets by simply increasing their capillary number. The capillary number is the ratio of the viscous stress and the Laplace pressure $Ca = \frac{\mu R \dot{\gamma}}{\alpha}$, where μ is the viscosity of the suspending fluid R is the droplet radius, $\dot{\gamma}$ is the shear rate, and α is the surface tension. The surfactant role is affected by three additional mechanisms namely; surface dilution, which is due to the increase of the droplet area during deformation, tip-stretching which is caused by the convection of the surfactant towards the droplet tips due the bulk flow and the Marangoni stresses originating from the gradient in the surfactant concentration along the interface.

- Surfactants suppress coalescence leading to stabilization of the colloids. There are two different theories for the explanation of the suppression of coalescence shown in Fig 2. 3; the first (Fig 2.3(A)) advocates that the Marangoni stresses increase on the opposing interfaces due to the squeeze of the matrix between the droplets. This retards the local interface velocity, thus slows down the film drainage and consequently prevents coalescence. The second (Fig 2.3 (B)) claims that the suppression of coalescence is due to steric repulsive force generated by the compression of the surfactant layers, which are attached to the surfaces of two approaching droplets, and that steric repulsion is a surfactant molecular weight dependent force (Lyu et al.; 2002). Experimental works (Lyu et al., 2002; Kleshchanok and Lang, 2007) showed that block copolymers with higher molecular weights have greater tendency to suppress coalescence.

- Surfactants could also lead to aggregation or what is called adsorption flocculation. Two models are distinguished to explain this phenomenon. The bridging model (Lyu et al., 2002) is based on the principle that the adsorbed macromolecules on adjacent droplets surfaces create a bridging force which exceeds the forces of disaggregation, hence enhancing flocculation. The depletion model (Neu and Meiselman, 2002) proposes that droplets aggregation is due to an exclusion of the macromolecules from the droplet interface which creates an osmotic pressure difference favoring aggregation.

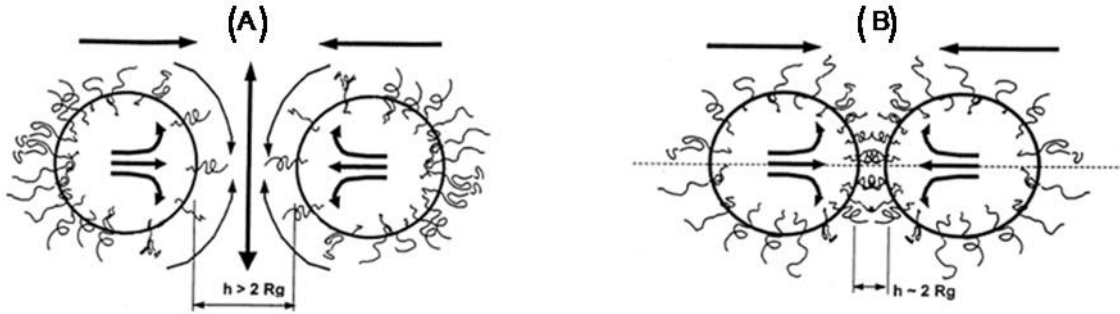


Fig 2.3 Two mechanisms for suppressing coalescence are presented here. (A) Surfactant concentration gradient. (B) Steric repulsion (Lyu et al., 2002).

- It is generally agreed that the following interaction forces are at work between two approaching surfactant covered droplets; steric repulsive interaction, electrostatic repulsive interaction, the van der Waals attractive interaction, and the bridging or depletion interactions. The resultant of these combined forces determines whether coalescence will occur or not. This force description does not deviate from the explanation given by Lipowski and Sakmann (1995) on the nature of force interactions between two biological membranes (with the exception of the presence of a repulsive hydration force). These forces decay depending on the distance between the droplets either by an exponential or by inverse square laws.

- Surfactants generally reduce significantly the particles terminal velocity below the classical Hadamard-Rybszynski prediction in the spherical region of the shape regime; however in other shape regions the particle retardation due to surfactants is less effective (Tasoglu et al., 2008).

b. Colloids rheology

Colloids are non-Newtonian fluids, i.e. their relative viscosity is dependent on the shear rate in the bulk flow. Two major approaches for the numerical study of colloids rheology are found in the literature: indirect and direct methods. The indirect methods

are those in which the rheological behavior of the suspension is usually incorporated in a single component model through the integration of some empirical formulae (Artoli, 2003; Ouared and Chopard, 2005; Chandran et al., 2006). The most famous of these is the Cason's $\sqrt{\mu|\dot{\gamma}|} = \sqrt{\sigma} - \sqrt{\sigma_y}$ which was used by Ouared and Chopard (2005) where σ is the shear stress, σ_y is yield stress, the power law $\sigma = \mu\dot{\gamma}^n$, and the Bingham plastic $\sigma = \sigma_y + \mu_b\dot{\gamma}$, (Chandran et al., 2006) where μ_b is the Bingham viscosity coefficient.

The direct methods are based on rather measuring the pressure drop Δp along the length of a channel and the flow rate Q in Poiseuille flow to deduce the apparent

viscosity by $\mu_{app} = \frac{(\Delta p / \Delta L) \pi r^4}{8Q}$ (Sun and Mann, 2005; Sun and Mann, 2006), or

measuring the shearing force per unit width F in Couette flows as in Fig 2.4, and calculate the effective viscosity $\mu_{eff} = \frac{HF}{LU_0}$ (Liu and Liu, 2006), where H is half the

channel width, L is the channel length and U_0 is the wall velocity.

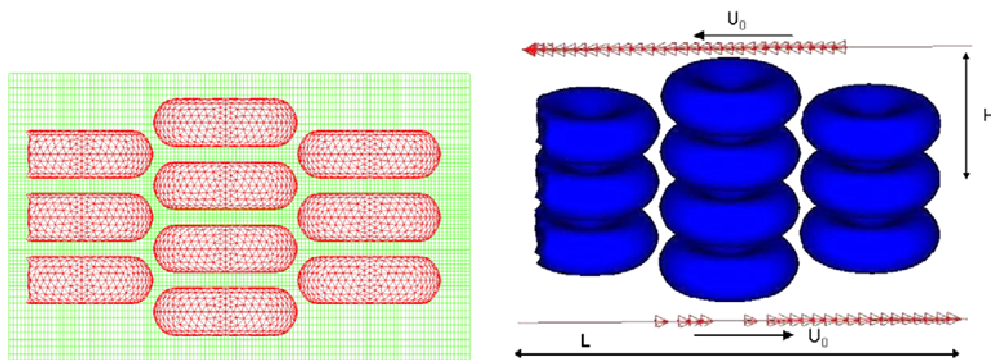


Fig 2.4 Illustration of the domain for the simple shear flow used to calculate effective viscosity Liu and Liu (2006).

c. Red blood cell deformability

Red blood cell (RBC) deformability is the most important physical property to study when analyzing blood flow inside the capillaries. Due to this extreme property RBCs are capable of streaming through vessel with diameters half of their size. Factors affecting RBCs deformability are many. These include some serious illnesses like malaria, diabetes, atherosclerosis, and others. A list of some facts related to RBC deformation mechanisms was extracted from the literature (Baskurt and Meiselman, 2003; Braasch, 1971; Gedde et al., 1995; Keller et al., 1998):

- In the microvasculature the velocity of the RBC is dependent on the level of its rigidity and shape.
- Deformability of the RBC generally helps reduce the blood viscosity both in large and small vessels.
 - Severe shocks, burns, and some snake bites rigidify the RBC membrane.
 - The deformability of the RBC is influenced by the surface area to volume ratio of the cell. Therefore swelling of the RBC due to a reduction in the blood osmolarity decreases its deformability.
 - Shrinking of the RBC (Crenated cells) due to increase in the osmolarity of the blood. This changes the internal cell fluid viscosity causing higher RBC rigidity.
 - The availability of metabolic energy i.e. adenosine triphosphate, which is very essential for the functioning of the cation pump in the RBC membrane. This pump maintains all required active substance exchange like intercellular cation and water, thereby maintaining the RBC surface area to volume ratio. This is also important for the reduction of cytosolic calcium concentration, which excesses rigidify the RBC

cytoskeleton. The lack of metabolic energy often happens in the events of glucose shortage in the RBC microenvironment.

- Oxygen-free radicals associated with an ischemia-reperfusion injury generate superoxide anions inside the RBC which decrease its deformability.
- Polymorph nuclear leukocytes are activated during injury or inflammation resulting in increased level of secretory activities which cause reduced RBC deformability.

Describing the RBC deformability, Baskurt and Meiselman (2003) claimed that the alteration in the composition of the lipid bilayer had a minor role in the mechanical behavior of the membrane, and that the cytoskeleton protein constituents had a major role in this process. The cytoskeleton is believed to be susceptible to chemical reactions which increase the cross-linkage among membrane skeletal proteins thereby reducing the cell deformability.

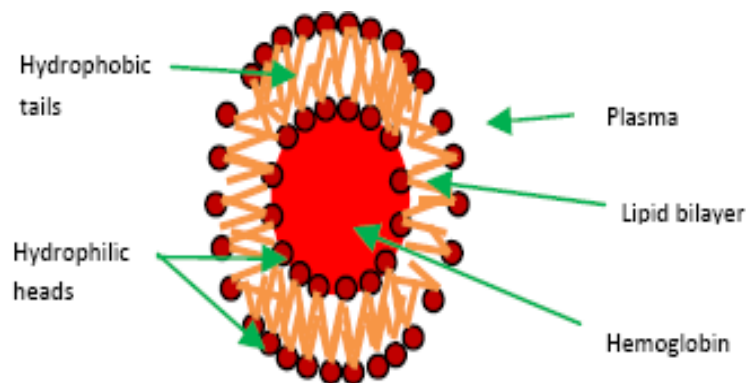


Fig. 2.5 Simplified representation of the blood cell as Liposome, justified by the assumption that the membrane liquefies under pressure in the microvasculature.

The role of the lipid bilayer alteration was more appreciated (Gedde et al., 1995; Braasch, 1971). Two possible mechanisms were explained by Gedde et al. (1995).

- The perturbation of the distribution of the phosphatidylcholine in the outer leaflet and the phosphatidylserine in the inner leaflet can cause a change in the membrane curvature.

- The change in the electrostatic interactions of the lipid head groups has a major influence on the membrane shape. Both mechanisms were tested by the titration of the cell PH (logarithmic measure of hydrogen ion concentration).

Braasch (1971) explained the Norris surface tension hypothesis and the role of surface active substances on the RBC shape and deformation. Braasch gave the following evidence in support of this hypothesis:

- The sphering ability of surface active substances, like saponin, free fatty acids, bile, lysolecithin, and some snake venoms.

- Crenated cells are induced by anionic and non-ionized compounds, while cup-shape cells are by cationic compounds. Chlorpromazine stretches biological membranes.

- Incubation of RBC in plasma at 37 degrees causes sphering of the cell due to esterification of the cholesterol in the plasma which was replaced by the cholesterol of the RBCs.

- Sphering and crenation of the RBC occurrence after severe shocks which was caused by the effects of adrenaline and catecholamine in the blood.

The influence of the lipid bilayer on the deformation of the RBC was further supported by the results of the experiment Keller et al (1998), which indicated that the RBC lipids formed immiscible fluid below pressures of 21 (dyne/cm) for the inner leaflet,

and 29 (dyne/cm) for the outer leaflet. At higher pressures the lipids mixed together and formed a homogeneous liquid.

CHAPTER 3

OUTLINE OF THE PRESENT WORK

3.1 Research objectives

The objectives of this work is to provide an efficient LBM based CFD model, capable of solving complex problems related in general to liquid-liquid colloids, and in particular to biological suspensions under specific conditions. This will be achieved through the following steps:

a. Code development

- Enhance the efficiency of the multi-component LBM, through accelerating the solution.
- Incorporate the surfactants effect on the interface of the immiscible fluids, through the coupling of the surfactant convection-diffusion equation with the Boltzmann equation.
- Impose suppression of coalescence, which allows the inclusion of the local inter-particle interaction forces to provide a realistic tool for the study of colloids rheology.

b. Validation

- The developed code should undergo rigorous validation at each stage of its development through comparison with other numerical, analytical and experimental results.

c. Application

- The various modules will be used to investigate the colloids morphology and rheology, and for the study of the RBC deformation, while streaming in the microvasculature.

3.2 Dissertation organization

The concept of the migrating multi-block for accelerating the LBM solutions is explained in Chapter 4. This will cover the single component, the Gunstensen multi-component and the particle-interaction-potential LBM, respectively. The migrating multi-block concept will be tested and validated in 2D and 3D geometries for a variety of flow conditions such as vortex shedding, shear lift of a neutrally buoyant droplet, buoyancy of bubbles, cavitations and settling droplets on a horizontal wall.

Chapter 5 presents a newly proposed Gunstensen based hybrid LBM-finite difference model for the study of surfactant-covered droplets. The coupling of the model is realized through the LBM velocity field and the surfactant equation of state. The model is tested and validated by studying the effects of surfactants on the flow deformation of a droplet in simple shear flow, uniaxial extensional flow and under buoyancy.

Chapter 6 introduces a novel method for the suppression of coalescence in the 2D Gunstensen LBM and shows two test cases of the model. The importance of the suppression of coalescence module is in providing a qualitative representation of the inter-particle forces which act on the interfaces of the approaching droplets. This allows the study of the rheology of colloids which results were validated by a comparison with some analytical solutions.

Chapter 7 discusses the RBC deformation in the microvasculature. A heuristic approach for simulating the RBC as surfactant-covered droplet is presented here to assess the validity of the concept. The velocity and deformation of the droplet are

studied as functions of the interfacial tension. The Fahraeus and the Fahraeus-Lindqvist effects are simulated and analyzed.

Chapter 8 Presents a summary of the research findings, and suggests some future recommendations.

CHAPTER 4

ACCELERATED LATTICE BOLTZMANN METHOD

4.1 Migrating multi-block schemes for the D2Q9 LBM

The present work's objective is to provide a simple algorithm, aiming at saving considerable computational time in simulations where local grid refinement is required, and especially applicable to multiphase and multi-component flows with highly deformable interface. To avoid the difficulties faced by Tolke et al. (2006), and to maintain a relatively simple approach using standard structured grid LBM, a Gunstensen based model combined with the multi-block method of Yu et al. (2002), is proposed here. The difference in the proposed model lies in that, a fine grid block covers the entire fluid interface and migrates with it, so that the physical interface does not cross the grid interface. This is performed by tracking the mass center or the average velocity of the suspended fluid, which acts as a trigger to impose node type exchange at the grid interfaces in a way that does not alter the physical properties of the various fluids. The node type exchange occurs without time lag during the propagation step in the coarse block. The grid interface is always imposed where a single phase exists.

a. The migrating multi-block algorithms

Single component algorithm for 2D geometries

The following is a brief description of Yu et al. (2002) multi-block LBM tailored for this work domain, in which the width is much smaller than the length. The domain shown in Fig 4.1 consists of three blocks: an upstream coarse block, a fine block, and a downstream coarse block.

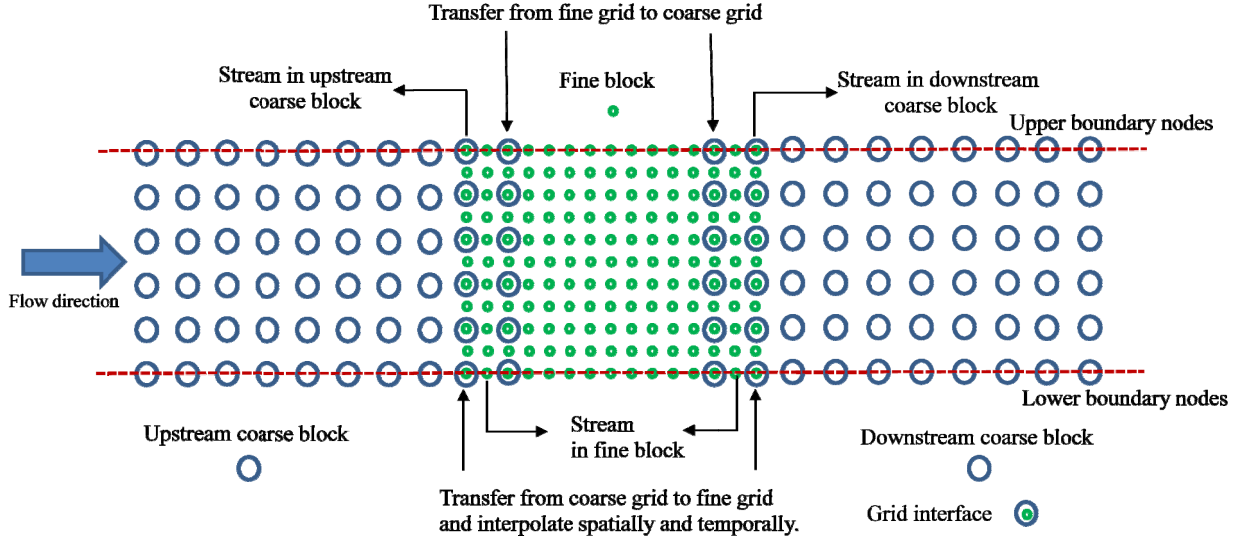


Fig 4.1 Illustration of the standard multi-block LBM domain as it pertains to the single component flow simulation of this work.

The ratio of the lattice spacing m between the fine and coarse blocks is defined by Eq. (2.39). To maintain the same viscosity, and therefore the same Reynolds number in the various blocks, the relaxation times have to satisfy Eq. (2.40). Each grid interface consists of overlapping two sets of coarse and fine nodes with one additional set of fine nodes filling in the gap as shown in Fig 4.1. The transfer of the post-collision distribution functions $\hat{f}_i^f \rightleftharpoons \hat{f}_i^c$ between the different grids occurs before the streaming step. To maintain the same lattice velocity ($\delta_x^c/\delta_t^c = \delta_x^f/\delta_t^f$) between the various grids, the time step ratio is the same as the spatial ratio ($m = \delta_x^c/\delta_x^f = \delta_t^c/\delta_t^f$). After one collision step in the coarse block a transfer of data ($\hat{f}_i^f \leftarrow \hat{f}_i^c$) is required at the indicated locations in Fig 4.1 by Eq. (2.41). After m collision steps in the fine grid a transfer of data ($\hat{f}_i^f \rightarrow \hat{f}_i^c$) is required at the indicated locations in Fig 4.1 by Eq. (2.42). A symmetric cubic spline interpolation is required for calculating \hat{f}_i^f on those fine nodes, which do not overlap with

the coarse nodes at the grid interface. This is done by the following formula (Rorres and Howard, 1984):

$$\widehat{f}_j^f(x) = a_j(x-x_j)^3 + b_j(x-x_j)^2 + c_j(x-x_j) + d_j \quad (4.1)$$

The coefficients in Eq. (4.1) are calculated as follows:

$$\begin{aligned} a_j &= M_{j+1} - \frac{M_j}{6h} \\ b_j &= \frac{M_j}{2} \\ c_j &= (f_{j+1}^f - f_j^f) - \left(\frac{M_{j+1} + 2M_j}{6} \right) h \\ d_j &= f_j^f \end{aligned} \quad (4.2)$$

where M_j are second order derivatives of the function \widehat{f}_j^f and $h = x_j - x_{j-1}$ measured in the coarse block. The M_j functions are calculated by solving a matrix equation, which leads to a tridiagonal coefficients matrix suitable for the Thomas algorithm, and the natural spline condition is stipulated where $M_0 = M_n = 0$.

A three-point Lagrangian interpolation scheme is used to calculate the post collision distribution function on the grid intersection by Eq. (2.43). This leads to the following relation for the temporal interpolation with for example a spacing ratio $m = 4$ and time measured in coarse steps:

$$\begin{aligned} \widehat{f}_i^f(t_{+0.25}) &= -0.09375\widehat{f}_i^f(t_{-1}) + 0.4375\widehat{f}_i^f(t) + 0.65625\widehat{f}_i^f(t_{+1}) \\ \widehat{f}_i^f(t_{+0.5}) &= -0.125\widehat{f}_i^f(t_{-1}) + 0.75\widehat{f}_i^f(t) + 0.375\widehat{f}_i^f(t_{+1}) \\ \widehat{f}_i^f(t_{+0.75}) &= -0.09375\widehat{f}_i^f(t_{-1}) + 0.9375\widehat{f}_i^f(t) + 0.15625\widehat{f}_i^f(t_{+1}) \end{aligned} \quad (4.3)$$

For simplicity a ratio $m = 2$ was used throughout this work. This required the utilization of only $\widehat{f}_i^f(t_{+0.5})$ from Eq. (32) for the temporal interpolation.

Gunstensen multi-component algorithm for 2D geometries

To implement the multi-block concept on the Gunstensen model care should be taken of the collision step which involves the sum $f_i^f(\mathbf{x}, t)$ of the two distribution functions $R_i(\mathbf{x}, t)$ and $B_i(\mathbf{x}, t)$ as it was expressed in Eq. (2.10) and Eq. (2.11). Therefore the sum post-collision distribution function $\widehat{f}_i^f(\mathbf{x}, t + \delta_t)$ should be used in Eq. (2.41) and Eq. (2.42) for the required transfers at the grid interfaces. Since the streaming step in the Gunstensen model occurs with separate post-collision post-segregation distribution functions $\widehat{R}_i(\mathbf{x}, t)$ and $\widehat{B}_i(\mathbf{x}, t)$, a transfer of the grid interface information from the sum function $\widehat{f}_i^f(\mathbf{x}, t + \delta_t)$ to the suspending component function $\widehat{B}_i(\mathbf{x}, t + \delta_t)$ is necessary before streaming. This is to ensure that the transfer of information at the interface between the different grids is propagated through the function $\widehat{B}_i(\mathbf{x}, t + \delta_t)$ into the fine block. This transfer is not required for the function $\widehat{R}_i(\mathbf{x}, t)$ since the physical interface in the proposed model does not cross the grid interface contrary to the experiment of Tolke et al. (2006), and the exchange of information from the various grids is done only at the single phase interface nodes.

The migrating multi-block method's main feature is the exchange of node type at the grid interfaces. For the fluid-fluid interface to be constantly covered by a fine grid while moving, an exchange of boundary coarse nodes with fine nodes downstream of the fluid interface, and alternatively an exchange of fine boundary nodes with coarse nodes upstream of the interface are needed as shown in Fig 4.2. The node type exchange occurs when the distance travelled by the suspended fluid mass center exceeds one coarse lattice spacing in the flow direction. This exchange happens during one coarse time step and it starts with the streaming in the coarse block. Here a

distinction should be drawn between the two coarse blocks. The propagation step should start in the downstream coarse block first, because after propagation the coarse distribution function $f_i^{c,d}(\mathbf{x}, t)$ is set to zero at the location indicated as old diminishing coarse nodes in Fig 4.2, thereby allowing only fine nodes to occupy it. This can be done since the information needed for the propagation has already been passed.

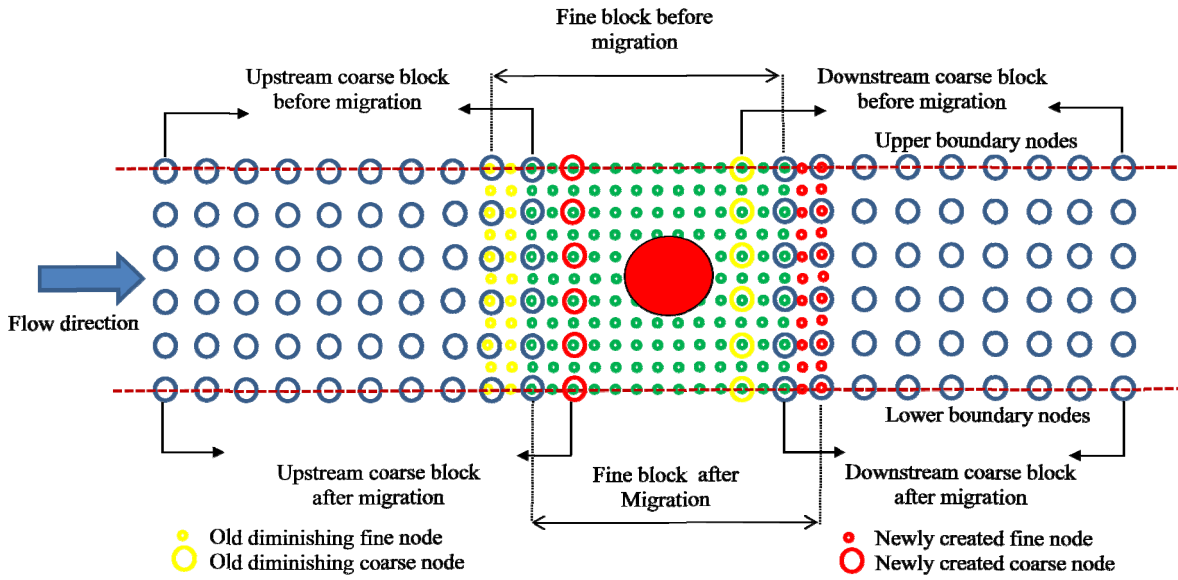


Fig 4.2 Illustration of the migrating multi-block LBM domain as it pertains to the multiphase flow simulation used in this paper.

To create two new sets of fine nodes $\widehat{\widehat{B}}_i(\mathbf{x}, t)$ on the new grid interface downstream of the suspended fluid, the extrapolation method is used at the location indicated as newly created fine nodes in Fig 4.2. For spacing ratio $m \gg 2$, a careful selection of the extrapolation scheme should be done in order to minimize any possible numerical diffusion, since the extrapolation method could become less accurate. Meanwhile, during the same coarse time step, at the grid interface the following functions $(\widehat{f}_i^f(\mathbf{x}, t), \widehat{\widehat{B}}_i(\mathbf{x}, t), \rho^N(\mathbf{x}, t))$ are set to zero in the locations designated as old

diminishing fine nodes in Fig 4.2. This will not influence the solution because the information stored in these fine nodes is not required for any subsequent calculations. The propagation in the fine block will not include the vanishing nodes, which position in the domain is now occupied by only coarse nodes. Extrapolation is used again to create a new set of coarse nodes $f_i^{c,u}(\mathbf{x}, t)$ at the locations indicated as newly created coarse nodes in Fig 4.2. This is followed by an immediate transfer of data from the fine node at the new interface to obtain $\widehat{f}_i^{c,u}(\mathbf{x}, t)$ needed for the propagation in the upstream coarse block. The next step is propagating the upstream coarse block followed by the steps provided in the flow chart of Fig 4.3 which resemble the steps of the standard multi-block model.

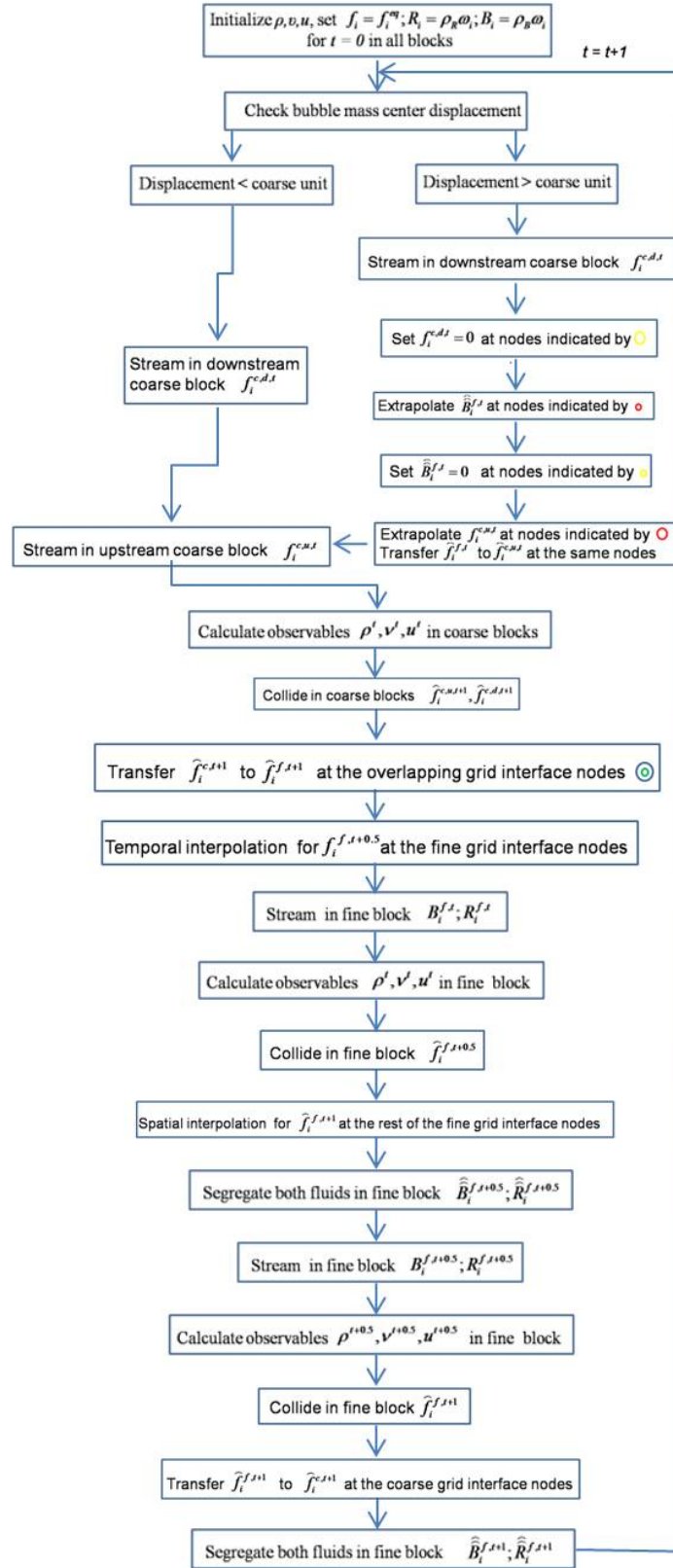


Fig 4.3 Flow chart for the migrating multi-block LBM for immiscible mixtures.

b. Simulation results and discussions

Asymmetrically placed cylinder in 2D channel

To investigate the effects of the migrating block on the numerical solution, an unsteady flow around an asymmetrically placed cylinder in 2D channel was simulated using fixed and migrating multi-block schemes simultaneously. The results were compared with some benchmark cases presented by Schaffer and Turek (1996).

The center of the cylinder was located at 4.0 radii from the lower wall, 4.2 radii from the upper wall and 4.0 radii from the inlet as shown in Fig 4.4. The fine block covered the whole cylinder, and it was 80 by 164 lattice squares. The total number of nodes in both coarse blocks was 32,800. The ratio between the coarse and the fine grids was $m = 2$. The relaxation times for the fine and the coarse grids were $\tau_f = 0.58$ and $\tau_c = 0.54$, respectively. The average velocity used for the calculation of the Reynolds number was:

$$\bar{U} = \frac{2}{3} U_{(0, \frac{H}{2}, t)} \quad (4.4)$$

where H is the channel height, t is time, and U is the centerline velocity. The average velocity used for this simulation was $\bar{U} = 0.0666$ lattice units per time step, resulting in a Reynolds number $Re = 100$. The extrapolation method was enforced on the outlet boundary, and the bounce back condition was implemented on the top and bottom walls as well as on the cylinder surface. The method of Zou and He (1997) was applied on the inlet of the domain using a parabolic velocity profile which was calculated by the following formula (Schaffer and Turek, 1996):

$$U_{(0,y,t)} = \frac{4U_{(0,\frac{H}{2},t)}y(H-y)}{H^2} \quad (4.5)$$

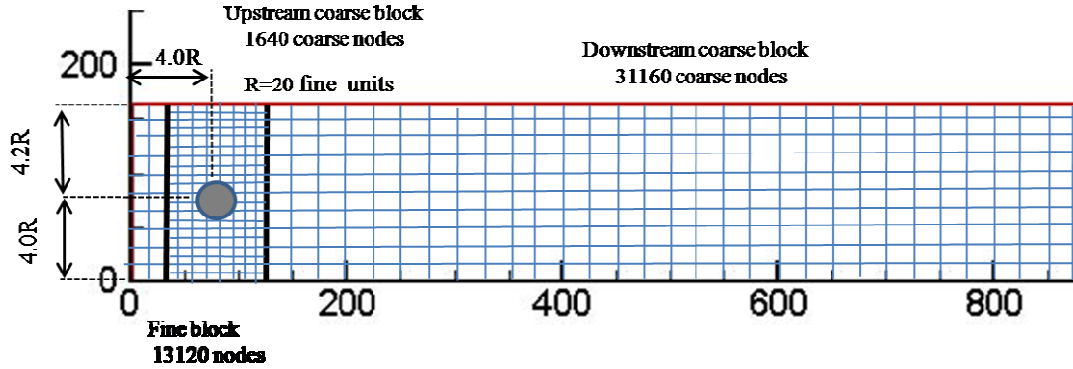


Fig 4.4 Migrating multi-block LBM domain for the flow around an asymmetrically placed cylinder in a channel, with the cylinder center location expressed as a function of its radius.

Under these conditions an unsteady flow was developed and a periodic vortex shedding was witnessed. Instantaneous streamlines for the fixed block simulation are shown in Fig 4.5 (a). The Strouhal number defined as $St = \frac{Df}{U}$ where D is the cylinder diameter, f is the frequency of separation (the inverse of the period from peak to peak values of the lift coefficient) was $St = 0.293$. This value matched well with the results given by Schafer and Turek (1996). The same simulation was carried out again with the fine block migrating by one coarse lattice each 5×10^3 coarse time steps. The Strouhal number was calculated as $St = 0.297$. This value agreed well with those given by Schafer and Turek (1996) ($0.295 \leq St \leq 0.305$). A qualitative comparison between the instantaneous streamlines of Fig 4.5 (b), with the streamlines of Fig 4.5 (a), shows a very marginal difference caused by the moving fine block after five consecutive shifts.

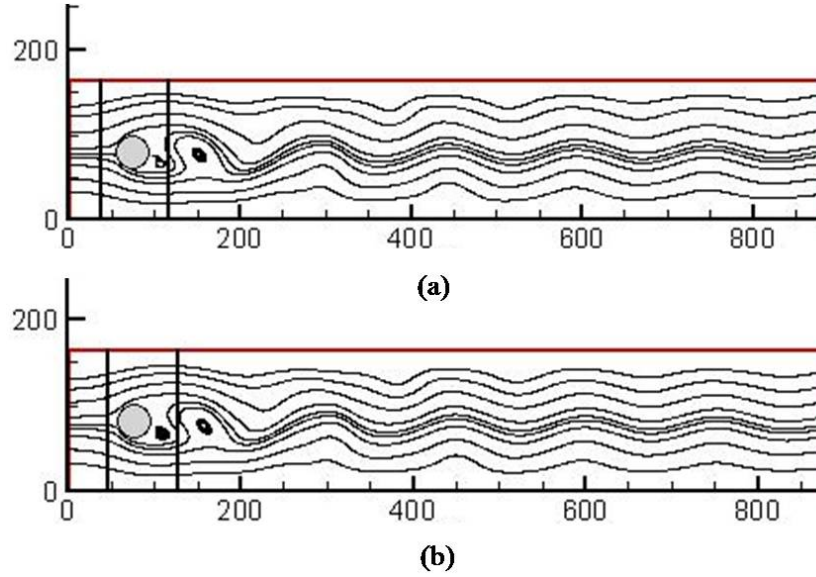


Fig 4.5 Instantaneous streamlines of a 2D channel flow over an asymmetrically placed cylinder with $Re = 100$ time step 2.9×10^4 measured in coarse time units. (a) fixed multi-block in which the fine block is static having a center coinciding with the cylinder center (b) migrating multi-block in which the fine block migrated in the direction of the flow by one coarse space unit each 5.0×10^3 coarse time steps and having its center advanced by 10 fine space units in the flow direction with respect to the cylinder center.

The Strouhal numbers in both simulations were derived using the lift coefficients graph of Fig 4.6, which was plotted together with the drag coefficients between coarse time steps 3.7×10^4 and 4.0×10^4 . The lift and the drag coefficients were calculated using the following formulae, respectively (Schaffer and Turek, 1996):

$$C_L = \frac{2F_L}{\rho \bar{U}^2 D} \quad (4.6)$$

$$C_D = \frac{2F_D}{\rho \bar{U}^2 D}$$

The lift and the drag forces were computed by the following equations, respectively:

$$F_L = - \int_S \left(\mu \frac{\partial v_t}{\partial n} n_x + P n_y \right) dS \quad (4.7)$$

$$F_D = \int_S \left(\mu \frac{\partial v_t}{\partial n} n_y - P n_x \right) dS$$

where F_L was the lift force, F_D the drag force, μ was the fluid dynamic viscosity, P was the local pressure, v_t was the tangential velocity, and n_x, n_y were the x and y components of the normal to the surface of the cylinder S .

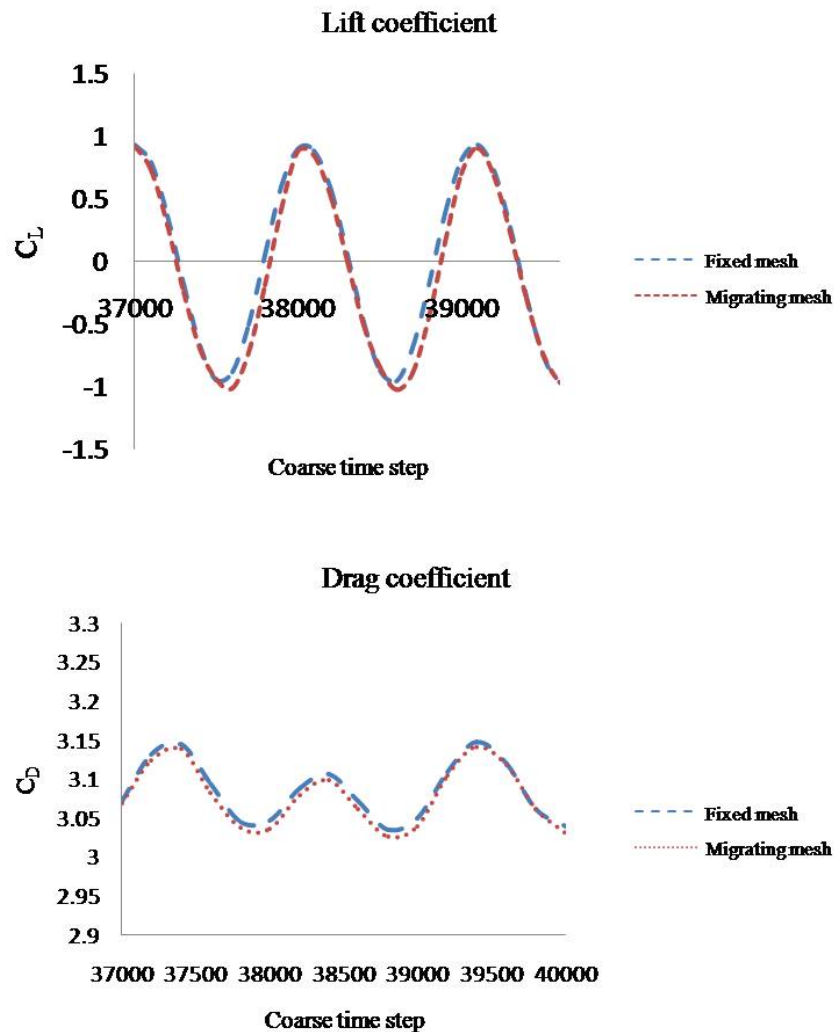


Fig 4.6 Lift and drag coefficients for fixed and migrating multi-block cases, calculated for results taken between coarse time steps 3.7×10^4 and 4.0×10^4 . A comparison of the two cases indicates that the block migration altered the results just marginally.

The comparison in Fig 4.6 shows a reasonable agreement between the two cases and the lift coefficients were not symmetrical with respect to the x axis. This was

due to the asymmetrical placement of the cylinder (Yu et al., 2002). The maximum absolute values for the lift coefficient, which was in the negative region, were different in both simulations (0.98 for the fixed block, and 1.03 for the moving block); However both maximum values agreed well with the values given by Schafer and Turek (1996) (0.99 to 1.01). The drag coefficients were $3.03 \leq C_D \leq 3.14$ for the fixed block and $3.02 \leq C_D \leq 3.138$ for the migrating block. Both maximum values were little below those reported by Schafer and Turek (1996) ($C_{D,\max} = 3.22 - 3.24$). Figure 4.7 shows the vertical velocity contour and the fine block position after the seventh block shift at coarse time step 3.6×10^4 .

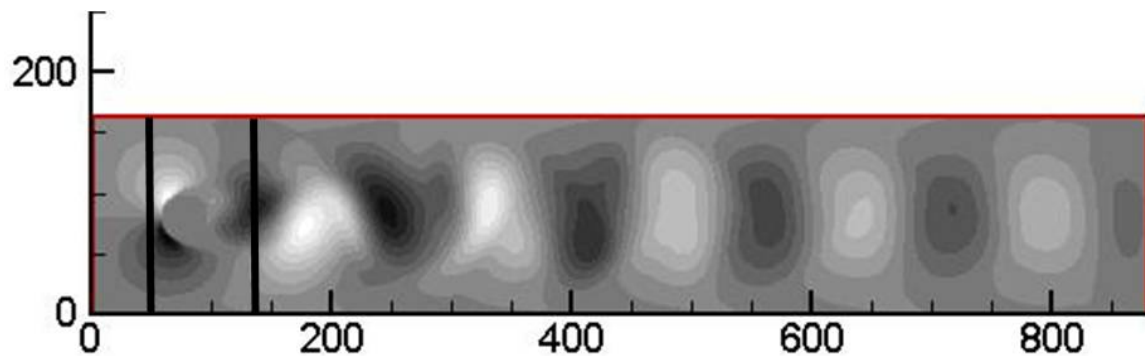


Fig 4.7 Vertical velocity contours, and location of the fine block with respect to the cylinder at coarse time step 3.6×10^4 .

To test the quality of the data transfer through the grid interfaces and the effects of the fine block migration on the model results, the mass flux and the momentum flux were calculated at the grid interface downstream of the cylinder as shown in Fig 4.8. The data were collected from the overlapping coarse and fine nodes of the migrating block at the grid interface, and from the fixed multi-block nodes which occupied the same spatial locations. The good match between the results of the fine and the coarse

block calculations at the migrating block interface was a measure of the used interpolation scheme's accuracy, and it showed that the migrating block algorithm did not alter the outcome of the calculations. The slight difference in the y components between the migrating and the fixed block results was due to the difference in the grid size, used for calculating the fluxes in both cases, and also due to the fact that the nodes where the data collection occurred in the fixed multi-block were not grid intersection nodes.

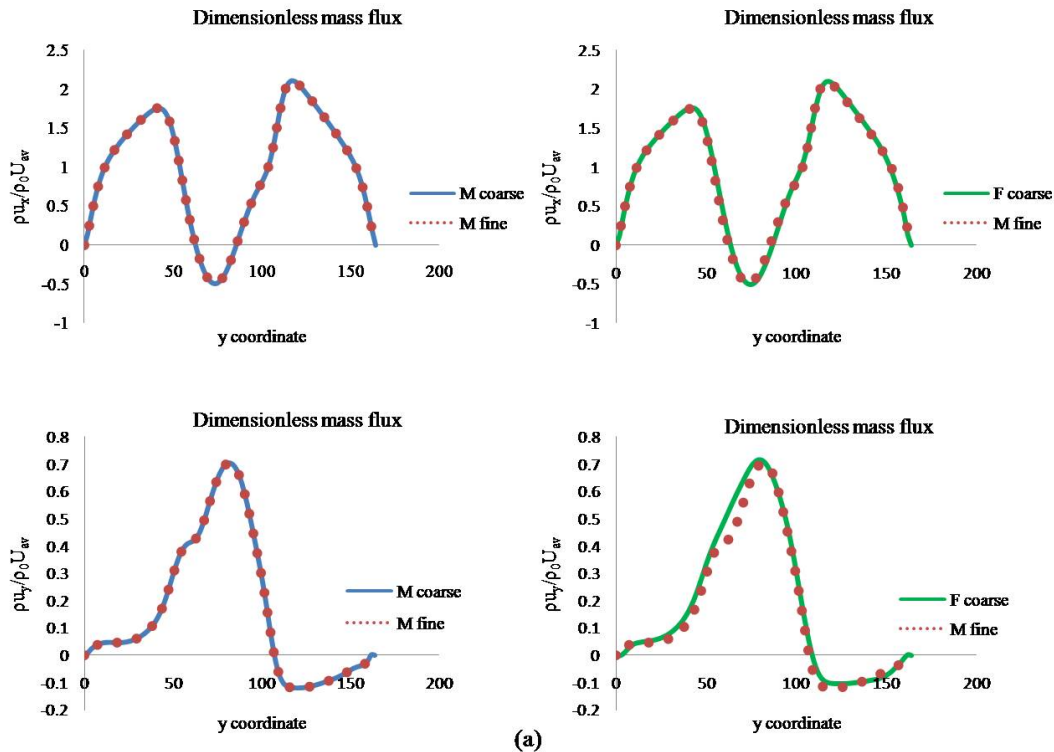


Fig 4.8 (a) Graphs for the dimensionless mass flux at coarse time step 3.5×10^4 , calculated for checking the quality of the data transfer through the grid interface between the fine block and the downstream coarse block in the migrating multi-block model. Comparison between the results of the moving fine grid interface's nodes with those collected from the fixed multi-block coarse nodes which occupy the same locations. M and F in the figure stand for moving and fixed blocks, respectively.

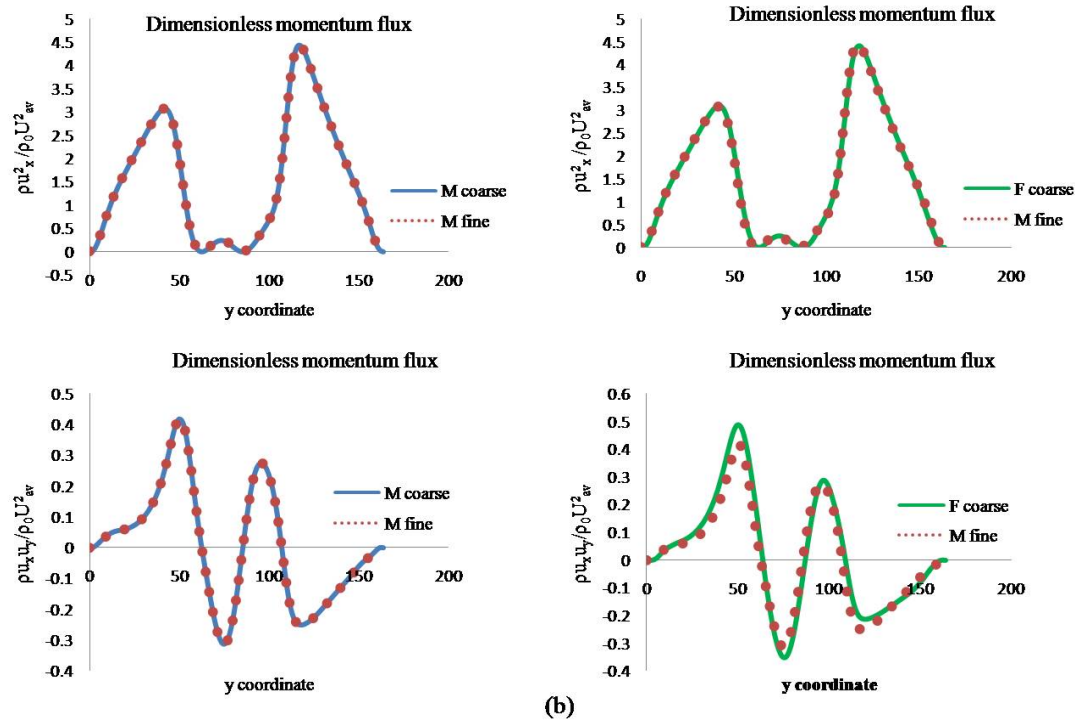


Fig 4.8 (b) Graphs for the dimensionless momentum flux at coarse time step 3.5×10^4 , calculated for checking the quality of the data transfer through the grid interface between the fine block and the downstream coarse block in the migrating multi-block model. Comparison between the results of the moving fine grid interface's nodes with those collected from the fixed multi-block coarse nodes which occupy the same locations. M and F in the figure stand for moving and fixed blocks, respectively.

Lift of a neutrally buoyant drop in parabolic flow

The study of multiphase flows at low to moderate Reynolds and Weber numbers, where the effect of gravity is neglected, is of interest in many applications such as the study of drop suspension in microgravity, and in the study of microfluidics. In very low gravity shear and parabolic flows, the hydrodynamic lift force becomes very important, since it is no longer overshadowed by the buoyancy. The lift force is due to the hydrodynamic interaction of the drop with neighboring boundary (Halliday et al., 2005)

or it is caused by a secondary velocity field at the drop surface (Legendre and Magnaudet, 1998).

The goal of this section's simulation was to validate the proposed model by comparing the results for the lateral migration of a 2D neutrally buoyant drop placed near a wall in parabolic flow with other numerical work. The other goal was to assess the quality of the proposed migrating multi-block model results for the lift trajectory and velocity, in comparison with those from the standard Gunstensen model. The approach for the estimation of the shear lift velocity was based on tracking the mass center of the drop. The result was a displacement-time function used for the calculation of the drop lateral velocity. The quality of the measurements depended heavily on the nature of the grid, since the lift force was small likewise the change in the lateral position of the drop mass center. To minimize the effect of periodicity in the flow direction while attaining the drop equilibrium distance from the wall, a longer channel was required. For a better interface representation it was crucial to refine the grid surrounding the drop. All of this resulted in a high computational cost for the standard LBM meanwhile it provided a good test ground for the proposed migrating multi-block method.

Mortazavi and Tryggvason (2000) carried out a thorough numerical investigation of the drop shear lift in Poiseuille flow. For the case in which the ratio of the drop radius to the channel height was given as $\zeta = 0.125$, the viscosity ratio $\eta = \frac{\mu_d}{\mu_s} = 8$, the drop Reynolds number $Re_d = 10.0$ and the Weber number $We = 16$, a normalized equilibrium distance from the wall of $\frac{y_{eq}}{H} \approx 0.30$ was reported.

The drop behavior in parabolic flows is characterized by the following dimensionless numbers. The channel Reynolds number:

$$\text{Re}_{ch} = \frac{\bar{U}H}{\nu} \quad (4.8)$$

where H is the channel height, \bar{U} is the flow average velocity.

The drop Reynolds number is given by:

$$\text{Re}_d = \frac{\bar{U}d}{\nu} \quad (4.9)$$

The Weber number is expressed as follows:

$$\text{We} = \frac{\rho\bar{U}^2 d}{\alpha} \quad (4.10)$$

A domain made of 287,400 coarse lattice nodes and 168 by 300 fine lattice nodes, covered a drop with diameter $d=76$ fine lattice units, yielding a ratio $\zeta = d/2H \approx 0.125$. The drop was placed at coordinate (94, 245) measured in fine lattice nodes, the density of both fluids was set to $\rho = 0.514$ and the surface tension parameter to $\alpha = 1.0 \times 10^{-4}$. The relaxation times for the ambient fluid in the fine and coarse grids were set to $\tau_f = 0.646$ and $\tau_c = 0.573$, respectively. The drop relaxation time was $\tau_d = 1.666$ leading to a viscosity ratio $\eta = 8$. The grid ratio between the coarse and fine blocks was $m = 2$. A constant force $|\mathbf{F}| = 2.14 \times 10^{-8}$ was used in Eq. (2.20) to induce a flow with an average velocity $\bar{U} = 0.0064$, a drop Reynolds number $\text{Re}_d = 10.0$ and Weber number $\text{We} \approx 16$. The bounce back condition was applied on the upper and the lower walls, and the periodic condition was imposed at the inlet and the outlet boundaries. In

the migrating multi-block the following equalities were required in the upstream coarse block after streaming:

$$\begin{aligned}
 f_i^{c,u}(x_{first}, y, 1) &= f_i^{c,d}(x_{last}, y, 1) \\
 f_i^{c,u}(x_{first}, y, 2) &= f_i^{c,d}(x_{last}, y, 2) \\
 f_i^{c,u}(x_{first}, y, 8) &= f_i^{c,d}(x_{last}, y, 8)
 \end{aligned} \tag{4.11}$$

where $f_i^{c,u}$ and $f_i^{c,d}$ are the distribution functions in the upstream and downstream blocks, respectively. x_{first} and x_{last} refer to the first and the last fluid nodes in the horizontal direction, the numbers indicate the lattice directions. In the downstream coarse block the following was applied:

$$\begin{aligned}
 f_i^{c,d}(x_{last}, y, 4) &= f_i^{c,u}(x_{first}, y, 4) \\
 f_i^{c,d}(x_{last}, y, 5) &= f_i^{c,u}(x_{first}, y, 5) \\
 f_i^{c,d}(x_{last}, y, 6) &= f_i^{c,u}(x_{first}, y, 6)
 \end{aligned} \tag{4.12}$$

The source term of Eq. (2.20) was augmented by the grid ratio m in the coarse blocks as follows:

$$\phi_i = \omega_i \frac{m}{k_2} \mathbf{F} \cdot \mathbf{c}_i \tag{4.13}$$

The drop center of gravity normalized position with respect to the drop axial normalized position is shown in Fig 4.9. The migrating multi-block result was compared with the solution of Murtazavi and Tryggvason (2000). The normalized equilibrium distance resulting from the migrating multi-block was $\frac{y_{eq}}{H} \approx 0.31$. The proposed model results were fairly good, in comparison with those of Murtazavi and Tryggvason (2000).

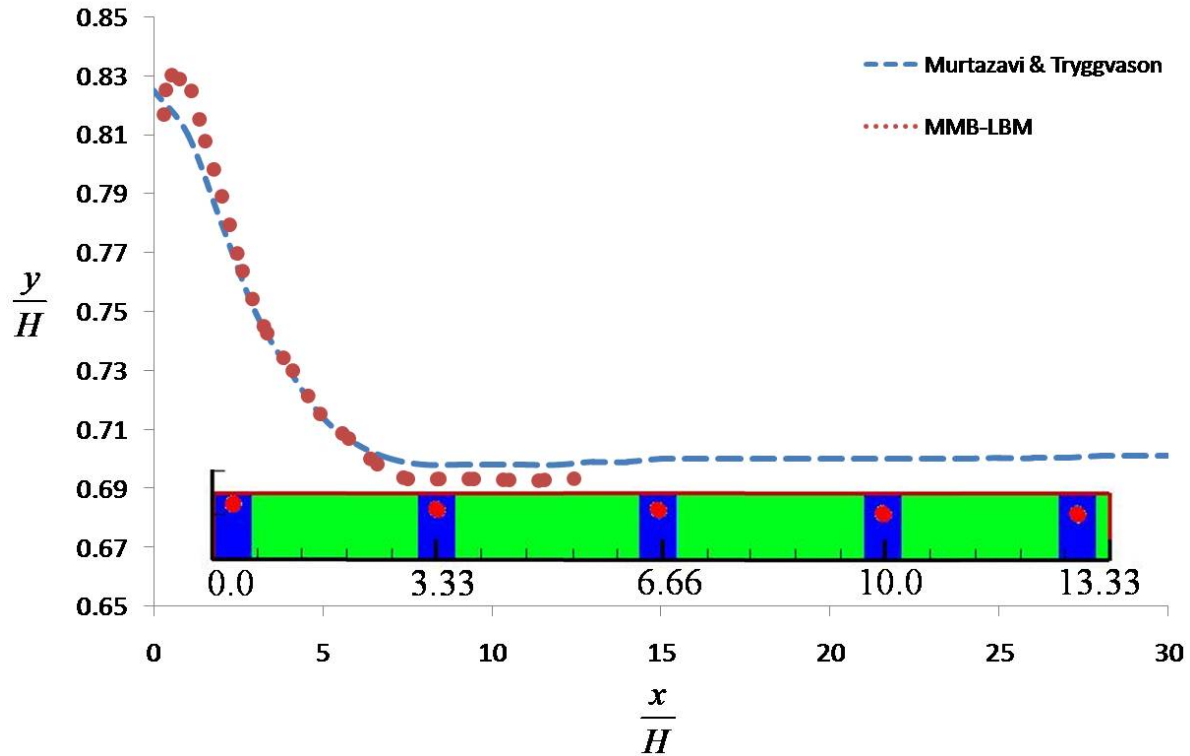


Fig 4.9 Drop mass center normalized lateral displacement by the migrating multi-block LBM compared with the solution of Murtazavi and Tryggvason (2000) for the case with $Re_d = 10.0$, $We = 16$, $\lambda = 8$ and $\zeta = 0.125$. No further data was provided for $x/H > 13.3$ since the drop reached the end of the domain (4000×300) in the MMB model measured in fine lattice. The inset in the figure is for the phase field contours of the droplet with superimposed snap shot from different time steps.

To compare the results of the proposed model with those of the standard LBM, the same flow condition and geometric settings were used for a domain consisting of 2,000 by 300 lattice squares to avoid excessive computations in the standard LBM. The equivalent domain for the migrating block scheme consisted of 137,400 coarse lattice nodes and 168 by 300 fine lattice nodes. The drop was placed at coordinate (94, 248) measured in fine lattice nodes.

A dimensionless approach was used for the analysis of the results. H was selected as a characteristic length, $U_0 = \frac{3}{2}\bar{U}$ the undisturbed centerline flow velocity, as characteristic velocity, and the inverse shearing strain rate $\dot{\gamma}^{-1} = \frac{H}{2U_0}$ as characteristic time. The shear rate was calculated at the vertical position $3H/4$ since this position was representative of the equilibrium point in the drop lift activity space. The normalized fluid average velocities and the normalized displacements of the drop mass center in the flow direction versus dimensionless time from the two simulations are shown in Fig 4.10.

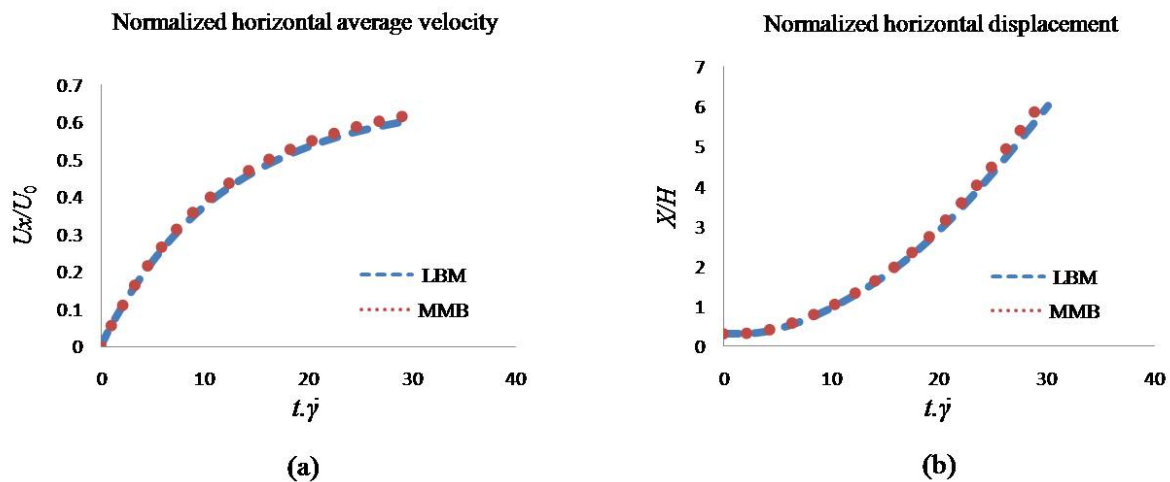


Fig 4.10 Normalized fluid average horizontal velocities (a), and normalized drop mass center displacements in the flow direction (b), for both the migrating block and the standard Gunstensen model versus dimensionless time.

The lateral displacements normalized by the channel width, versus the dimensionless time from both simulations are shown in Fig 4.11. The lift velocities were calculated from the lift displacement-time data as time derivative by a finite difference

scheme with second order accuracy, then were normalized by the centerline flow velocity as shown in Fig 4.11.

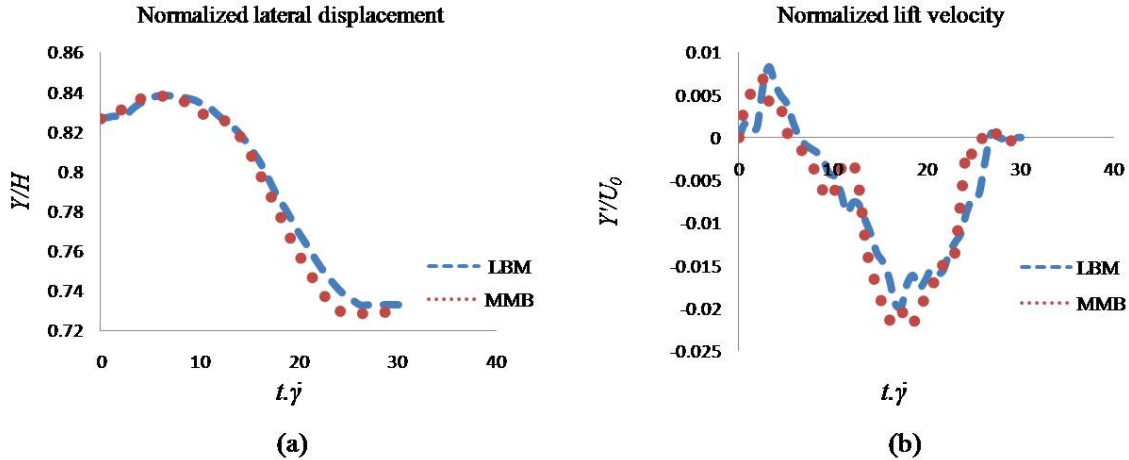


Fig 4.11 Normalized lateral trajectory of the drop mass center (a) for the migrating block and the standard LBM measured with respect to dimensionless time. Normalized lift velocity (b) for the migrating block and the standard LBM calculated with respect to the dimensionless time.

It was clear from Fig 4.11 that the velocities observed at $t\dot{\gamma} < 7$ should be neglected due to the drop tilt during the initialization of the simulations, and that the drop's lift velocity is an order of magnitude smaller than its translational velocity. The same was extracted in the work of Sukumaran and Siefert (2001) who studied the lift of the near-wall neutrally buoyant vesicles in shear flow. The distance from the top wall at dimensionless time step $t\dot{\gamma} = 28.8$ for the standard LBM was $\frac{y}{H} = 0.2733$ versus

$\frac{y}{H} = 0.2728$ for the migrating block.

The deformation index $DI = \frac{(a-b)}{(a+b)}$, where a is the drop major axis and b is the drop

minor axis, varied between the values $0 \leq DI \leq 0.12$ during the simulations as shown in

Fig 4.12. The reduction in the DI associated with time was due to the reduction in the viscous stress, when the drop drifted away from the wall leading to a reduced DI . Cox (1969) proposed a theoretical formula for the calculation of the drop deformation in a general time-dependent fluid flow with a range of capillary numbers and viscosity ratios. The time dependence of the DI was through a decaying exponential function which led after long time (steady state) to the following relationship:

$$DI = \frac{5(19\lambda + 16)}{4(\lambda + 1) \sqrt{\left(\frac{20}{Ca}\right)^2 + (19\lambda)^2}} \quad (4.14)$$

where $Ca = \mu_s \dot{\gamma} d / 2\alpha$ is the capillary number. The strain rate used in the calculation of this work's capillary number was locally defined by $\dot{\gamma}(y) = \left| \frac{8U_0}{H^2} \left(\frac{H}{2} - y \right) \right|$. The deformation index calculated by Eq. (43) yielded $DI = 0.151$ for the dimensionless time step $\dot{\gamma}t = 12.8$ and the calculated capillary number $Ca = 0.78$. The dimensionless mass center location was $\frac{y}{H} = 0.824$, which corresponded to the location where the simulation results led to the highest value $DI = 0.12$ as shown in Fig.12. The difference between the measured and the calculated deformation indices could be resulting from the transient nature of the drop deformation under the shear lift as measured from the simulation, compared to the steady state deformation described by Eq. (43).

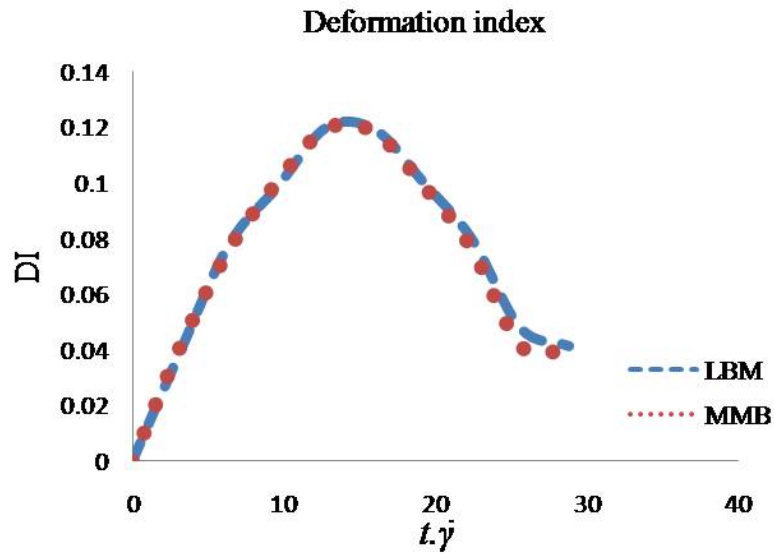


Fig 4.12 Deformation indexes of the drops from both the standard LBM and the migrating multi-block calculated with respect to the dimensionless time.

Figure 4.13 presents the phase field contours, with the various positions of the drop generated by super-imposing consecutive snapshots taken at different time steps.

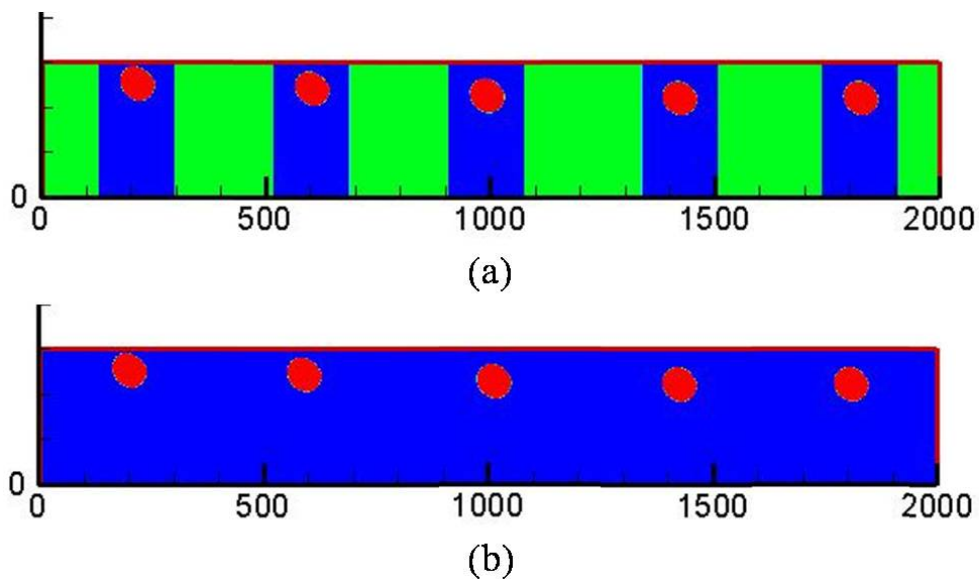


Fig 4.13 Phase field contour for five consecutive snapshots taken at different time steps and superimposed in the figure. The blue blocks are fine, and the green blocks are coarse: (a) migrating multi-block and (b) standard LBM.

To analyze the computational time advantage of the proposed model the following formula was introduced:

$$Ga = m \frac{N_x N_y}{m L_x N_y + \frac{1}{m^2} (N_x - L_x) N_y} \quad (4.15)$$

where N_x and N_y are the domain length and width measured in fine grids spacing respectively, and L_x is the length of the fine block. Equation (4.15) was based on the idea that for the calculation of one time step in the coarse blocks expressed in fine lattice units as $(N_x - L_x) N_y / m^2$, there is a need for m time steps in the fine block having dimensions $L_x N_y$ and in the standard LBM with dimensions $N_x N_y$, respectively. Equation (4.15) is applicable only for 2D models, with the fine block covering the entire width. For the current simulation the formula leads to a time gain $Ga = 5.04$. This was also confirmed by comparing the computational time required for the simulations using the standard Gunstensen model and the proposed migrating multi-block method simultaneously. Using DELL Precision 490 workstation, one time step in the standard model required 0.516 second for execution, while the time needed for the same time step in the migrating multi-block was 0.108 second leading to $Ga = \frac{t_{st}}{t_{mb}} = 4.77$. The difference between the calculated and the measured computational time gain could be used to evaluate the code level of efficiency.

4.2 Migrating multi-block scheme for the D3Q19 LBM

It is always desired to simulate fluid problems in 3D geometries, because they provide a better representation of the underlying physics. However 3D simulations

are computationally costly. This prompted the extension of the migrating multi-block to 3D geometries.

a. Modified model with density contrast

The standard Gunstensen model does not tolerate a density contrast between the constituent fluids of the mixture meanwhile in this section the density contrast is required for the simulation of a rising bubble in infinite medium. Therefore the method of Grunau et al. (1993) is used with some suitable modifications for this purpose. The main collision step is described by two distribution functions instead of the standard Gunstensen color blind function $f_i(\mathbf{x}, t)$, and it is expressed through the following:

$$\widehat{f}_i^k(\mathbf{x}, t + \delta_t) = f_i^k(\mathbf{x}, t) - \frac{1}{\tau^k} [f_i^k(\mathbf{x}, t) - f_i^{k,eq}(\rho, \rho \mathbf{u})] + \phi_i(\mathbf{x}) \quad (4.16)$$

where \widehat{f}_i^k refers to post-collision distribution functions for the lighter and heavier fluids ($k = L, H$), τ^k are the relaxation times for both fluids, and $\phi_i(x)$ is a source term used for the introduction of a force into the fluid, which could be utilized to induce the necessary surface tension and to account for the difference in density between the various fluids, thus creating buoyancy force. The surface tension is created by the method of Lishchuk et al. (2003) which imposes a normal force at the interface by Eq. (2.16). The choice of the equilibrium distribution functions is in principle arbitrary provided that these functions satisfy the following mass and momentum conservation laws:

$$\begin{aligned} \rho^L(\mathbf{x}, t) &= \sum_{i=0}^{Q-1} f_i^L = \sum_{i=0}^{Q-1} f_i^{L,eq} \\ \rho^H(\mathbf{x}, t) &= \sum_{i=0}^{Q-1} f_i^H = \sum_{i=0}^{Q-1} f_i^{H,eq} \\ \rho \mathbf{u} &= \sum_{i,k} \mathbf{c}_i f_i^k = \sum_{i,k} \mathbf{c}_i f_i^{k,eq} \end{aligned} \quad (4.17)$$

where $\rho = \rho^L + \rho^H$ is the total density, ρ^L is density of the light fluid, ρ^H is the density of the heavier fluid. The following equilibrium distribution functions are used in the proposed model and they were taken from the work of Maini (2007) due to the simplicity of their derivation and application:

$$\begin{aligned} f_i^{L,eq} &= \rho^L \omega_i \left[1 + \frac{3}{c^2} \mathbf{c}_i \cdot \mathbf{u} + \frac{9}{2c^4} (\mathbf{c}_i \cdot \mathbf{u})^2 - \frac{3}{2c^2} \mathbf{u} \cdot \mathbf{u} \right] \\ f_i^{H,eq} &= \rho^H \omega_i \left[r_i + \frac{3}{c^2} \mathbf{c}_i \cdot \mathbf{u} + \frac{9}{2c^4} (\mathbf{c}_i \cdot \mathbf{u})^2 - \frac{3}{2c^2} \mathbf{u} \cdot \mathbf{u} \right] \end{aligned} \quad (4.18)$$

where the constant is calculated as follows:

$$r_i = \begin{cases} 3 - 2\gamma, & \rightarrow i = 0 \\ \gamma, & \rightarrow i \neq 0 \end{cases} \quad (4.19)$$

$\gamma = \frac{\rho^L}{\rho^H} = \frac{(c_s^H)^2}{(c_s^L)^2}$ is the dimensionless parameter for the density ratio. c_s^L, c_s^H are the speeds

of sound used in conjunction with τ^k for determining the kinematic viscosities of the two fluids. This is realized through the use of Eq. (2.5). The relationship between the source term $\phi_i(\mathbf{x})$ and a constant macroscopic force $F(\mathbf{x})$ such as a body force is expressed by Eq. (2.20). The ratio between the various fluids weighting constants is expressed through the following relationship $\omega_0^H = \omega_0^L (3 - 2\gamma)$; $\omega_{i \neq 0}^H = \gamma \omega_{i \neq 0}^L$.

In the proposed model, the post-collision distribution functions are calculated by Eq. (4.16) for each fluid using a sweep throughout the whole domain. This will not alter by any means the light and heavy fluid mix at the interface and it allows the use of the appropriate equilibrium distribution function, based on the right proportion of masses present at the individual interfacial nodes from both fluids. The total color blind post-collision distribution function is hence after invoked using $\widehat{f}_i = \widehat{f}_i^L + \widehat{f}_i^H$. This paves the

way for the segregation process which is achieved by not allowing color diffusion at the fluid interfacial nodes. The formulaic method of D'Ortona et al. (1995) is applied in the model using Halliday et al. (2007) generalized formula for the implementation of the method in 3D models:

$$\begin{aligned}\widehat{f}_i^L(\mathbf{x}, t + \delta_t) &= \frac{\rho^L}{\rho^L + \rho^H} \widehat{f}_i(\mathbf{x}, t + \delta_t) + \beta \frac{\rho^L \rho^H}{\rho^L + \rho^H} \omega_i \nabla \rho^N \cdot \mathbf{c}_i \\ \widehat{f}_i^H(\mathbf{x}, t + \delta_t) &= \widehat{f}_i(\mathbf{x}, t + \delta_t) - \widehat{f}_i^L(\mathbf{x}, t + \delta_t)\end{aligned}\quad (4.20)$$

β is the segregation parameter. $\widehat{f}_i^L, \widehat{f}_i^H$ refer to post-collision post-segregation distribution functions of the light (red) and heavy (blue) fluids respectively. The streaming step follows the segregation step through the following:

$$\begin{aligned}f_i^L(\mathbf{x} + \mathbf{c}_i \delta_t, t + \delta_t) &= \widehat{f}_i^L(\mathbf{x}, t + \delta_t) \\ f_i^H(\mathbf{x} + \mathbf{c}_i \delta_t, t + \delta_t) &= \widehat{f}_i^H(\mathbf{x}, t + \delta_t)\end{aligned}\quad (4.21)$$

b. The migrating multi-block algorithm

A 3D domain shown in Fig 4.14 describes three blocks in which the central is cast with fine grid and the others are with coarse grid. The spatial and temporal ratio of the lattice spacing for both fine and coarse grid m is defined by Eq. (2.39).

The relaxation times are linked through Eq. (2.40) which guarantees uniform viscosity throughout the fluid in all blocks (Yu and Shyy, 2002). Each grid interface is formed by two sets of overlapping planes of coarse and fine nodes (A, C & B, D) and one additional plane of fine nodes in between for each interface (not shown in Fig 4.14).

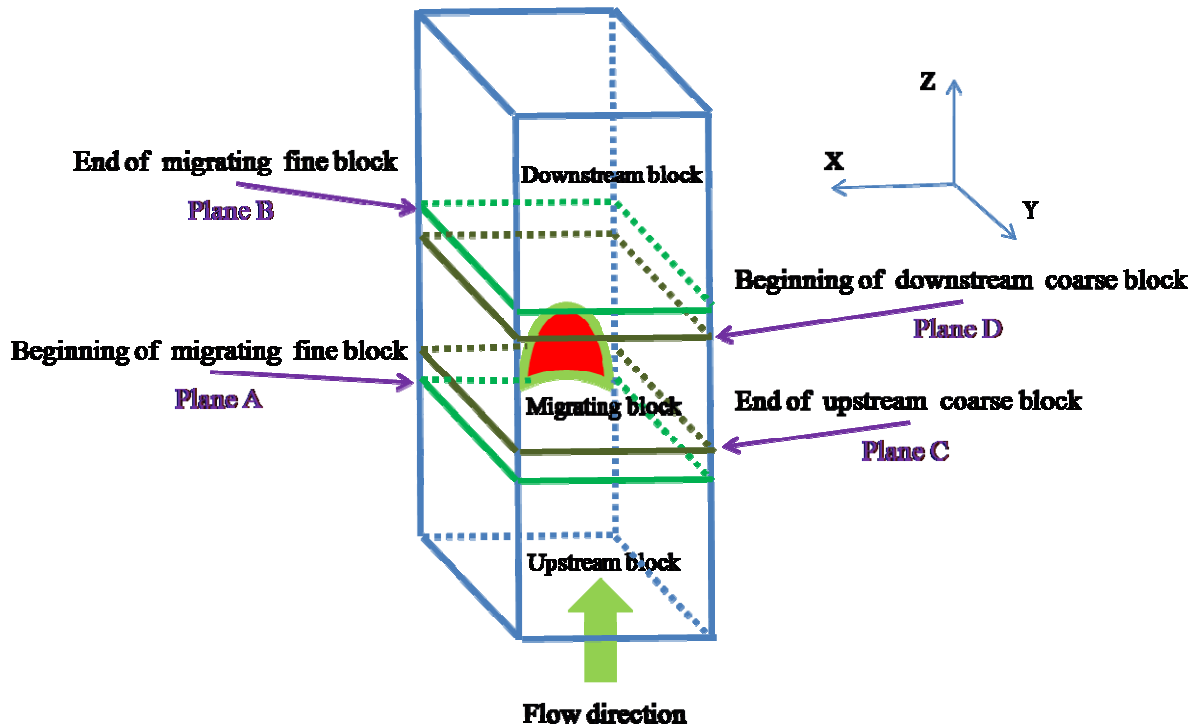


Fig 4.14 Illustration of the 3D multi-block lattice Boltzmann method domain comprising of two coarse blocks and one fine block.

The transfer of information between the various grids is executed on all interfacial planes by the same formulae which were implemented in the 2D model and were extracted from the work of Yu and Shyy, (2002). At the fine plane (A & B) Eq. (2.41) is used for the transfer. At the coarse plane (C & D) the transfer is executed by Eq. (2.42).

Symmetric cubic spline interpolation is needed for calculating \hat{f}_i^f on those fine nodes designated with asterisks and red circles in Fig 4.15 by Eq. (4.1) and Eq. (4.2). Spatial and temporal interpolations are only needed at planes (A & B) illustrated in Fig 4.15. A constructive suggestion on the sequence used for the spatial interpolation is to start first by calculating the values of the post-collision distribution functions at the asterisks positions following the y direction through a sweep by x coarse spatial steps.

This is followed by the calculation of the post-collision distribution functions at the red circles in the x direction through a sweep by y fine spatial steps.

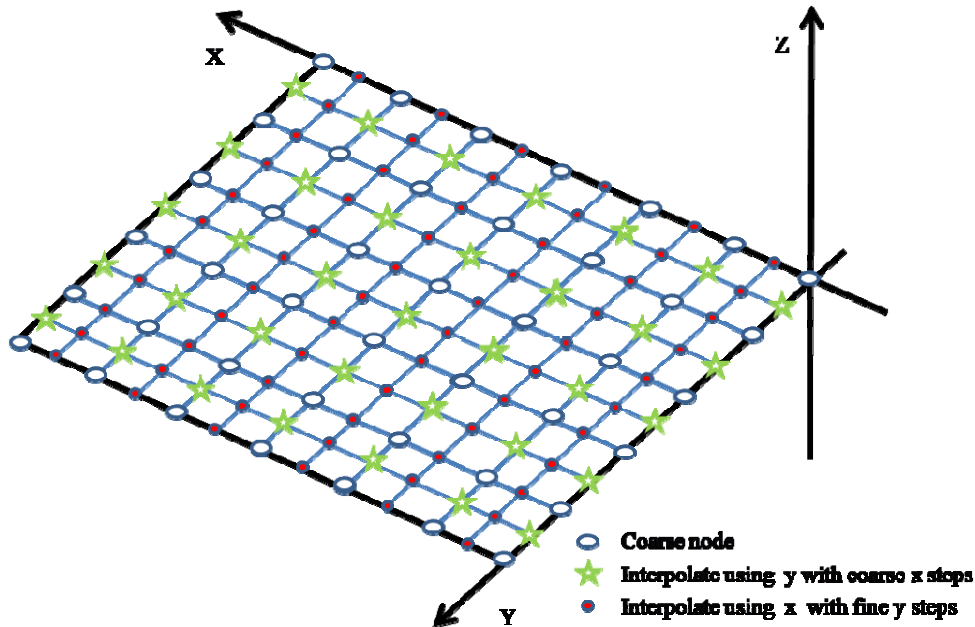


Fig 4.15 Illustration of the grid interface plane at the beginning or the end of the fine block, where spatial and temporal interpolation are required.

A three-point Lagrangian temporal interpolation is required for all fine nodes shown in Fig 4.15 in order to synchronize the solution and it is executed by Eq. (2.43).

The migrating multi-block algorithm is based on the idea of exchanging nodes type at the grid interfaces. This is driven by the necessity of covering the fluid interface with fine grid throughout the simulation time. The condition for the occurrence of the node type exchange is implied by the displacement of the interface in the flow direction by a value greater than one coarse unit. The exchange requires the creation of two planes of fine nodes and the extinction of one plane of coarse node in the downstream block, and the creation of one plane of coarse nodes and diminishing two planes of fine nodes in the upstream block. The creation of new nodes requires the use of extrapolation method which could be of first or second order. The aim is to minimize

numerical diffusion, which is usually marginal, since the newly created nodes undergo information transfer by Eq. (2.41) and Eq. (2.42), before proceeding with any further calculation.

c. Simulation results and discussion

The velocity and the shape of a light bubble moving in a denser fluid is strongly dependent on the ratio among three forces -- the driving force from buoyancy, the resistance from the viscous friction, and the surface tension which tries to maintain the shape of the bubble spherical. For the simulation of a free rising bubble in infinite medium with periodic boundary condition the effects from the noted forces can be represented by the following dimensionless parameters (Tolke et al., 2002):

$$E_o = \frac{g\Delta\rho d^2}{\sigma_0}, M_o = \frac{g\mu^4\Delta\rho}{(\rho^H)^2\sigma_0^3}, \text{Re} = \frac{U_T d \rho^H}{\mu} \quad (4.22)$$

Here g is the acceleration due to gravity, d is the bubble diameter, ρ^H is the density of the heavy fluid and σ_0 is the surface tension at the interface. The Eotvos number E_o is the ratio between buoyancy and the surface tension, the Morton number M_o compares the inertial effects, viscous drag and the surface tension, the Reynolds number Re represents the ratio between the inertial force and the viscous drag. The interplay between these parameters determines the shape of the bubble which could vary from spherical, ellipsoidal, ellipsoidal cap, spherical cap and eventually to skirted as this was demonstrated through the experimental work of Bhaga and Weber (1981).

Terminal velocity

The terminal velocity of a rising bubble in infinite medium with $E_o > 40$ and $M_o > 200$ can be estimated analytically through solving the following equation with respect to the Reynolds number (Clift et al. 2005):

$$2\text{Re}^2 + 6\text{Re} \frac{2+3\eta}{1+\eta} - E_o^{3/2} M_o^{-1/2} = 0 \quad (4.23)$$

where $\eta = \mu_L / \mu_H$ is the viscosity ratio for the light and heavier fluids.

The demonstration of the proposed method is performed as follows: The simulation domain was $61 \times 61 \times 351$ measured in fine lattice units, and the bubble initial radius was $d = 12$ lattice fine units as shown in Fig 4.16.

Periodic condition was imposed in all directions. The fine block consisted of $61 \times 61 \times 48$ lattice cubes yielding 178,608 fine nodes; meanwhile the upstream and the downstream blocks comprised of 140,933 coarse nodes. The spacing ratio was $m = 2$, the relaxation times were $\tau_f = 0.9$ and $\tau_c = 0.7$ for the fine and coarse blocks respectively, and the segregation parameter was $\beta = 0.55$. A density $\rho^H = 2$, density ratio $\gamma = 0.5$ leading to a density contrast $\gamma^{-1} = 2.0$, kinematic viscosity ratio $\eta = 1$, dynamic viscosity $\mu = 0.266$ and a surface tension $\alpha = 0.001$ were used in five cases where the gravitational acceleration g was varied consecutively.

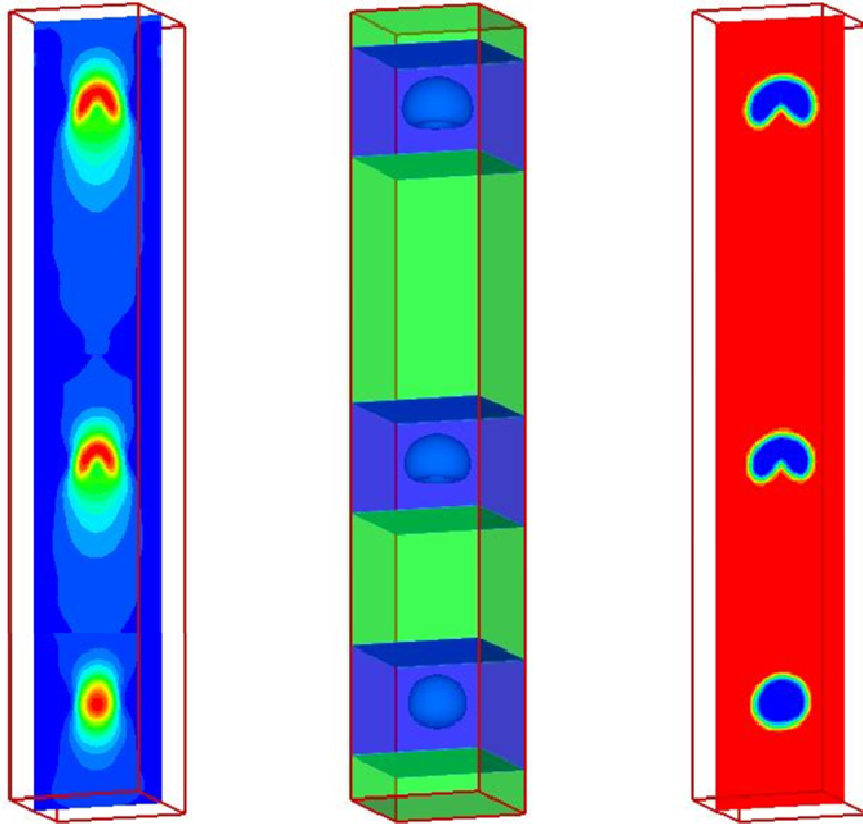


Fig 4.16 3D simulation of a rising bubble in an infinite medium with $M_0 = 821$, $E_0 = 374$ and $Re = 8.10$, velocity contour in the z direction for superimposed snap shots at three different time steps (left), 3D phase field contours where the fine migrating superimposed blocks are shown in blue and the coarse blocks in green (center), 2D cut of the density contour depicting the droplet profile during the various time steps (right).

The values for the acceleration g from five different cases and their corresponding Eotvos, Morton, Reynolds numbers and theoretical terminal velocities are presented in Table 4.1.

Table 4.1 Simulation results for five different cases, U_T terminal velocity from Eq. (4.23), U_M terminal velocity from the numerical simulation.

g	E_0	M_0	Re	U_T	U_M
0.00036	207	455	5.42	0.0301	0.0304
0.00045	259	568	6.33	0.0351	0.0359
0.00054	311	682	7.16	0.0397	0.0401
0.00065	374	821	8.10	0.0450	0.0444
0.00078	449	985	9.125	0.0506	0.0489

A comparison between the terminal velocities calculated by the semi-analytical Eq. (4.23) and the model terminal velocities for the various cases is shown in Fig 4.17.

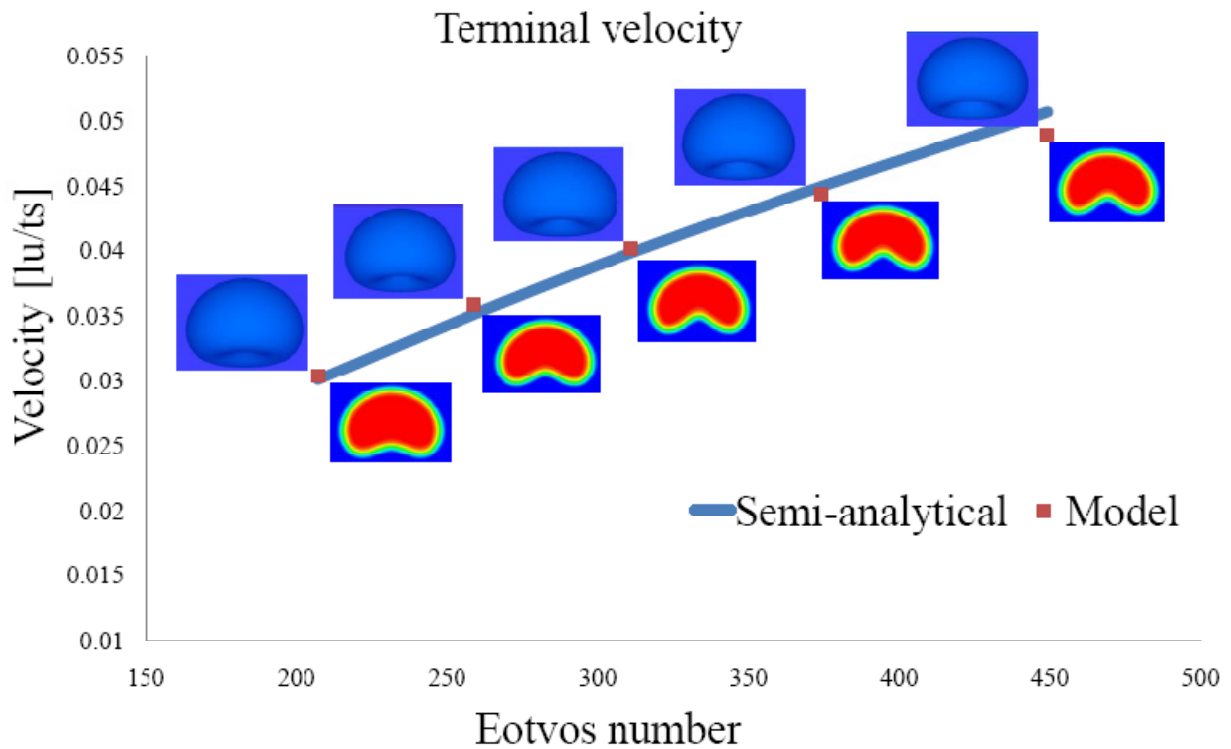


Fig 4.17 Terminal velocity comparison and shape change with respect to the Eotvos number for values stated in Table 4.1.

The figure also shows the effects of the change in the dimensionless parameters of Eq. (4.22) and in particular the Eotvos number due to the change in the gravitational force on the steady state shape of the rising bubble.

Bubble shape

Grace (1973) brought together the results of several experiments which focused on the case of a single rising bubble in infinite media.

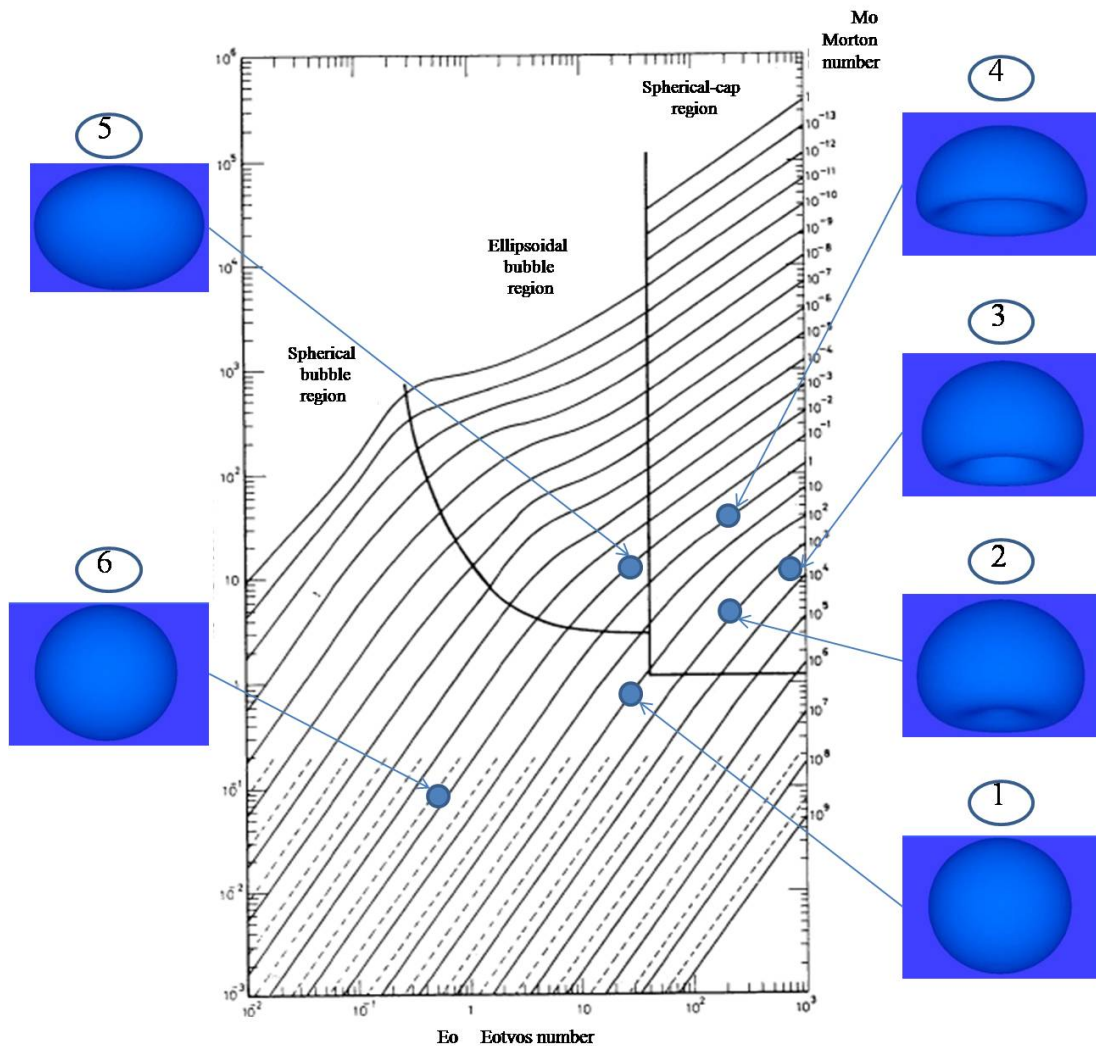


Fig 4.18 Shape regime map by Grace 1973 used for locating the proposed model results for the various cases presented in Table 4.2. The model shows good fit within the three shape map regions.

Grace delineated three major regions where the shape of the bubble was determined by the dimensionless parameters of Eq. (4.22). The regions were as follows: spherical bubble, ellipsoidal bubble, and spherical cap regions. The various regions were demarcated in a shape regime map shown in Fig 4.18. This map was further expanded by Bhaga and Weber (2002) and more distinct regions were added which included oblate ellipsoidal, oblate ellipsoidal cap, and skirted bubble shapes.

Data from six simulations are presented in Table 4.2. The shapes obtained by the proposed model for the parameters of Table 4.2 were plotted with their corresponding location in the three map regions. The results as seen from Fig 4.18 indicate that the model yielded droplet shapes which matched well the experimental observation at the various regions of Grace's shape regime map.

Table 4.2 Variables and dimensionless numbers for a few shape region simulations

g	E_0	M_0	Re	μ	Region
0.00005	29	63	0.63	0.2666	SBR -1
0.00036	207	455	5.42	0.2666	SCR -2
0.0015	864	1894	11.70	0.2666	SCR -3
0.00036	207	0.73	33.32	0.0533	SCR -4
0.00005	29	0.10	12.60	0.0533	EBR -5

(SBR) Spherical bubble region; (SCR) Spherical cap region; (EBR) Ellipsoidal bubble region

Density ratio

Although the proposed algorithm deviated slightly from the original Gunstensen model in order to tolerate a density contrast among the constituent fluids, the highest density contrast which was achieved in the present work did not exceed a value $\gamma^{-1} = 10$.

The main concern emanated from the formation of a thick interface in the phase field presentation of the suspended phase. A density ratio $\gamma = 0.1$, segregation parameter $\beta = 0.15$ and a gravitational constant $g = 8.5 \times 10^{-5}$ were used in a simulation, in which the domain and all other fluid properties were similar to those used in the terminal velocity section. This led to $Re = 4.2$, $M_o = 193.23$ and $E_o = 88.13$. The outcome of the analytical formula for the terminal velocity differed from the simulation result since the formula was not applicable for $M_o < 200$, however the bubble shape and despite of the thick interface still fitted well Grace's shape regime map and it fell in the spherical cap region.

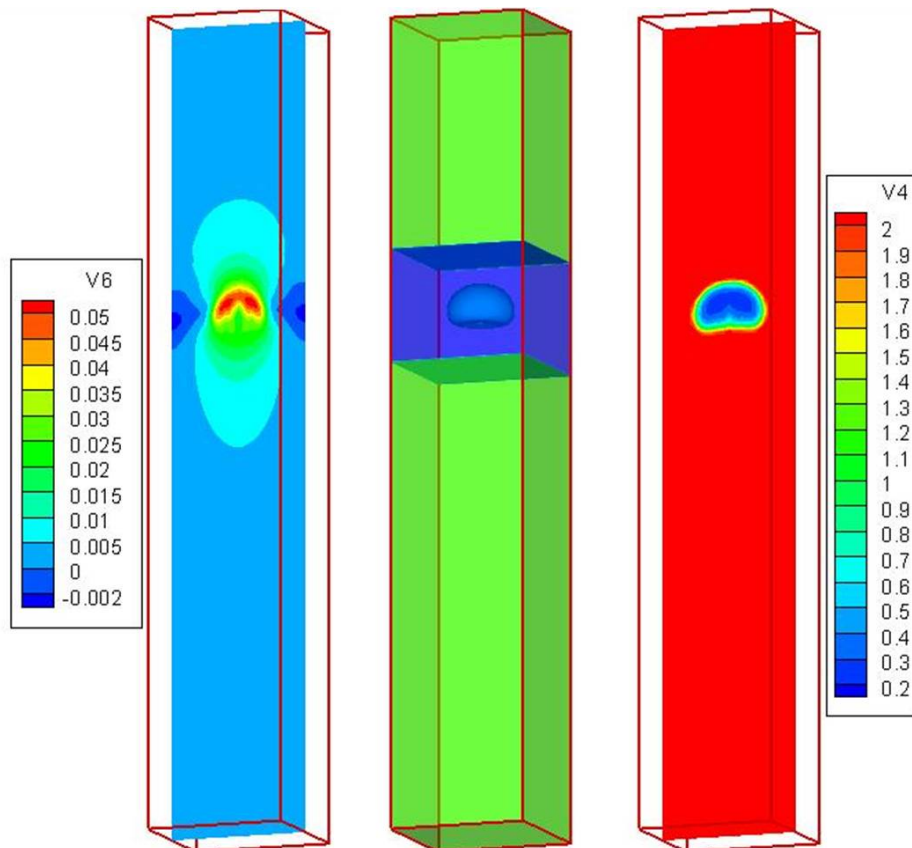


Fig 4.19 Vertical velocity contour (left), phase field contour (center), and density contour (right) for a rising bubble with a density contrast $\gamma^{-1} = 10$, $M_o = 193$, $E_o = 88$ and $Re = 4.2$.

Figure 4.19 shows the vertical velocity, the phase field and the density contours of a rising bubble with a density contrast $\gamma^{-1} = 10$.

Multiple bubbles

To illustrate the migrating multi-block capability of dealing with multiple bubbles seeded in the fine block, a two trailing bubbles case was studied. The two bubbles were initialized in the same domain described by the fifth case from Table 4.1, with the bubbles mass centers lying on the domain central vertical axis and separated by a distance of $2d$. The fine block was made of $61 \times 61 \times 84$ fine lattice units, to accommodate for the two bubbles.

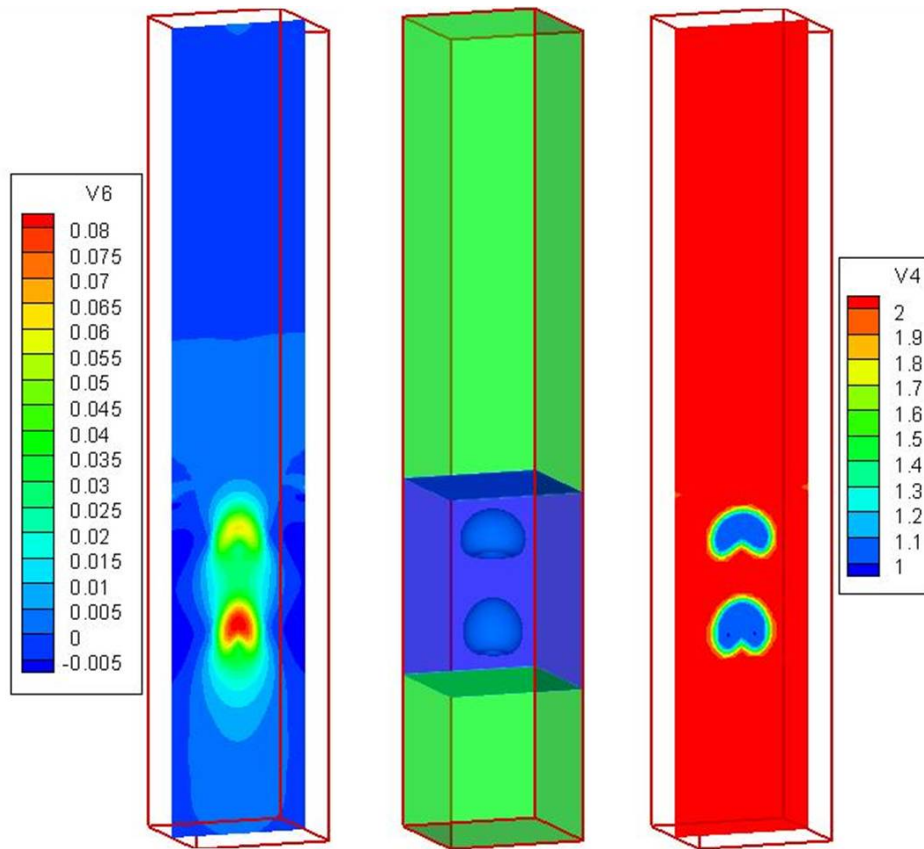


Fig 4.20 Vertical velocity contour (Left), phase field contour (center), and density contour (right) for two trailing bubbles with a density contrast $\gamma^{-1} = 2$, $M_0 = 985$, and $E_0 = 449$.

The upper bubble moved in a quiescent liquid while the lower bubble followed into a low-drag region resulting from the wake caused by the upper bubble. Therefore the two bubbles had different deformation characteristics, and a non-zero relative velocity diminished the separating distance between them, which eventually led to their collision and coalescence. Figure 4.20 shows the vertical velocity contour of the trailing bubbles which indicates a higher velocity of the lower bubble in comparison with the velocity of the upper bubble. Fig 4.20 shows also the phase field contour and the density contour of the trailing bubbles.

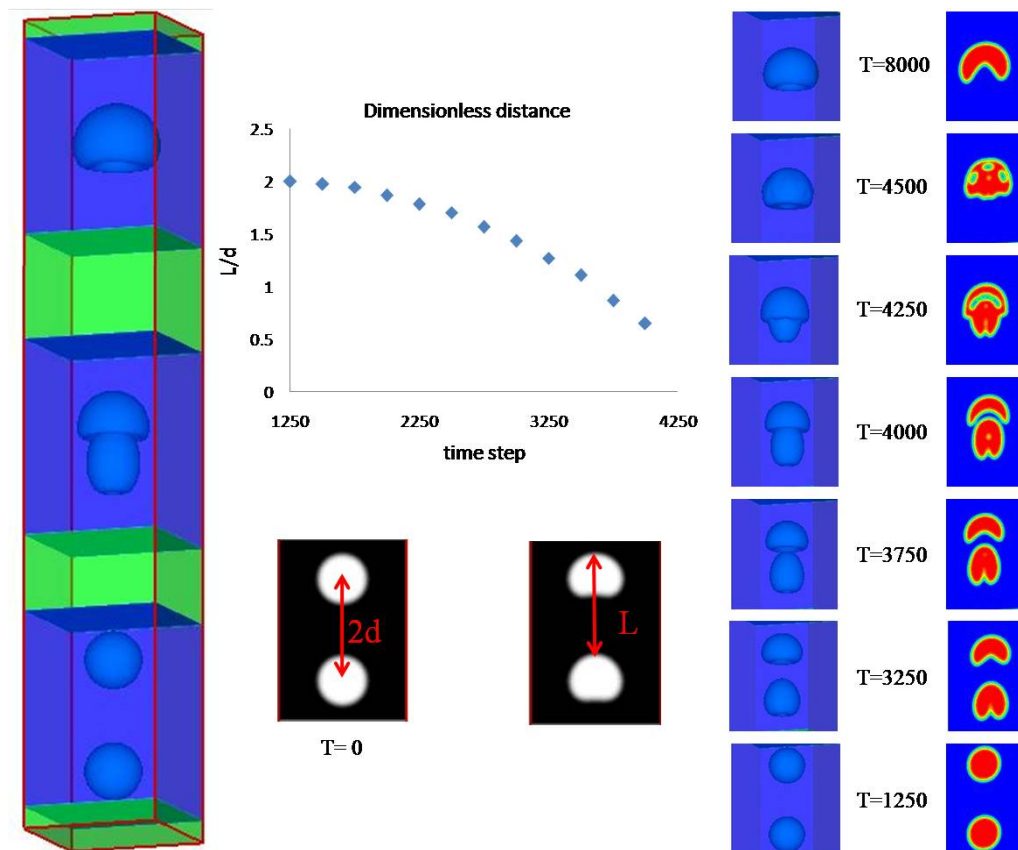


Fig 4.21 Phase field contours of two trailing bubbles taken at different time steps and superimposed in the same frame (left), graph for the changing dimensionless distance between the trailing bubbles with respect to time (center), 3 D phase field contours and their respective 2D cut views of selective snap shots intended to show various events such as trailing, collision and coalescence of the two bubbles (left).

The snap shots in Fig 4.21 for the phase field contours taken at different time steps suggest that the coalescence of the two bubbles did not occur instantaneously and that some liquid was trapped inside the newly formed bubble due to the high inertia impact and to the lack of enough time for the liquid to squeeze out of the bubble. This was also observed by Gupta and Kumar (2008). The liquid eventually drained off the bubble, hence allowing it to attain its steady size which was double the original size of the seeded droplets. Figure 4.21 shows the change in the dimensionless distance measured between the tops of the lower and the upper bubbles. The graph in Fig 4.21 agreed qualitatively with the results of Takada et al (2001). This simulation suggests that the proposed model is capable of handling multiple bubbles clustered in the fine blocks, however it is unsuitable for solving problems with bubbles scattered randomly inside the whole domain.

Grid interface data transfer integrity test

The accuracy of the proposed scheme depends heavily on the quality of the data transfer required at the various grid interfaces. This transfer is directly influenced by the schemes used for both the spatial and the temporal interpolation. The test of the data transfer is also relevant for investigating the effects of the moving fine block on the total outcome of the problem. A good scheme should perform well at the grid interface of the downstream block and after numerous time steps.

The fifth case from Table 4.1 was again used for the investigation of the smoothness of the data transfer at the location indicated as (plane B) in Fig 4.14 and at 9000 coarse time steps. The dimensionless mass flux $\frac{\rho u_z}{\rho^H U_T}$ and the dimensionless

momentum flux $\frac{\rho u_z^2}{\rho^H U_T^2}$ in the vertical direction were calculated locally using the data stored at the grid interface coarse nodes, the overlapping fine nodes and at all the fine nodes respectively. Figure 4.22 shows a qualitative comparison between the three readings for the dimensionless mass flux, while Fig 4.23 represents a comparison between the results of the dimensionless momentum flux.

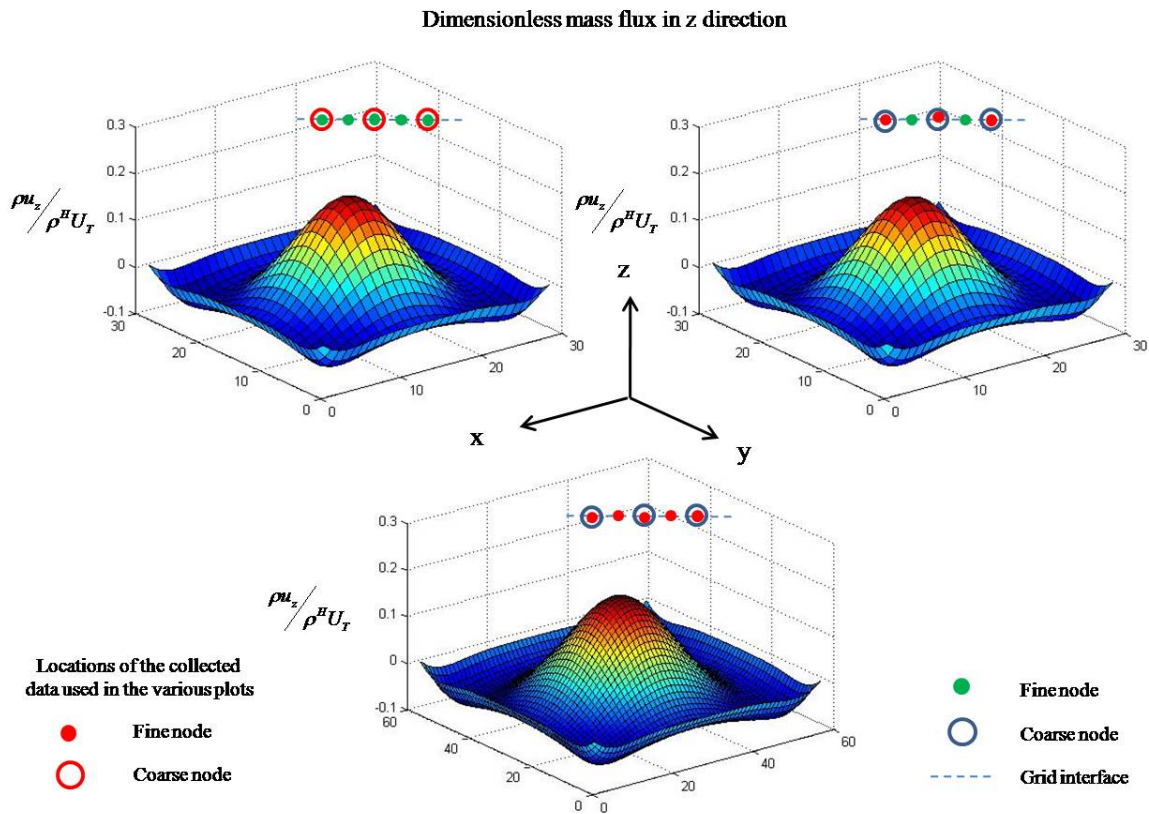


Fig 4.22 Dimensionless mass flux measured at the upstream grid interface (plane B in Fig 4.14) for case five from Table 4.1 at 9000 coarse time steps, data collected from the coarse nodes (top left), data collected from the overlapping fine nodes (top right), and data collected from all the fine nodes (bottom).

Both figures show good qualitative agreement which indicates that the migration of the fine block did not alter the quality of the data transfer at the grid interfaces.

Dimensionless momentum flux in z direction

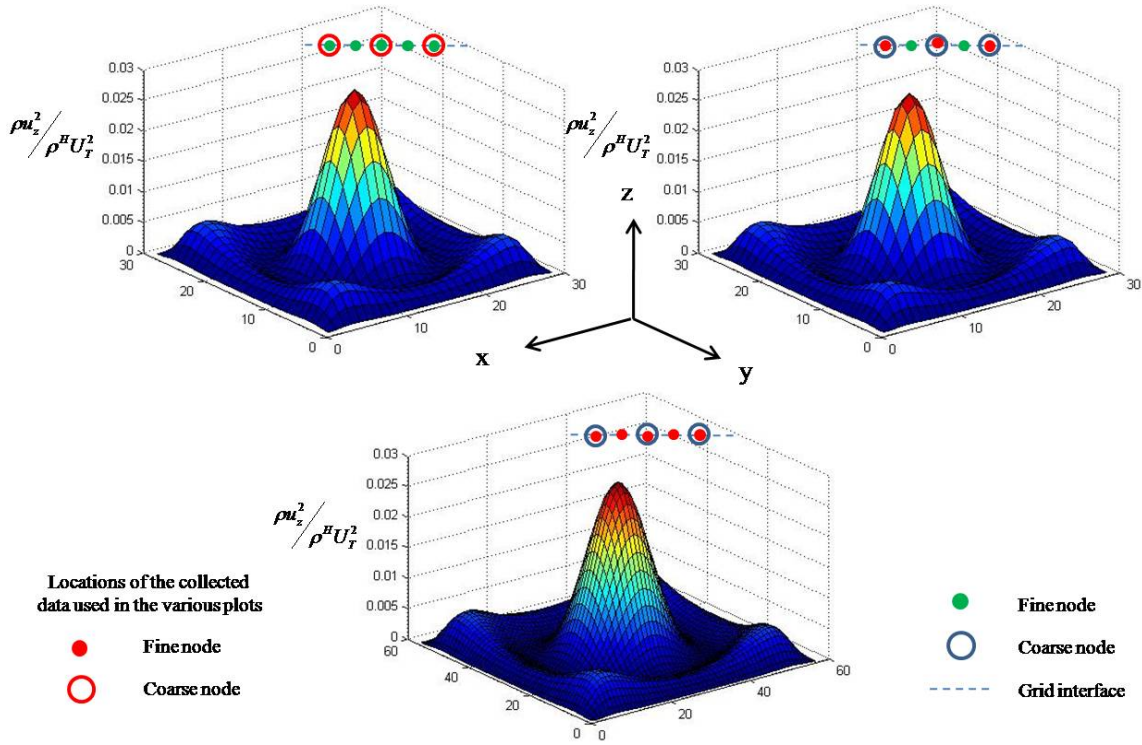


Fig 4.23 Dimensionless momentum flux measured at the upstream grid interface (plane B in Fig 4.14) for case five from Table 4.1 at 9000 coarse time steps; data collected from the coarse nodes (top left), data collected from the overlapping fine nodes (top right), and data collected from all the fine nodes (bottom).

For a quantitative comparison the following composite Simpson's rule was used to calculate both fluxes (Rostam and Mahdi, 2009):

$$\begin{aligned}
 \iint_D f(x, y) dx dy = & \frac{hk}{9} \left\{ f(x_0, y_0) + 2 \sum_{i=1}^{(n/2)-1} f(x_{2i}, y_0) + 4 \sum_{i=1}^{(n/2)} f(x_{2i-1}, y_0) + f(x_n, y_0) \right. \\
 & + 2 \left[\sum_{j=1}^{(m/2)-1} f(x_0, y_{2j}) + 2 \sum_{j=1}^{(m/2)-1} \sum_{i=1}^{(n/2)-1} f(x_{2i}, y_{2j}) + 4 \sum_{j=1}^{(m/2)-1} \sum_{i=1}^{(n/2)} f(x_{2i-1}, y_{2j}) + \sum_{j=1}^{(m/2)-1} f(x_n, y_{2j}) \right] \\
 & + 4 \left[\sum_{j=1}^{(m/2)} f(x_0, y_{2j-1}) + 2 \sum_{j=1}^{(m/2)} \sum_{i=1}^{(n/2)-1} f(x_{2i}, y_{2j-1}) + 4 \sum_{j=1}^{(m/2)} \sum_{i=1}^{(n/2)} f(x_{2i-1}, y_{2j-1}) + \sum_{j=1}^{(m/2)} f(x_n, y_{2j-1}) \right] \\
 & \left. + f(x_0, y_m) + 2 \sum_{i=1}^{(n/2)-1} f(x_{2i}, y_m) + 4 \sum_{i=1}^{(n/2)} f(x_{2i-1}, y_m) + f(x_n, y_m) \right\} \quad (4.24)
 \end{aligned}$$

where $h = k = 2$ lattice units, and $m = n = 30$ for the coarse and the overlapping fine nodes calculations, and $h = k = 1$ lattice unit, and $m = n = 60$ for the fine nodes calculation.

The results presented in Table 4.3 show a good match between the various calculations, thus indicating that the interpolation schemes used in the proposed model had delivered the expected task, and that the smoothness of the data transfer was acceptable.

Table 4.3 Comparison of the calculated mass flux and momentum flux for the fifth case from Table 4.1 at 9000 coarse time steps, with data collected from the various grid nodes which constitute the upstream grid interface.

Nodes type	Mass flux [μ /ts]	Momentum flux [$\mu \cdot \text{lu}/\text{ts}^2$]
Coarse	-2.76074	0.04734
Overlapping fine	-2.51919	0.04569
All fine	-2.60329	0.04548

[μ] lattice mass unit, [lu] lattice space unit, [ts] time step

Computational time advantage

To analyze the computational time advantage of the proposed model, the third case from Table 4.1 was repeated using the approach for density contrast proposed in section 2.1. The grid spacing for the entire domain was similar to the spacing used for the fine block in the previous runs. The ratio between the computational times required for both cases was $Ga = t_{std} / t_{mmb} = 4.92$. The phase field contours, and the bubble vertical displacement versus time steps from the two runs are shown in Fig 4.24.

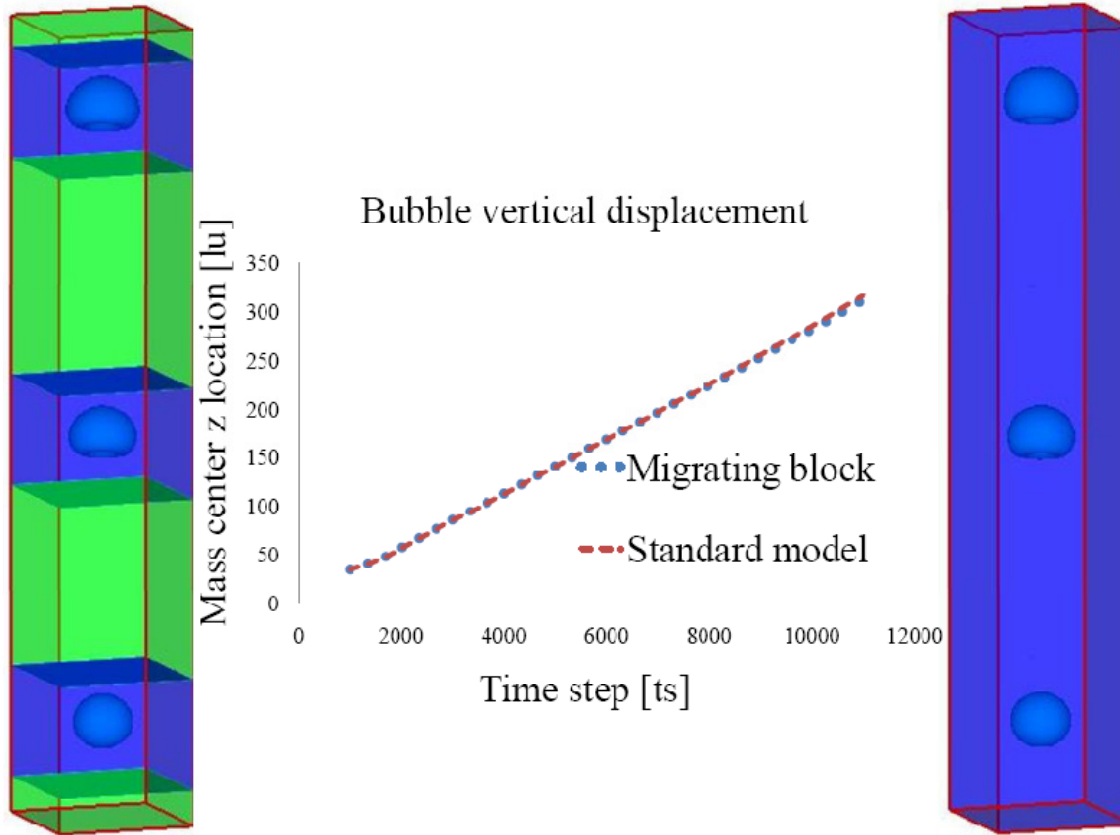


Fig 4.24 Phase field contours and bubble vertical displacement versus time steps comparison between the migrating multi-block simulation and the standard model with $M_0 = 682$, $E_0 = 311$, and $Re = 7.1$.

The following formula is proposed for the estimation of the time saving resulting from the migrating multi-block model:

$$Ga = \frac{N_x N_y N_z}{L_z N_x N_y + \frac{1}{m^4} (N_z - L_z) N_x N_y} \quad (4.24)$$

where N_x , N_y and N_z are the domain length and width and height expressed in fine grids spacing respectively, and L_z is the height of the fine block. The formula is applicable only for 3D models, with the fine block covering the entire width and length. The time saving calculated by Eq. (4.24) is $Ga = 5.24$. The formula overestimated the time gain by 6%. This could be used as an indication of the code level of efficiency.

4.3 Migrating multi-block for the particle-interaction-potential LBM

The particle-interaction-potential LBM (SC model) is a very attractive numerical tool for simulating multi-phase and multi-component flows. The SC's main advantage over other LBM models lays in its capability of handling multiphase fluids with density and viscosity contrast.

a. The migrating multi-block algorithm

A description of a 2D domain shown in Fig 4.25 is used to explain the idea of the MMB, where three blocks of which the central is fine while the others are coarse collectively form the simulation domain. In 3D models the same concept is applicable but the grid intersection lines are replaced by grid intersection planes. The spatial and temporal ratio m between the lattice spacing and the time steps of the fine and coarse grid blocks is the same and it is defined by Eq. (2.39). The fluid and in particular at the grid intersections has to have the same viscosity in order to maintain the same flow conditions (Reynolds number), therefore Eq. (2.40) should be imposed on the fine and the coarse blocks relaxation times (Yu et al., 2002) . The grid intersection between the coarse blocks and the fine block is composed of two lines (planes) on each side of the fine block, where the fine and coarse grids overlap as shown in Fig 4.25 (A, B, C, D).

Information transfer is required at the grid intersections from the post-collision pre-streaming distribution functions which are calculated separately in each individual block. When phase transition is not needed this transfer occurs at intersection nodes of a single phase single component fluids in all blocks, as is the situation in many multi-component simulation cases where these nodes belong to the suspending fluid. This simplifies the algorithm. When phase transition is important the bulk fluid and therefore

the grid intersection nodes should be treated as multiphase fluid by imposing the particle interaction force of Eq. (2.27) with the potential function of Eq. (2.28) throughout the various blocks. The transfer formulae are the same ones used in the model of Yu et al. (2002). At the fine vertical lines (A & B) Eq. (2.41) is applied. At the coarse lines (C & D) the transfer is executed by Eq. (2.42).

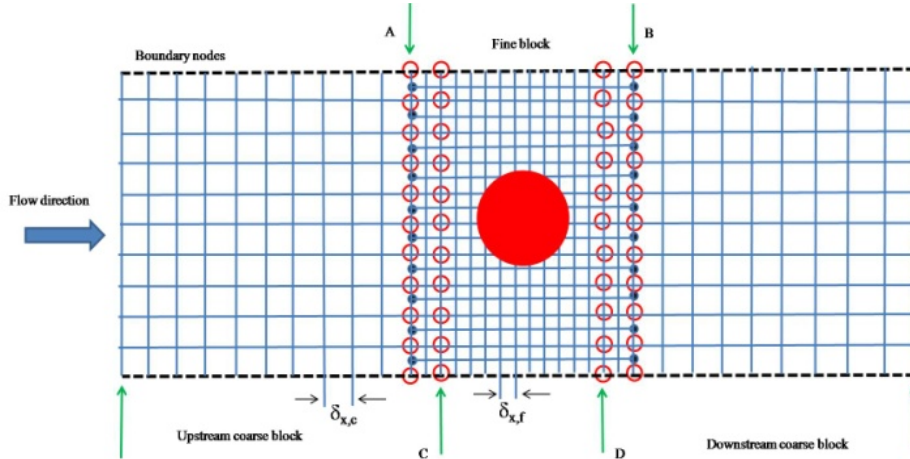


Fig 4.25 Illustration of 2D multi-block LBM domain, with two coarse blocks and one fine block.

b. Simulation results and discussion

Cavitations in 2D orifice flows

Orifice flow is very common in many practical applications (flow meters, flow and pressure reducing valves, microchannels, etc.). While flowing through an orifice the fluid is forced to converge and the maximum convergence occurs in close proximity downstream of the physical orifice. This location is called the vena-contracta, where the velocity increases and the pressure decreases. If the pressure decreases at a nearby location below the vapor pressure the fluid will experience local phase transition (cavitations) which is typically associated with shockwaves capable of significantly damaging the inner walls of a system.

Phase transition occurs in single component fluids when they reach their spinodal point. Spinodal is a point on the fluid equation of state (EOS) graph which represents the maximum tension that a pure liquid can sustain (Sukop and Thorne, 2006). (Sukop and Or, 2005; Sukop and Thorne, 2006) plotted Eq. (2.28) and Eq. (2.30) using the following constants $\psi_0 = 4$, and $\rho_0 = 200$ and had a qualitatively similar EOS graph to that of van der Waals. The graph is shown in Fig 4.26.

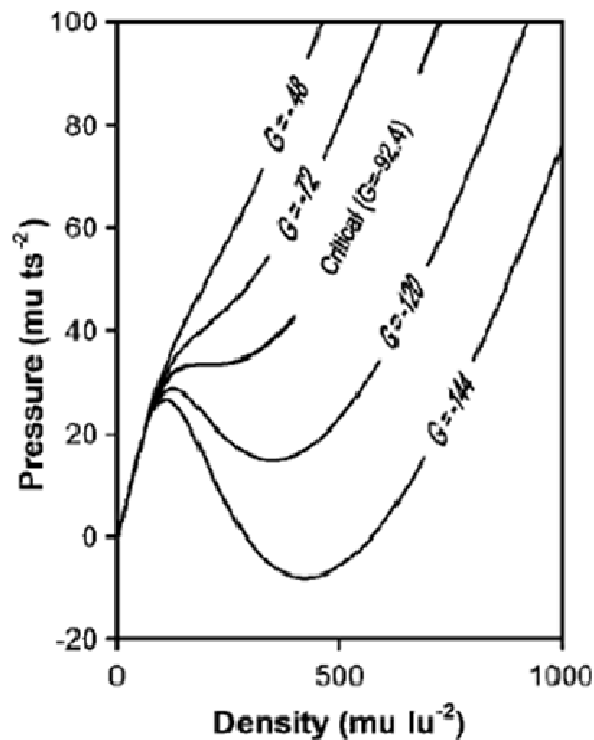


Fig 4.26 Single component multiphase fluid EOS for different values of the interaction potential constant presented by Sukop and Or (2005), (Reprinted with permission).

For a 2D simulation and $G = -120$ which was used in this section, the graph of Fig 4.26 indicates a spinodal fluid density $\rho_{sp} \approx 353 \left[\frac{mu}{lu^2} \right]$ and pressure $p_{sp} \approx 14.62 \left[\frac{mu}{ts^2} \right]$ expressed in lattice units. Lattice units were used in all of the subsequent simulations (mu is mass unit, lu is spacing unit, and ts is time step). A fluid

having conditions under which the density-pressure relationship produces a point which coordinates fall to the left of the spinodal point is expected to have a negative unphysical compressibility and to experience phase transition.

A domain of 601×61 measured in fine lattice units was used to simulate an orifice flow, in which 5,368 lattice squares were fine and 7,967 were coarse. The lattice spacing ratio was $m = 2$. The fine block center was positioned at coordinate point (158, 30) and extended 44 lattice sites in both horizontal directions and through the full height in the vertical direction. This placed the fine block immediately behind an orifice with $7lu$ size as shown in Fig 4.27.

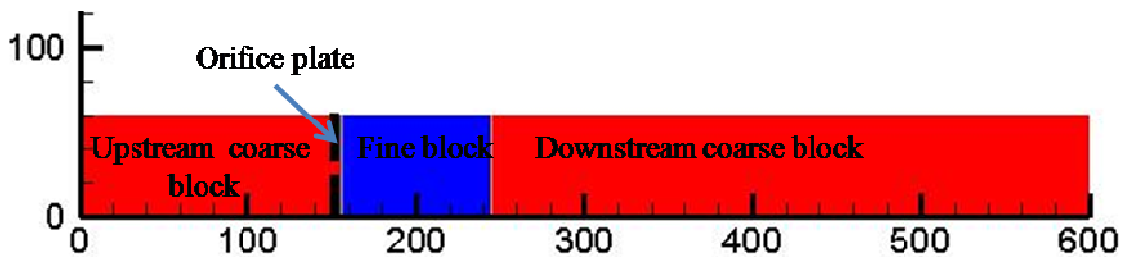


Fig 4.27 Simulation domain with a fine block colored with blue placed immediately behind the orifice and two coarse blocks colored with red.

The relaxation times for the fine and the coarse grids were $\tau_f = 0.58$ and $\tau_c = 0.54$ respectively leading to kinematic viscosity $\nu = 0.0266 [lu^2/ts]$. A parabolic velocity profile was imposed on the inlet boundary with a central velocity $U_c = 0.35 [lu/ts]$ and the no slip boundary condition on the upper and lower walls as well as on the orifice wall faces. The extrapolation method was used for the treatment of the outlet boundary. The orifice Reynolds number was calculated as follows:

$$\text{Re} = \frac{U_0 H_{orif}}{\nu} \approx 105 \quad (4.25)$$

where H_{orif} is the orifice height, U_0 is the average orifice velocity .

Three initial densities ρ_i were used to investigate whether local phase transition had occurred under the above mentioned conditions. Low density fluids were simulated (close to spinodal) since the LBM is unstable when used with high Reynolds numbers needed for the initiation of orifice flow cavitations in fluids with higher densities. The fine block was not allowed to move since the subject of interest was the location of the vena-contracta, positioned directly behind the orifice as shown in Fig 4.28.

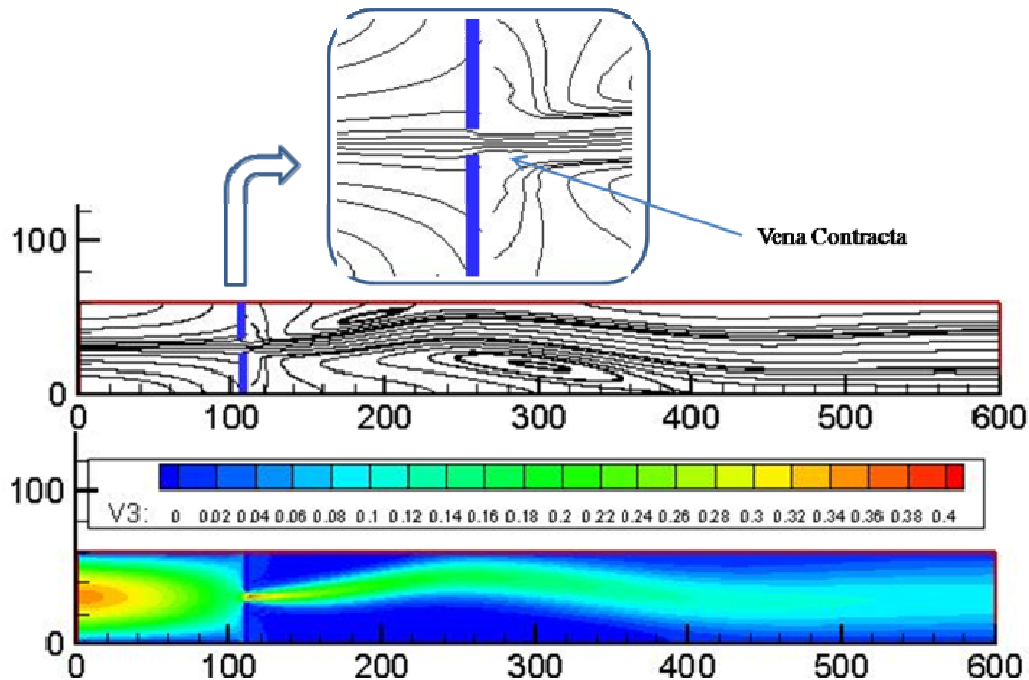


Fig 4.28 Top: Instantaneous streamlines of the flow through a non-central orifice with $Re \approx 788$ and $\rho_i = 450 [\mu/lv^2]$. The vena contracta location was determined as the position where the streamlines were most densely packed indicating higher velocity and lower pressure region. Bottom: Velocity contour in the horizontal direction.

The cavitation number is a dimensionless parameter, used for the description of the magnitude and the intensity of cavitations in a flow (Mishra and Peles, 2005) and it is given by:

$$\lambda_c = \frac{p_3 - p_v}{\frac{1}{2} \rho U_0^2} \quad (4.26)$$

where p_3 is the average pressure downstream of the orifice, p_v is the fluid vapor pressure, and U_0 is the average orifice flow velocity.

The pressure and density values were collected at the location of the vena-contracta from the three simulations. Results presented in Table 4.4 show that phase separation occurred only in the first case when $\rho_i = 360 \text{ [} \mu\text{u/lu}^2 \text{]}$ was used which led to a density and pressure drop below spinodal in correspondence with the graph of Fig 4.26. This was also evident from the insets of Fig 4.29. The calculated cavitation number was $\lambda_c = 0.00063$. The small value of the cavitation number stemmed from the use of a small pressure difference in Eq. (4.26), which was a consequence of using low initial density and low orifice Reynolds number in the simulation.

Table 4.4 Pressure-density measurements at the vena-contracta location from the three simulations are presented below

Initial density	360	400	450
Local density	348.38	387.09	435.47
pressure	14.61	15.17	17.44

The pressure-density relationship from the three simulations was plotted in Fig 4.29, with the insets showing the density contours of the various cases. The experimental picture of Mishra and Peles (2005) shown in the left top inset of Fig 4.29 is for qualitative comparison.

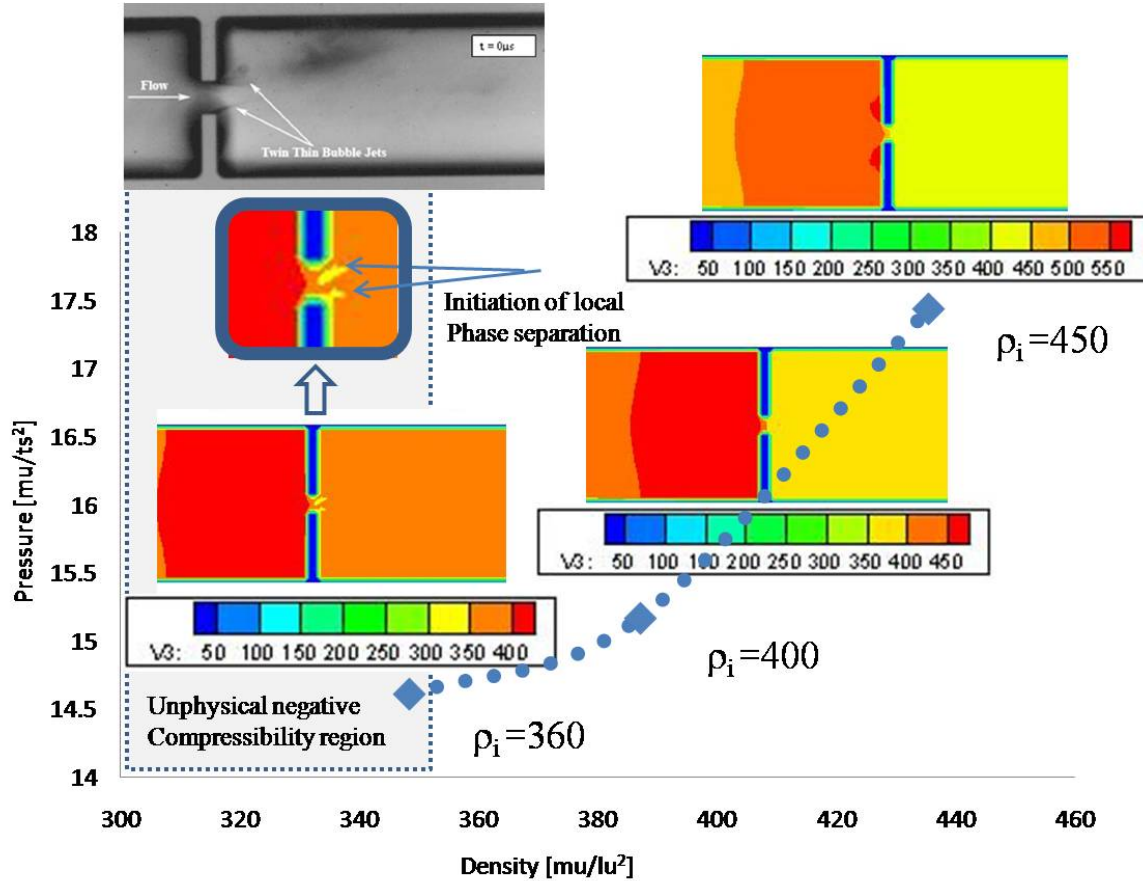


Fig 4.29 Pressure-density relationship for three different initial densities (Dotted line is to guide the eye). Phase separation occurred only for the initial density $\rho_i = 360 \text{ [mu/lu}^2\text{]}$ since the pressure-density intersection point fell into the unphysical negative compressibility region shown in gray color. The figure insets are for the density contours from the three cases. The top left inset is from the experimental work of Mishra and Peles (2005). (Reprinted with permission).

Transient flow metering in 2D orifice

To demonstrate the MMB applicability to single component flows, the input velocity was changed gradually between $0.05 \leq U_0 \leq 0.165 \text{ [lu/ts]}$ with a step $\Delta U_0 = 0.005 \text{ [lu/ts]}$ once every 2,000 time steps. This was to mimic an orifice flow under transient conditions. The initial density used for this simulation was $\rho_i = 800 \text{ [mu/lu}^2\text{]}$ to minimize the compressibility effects. The fine block was increased to cover 10,248

lattice squares (168x61) and it was allowed to shift one coarse lattice unit each 8,000 time steps in the flow direction. The objective was to let the fine block cover the region behind the orifice to enhance the accuracy of the calculations results as shown in Fig 4.30

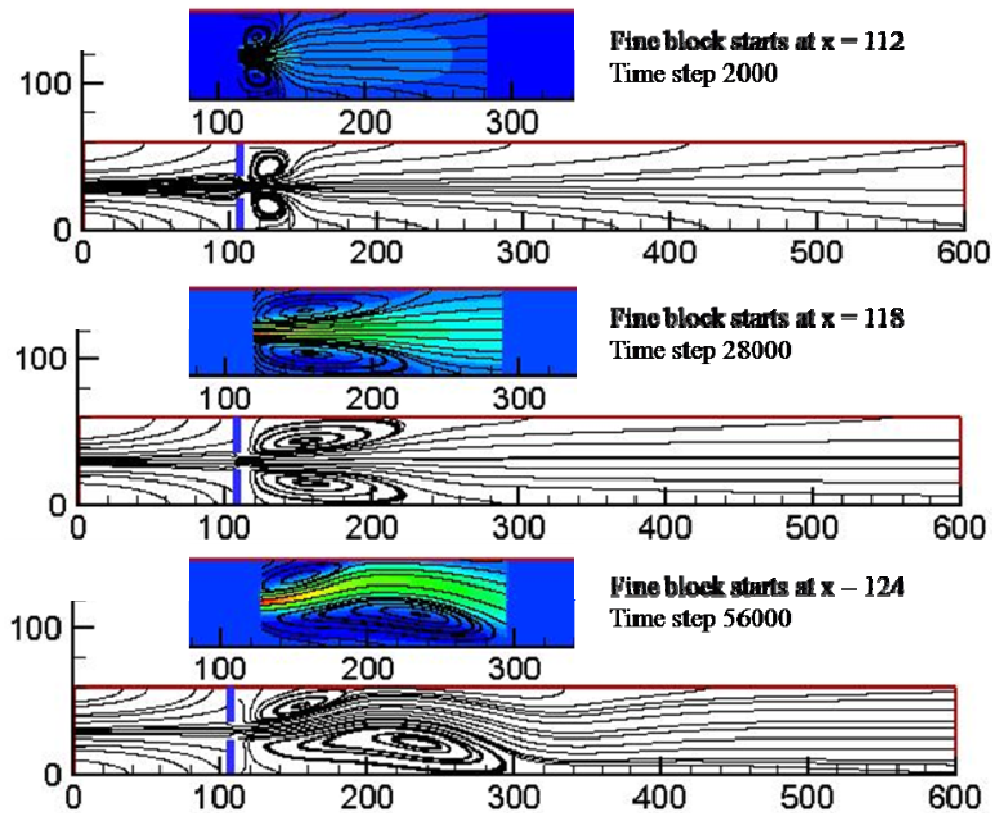


Fig 4.30 Instantaneous streamlines for time steps 2,000, 28,000 and 56,000 with increasing input velocity. The insets show the time advancing fine block in which the calculation is performed with more iterative steps.

For an orifice flow the following analytical formula is applicable for the calculation of the mass flux for an incompressible laminar fluid in a horizontal section (Mishra and Peles, 2005):

$$Q = C_d A_o \sqrt{\frac{2(p_1 - p_2)}{\rho_i (1 - [A_o/A_1]^2)}} \quad (4.27)$$

$$\dot{m} = \rho_i Q = C_d A_o \sqrt{\frac{2\rho_i(p_1 - p_2)}{1 - \beta^4}}$$

where $C_d = f(\beta, Re)$ is an experimentally determined coefficient, A_o is the area of the orifice, $\beta = d/H$ is the orifice size over the channel height, and p_1, p_2 are the pressure in the upstream section of the orifice and the vena- contracta, respectively.

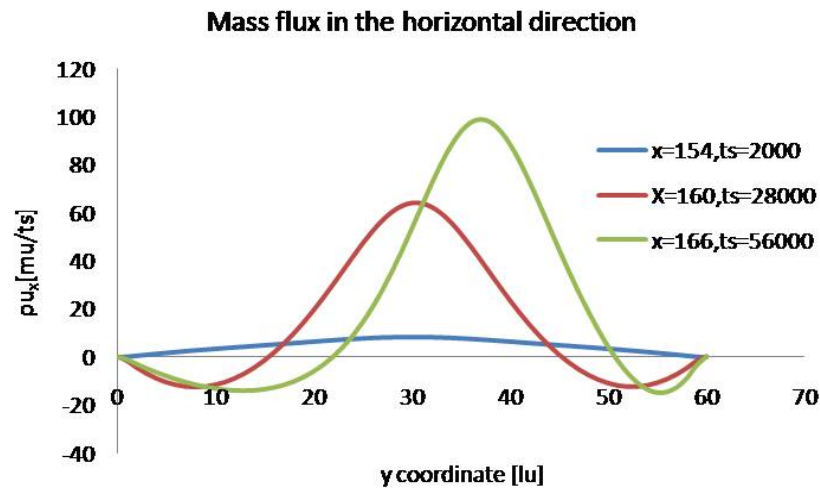


Fig 4.31 Horizontal component of the mass flux presented at three locations and three consecutive time steps.

The mass flux can be also determined directly from the simulation results, assuming a domain of a unity thickness by the following formula:

$$\dot{m}_{ab} = w \int_a^b \rho u dy \quad (4.28)$$

where the thickness $w = 1[lu]$, u is the horizontal component of the velocity and a, b are points with the same horizontal coordinate located on the lower and the upper walls,

respectively. The horizontal component of the mass flux was calculated for the described locations and time steps as shown in Fig 4.31.

Equation (4.28) was solved numerically and Eq. (4.27) for $C_d = 1.0$ was calculated analytically. The pressures p_1 and p_2 were collected from the simulation results and used in Eq. (4.27). The results are presented in Table 4.5. The coefficient C_D accounts for the orifice geometry discharge effects and for the viscous effect which were neglected in the derivation of Eq. (4.27) from Bernoulli's equation.

Table 4.5 Calculation of the mass flow rate by the analytical formula of Eq. (4.27) and directly by Eq. (4.28) for three time steps.

Time step	2000	28000	56000
x [lu]	154	160	166
Re_{ch}	126	275	436
Eq. (28)	534.98	892.13	1196.27
Eq. (29)	298.74	787.63	1197.78

The difference between the two sets of results presented in Table 4.5 could be used for the derivation of the discharge coefficient, although care should be taken since the outcome could deviate from the experimental one due to the compressibility effect of the LBM (Guo et al., 2000), and the two dimensional nature of the domain used in this simulation.

Computational time saving

To estimate the computational time advantage of the MMB model the following formula was introduced:

$$Ga = C_c \frac{N_x N_y}{L_x N_y + \frac{1}{m^3} (N_x - L_x) N_y} \quad (4.29)$$

where Ga is the time gain ratio, N_x and N_y are the domain length and width in fine grids spacing respectively, $0.9 \leq C_c \leq 1.0$ is a code efficiency coefficient, and L_x is the length of the fine block. This formula is applicable only for 2D models, with the fine block covering the entire width. For the first simulation with $L_x = 88$ and estimated $C_c = 0.95$ the time gain ratio calculated by Eq. (4.29) was $Ga = 3.75$. This gave the MMB algorithm a 375% lead in computational time over the standard LBM for the aforementioned case.

Droplet sedimentation and settling on a horizontal wall in 3D geometry

The SC multi-component model lends itself as a convenient tool for simulating the sedimentation of a droplet on a wall with the inclusion of the wall surface energy role due to the incorporation of the fluid-solid interaction force by Eq. (2.34). This is a relevant problem to many applications, and in particular to those dealing with hydrophobic and hydrophilic surfaces. On the other hand the MMB offers computational time saving and enhanced interface resolution which is highly valued in 3D simulations.

Droplet sedimentation towards a horizontal plane is characterized by the Bond number which is a measure of the relative influence of gravity with respect to the surface tension:

$$B = \frac{\Delta\rho g R^2}{\gamma} \quad (4.30)$$

where $\Delta\rho$ is the density difference between the constituent fluids, R is the undistorted droplet radius, and γ is the uniform surface tension.

A domain of $60 \times 60 \times 340$ measured in fine lattice units was used and it was composed of one fine block consisting of 216,000 nodes and two coarse blocks with a total of 126,000 nodes. The spacing ratio was $m = 2$, the relaxation times were $\tau_f = 0.9$ and $\tau_c = 0.7$ for the fine and coarse blocks, respectively. This yielded a kinematic viscosity $\nu = 0.133 [lu^2/ts]$. The suspending fluid had a density $\rho_B = 1 [mu/lu^3]$, while the suspended fluid density was $\rho_R = 4 [mu/lu^3]$. The fluid-fluid interaction constant was $G_{\sigma\sigma} = 0.5$.

Sessile static non-wetting droplet

The droplet static shape was investigated by letting it sediment under gravity towards the horizontal wall. The fluid-solid interaction was turned off. The droplet was positioned in the center of the fine block and had a diameter $D = 36 [lu]$. The no-slip boundary condition was imposed on the lower and upper horizontal walls and a periodic condition was applied in all other directions. The migrating fine block followed the droplet mass center until the lower grid interface reached the fine grid coordinate $z = 2$ which was treated as a wall, and then the droplet was left to sediment alone until it settled on the lower wall as shown in Fig 4.32 Under these conditions the droplet is expected to assume a non-wetting sessile shape.

To determine the characteristics of a non-wetting drop resting on a horizontal wall Hodges et al. (2004) solved the following dimensionless Young-Laplace relationship $P_d - BH = k$ where P_d was the droplet static pressure, B the Bond number, H the height of the drop, and k the droplet curvature. Hodges et al. (2004) presented their results in a graph with the Bond number used as the independent variable.

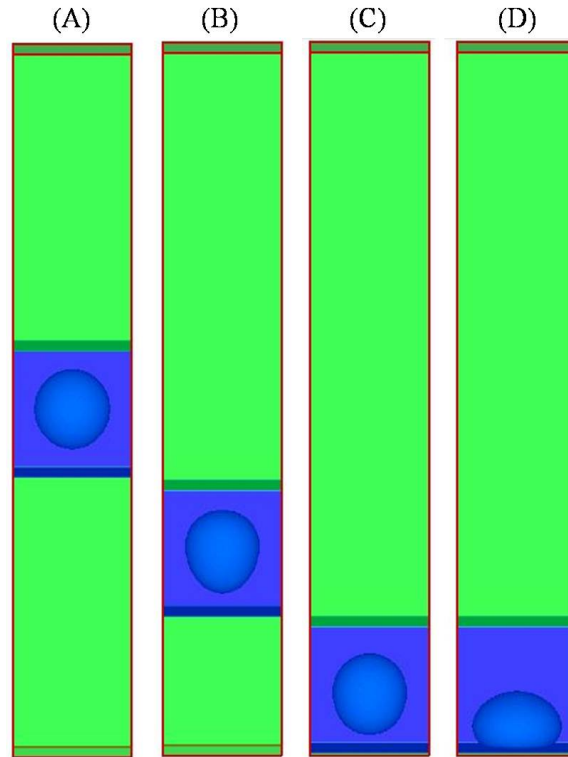


Fig 4.32 Phase field contours for four consecutive time steps, $Re_d = 9.07$ and $B = 1.66$. The migrating fine block (in blue) moved with the droplet in (A) and (B), then the droplet moved alone in (C) and settled on the wall in (D).

Seven values for the gravitational constant were used in the proposed model to produce a variety of conditions ($0.11 \leq B \leq 3.33$) which resulted in different droplet static shapes. The uniform surface tension from Eq. (4.30) was calculated by the following relation: $\sigma_0 = \Delta p R$ where Δp was the pressure difference measured between the fluid inside and outside of the droplet before it settled on the wall. The droplet height and wall contact length were measured and scaled by the droplet radius. The presented results in Fig 4.33 matched reasonably well the 2D results of Hodges et al. (2004).

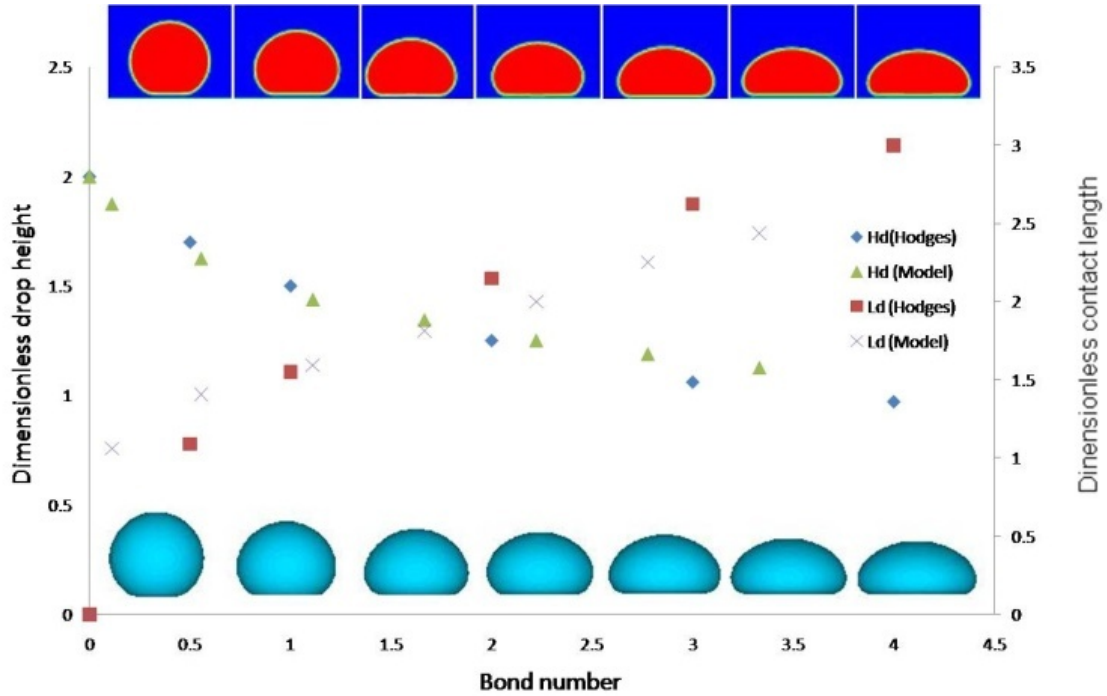


Fig 4.33 Dimensionless droplet height and wall contact length for various Bond numbers. The lower inset show the 3D view of the droplet shapes and the upper inset is their 2D cuts.

Static wetting droplet

For stationary wetting droplet resting on a horizontal wall the contact angle is determined by Young's equation:

$$\cos \theta = \frac{\sigma_{SB} - \sigma_{SR}}{\sigma_{RB}} \quad (4.31)$$

where σ_{SB} , σ_{SR} , and σ_{BR} are the interfacial tension between the solid wall and the droplet, the solid wall and the suspending fluid, and between the two immiscible fluids respectively. In the SC model the interfacial tensions are directly proportional to the interaction forces of Eq. (2.33), and Eq. (2.34), and these forces are dependent on the constant which determines their magnitude.

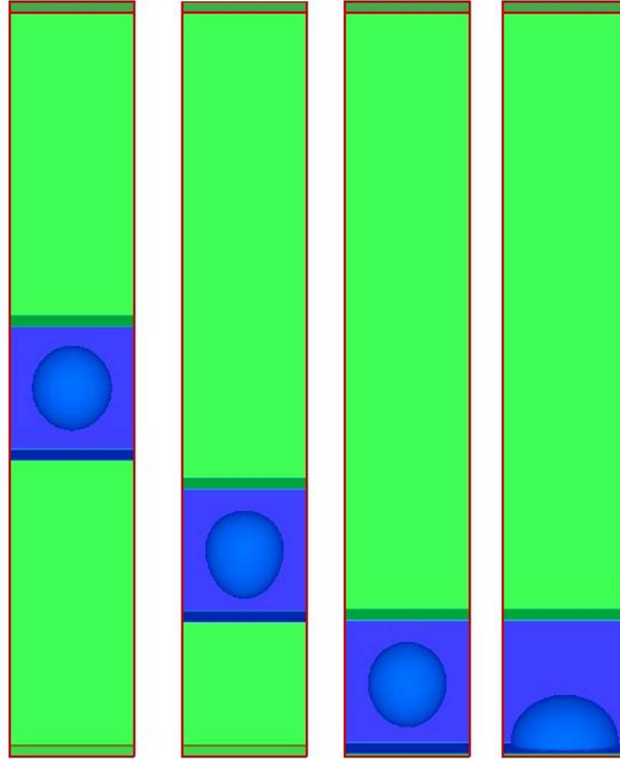


Fig 4.34 Phase field contours for four consecutive time steps with $G_{ads}^R = -0.11$, $G_{ads}^B = 0.14$, $B = 1.11$ and $Re_d = 5.52$.

Huang et al. (2007) proposed the following relation for the calculation of the contact angle using LBM cohesion parameters:

$$\cos \theta = \frac{G_{ads}^B - G_{ads}^R}{G_{\sigma\sigma'} \frac{\rho_1 - \rho_2}{2}} \quad (4.32)$$

where $\rho_1 = \rho_R$ and ρ_2 is a dissolved density of the suspending fluid into the droplet. The fluid-solid interaction constants for the suspending fluid $G_{ads}^B = -0.11$, and for the droplet $G_{ads}^R = 0.14$ were selected carefully so that their corresponding contact angle was in agreement with the calculated value by Eq. (4.32) and yielded a wetting droplet with an acute contact angle $\theta \approx 76^\circ$. The dissolved density in Eq. (4.32) was $\rho_2 = 0.04 [mu / lu^3]$.

Three values for the gravitation constant were used in this simulation to modify the Bond number $4.0 \times 10^{-5} \leq g \leq 1.2 \times 10^{-4}$. The phase field contours of four consecutive time steps are shown in Fig 4.34.

Comparison of the results from the wetting and non-wetting droplet cases is presented in Fig 4.35. The inclusion of the surface energy caused an increase in the droplet dimensionless contact length, and a decrease in the dimensionless height. However the droplet contact angle was not affected by the change in the Bond number as shown in the insets of Fig 4.35, and this was consistent with Eq. (4.31) and Eq. (4.32) since both equations were independent of the acceleration constants which was used to vary the Bond number.

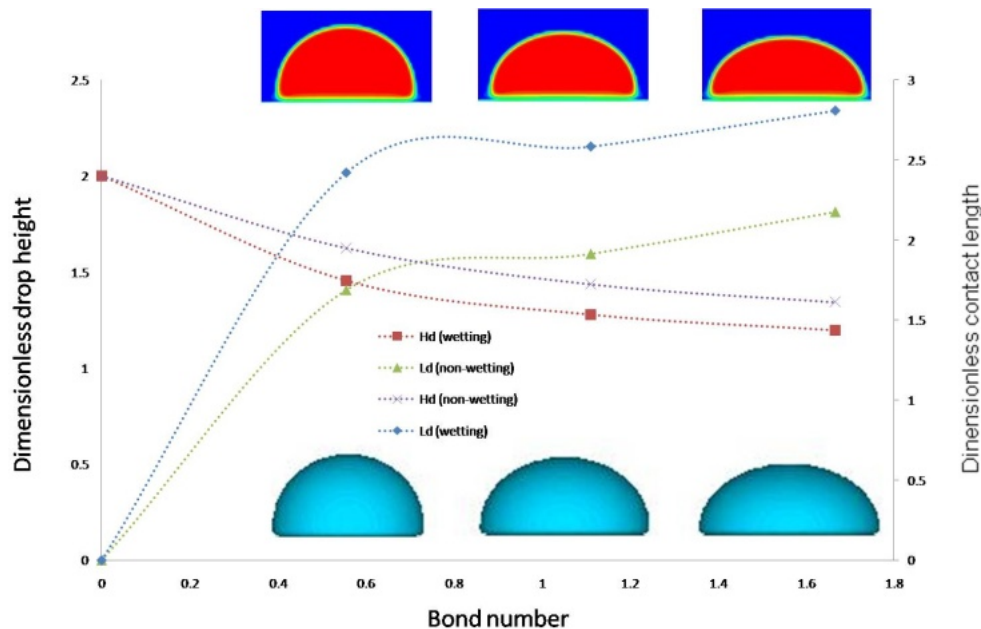


Fig 4.35 Comparison of the dimensionless droplet height and wall contact length for various Bond numbers between the wetting and the non-wetting droplet cases. The insets are the phase field contours for the wetting droplets.

Effects of the solid-fluid interaction constants on the drainage underneath wetting droplets

Lister et al. (2006) studied the drainage underneath sedimenting quasi-static drops using the lubrication theory. A regime diagram was produced by solving a modified pressure equation for the fluid just outside the drop by:

$$p = \frac{\sigma P_d}{b} - \Delta\rho gh - \frac{\sigma h_{xx}}{(1+h_x^2)^{3/2}} \quad (4.33)$$










and solving a film evolution equation expressed as follows:

$$h_t + \left(\frac{h^3}{3} \left(Bh + \frac{h_{xx}}{(1+h_x^2)^{3/2}} \right) \right)_x = 0 \quad (4.34)$$

where h is the height, σ is the surface tension, B is the Bond number, and $\Delta\rho$ is the density excess. Several regions of drop solutions were delineated and they included a sessile-drop with no fluid trapped underneath the drop, equilibrium region with trapped fluid, which extremes led to drop break up or to drainage, and a non equilibrium region (sliding collar). It is obvious from Eq. (4.33) and Eq. (4.34) that the fluid-solid interaction was not considered in the governing equations.

In the proposed model the fluid trapped underneath the droplet is approached through analyzing the dependence of this process on the selection of the fluid-solid interaction constants. The trapping of fluid under the droplet occurs when the magnitudes of the attraction force between the droplet and the wall is relatively large, and for critical values for the interaction constant of the suspending fluid with the wall as shown in Table 4.6. The characteristics of the flow in the trapped film are determined by the balance of the forces due to the hydrostatics, the capillary pressures, and the fluid-solid interaction forces.

Table 4.6 Droplet characteristics dependence on the selection of the fluid-solid interaction constants, for a constant Bond number $B = 0.55$

$G_{\alpha ks}^R$	$G_{\alpha ks}^B$	SD	$G_{\alpha ks}^B$	QE	$G_{\alpha ks}^B$	NE
-0.11	$G_{\text{ads}} < 0.16$		$G_{\text{ads}} \sim 0.16$		$G_{\text{ads}} > 0.16$	
-0.12	$G_{\text{ads}} < 0.11$		$G_{\text{ads}} \sim 0.11$		$G_{\text{ads}} > 0.11$	
-0.14	$G_{\text{ads}} < -0.004$		$G_{\text{ads}} \sim -0.004$		$G_{\text{ads}} > -0.004$	

G_{ads} interaction constant , SD Static drop, QE quasi-equilibrium, NE non-equilibrium

Three major regions were identified: a) static drop region in which the droplet wets the surface and the attraction force with the wall supported by the droplet weight dominates all other forces, thus leading to complete film drainage, b) quasi-static region where the interaction of the suspended fluid with the wall and the hydrostatic (buoyancy of the trapped lighter fluid) and capillary forces counterbalance the droplet wall attraction leading to a stable film underneath the droplet, c) non-equilibrium region in which the force dominance favors a non-static film shape, and this leads to droplet random shift from its initial location and potentially to its break-up.

Computational time saving

For the estimation of the time gain ratio resulting from the use of MMB in the 3D simulations the following formula was used:

$$Ga = C_c \frac{N_x N_y N_z}{L_z N_x N_y + \frac{1}{m^4} (N_z - L_z) N_x N_y} \quad (4.35)$$

where N_x , N_y , and N_z are the domain length and width and height respectively expressed in fine grids spacing, and L_z is the height of the fine block. The formula is applicable only

to 3D models, with the fine block covering the entire width and length. A time gain ratio $G_a \approx 4.17$ was calculated for the above presented simulations using Eq. (4.35) for $L_z = 60$ and estimated $C_c = 0.95$.

CHAPTER 5

HYBRID LBM FOR SURFACTANT-COVERED DROPLETS

This work aims at adding a humble contribution to the wealth of several numerical methods proposed by some devoted researchers for the study of surfactant covered drop's behavior under diverse flow conditions. The work proposes an expansion of the Gunstensen model applicability to cover the study of immiscible droplets with nonionic insoluble surfactant adhering to their interfaces. Adding the surfactant effects on the Gunstensen model is facilitated by the ease in the initialization and the tracking of the surfactant concentration on the interface, which location is well defined in the LBM model at each time step, and by the independent local application of a non-isotropic interfacial tension on the droplet external surface.

5.1 Surfactants convection-diffusion equation

The surfactant concentration distribution on the interface of an immiscible mixture is governed by the following dimensional form of the general time-dependent surfactant convection-diffusion equation (Milliken et al. 1992):

$$\partial_t \Gamma + \nabla_s \cdot (\mathbf{u}_s \Gamma) + k \Gamma u_n = D_s \nabla_s^2 \Gamma + q_{chem} + q_f \quad (5.1)$$

In Eq. (5.1) $\partial_t \Gamma$ accounts for the temporal change in the interface surfactant concentration, $\nabla_s \cdot (\mathbf{u}_s \Gamma)$ is the convection term, and $k \Gamma u_n$ models the effects of the change in the surface curvature on the surfactant concentration distribution. $D_s \nabla_s^2 \Gamma$ is the diffusion term, q_{chem} accounts for the interface surfactant formation due to chemical reaction and q_f accounts for the net flux to the interface from the bulk phases due to adsorption-desorption (both q_{chem} and q_f effects are not considered in this work).

The objective of this sub- section is to rewrite Eq. (5.1) as a function of the LBM variables in 2D geometry. The units used in this work are identified as follows: spatial lattice unit [lu], time step [ts], mass unit [mu], lattice mole [$lmol$].

For insoluble surfactant, subjected to flow conditions, in which the convection time scale is much greater than the diffusion time scale, the time-dependent convection-diffusion equation is reduced to the following form:

$$\partial_t \Gamma + \nabla_s \cdot (\mathbf{u}_s \Gamma) + k \Gamma u_n = 0 \quad (5.2)$$

where ∇_s is the surface gradient, Γ is the surfactant concentration, k is the curvature calculated by Eq. (2.17), u_n is the normal velocity magnitude at the interface and it is given by:

$$u_n = \mathbf{u} \cdot \mathbf{n} = u_x n_x + u_y n_y \quad (5.3)$$

where \mathbf{u} is the macroscopic velocity derived from Eq. (2.9). \mathbf{u}_s is the tangential velocity with vertical and horizontal component magnitudes expressed respectively as:

$$\begin{aligned} u_{sx} &= u_x - n_x^2 u_x - n_x n_y u_y \\ u_{sy} &= u_y - n_y^2 u_y - n_x n_y u_x \end{aligned} \quad (5.4)$$

Using the product rule $\nabla_s \cdot (\mathbf{u}_s \Gamma)$ can be expressed as a function of the tangential velocity and the normal to the interface components, respectively. The term $k \Gamma u_n$ is straightforwardly derived as the multiplication of three scalar quantities. Combining all the terms of Eq. (5.2) leads to the following simplified equation:

$$\partial_t \Gamma + C_1 \partial_x \Gamma + C_2 \partial_y \Gamma + C_3 \Gamma = 0 \quad (5.5)$$

where the coefficients C_j are expressed as follows:

$$\begin{aligned}
C_1 &= u_{sx} \\
C_2 &= u_{sy} \\
C_3 &= (kn_x u_x + kn_y u_y) + n_y^2 \partial_x u_{sx} + n_x^2 \partial_y u_{sy} - n_x n_y (\partial_y u_{sx} + \partial_x u_{sy})
\end{aligned} \tag{5.6}$$

When the diffusion of the interface surfactant is considered, the surfactant concentration time dependent convection-diffusion equation is given by the following:

$$\partial_t \Gamma + \nabla_s \cdot (\mathbf{u}_s \Gamma) + k \Gamma u_n = D_s \nabla_s^2 \Gamma \tag{5.7}$$

D_s is the surface diffusion constant which can be determined in lattice units $[lu^2 ts^{-1}]$ from the following relationship: $Pe_s = \dot{\gamma} R_0^2 / D_s$, where Pe_s is the surface Péclet number which represents the ratio between the convection and diffusion of the surfactants on the interface and R_0 is the droplet radius. The final form of the equation is given by:

$$\partial_t \Gamma + C_1 \partial_x \Gamma + C_2 \partial_y \Gamma + C_3 \Gamma + C_4 \partial_{xx}^2 \Gamma + C_5 \partial_{yy}^2 \Gamma + C_6 \partial_{xy}^2 \Gamma = 0 \tag{5.8}$$

where the coefficients C_j are calculated by the following:

$$\begin{aligned}
C_4 &= (n_x^2 - 1) D_s \\
C_5 &= (n_y^2 - 1) D_s \\
C_6 &= 2n_x n_y D_s
\end{aligned} \tag{5.9}$$

The surfactant concentration effect on the interfacial tension of the droplet can be imposed by either one of the surfactant equations of state; the Adamson linear equation (Valenkar et al., 2004):

$$\sigma_s = \sigma_0 - \Gamma RT \tag{5.10}$$

or the Langmuir non-linear equation (Eggleton et al., 2001):

$$\sigma_s = \sigma_0 + RT \Gamma_\infty \ln \left(1 - \frac{\Gamma}{\Gamma_\infty} \right) \tag{5.11}$$

where σ_s is contaminated interfacial tension, R is the universal gas constant and T is the temperature in Kelvin. The two equations can be rewritten for convenience as follows:

$$\sigma_s = \sigma_0(1 - E_0\Gamma^*) \quad (5.12)$$

$$\sigma_s = \sigma_0 \left[1 + E_0 \ln(1 - \Gamma^*) \right] \quad (5.13)$$

where σ_0 is the surface tension of a clean droplet, E_0 the surfactant elasticity. E_0 is a positive dimensionless parameter which determines the strength of the surfactant concentration effects on the droplet interfacial tension and it is given by (Valenkar et al., 2004):

$$E_0 = \frac{\Gamma_\infty RT}{\sigma_0} < 1 \quad (5.14)$$

The dimensionless surfactant concentration is calculated by the following ratio:

$$\Gamma^* = \frac{\Gamma}{\Gamma_\infty} \quad (5.15)$$

where Γ_∞ is the saturation surfactant concentration which can be derived from Eq. (5.14)

in lattice units as $\Gamma_\infty = \frac{E_0\sigma_0}{RT} [lmol/lu^2]$ and the product $RT=1/3$ is used for the isothermal LBM.

5.2 The hybrid LBM model

The proposed model uses the Gunstensen LBM for the calculation of the flow pressure, the velocity field and for tracking the fluid-fluid interface. During initialization of the LBM, and after locating the interface's nodes through the magnitude of the phase field gradient $\nabla\rho^N$ of Eq. (2.16), an initial surfactant concentration Γ_i is imposed on the interface with a controllable thickness as shown in Fig 5.1 (C). The selected value of Γ_i

should produce the desired surfactant coverage $c_{in} = \Gamma_i / \Gamma_\infty$ needed for the particular case.

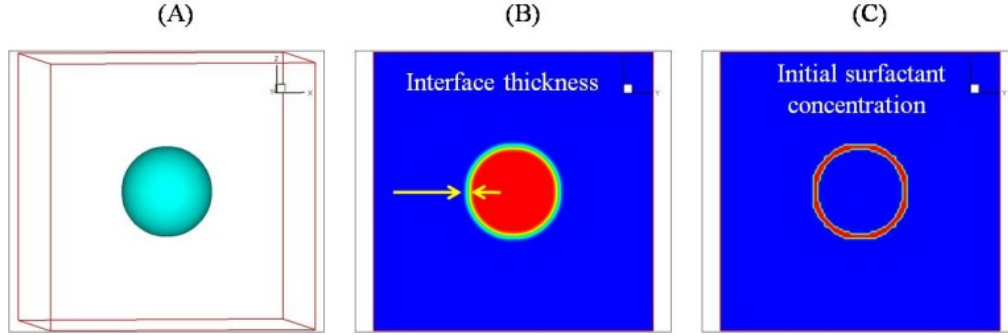


Fig 5.1 Initialization of the surfactant concentration at the interface of a 3D droplet: (A) 3D domain with a central droplet, (B) 2D view of the phase field showing the interface thickness, (C) 2D view of the uniform surfactant concentration contour on the interface.

The calculated velocity component magnitudes (u_x, u_y) , the droplet curvature and the interface normal component magnitudes (k, n_x, n_y) are then used for the derivation of the simplified surfactant-diffusion equation, which is eventually solved by a finite difference scheme resolved on the same spatial lattice grid. The hopscotch explicit and unconditionally stable finite difference scheme (Tanehill et al., 1998) is used here. This scheme uses two consecutive sweeps through the domain. For the first sweep $\Gamma_{i,j}^{n+1}$ is calculated at each grid point, for which $i + j + n$ is even, by a simple explicit scheme:

$$\begin{aligned} & \frac{\Gamma_{i,j}^{n+1} - \Gamma_{i,j}^n}{\Delta t} + C_1 \frac{\Gamma_{i+1,j}^n - \Gamma_{i-1,j}^n}{2\Delta x} + C_2 \frac{\Gamma_{i,j+1}^n - \Gamma_{i,j-1}^n}{2\Delta y} + C_3 \Gamma^n + C_4 \frac{\Gamma_{i+1,j}^n - 2\Gamma_{i,j}^n + \Gamma_{i-1,j}^n}{\Delta x^2} \\ & + C_5 \frac{\Gamma_{i,j+1}^n - 2\Gamma_{i,j}^n + \Gamma_{i,j-1}^n}{\Delta y^2} + C_6 \left(\frac{\Gamma_{i+1,j+1}^n - \Gamma_{i+1,j-1}^n}{2\Delta y} - \frac{\Gamma_{i-1,j+1}^n - \Gamma_{i-1,j-1}^n}{2\Delta y} \right) = 0 \end{aligned} \quad (5.16)$$

For the second sweep $\Gamma_{i,j}^{n+1}$ is calculated at each grid point, for which $i + j + n$ is odd, by a simple apparent implicit scheme:

$$\begin{aligned}
& \frac{\Gamma_{i,j}^{n+1} - \Gamma_{i,j}^n}{\Delta t} + C_1 \frac{\Gamma_{i+1,j}^{n+1} - \Gamma_{i-1,j}^{n+1}}{2\Delta x} + C_2 \frac{\Gamma_{i,j+1,k}^{n+1} - \Gamma_{i,j-1,k}^{n+1}}{2\Delta y} + C_4 \frac{\Gamma_{i+1,j}^{n+1} - 2\Gamma_{i,j}^{n+1} + \Gamma_{i-1,j}^{n+1}}{\Delta x^2} \\
& + C_5 \frac{\Gamma_{i,j+1}^{n+1} - 2\Gamma_{i,j}^{n+1} + \Gamma_{i,j-1}^{n+1}}{\Delta y^2} + C_3 \Gamma^{n+1} + \frac{C_6}{2\Delta x} \left(\frac{\Gamma_{i+1,j+1}^{n+1} - \Gamma_{i+1,j-1}^{n+1}}{2\Delta y} - \frac{\Gamma_{i-1,j+1}^{n+1} - \Gamma_{i-1,j-1}^{n+1}}{2\Delta y} \right) = 0
\end{aligned} \tag{5.17}$$

The second sweep is expressed in an implicit form, but it is solved as an explicit equation, because the first sweep provides the necessary information needed for the computation of $\Gamma_{i,j}^{n+1}$. The truncation error for the used hopscotch scheme in the proposed model is of the following order $O[\Delta t, (\Delta x)^2, (\Delta y)^2]$.

Beside the fact that the hopscotch scheme is unconditionally stable, it is also simple for coding especially if the time step for the finite difference is to be modified from that of the LBM. This can be achieved by using the three-point Lagrangian interpolation for the calculation of the required coefficients C_j at a fraction of the LBM time step as follows:

$$\underbrace{C_j^{t_3-r/n}}_{1 \leq r < n} = \sum_{p=1}^3 [C_j^{t_p} \prod_{q=1, p \neq q}^3 \frac{(t_3 - r/n) - t_q}{t_p - t_q}] \tag{5.18}$$

A ratio $n = t_{LBM}/t_{FD} = 4$ was used in this model unless otherwise was mentioned, and r is a positive integer $1 \leq r < n$. The coupling of the finite difference scheme with the LBM is realized through the surfactant equation of state. In this model the non-linear equation of state was more often used in the simulations.

Halliday et al. (2007) derived the following relationship between the pressure jump across the interface and the surface tension parameter:

$$\Delta P = \left| \int_{P_B}^{P_R} \mathbf{F} dn \right| = \alpha k \tag{5.19}$$

where F is the force from Eq. (2.16) and \mathbf{n} is the interface normal, k is the curvature from Eq. (2.17), and P_B, P_R are the measured pressures outside and inside the droplet, respectively. This suggests based on Laplace's law for the surface tension that the magnitude of the surface tension in the model is equal to that of the surface tension parameter α from Eq. (2.16); therefore Eq. (5.13) can be re-evaluated as follows:

$$\alpha = \alpha_0 \left[1 + E_0 \ln(1 - \Gamma^*) \right] \quad (5.20)$$

where α_0 is the surface tension parameter for a clean droplet. The surface tension parameter in the proposed model is thus non-isotropic, and it rather changes locally based on the outcome of Eq. (5.20), which is mainly dependent on the calculated local surfactant concentration by Eq. (5.8).

No upper bond on the surfactant concentration is required in this model. An important factor which prevents any further build-up of the concentration is the Marangoni stress which is expressed as follows (Hu and Lips, 2003):

$$-\nabla_s \sigma_s = -\partial_\Gamma \sigma_s \cdot \nabla_s \Gamma \quad (5.21)$$

The partial derivative $\partial_\Gamma \sigma$ where σ is expressed by Eq. (5.13) yields the following equation:

$$\partial_\Gamma \sigma_s = -\frac{RT}{(1 - \Gamma/\Gamma_\infty)} \quad (5.22)$$

Equation (5.21) and Eq. (5.22) indicate that an increase in the surfactant surface concentration leads to an increase in the Marangoni stress, which in turn slows down the surface velocity and hampers any further build up of surfactant towards the regions of higher concentration.

The flow chart for the hybrid LBM for surfactant covered droplets is presented in Fig 5.2.

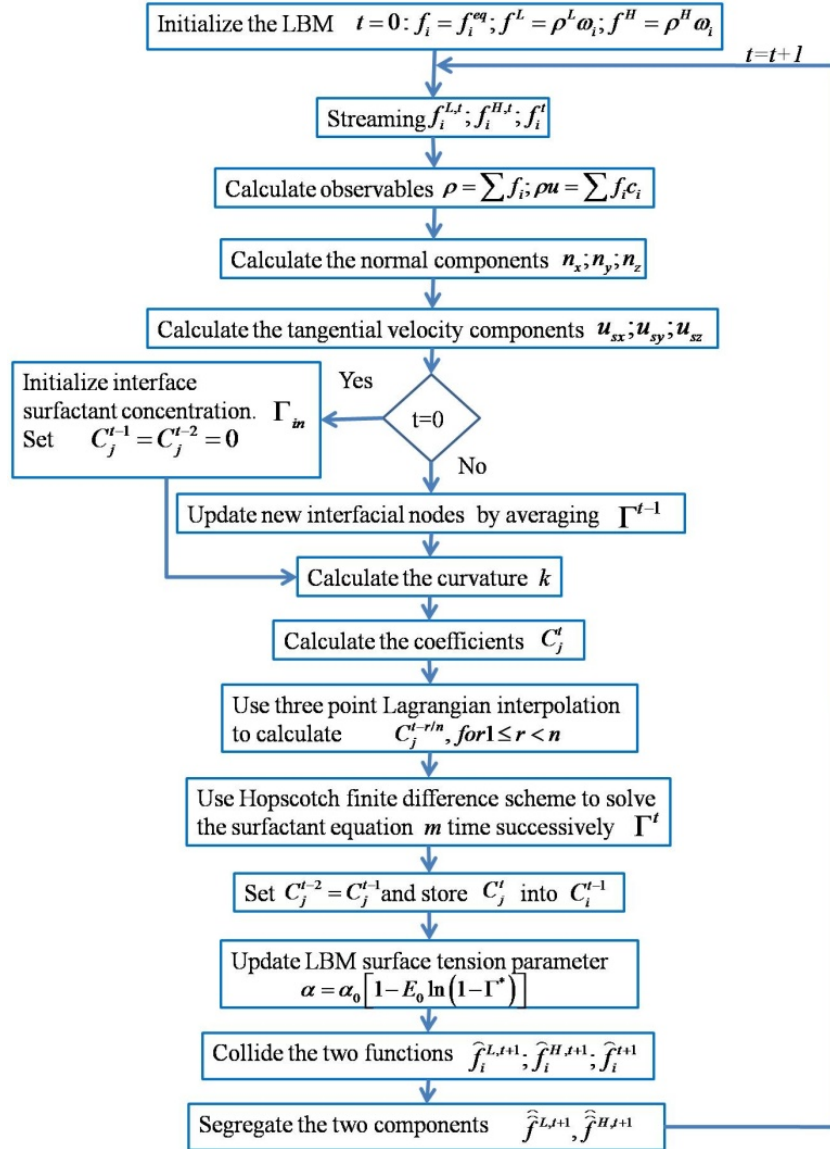


Fig 5.2 Flow chart for the hybrid LBM for surfactant covered- droplets.

5.3 Simulation results and discussions

To demonstrate the proposed model suitability as a tool for investigating the surfactant-covered droplet behavior under diverse flow conditions, the model was used for the study of the surfactant effects on the droplet deformation in simple shear flow, uniaxial extensional flow and on the terminal velocity of a buoyant surfactant-covered droplet.

a. Surfactant-covered droplets in simple shear flows

To study the effects of surfactants on the droplet behavior in simple shear flows, the setting of the base model parameters was decided through studying the flow deformation characteristics of a surfactant-free droplet ($\Gamma_i = 0$). The numerical results were then compared with the experimental work of Cristini et al. (2002), who investigated the transient deformation of clean droplets in dilute emulsions for large values of the capillary numbers. Cristini et al. (2002) studied the transient lamellar microstructures of some polymer blends which exhibited elongation and flattening of the droplets under strong shear flow conditions and for low viscosity ratio. Such blend morphologies were attractive because they caused a reduction in the permeability of certain blends to hydrocarbon and to oxygen, and increased their impact strength (Cristini et al., 2002).

The droplet lamellar structure shown in Fig 5.3 is characterized by the normalized length R_1/R_0 , thickness R_2/R_0 and width R_3/R_0 , where R_0 is the initial droplet radius. The interfacial area generation during the droplet deformation is calculated by $R_1 R_3/R_0^2$.

A domain consisting of $123[l\mu^3]$ was used in this simulation with a suspended central clean droplet having a radius $R_0 = 20[l\mu]$. The interfacial tension parameter was $\alpha_0 = 2 \times 10^{-4}$, and a shear rate $\dot{\gamma} = 9.75 \times 10^{-5}[ts^{-1}]$ was imposed through moving the upper and lower walls in the directions shown in Fig 5.3 by the following:

$$\mathbf{u}^\infty(\mathbf{x}) = \begin{pmatrix} 0 & 0 & \dot{\gamma} \\ 0 & 0 & 0 \\ 0 & 0 & 0 \end{pmatrix} \cdot \mathbf{x} \quad (5.23)$$

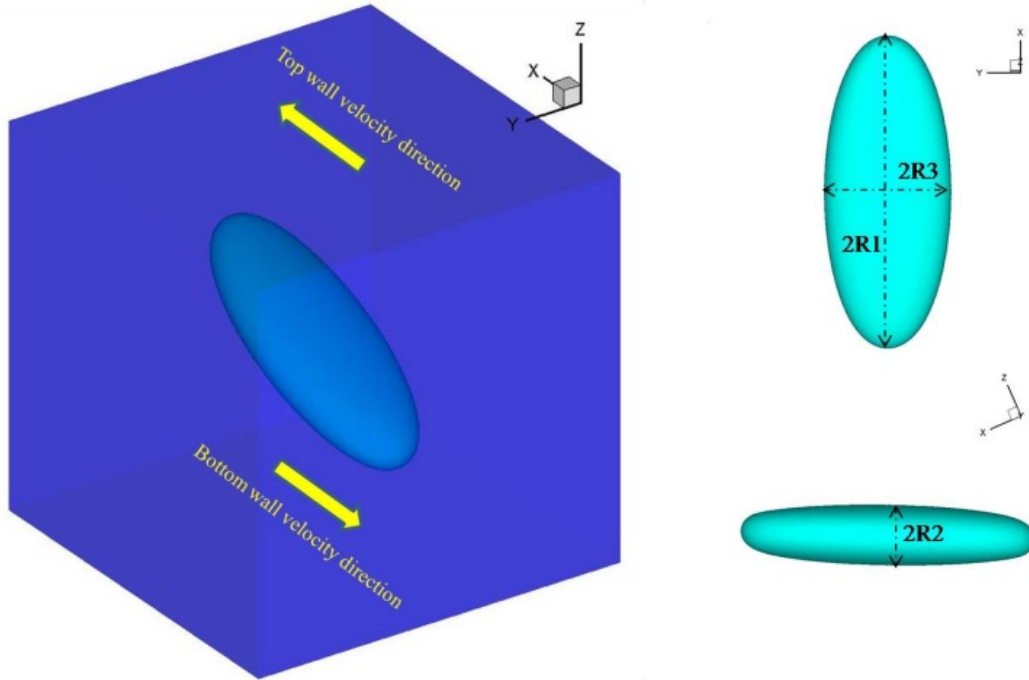


Fig 5.3 Illustration of the LBM simulation domain with a central clean droplet under simple shear stress and the three characteristic radii used in the analysis of the results.

The periodic boundary condition was used in all other directions. The relaxation time for the ambient fluid was $\tau_m = 1.213$ and for the droplet $\tau_d = 0.571$ leading to a viscosity ratio $\eta = 0.1$. The interface viscosity was calculated by Eq. (2.15). The density of both fluids was set to $\rho = 2 \left[\frac{mu}{lu^3} \right]$.

The droplet deformation in simple shear flows is characterized by the capillary number which is the ratio of the droplet deforming shear stress and the restoring stress due to the interfacial tension:

$$Ca = \frac{R_0 \mu_m \dot{\gamma}}{\sigma_0} \quad (5.24)$$

where σ_0 is the interfacial tension of a clean droplet and μ_m is the dynamic viscosity of the matrix. Equation (5.24) yielded a capillary number $Ca = 4.6$ in correspondence with one of the experimental condition of Cristini et al. (2002). The resulting dimensionless width of the droplet from the proposed model with respect to the dimensionless time is presented in Fig 5.4.

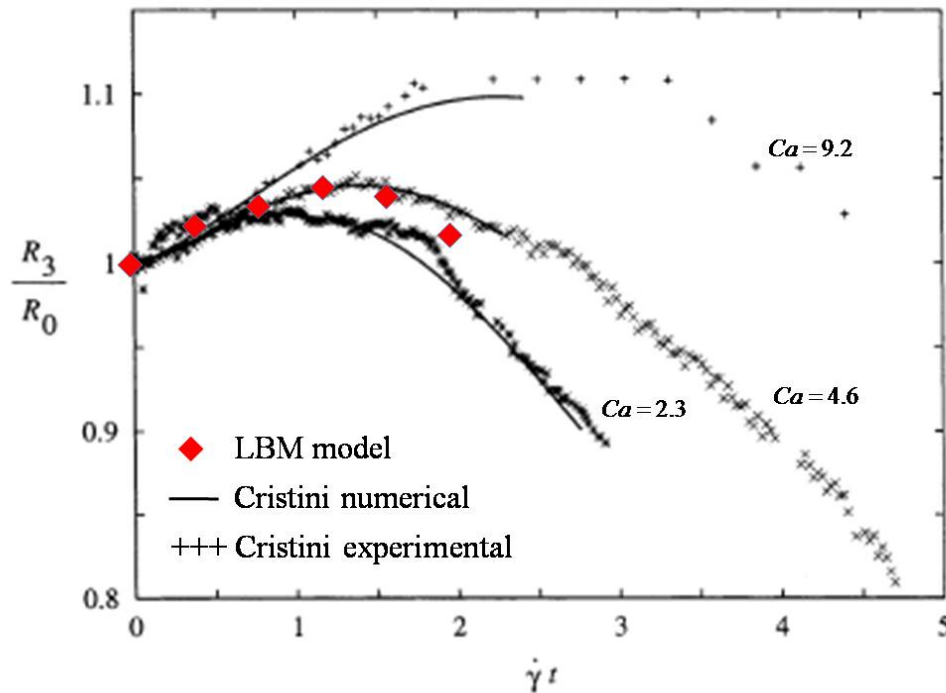


Fig 5.4 Comparison of the proposed numerical model results with the experimental and numerical results of Cristini et al. (2002) for a clean droplet dimensionless width as a function of the dimensionless time. The viscosity ratio is $\lambda = 0.1$, and the capillary number is $Ca = 4.6$. (Reprinted with permission)

The clean droplet case showed a good agreement with the experimental data for the dimensionless time $\dot{\gamma}t \leq 2.0$; Therefore the investigation of the area generation due to the presence of surfactants will be limited to values of the dimensionless time $\dot{\gamma}t < 2.0$ while other droplet flow deformation characteristics will be discussed for time step

$\dot{\gamma}t = 3.12$ corresponding to the end of the simulation time which was dictated by the desire of not allowing the droplet to deform beyond the periodic boundaries.

Surfactant coverage effects

To test the effects of surfactant coverage c_{in} on the droplet deformation under simple shear flow, the surfactant elasticity was set to $E_0 = 0.2$ as the use of this value was justified by Velankar et al. (2002) for low-molecular-weight surfactants. The saturation surfactant concentration was calculated using Eq. (5.14) and the resulting value was $\Gamma_\infty = 1.2 \times 10^{-4} [lmol/lu^2]$. This allowed the selection of the various initial surfactant concentrations Γ_i in order to achieve the range of surfactant coverage $0.2 \leq c_{in} \leq 0.6$. The surface Péclet number was set to $Pe_s = 10$.

The interfacial area generation was calculated for the various cases at a dimensionless time step $\dot{\gamma}t = 1.17$ corresponding to the greatest value for the ratio $\frac{R_3}{R_0}$ which was presented in Fig 5.4. The results shown in Fig 5.5 indicate an increase in the area generation with the increase in the surfactant coverage as a consequence of the simultaneous increase in the droplet elongation (R_1), and flattening (R_3).

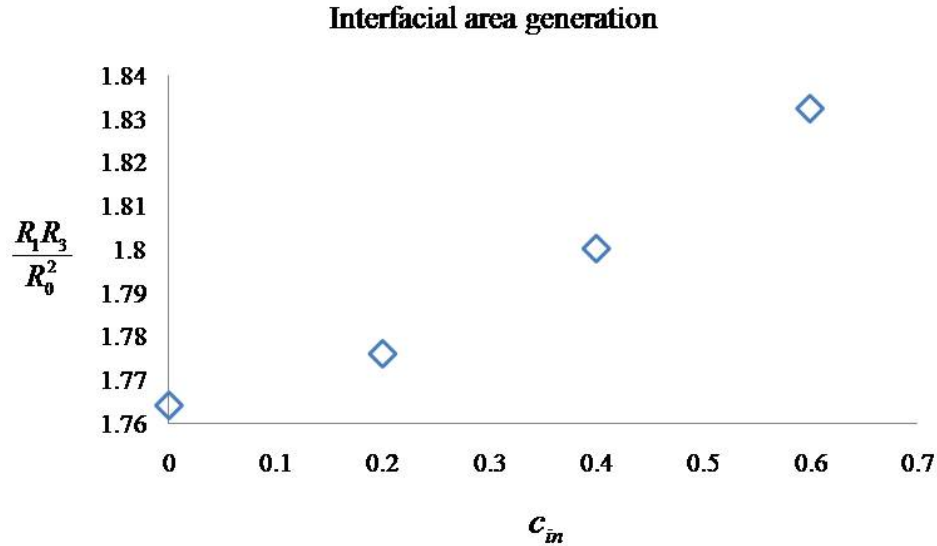


Fig 5.5 Interfacial area generation for droplets in simple shear flow with respect to initial surfactant coverage presented at a dimensionless time step $\dot{\gamma}t = 1.17$ and capillary number $Ca = 4.6$.

The dimensionless length R_1/R_0 , the percentage elongation increase relative to the clean drop, and the reference angle θ° of the droplet inclination with respect to the horizontal direction were calculated at dimensionless time step $\dot{\gamma}t = 3.12$. The results presented in Table 5.1 imply that the greater the surfactant coverage the higher the values of the dimensionless length, the percentage elongation, and the lower the angle of the droplet inclination.

It is clear from the surfactant concentration contours in Fig 5.6 (C), that the regions of higher surfactant concentration are located around the tips of the droplet in the directions of the walls velocities, as a consequence of the convection of surfactants on the droplet interface. This also led to a greater droplet deformation as this was evident from the results of Table 5.1.

Table 5.1 Transient dimensionless length, percentage elongation, and reference angle of inclination measured in degrees, for the clean droplet and for the droplets with three initial values of surfactant coverage c_{in} at dimensionless time step $\dot{\gamma}t = 3.12$.

c_{in}	R_1/R_0	%	θ^0
0	2.66	100.0	20.30
0.2	2.71	101.9	19.67
0.4	2.78	104.6	19.08
0.6	2.87	108.0	18.17

The phase field contours for clean and contaminated droplets and the surfactant concentration contours corresponding to the various values of the surfactant coverage for dimensionless time $\dot{\gamma}t = 3.12$ are presented in Fig 5.6 (A-E).

The graph in Fig 5.6 (F) shows the transient values of the maximum dimensionless surfactant concentration with respect to the dimensionless time. The graph indicates a temporal increase in the maximum concentration due to convection followed by a slight decrease in these values, which is an expression on the interplay between the convection and the dilution of the surfactant due to the increase in the interfacial area of the droplet. This effect is slightly less pronounced in the case of surfactant coverage $c_{in} = 0.2$ since the droplet surface is relatively smaller.

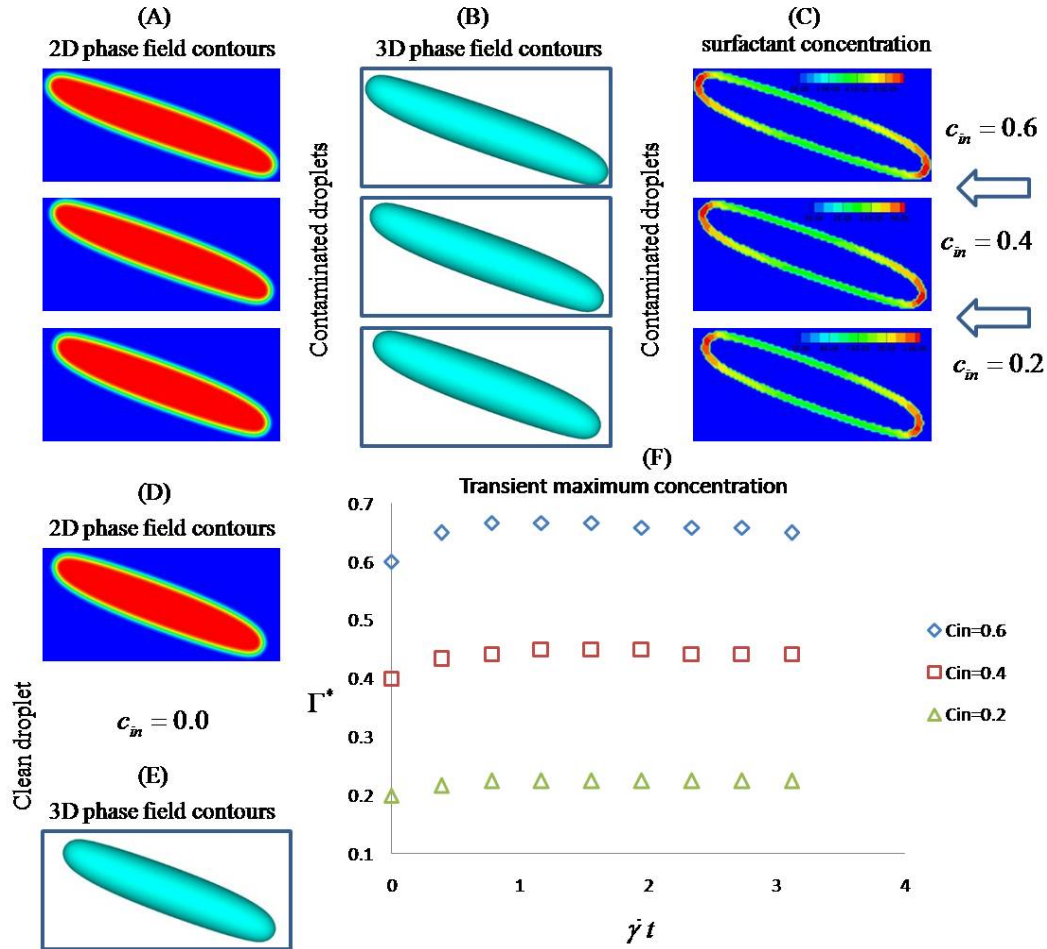


Fig 5.6 (A) 2D view of the phase field contours from the central xz plane for the contaminated droplets. (B) 3D view of the phase field contours for the contaminated droplets surrounded by a fictitious block to show the variance in their dimensions. (C) 2D xz plane view of the surfactant concentration contours. (D) 2D xz plane view of the phase field contour for a clean drop. (E) 3D view of the phase field contour for the clean drop. (F) Graph representing the transient maximum values of the dimensionless surfactant concentration relative to dimensionless times. The results are for dimensionless time step $\dot{\gamma}t = 3.12$, capillary number $Ca = 4.6$, surfactant elasticity $E_0 = 0.2$ and Péclet number $Pe_s = 10$.

Surfactant elasticity effects

Surfactant elasticity constants in the range of $0.2 \leq E_0 \leq 0.6$ were used to test the effects of the elasticity on the deformation of the droplet in simple shear flow. The saturation surfactant concentration was modified to affect a change in the surfactant

elasticity since the proposed model was isothermal, and several values were calculated by Eq. (5.14) which gave the following range of saturation concentration $1.2 \times 10^{-4} \leq \Gamma_{\infty} \leq 3.6 \times 10^{-4} [\text{lmol}/\text{lu}^2]$. The values for the initial concentration Γ_i were selected accordingly in order to maintain constant surfactant coverage $c_{in} = 0.2$. A surface Péclet number $Pe_s = 100$ was used in the simulations. The interfacial area generation was calculated for the various cases with varying surfactant elasticity at the dimensionless time step $\dot{\gamma}t = 1.17$. The results presented in Fig 5.7 shows an increase in the area generation with the increase in the surfactant elasticity.

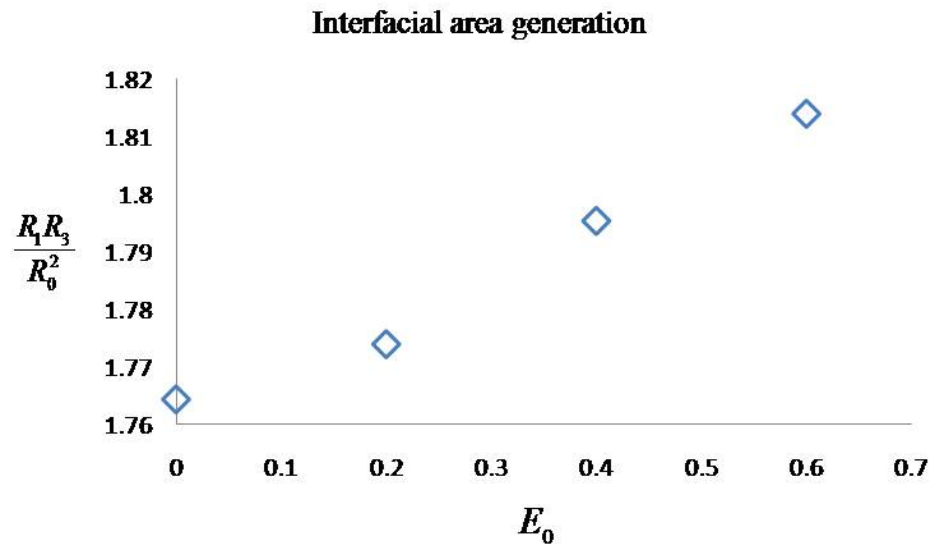


Fig 5.7 Interfacial area generation for droplets in simple shear flow with respect to surfactant elasticity presented at a dimensionless time step $\dot{\gamma}t = 1.17$ and capillary number $Ca = 4.6$.

The dimensionless droplet length, percentage elongation, and the angle of inclination of the droplet relative to the horizontal axis are presented in Table 5.2. A trend of increased dimensionless length, percentage elongation, and decreased

inclination angle of the droplet with the increase of the surfactant elasticity is observed from the results of Table 5.2.

Table 5.2 Transient dimensionless length, percentage elongation, and angle of inclination measured in degrees, for three initial values of surfactant elasticity E_0 at dimensionless time step $\dot{\gamma}t = 3.12$.

E_0	R_1/R_0	%	θ°
0	2.66	100.0	20.3
0.2	2.72	102.1	19.45
0.4	2.76	103.8	19.18
0.6	2.82	106.0	19.06

The angle of inclination is dependent on the Marangoni stress which was given by Eq. (5.21). At the droplet caps the interfacial tension changes largely, hence larger Marangoni stress forces the droplet to align with the flow direction (Drumright-Clarke, 2004). The slow decrease in the inclination angle between the three contaminated droplets cases is indicative of the small difference in their Marangoni stress due to the constant surfactant coverage used in the various cases and the similarity of the flow conditions.

The phase field contours for clean and contaminated droplets, and the surfactant concentration contours are shown in Fig 5.8 (A-E). Lower regions of surfactants concentration are observed around the droplet waist and higher regions around its tips. The graph in Fig 5.8 (F) shows the droplet transient minimum dimensionless surfactant concentration relative to the dimensionless time steps.

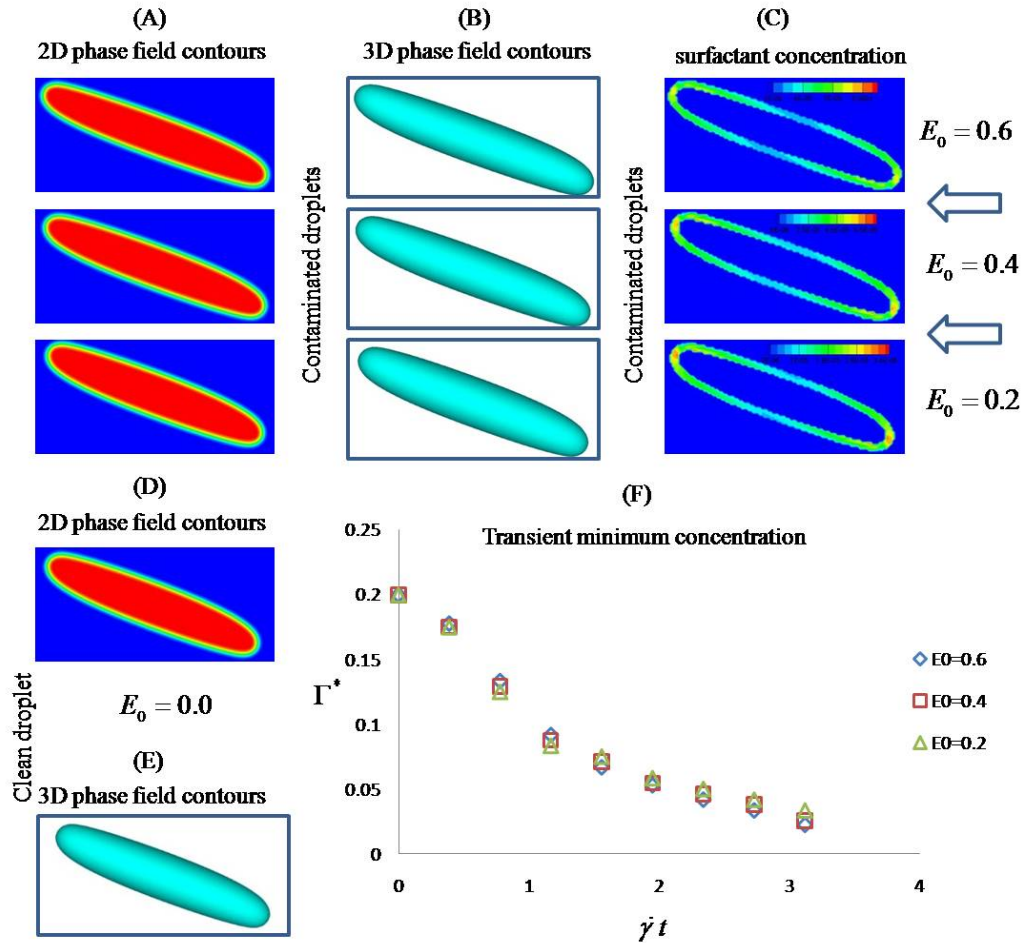


Fig 5.8 (A) 2D view of the phase field contours from the central xz plane for clean droplets. (B) 3D view of the phase field contours for the contaminated droplets. (C) 2D view of the surfactant concentration contours in the xz plane. (D) 2D view of the phase field contour for the clean droplet in the xz plane. (E) 3D phase field contour for the clean droplet. (F) The graph represents the transient minimum values of the dimensionless surfactant concentration relative to dimensionless times. The results are for dimensionless time step $\dot{\gamma}t = 3.12$, capillary number $Ca = 4.6$, surfactant coverage $c_{in} = 0.2$, and Péclet number $Pe_s = 100$.

The minimum concentration decreased steadily due to the combined effects of surfactant convection and dilution. Slightly higher values were observed in the case of $E_0 = 0.2$ due to a relatively smaller droplet interfacial surface.

Péclet number effects

The effects of the Péclet number were investigated for the simple shear flow case with surfactant elasticity $E_0 = 0.2$, surfactant coverage $c_{in} = 0.2$ and saturation concentration $\Gamma_\infty = 1.2 \times 10^{-4} [lmol/lu^2]$. The following range of Péclet numbers was used $1 \leq Pe_s \leq 100$.

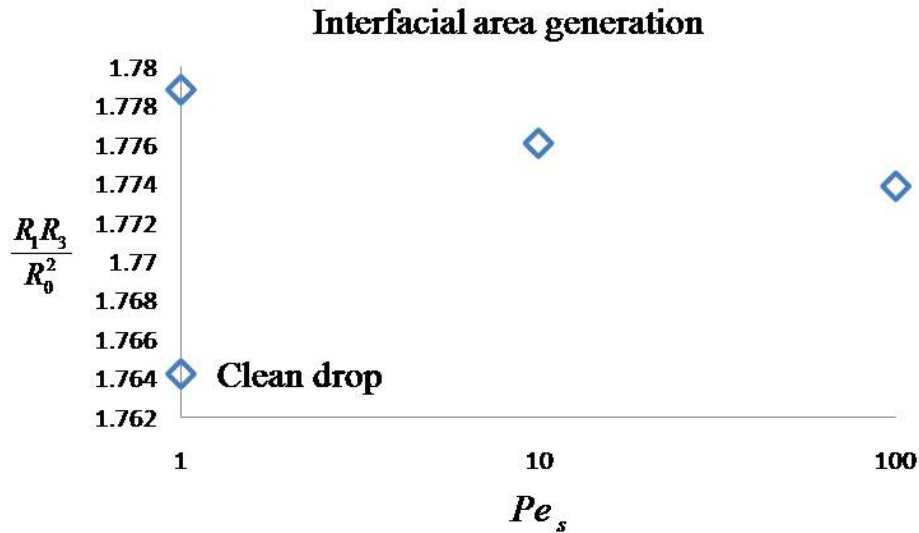


Fig 5.9 Interfacial area generation for droplets in simple shear flow with respect to the surface Péclet number presented at a dimensionless time step $\dot{\gamma}t = 1.17$ and capillary number $Ca = 4.6$.

The change in the interfacial area generation due to the change in the surface Péclet number is presented in Fig 5.9. The graph shows very minimal decrease in the area generation with the increase in the values of the Péclet number. This could be explained by the fact that at low Péclet numbers, surfactants are resistant to convection. Therefore in greater part of the interface, the droplet interfacial tension is lower than that of the clean droplet. This increases the droplet width R_3 and helps increase the area generation.

The dimensionless length, the percentage elongation, and the angle of the droplet inclination are presented in Table 5.2. The results reveal a marginal Péclet number influence on the droplet elongation, because at low surfactant coverage, and low surfactant elasticity, severe flow conditions are required to increase the surfactant concentration to levels capable of affecting a substantial influence on the interfacial tension due to the nonlinear nature of the surfactant equation of state used in this work.

Table 5.3 Droplet transient dimensionless length, percentage elongation and angle of inclination measured in degrees for $1 \leq Pe_s \leq 100$ at dimensionless time step $\dot{\gamma}t = 3.12$.

Pe_s	R_1/R_0	%	θ°
1	2.69	101.3	19.74
10	2.71	101.9	19.67
100	2.72	102.1	19.45

The dimensionless surfactant concentration values Γ^* were calculated in a central xz plane along the lower circumference of the droplet. The calculation was done in the direction of the major axis. The coordinates $x_{m,a} = x/\cos\theta$ were normalized by the droplet radius R_0 , and the corresponding dimensionless concentrations are shown in Fig 5.10 (D). The phase field and surfactant concentration contours are shown in Fig 5.10 (A-C).

It is evident from Fig 5.10 (C, D) that at high Péclet numbers more surfactants are convected towards the tips and away from the middle of the droplet, and this is due to the dominance of the convection role over the diffusion effects.

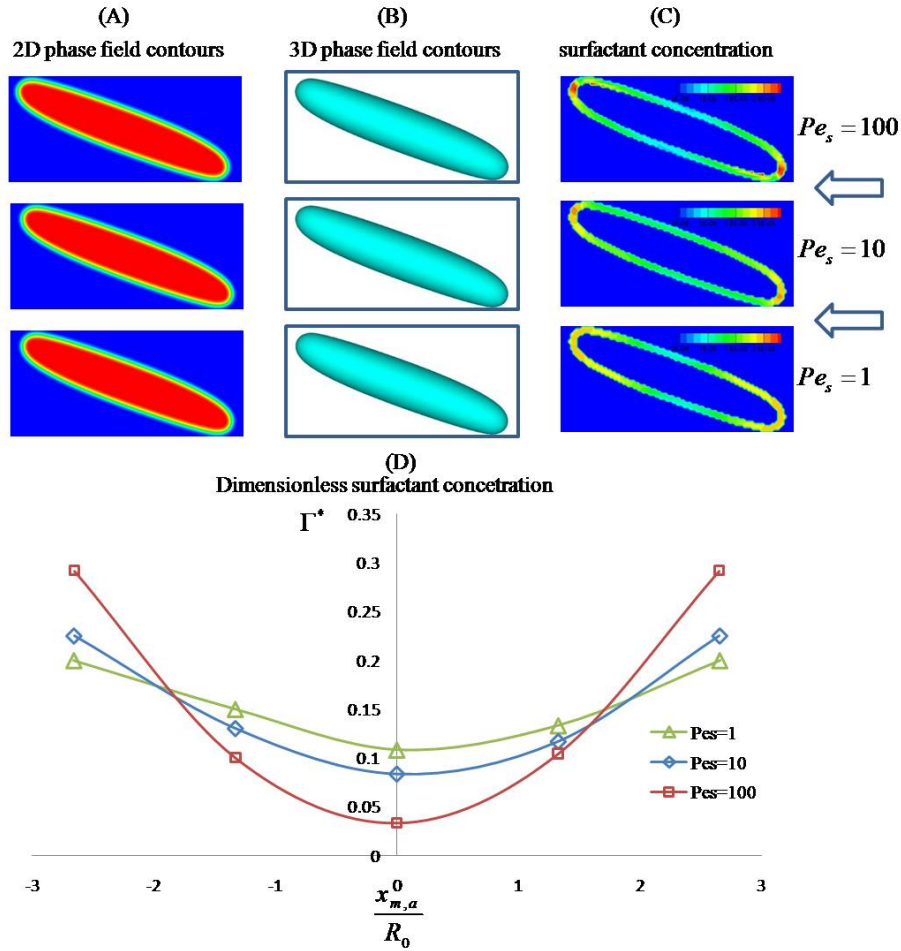


Fig 5.10 (A) 2D xz view of the droplets phase field contours.(B) 3D view of the droplet phase field contours. (C) 2D view of the surfactant concentration contours. (D) The graph represents the dimensionless surfactant concentration relative to a position measured on the lower droplet circumference in the direction of the major axis. The results are for dimensionless time step $\dot{\gamma}t = 3.12$, surfactant elasticity $E_0 = 0.2$, surfactant coverage $c_{in} = 0.2$ and capillary number $Ca = 4.6$.

b. Surfactant-covered droplets in uniaxial extensional flows

To simulate uniaxial extensional flow in the same domain used for the previous cases, the velocity field was modified as follows:

$$\mathbf{u}^\infty(\mathbf{x}) = \dot{\gamma} \begin{pmatrix} 1 & 0 & 0 \\ 0 & -0.5 & 0 \\ 0 & 0 & -0.5 \end{pmatrix} \cdot \mathbf{x} \quad (5.25)$$

where shear rate $\dot{\gamma} = 1.68 \times 10^{-5} [ts^{-1}]$ was used, yielding a capillary number $Ca = 0.8$.

Surfactant coverage effects

The surface Péclet number was set to $Pe_s = 100$ and the surfactant elasticity to $E_0 = 0.2$. The surfactant coverage was varied in the range of $0.2 \leq c_{in} \leq 0.6$. All other fluid properties were kept unchanged. The simulation domain for a central droplet subjected to uniaxial extensional flow is shown in Fig 5.11.

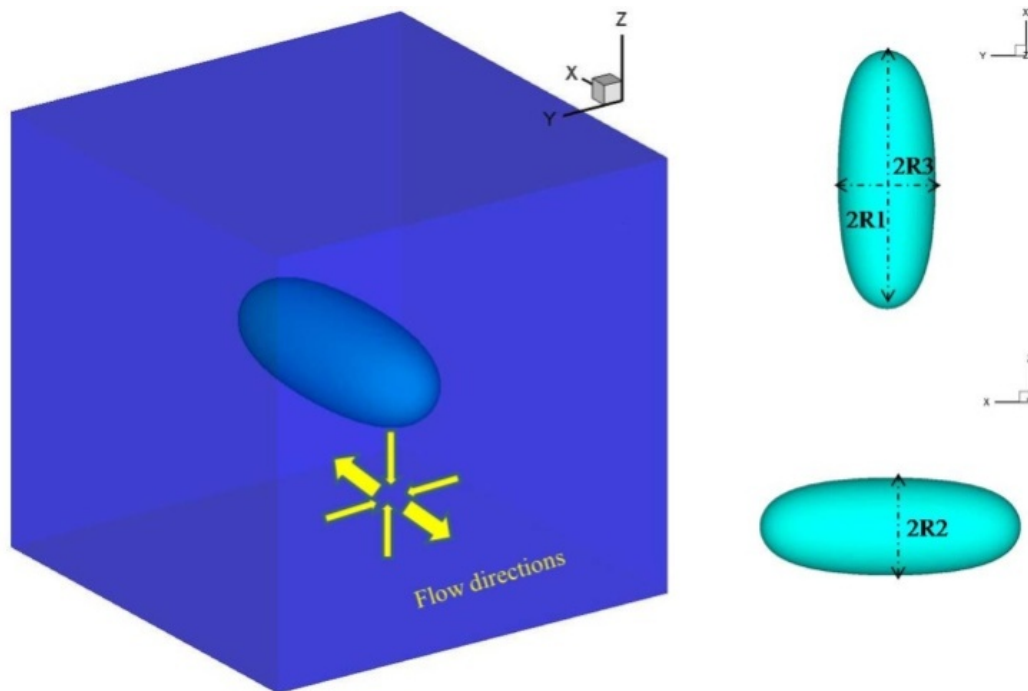


Fig 5.11 Phase field contours for a central droplet in uniaxial extensional flow.

The surfactant concentration distribution under such flow conditions is symmetric and it exhibit higher values towards the tips of the droplet and lower values in the center as this is shown in Fig 5.12 (A-C). The graph in the Fig 5.12 (D) represents the dimensionless surfactant concentration with respect to the x coordinates normalized by the droplet radius R_0 .

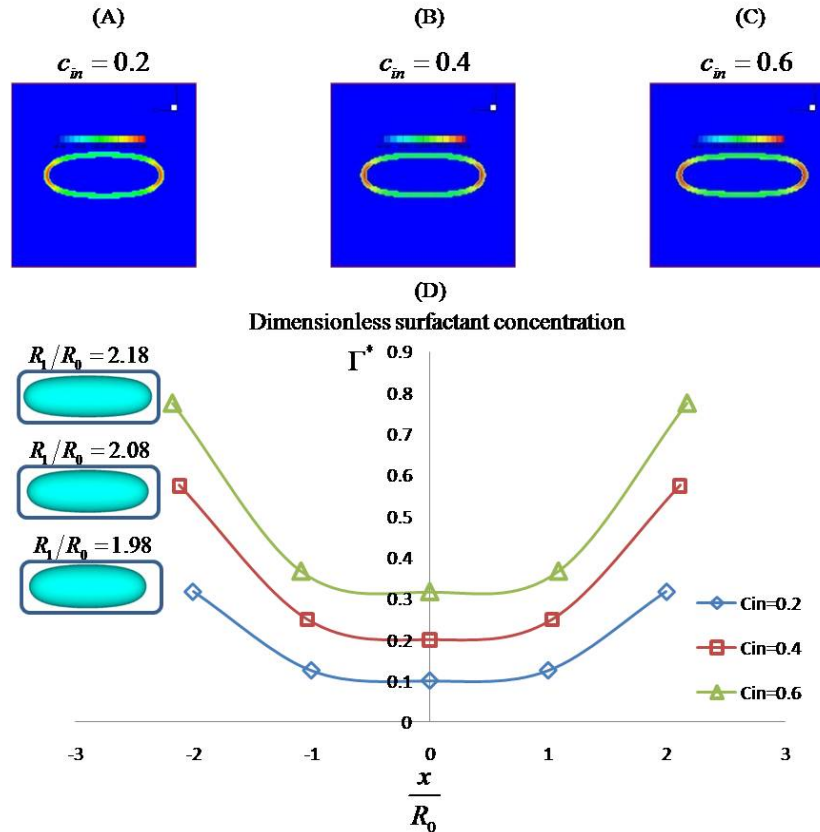


Fig 5.12 (A-C) 2D xz view of the surfactant concentration contours for a central droplet in uniaxial extensional flow, for three values of the surfactant coverage. (D) Graph representing the dimensionless surfactant concentration in the xz plane as a function of the horizontal coordinate normalized by the droplet radius for $\dot{\gamma}t = 0.604$, $Ca = 0.8$, $Pe_s = 100$ and $E_0 = 0.2$. The insets in the graph are for the 3D view of the phase field contours.

It is clear from the 3D phase field contours insets of Fig 5.12 that the droplet dimensionless length increased with the increase of the surfactant coverage.

Capillary number effects

To check the effect of the capillary number on the transient droplet behavior in extensional flows the following range of numbers was used $0.8 \leq Ca \leq 1.2$.

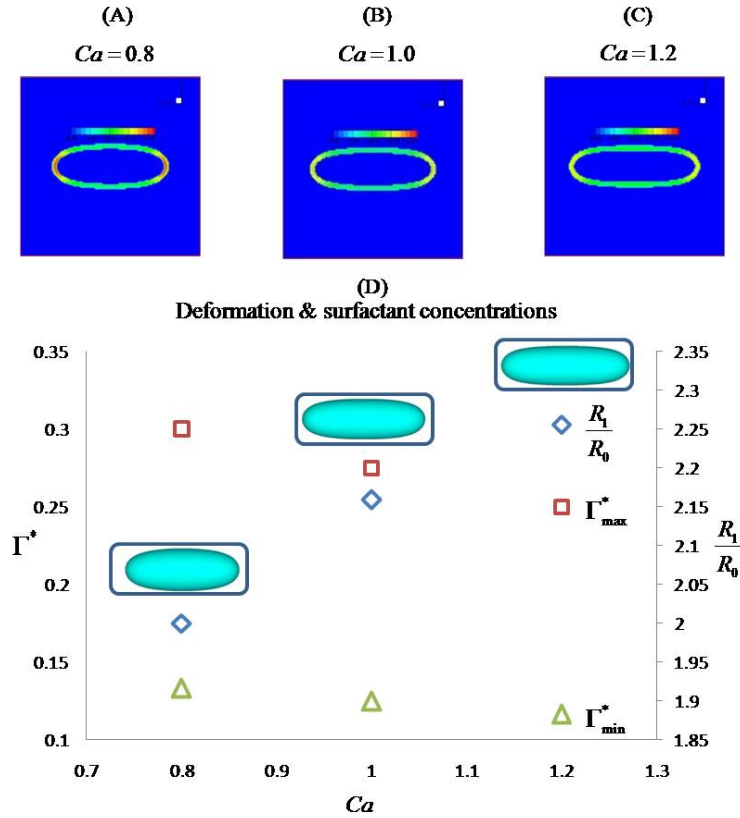


Fig 5.13 (A-C) 2D view of the surfactant concentration contours on droplets in uniaxial extensional for a range of capillary number $0.8 \leq Ca \leq 1.2$. (D) Graph representing the values of the droplet dimensionless R_1/R_0 , the dimensionless maximum Γ_{\max}^* and minimum Γ_{\min}^* surfactant concentration, respectively at dimensionless time step $\dot{\gamma}t = 0.604$. The insets in the graph are for the 3D view phase field contours.

The dimensionless length R_1/R_0 , the maximum dimensionless surfactant concentration Γ_{\max}^* , the minimum dimensionless surfactant concentration Γ_{\min}^* were calculated at the dimensionless time step $\dot{\gamma}t = 0.604$, which corresponded to the end of the simulation time. It is clear from the presented results in Fig 5.13 (D), that the effects of surfactant dilution is dominant under supercritical capillary numbers, since the dimensionless length increased and both maximum and minimum surfactant concentration decreased with the increase in the capillary numbers.

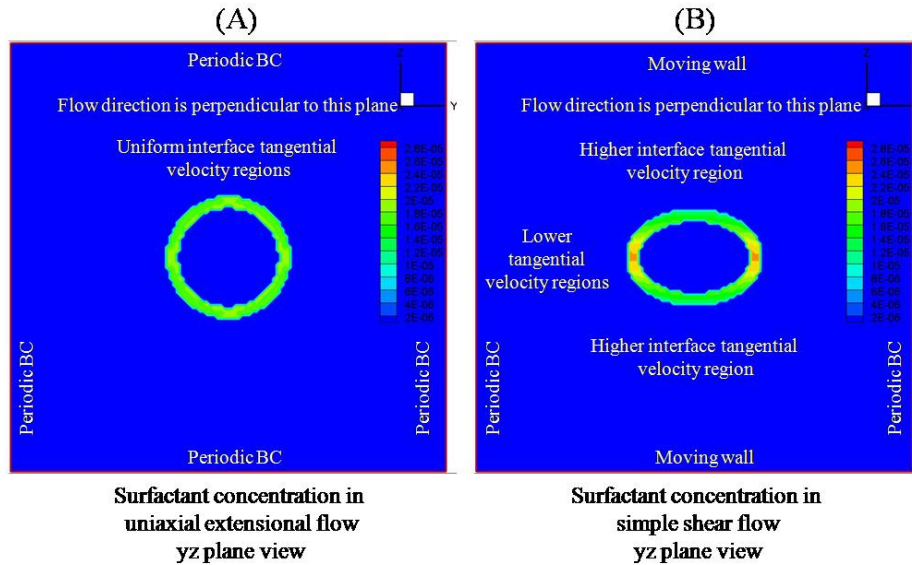


Fig 5.14 (A) 2D yz view of the surfactant concentration contours is shown for a central droplet in uniaxial extensional (B) 2D yz view of the surfactant concentration of a droplet in simple shear flows. The capillary number for the extensional flow is $Ca = 0.8$ and the dimensionless time step $\dot{\gamma}t = 0.536$. The capillary number for the shear flow is $Ca = 4.6$ and the time step is $\dot{\gamma}t = 1.95$.

No lamellar structure ($R_2 = R_3$) was observed under the uniaxial extensional flow conditions, since the compressional components in the xy and the xz planes were equivalent contrary to the case of the simple shear flow in which the compressional components were unbalanced. This is also true because the lamellar morphology is flow and viscosity ratio dependent for cases with finite capillary numbers (Cristini et al., 2002). Another factor which could potentially help the formation of the lamellar structure in simple shear flows is due to the nature of surfactant concentration distribution on the peripheries of a contaminated droplet in the low interface tangential velocity regions of the flow in the yz planes as shown in Fig 5.14 (B). These regions are characterized by lower convection effects leading to higher local surfactant concentrations which act to reduce the droplet interfacial tension, hence locally lowering its capillary number and

making it more deformable. This does not occur in the uniaxial extensional flow due to its uniform tangential velocity profile in the indicated region of Fig 5.14 (A).

c. Buoyancy of surfactant-covered droplets in infinite medium

The effect of surfactants on buoyant droplets and bubbles named here as fluid particles was studied both experimentally (Almatroushi and Borhan, 2004; Griffith, 1962; Bel Fdhila and Dwineveld, 1996; Alves et al., 2004) and numerically (Bel Fdhila and Dwineveld, 1996; Tasoglu, et al., 2008). It was found that surfactants generally reduce significantly the particles terminal velocity below the classical Hadamard-Rybszynski prediction in the spherical region of the shape regime; however in other shape regions the particle retardation due to surfactants is less effective (Tasoglu et al., 2008).

Buoyancy-driven fluid particles are characterized by the following dimensionless numbers:

$$E_o = \frac{g\Delta\rho d^2}{\sigma_0}, M_o = \frac{g\mu_f^4 \Delta\rho}{\rho_f^2 \sigma_0^3}, \text{Re} = \frac{U_T d \rho_f}{\mu_f} \quad (5.26)$$

where E_o is the Eotvos number, M_o is the Morton number, and Re is the Reynolds number, d is the particle diameter, σ_0 is the interfacial tension, g is the acceleration constant, μ_f is the ambient fluid dynamic viscosity, and U_T is the particle terminal velocity.

The predicted Hadamard-Rybszynski terminal velocity for a spherical fluid particle rising in infinite medium is given by Clift et al. (2005):

$$U_{HR} = \frac{2}{3} \frac{ga^2 \Delta\rho}{\mu_f} \frac{\mu_f + \mu_d}{2\mu_f + 3\mu_d} \quad (5.27)$$

where a is the particle radius and μ_d is the particle dynamic viscosity.

The terminal velocity for a rising fluid particle in infinite medium with $E_0 > 40$ and $M_0 > 200$ can be estimated analytically through solving the following equation Clift et al. (2005):

$$2\text{Re}^2 + 6\text{Re} \frac{2+3\eta}{1+\eta} - E_o^{3/2} M_o^{-1/2} = 0 \quad (5.28)$$

where $\eta = \mu_d / \mu_f$ is the viscosity ratio.

A domain consisting of $61 \times 61 \times 351 [lu^3]$ was used to investigate the effects of surfactants on the terminal velocity of a single droplet of radius $a = 12 [lu]$, rising in an infinite medium, in the spherical and the spherical cap regions, respectively. The density of the suspending fluid was $\rho_f = 2 [mu/lu^3]$, and the droplet density was $\rho_d = 1.0 [mu/lu^3]$. The relaxation time was set to $\tau = 1.0$ leading to dynamic viscosities $\mu_f = 0.333$ and $\mu_d = 0.1666$ for the surrounding fluid and the droplet, respectively. The periodic condition was applied in all directions. The interfacial tension was set to $\sigma_0 = 10^{-3}$.

Two set of simulations were executed in this section, in which the acceleration constants were varied to produce the two required shapes. In each set of simulations the clean and the contaminated droplet terminal velocities were calculated and measured consecutively. The contaminated droplets cases had their surfactant elasticity set to $E_0 = 0.5$ leading to a saturation surfactant concentration $\Gamma_\infty = 1.5 \times 10^{-3}$ and the surfactant coverage was set to $c_{in} = 0.4$. The Péclet number was set to $Pe_s = 40$ and the diffusion coefficient was evaluated based on the following relation:

$$Pe_s = \frac{U_T \ell}{D_s} \quad (5.29)$$

where U_T is the terminal velocity, ℓ is the vertical distance required for the clean droplet to attain its terminal velocity.

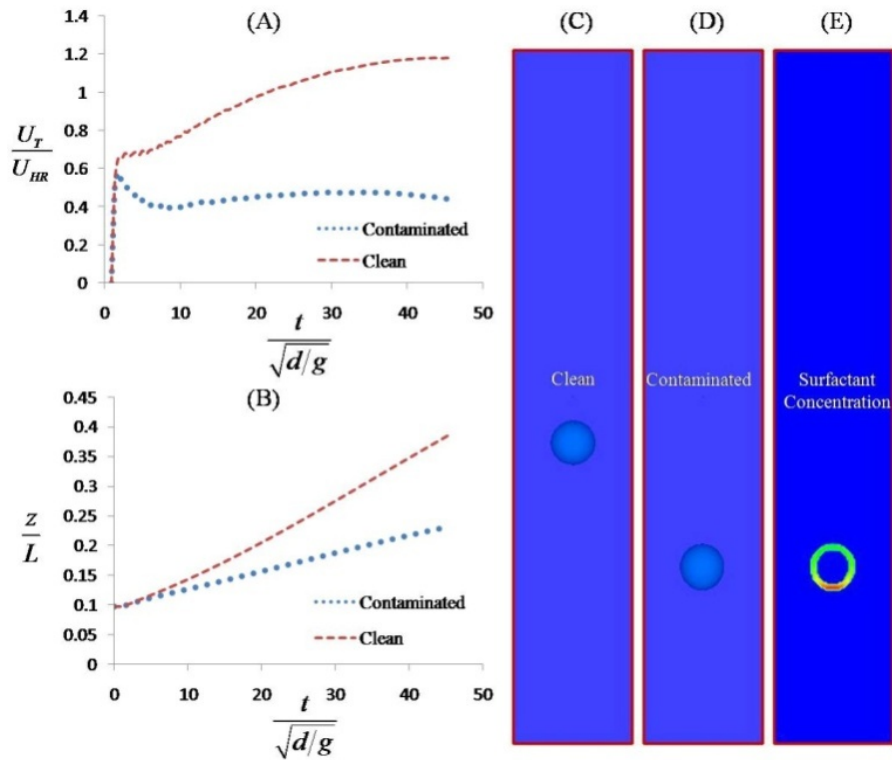


Fig 5.15 (A) Dimensionless terminal velocities for clean and contaminated buoyant droplets presented in the spherical region. (B) Dimensionless vertical location of the droplet mass center for the clean and the contaminated droplets. (C) 3D phase field contours for the clean droplet, (D) 3D phase field contour for the contaminated droplet. (E) 2D xz plane view of the surfactant concentration contour for the contaminated droplet. The dimensionless time step is $t/\sqrt{d/g} = 43.3$. The simulation was executed with acceleration constant $g = 2.0 \times 10^{-5}$, Morton number $M_o = 61.7$, Eotvos number $E_o = 11.5$ and Reynolds number $Re = 0.34$.

The resulting terminal velocities of the clean and the contaminated buoyant droplets in the spherical shape region were due to acceleration constant $g = 2.0 \times 10^{-5} [lu/ts^{-2}]$ which led to Morton number $M_o = 61.7$, Eotvos number $E_o = 11.5$

and Reynolds number $Re = 0.34$. The normalized terminal velocities by the Hadamard-Rybszynski terminal velocity U_{HR} and the normalized mass center vertical locations by the domain length L , calculated with respect to normalized time by $\sqrt{d/g}$ are shown in Fig 5.15.

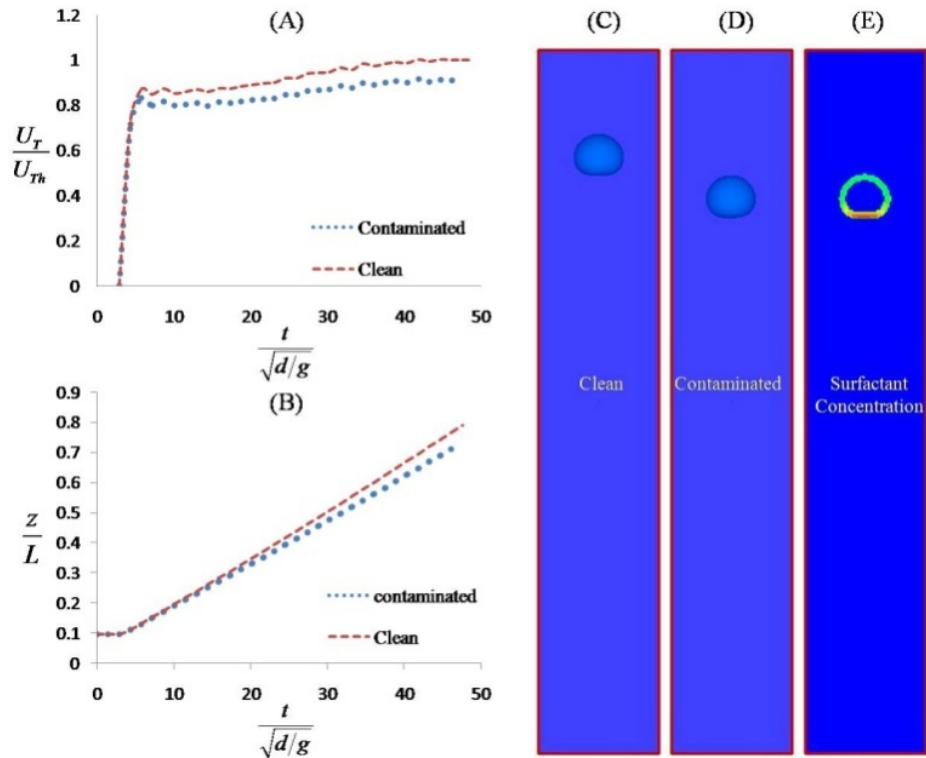


Fig 5.16 (A) Dimensionless terminal velocities for clean and contaminated buoyant droplets presented in the spherical-cap region. (B) Dimensionless vertical location of the droplet mass center for the clean and the contaminated droplets. (C) 3D phase field contours for the clean droplet. (D) 3D phase field contour for the contaminated droplet. (E) 2D view of the surfactant concentration contour for the contaminated droplet. The dimensionless time step is $t/\sqrt{d/g} = 49.07$. The simulation was executed with acceleration constant $g = 2.0 \times 10^{-4}$, Morton number $M_o = 617$, Eotvos number $E_o = 115$ and Reynolds number $Re = 2.6$.

The terminal velocities of the clean and contaminated buoyant droplets in the spherical-cap shape region were produced by acceleration constant $g = 2.0 \times 10^{-4} [lu/ts^{-2}]$ which yielded Morton number $M_o = 617$, Eotvos number $E_o = 115$

and Reynolds number $Re = 2.6$. The normalized terminal velocities by the theoretical droplet terminal velocity U_{Th} and the normalized mass center vertical locations by the domain length L , calculated with respect to normalized time by $\sqrt{d/g}$ are shown in Fig 5.16.

The results for the terminal velocities and their ratio with respect to the theoretical values calculated by Eq. (5.27) and Eq. (5.28) from both set of simulations are summarized in Table 5.4.

Table 5.4 Comparison of the terminal velocities from the two sets of simulations in the spherical and spherical-cap regions with their respective theoretical terminal velocities.

Condition	Region	U_r	$U_{rr/Th}$	%
Clean	spherical	0.00290	0.00247	1.175
Contaminated	Spherical	0.0011	0.00247	0.451
Clean	Spherical-cap	0.01803	0.01801	1.001
Contaminated	Spherical-cap	0.01641	0.01801	0.911

The surfactant concentration phase field contours in Fig 5.15 (E) and Fig 5.16 (E) and the terminal velocity results from Table 5.4 are clear indications of the proposed model compliance with the known physical mechanism governing the buoyant droplet behavior due to the influence of surfactants which was introduced by Frumkin and Levich (Tasoglu et al., 2008). This mechanism considers the droplet retardation as a result of the surfactants convection toward the back of the droplet, which in turn creates Marangoni stress and slows down its surface mobility. This leads to increased drag force and decreased terminal velocity. The model also shows that the effects of surfactants on the droplet terminal velocity are more influential in the spherical region relative to the spherical-cap region.

CHAPTER 6

SUPPRESSING THE COALESCENCE IN THE LBM: COLLOIDS RHEOLOGY

The multi-component lattice Boltzmann method (LBM) has emerged as a powerful tool for simulating variety of fluid problems related to the droplet deformation, break up and coalescence. However this method is incapable of simulating cases where neighboring contaminated droplets of the same make-up, amalgamate rather than coalesce. This problem can be solved in the LBM if different colors are assigned to the various droplets. The disadvantages of such an approach are: the requirement for more computational resources (Dupin et al., 2003), and the undermining of the molecular interaction forces which act between the approaching droplets. The latter is important for determining the rheological behavior of colloids. Suppressing coalescence in the LBM enables the model to handle issues of aggregation and disaggregation under shear stress, and to deal with the rheology of polymers and colloids in a variety of flows under low and moderate Reynolds numbers. These problems are of fundamental and practical interest to many industries, since the rheology of such systems plays a decisive role in their transport properties, physical and thermal qualities. This work aims at proposing a heuristic LBM scheme suitable for the study of soft colloid rheology. The advantages of such a model are the simplicity in its implementation, the requirement of less computational resources, and most importantly is the break-away from the empirical models, since the effective viscosity of the non-Newtonian fluids is calculated directly.

6.1 Suppressing the coalescence in the LBM

Two droplets situated at a close proximity from each other in the multi-component LBM tend to coalesce. The strength of the coalescence is dependent on the interfacial tension parameter α which determines the magnitude of the force in Eq. (2.16) responsible for the creation of a pressure difference between the neighboring droplets internal fluid and the narrow external fluid layer between them. Eventually the pressure difference leads to the depletion of the external layer and allows a direct contact between the droplets, which further destroys the droplets contacting interfaces and allow them to coalesce.

In the proposed model, the LBM inherent coalescence driving force is used heuristically to represent the attraction forces between the approaching interfaces and a counteracting steric repulsion is employed to represent the repulsive forces. The following formula is proposed for indirectly imposing a repulsive force in the LBM with a magnitude:

$$S(\mathbf{x}) = c_{in}^* \lambda(\alpha) \alpha(\mathbf{x}) \quad (6.1)$$

where λ is a dimensionless function of the interfacial tension parameter, which is related to the local surfactant concentration through Eq. (5.20), $c_{in}^* = f(c_{in}/c_{in}^{\min})$ is a nonlinear function of the ratio of the initial surfactant coverage c_{in} and the minimum coverage c_{in}^{\min} required for suppressing the coalescence in a particular mixture (Lyu et al., 2002). The application of the repulsive force is accomplished through first identifying an interfacial node belonging to a leading drop in the computational sweeping direction. A forward small loop scans whether another interfacial node is within the vicinity of the leading node and located at a distance $(x_l - x_f)^2 + (y_l - y_f)^2 \leq 2$. The span of the loop depends

on whether the leading droplet is approaching the following one in the horizontal or the vertical direction. For example for the horizontal direction, the loop is given by $x+1 \leq p < x+3; y-2 \leq q < y+3$, where x and y are the interface nodes coordinates in the main loop, p and q are the coordinate of the small loop. The normal to the interface components n_x, n_y signs are hence after checked. The fulfillment of the condition $\text{sgn}(n_{x,l}) \neq \text{sgn}(n_{x,f})$, and or $\text{sgn}(n_{y,l}) \neq \text{sgn}(n_{y,f})$ ensures that the two nodes belong to different droplets as shown in Fig 6.1. A set of forces are then applied in the tangential direction at the locations indicated by pressure inducing in Fig 6.1 as follows:

$$\mathbf{F}(\mathbf{x}) = \pm S(\mathbf{x})\mathbf{T} \quad (6.2)$$

where $\mathbf{T}(n_y, -n_x)$ is the unit tangent to the leading droplet interface and $\mathbf{n}(n_x, n_y)$ is the unit normal vector. The tangential forces are only applicable to the ambient fluid; therefore only the two diagonally opposite forces shown in blue from Fig 6.1 are active at any particular time.

The macroscopic force in Eq. (6.2) is applied through the source term of Eq. (2.11) by the following relation (Halliday et al. 2007):

$$\phi_i = \omega_i \frac{1}{k_2} \mathbf{F} \cdot \mathbf{c}_i \quad (6.3)$$

where the constant is given by $k_2 = 1/3$. The applied opposite body like forces act to create a pressure rise in the thin external fluid layer trapped between the two droplets. The distributed pressure over the area of the local interfaces yields a repulsive force which prevents the droplets from coalescing, without causing any significant local droplets deformation.

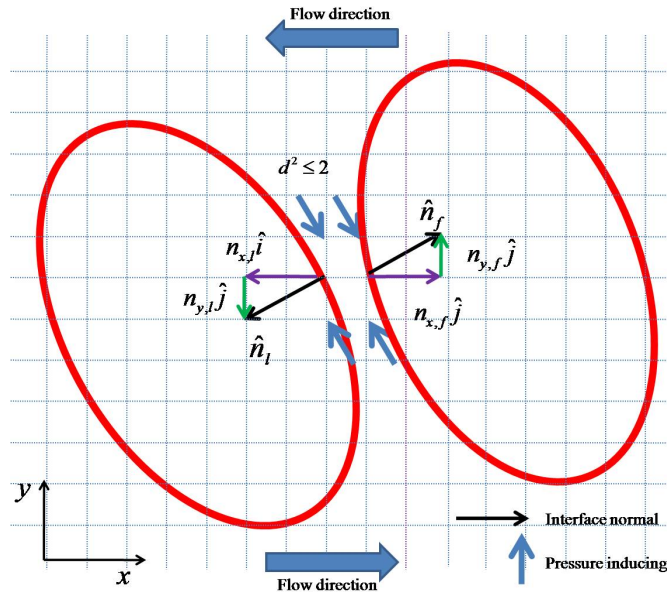


Fig 6.1 Two approaching droplets in a hypothetical shear flow, with the required forces for suppressing the coalescence without altering the droplets shape.

a. Optimizing the force equation for suppressing coalescence

The repulsive force magnitude used in Eq. (6.1) includes a function $\lambda(\alpha)$, which was needed for controlling the force when the interfacial tension parameter varied locally without changing the initial surfactant coverage. Due to the surfactant concentration evolution on the droplet interface, $\lambda(\alpha)$ should affect an automatic change in the force magnitude corresponding to the changing local interfacial tension. The tension relation to the local surfactant concentration is governed by the Langmuir equation of state.

In line with the above reasoning several simulations with uniform interfacial tension were executed to optimize Eq. (6.1). A $123[l u^2]$ square lattice unit domain was used for investigating the required force magnitude needed for suppressing the coalescence of two droplets with radius $R = 18[l u]$ placed initially at a distance of $4[l u]$

between their interfaces in a simple shear flow. A shear rate of 9.75×10^{-5} was induced by the opposite movement of the upper and lower walls. Periodic condition was applied on the side boundaries. The objective was to find some optimal values for λ capable of effecting droplets total separation during couple thousand of time steps for the value $c_{in}^* = 1$. Three viscosity ratios μ_d/μ_s were utilized 0.1, 1, and 10, and the highest values for λ were taken. A graph was produced and curve fitted to obtain the appropriate equation for $\lambda(\alpha)$. The graph is presented in Fig 6.2.

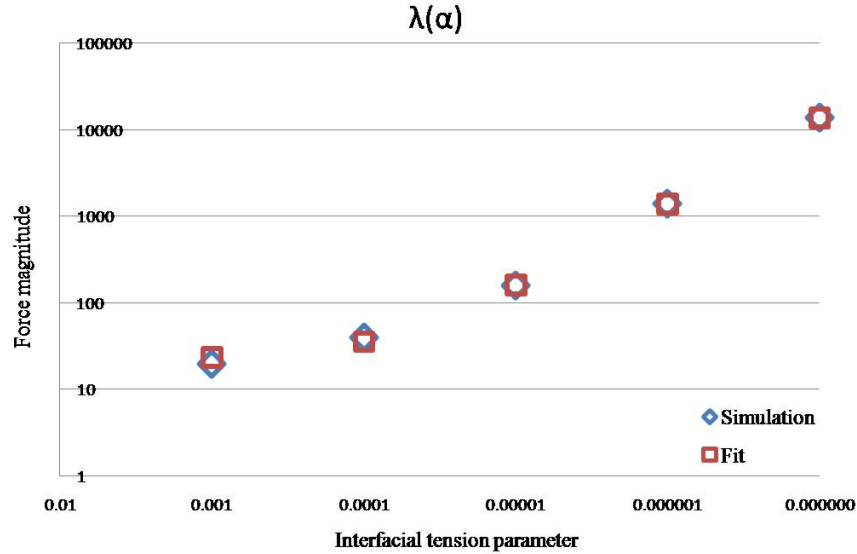


Fig 6.2 The limiting condition for determining the dimensionless function $\lambda(\alpha)$ and its curve fit, for $c_{in}^* = 1$.

Equation (9) was then replaced with the following formula:

$$S(\mathbf{x}) = c_{in}^* \left(22.2 + \frac{0.001398}{\alpha} \right) \alpha \quad (6.4)$$

by which for values $c_{in}^* < 1$ the force balance allows the occurrence of coalescence starting by a slow drainage from one droplet into the other for values closer to one, while the values $c_{in}^* \geq 1$ lead to suppressing the coalescence in the proposed model.

b. Test cases

suppressing the coalescence in a quiescent flow

To demonstrate the capability of the proposed algorithm in suppressing the coalescence of several droplets in a quiescent flow, a domain consisting of $123[lu^2]$, with a central droplet of radius $R = 18[lu]$ and four satellite droplets of radii $R_s = 12[lu]$ positioned equidistantly from the domain center was used. Periodic conditions were applied on the four boundaries. The interfacial tension parameter was $\alpha = 1.0 \times 10^{-4}$. The two fluids had the same density $\rho = 1.0[mu/lu^2]$ and the same kinematic viscosity $\nu = 0.166[lu^2ts^{-1}]$; hence the droplets were neutrally buoyant in their surrounding fluid. The selection of these conditions was dictated by a desire to maintain the droplets at a closed proximity in the absence of any external forces, and monitor their behavior. Very small value of the Péclet number was used to limit the convection of the surfactants on the interface of the droplets, which behaved as clean ones.

The phase field contours resulting from the model with the suppression of coalescence for $c_{in}^* = 1$ compared with the phase field contours of the standard model $c_{in}^* = 0$ are shown in Fig 6.3 for several dimensionless time steps. A characteristic time step $\mu R / \sigma_0$ was used here where μ is the dynamic viscosity and σ_0 is the interfacial tension. It is evident from Fig 6.3 that the coalescence was suppressed in the case of

$c_{in}^* = 1$, contrary to the standard case with $c_{in}^* = 0$ where a single drop resulted from the coalescence of all the droplets in the domain.

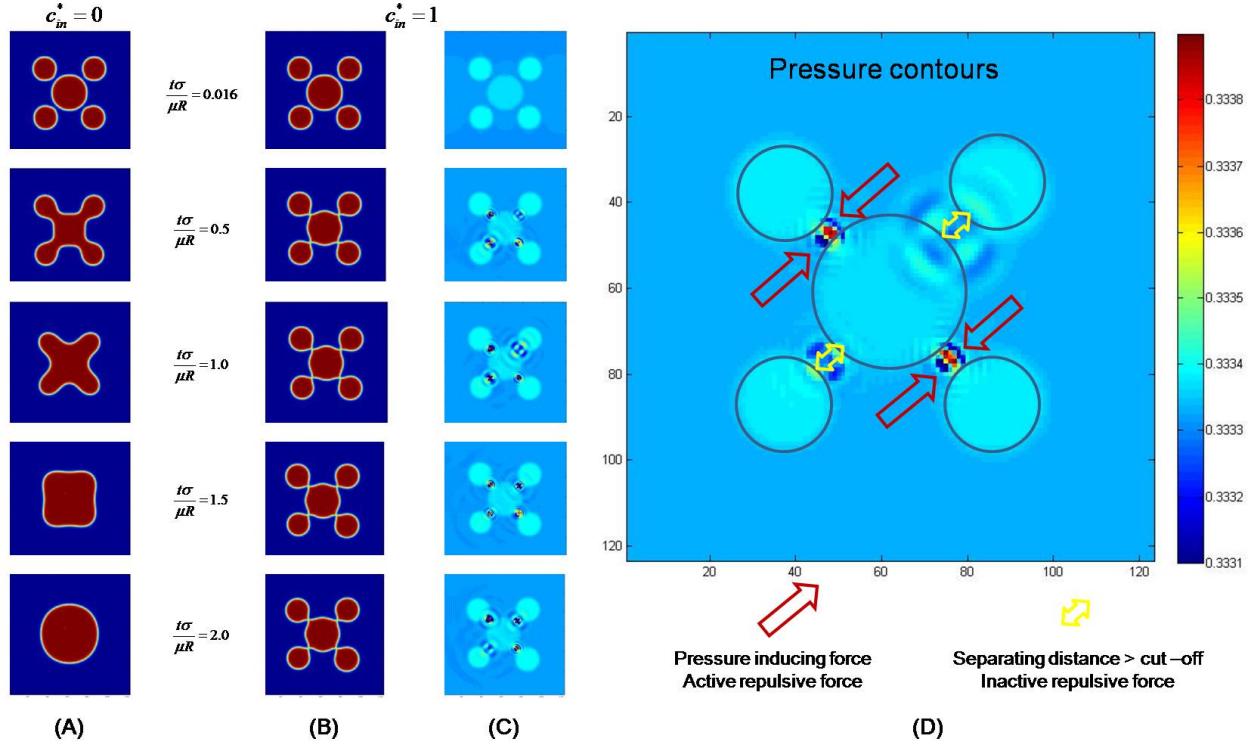


Fig 6.3 (A) Phase field contours for droplets in quiescent flow and $c_{in}^* = 0$ for the various dimensionless time steps $t\sigma/\mu R$. (B) Phase field contours for the droplets with $c_{in}^* = 1$ for the same time steps. (C-D) Pressure contours for the droplets with time varying interaction forces.

The pressure contours in Fig 6.3 show the continuous attempt by the coalescence force to bring the droplets to a minimal proximity, counteracted by the induced repulsive force which helped creating a higher pressure film between the approaching interfaces, leading to droplet amalgamation instead of coalescence.

Suppressing the coalescence in a dynamic flow

Parabolic flows are interesting in many research areas especially those related to droplet-based microfluidics. Another area of interest is the hemodynamics, since blood

circulation in the various vessels is by nature parabolic. The red blood cells (RBC) behavior in the microvasculature could be studied through modeling the RBC as a deformable droplet. The disadvantage of such assumption in parabolic flows is related to the changing strain rate with respect to the droplet location in the domain. Hence droplets situated in the central region move at higher velocity than those moving closer to the walls. This diminishes the distance between them and eventually leads to their collision and coalescence, unless the coalescence is interrupted.

Multiphase parabolic flows are characterized by the channel Reynolds number:

$$\text{Re}_{ch} = \frac{\bar{U}H}{\nu} \quad (6.5)$$

where H is the channel height, $\bar{U} = FH^2/12\rho\nu$ is the magnitude of the average undisturbed velocity of the flow, and F is the flow inducing macroscopic force. The Weber number is another important dimensionless parameter used for analyzing multiphase flows and is given by:

$$\text{We} = \frac{2\rho\bar{U}^2R}{\sigma_0} \quad (6.6)$$

where σ_0 is the droplet interfacial tension.

Four droplets with radii $R = 10[lu]$ were suspended in a fluid domain consisting of $351 \times 57[lu^2]$. The density of the droplets and the ambient fluid was set to $\rho = 1.0$, the viscosity ratio to $\eta = 1$. The interfacial tension parameter was $\alpha = 1.0 \times 10^{-3}$, and the kinematic viscosity was $\nu = 0.166[lu^2ts^{-1}]$. The bounce back was applied on the upper and lower boundaries to impose a no-slip velocity condition on the walls. Periodic condition was used for the inlet and the outlet of the domain, respectively. A force

$F = 2.5 \times 10^{-6} [\text{mulu/ts}^{-2}]$ was applied in the horizontal positive direction, and this led to a Reynolds number $Re_{ch} = 1.4$ and Weber number $We = 0.33$. The characteristic time was taken as the inverse of the strain rate $\dot{\gamma}_{H/4}^{-1}$ calculated for a distance equivalent to quarter of the channel height. The phase field contours from the standard LBM $c_{in}^* = 0$ and the proposed model $c_{in}^* = 6$, are shown in Fig 6.4.

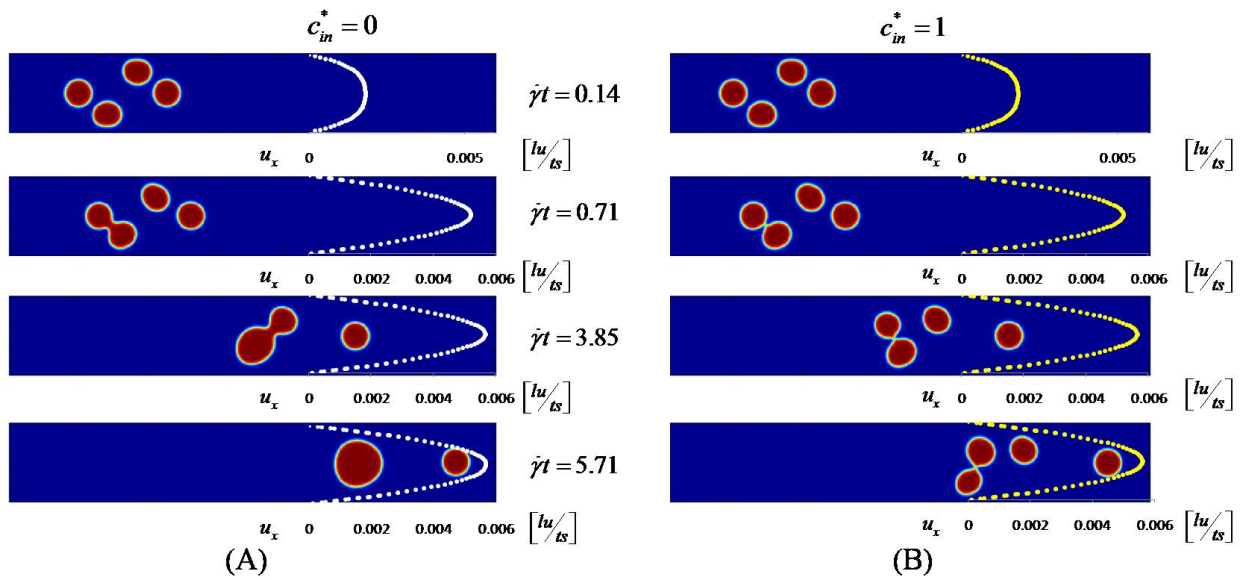


Fig 6.4 (A) Phase field contours from the standard LBM $c_{in}^* = 0$, in which coalescence occurs instantaneously after collision. (B) Phase field contours from the proposed model $c_{in}^* = 1$ in which the coalescence is suppressed. The horizontal velocity profile at $x/H = 0.77$ is superimposed on the phase field contours.

It is obvious from Fig 6.4 (B) that the coalescence was suppressed in the proposed model, and this has revealed the following observations. The collision between the two droplets was due to the higher velocity of the central drop. This led to a change in the trajectories and the velocities of the collided droplets. The first droplet velocity decreased while it was riding over the second droplet as this was evident from

the increasing dimensionless distance between the mass centers of the first and the fourth droplets as the simulation time evolved $(d/H)_{\dot{\gamma}t=0} = 1.04$ versus $(d/H)_{\dot{\gamma}t=5.7} = 1.61$. The second droplet shear lift was partially undermined, since its mass center dimensionless distance from the lower wall $(y_{lo}/H)_{\dot{\gamma}t=5.7} = 0.26$ was smaller than the one between the third droplet and the upper wall $(H - y_{up}/H)_{\dot{\gamma}t=5.7} = 0.35$ at the end of the simulation time.

6.2 Rheology

a. Direct calculation of the relative viscosity of colloids

Coaxial viscometers are used for determining the viscosity of fluids by measuring the torque needed to keep one of their cylinders stationary while the other rotates with the fluid placed between them. The torque induced on the stationary cylinder is proportional to the effective viscosity of the tested fluid, while the shear rate is decided by the rotational speed of the other. Following the same principle of the coaxial viscometers operation, the schematic in Fig 6.5 shows the propose model's domain used for the derivation of the effective viscosity, and the phase field of two non-coalescing droplets due to the application of the suppression of coalescence algorithm.

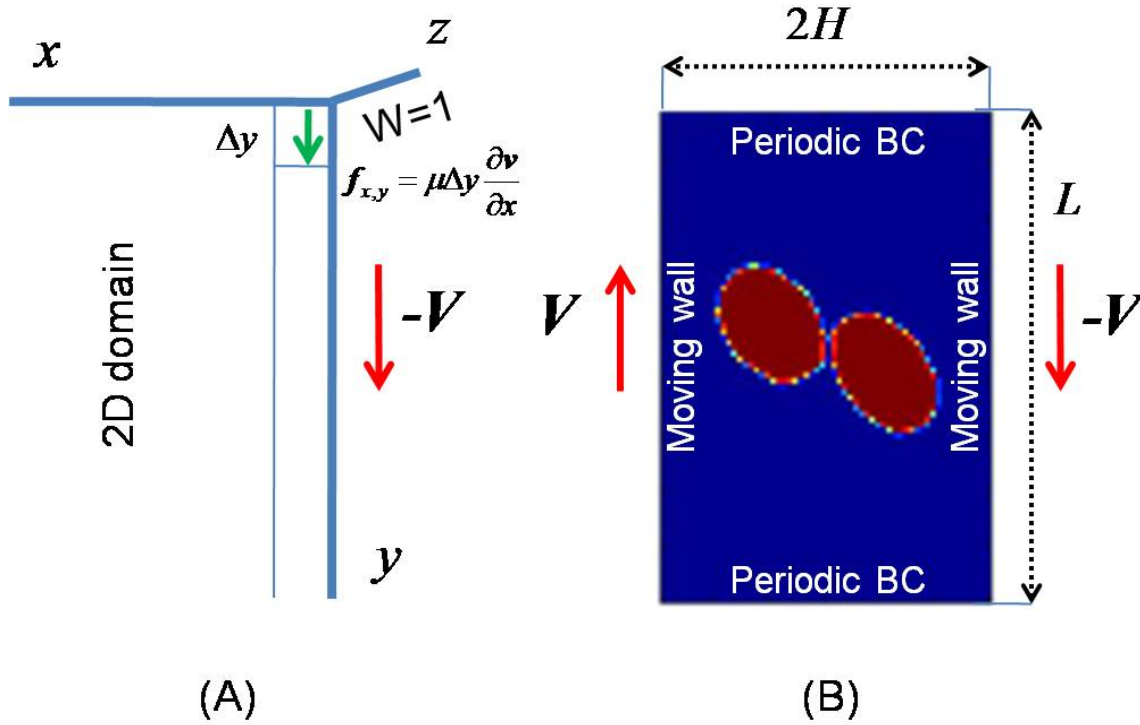


Fig 6.5 (A) Schematic of the 2D domain of thickness $W=1$ used for the derivation of the effective viscosity. (B) Phase field contours for two droplets in a simple shear flow with an indication of the used boundary conditions.

Assuming that μ is the suspending fluid dynamic viscosity, V the linear velocity of the walls, H is half the distance between the walls in the horizontal direction, L is the length of the walls in the vertical direction, then the shearing force per unit width exerted by the ambient fluid on the moving wall without suspended immiscible droplets is

$|\mathbf{F}| = \mu \frac{|V|}{H} A$. The undisturbed flow velocity in the y direction is $v = \frac{|V|x}{H}$. With suspended

droplets the effective viscosity of the whole fluid is $\mu_{eff} = \frac{H|\mathbf{F}|}{L|V|}$. The thickness in the z

direction is assumed as unity, thus the area $A = L$ and the total shearing force is:

$$|\mathbf{F}| = \sum |f_{x,y}| = \mu \Delta y \Delta z \sum \frac{\partial v}{\partial x} \quad (6.7)$$

This leads to the following formula for the effective viscosity:

$$\mu_{eff} = \mu \frac{H}{|V|} \frac{\Delta y \Delta z}{L} \sum \frac{\partial v}{\partial x} \quad (6.8)$$

The relative viscosity is the ratio of the effective viscosity and the viscosity of the suspending fluid, and it is given for an equidistant grid with spacing $\Delta y = \Delta x = 1$ by:

$$\mu_{rel} = \frac{H}{|V|L} \sum \frac{\partial v}{\partial x} \quad (6.9)$$

From Eq. (6.8) it is obvious that the effective viscosity is mainly decided by the change in the local shear rate near the wall, which is the only variable both spatially and temporally.

To investigate the effects of the suspended droplets on the velocity profile near the moving walls, several simulations were executed with a domain of $123[l u^2]$ and two central droplets of radius $R = 18[l u]$ subjected to a simple shear flow and a shear rate $\dot{\gamma} = 9.75 \times 10^{-6}$. Periodic conditions were applied on the upper and lower boundaries. A density $\rho = 1.0[m u/l u^2]$ and a kinematic viscosity $\nu = 0.166[l u^2 t s^{-1}]$ were used for both fluids. Simple shear flows are characterized by the capillary number given by:

$$Ca = \frac{\mu \dot{\gamma} R}{\sigma_0} \quad (6.10)$$

where σ_0 is the interfacial tension, which was the only variable used in the various cases, all other variables were left unchanged.

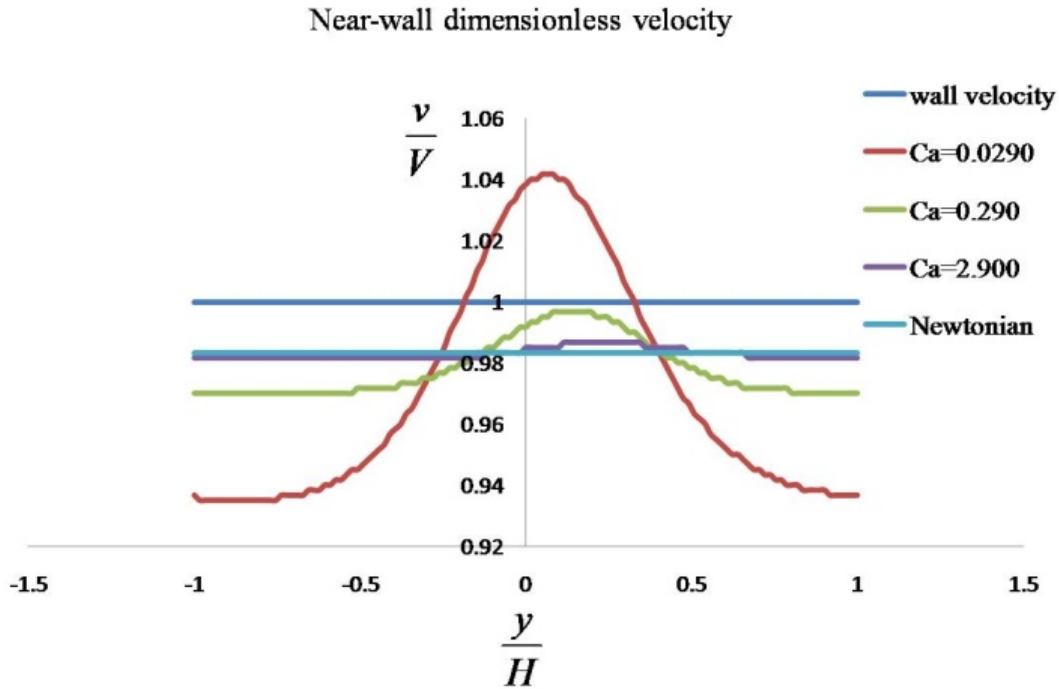


Fig 6.6 Dimensionless velocity profiles for the wall's adjacent nodes for various capillary numbers at dimensionless time steps $\dot{\gamma}t = 0.39$.

The dimensionless vertical velocities for the location adjacent to the moving wall for four capillary numbers including $Ca = \infty$ (Newtonian) are presented in Fig 6.6. From the graph of Fig 6.6 and Eq. (6.8), it is noticed that the greater the differential velocity the greater the effective viscosity. For the Newtonian fluid the differential velocity is a constant in the vertical direction, which is consistent with the theory.

b. Simulation results

Volume fraction effects

The influence of the volume fraction on the relative viscosity of suspensions with deformable polydispersed spheres was analyzed by Hsueh and Wei (2009). Hsueh and Wei used a modified Eshelby model to derive the elastic-strain relation for elastic composites, the elastic-viscous analogy to obtain the effective shear viscosity for the

suspensions and the Bruggman's differential model to derive the formula for the effective viscosity for polydispersed concentrated suspensions with deformable viscous spheres. The equation used for the calculation of the effective viscosity was given by:

$$\phi = 1 - \left(\frac{\eta_0}{\eta^*} \right)^{2/5} \frac{\eta_s - \eta^*}{\eta_s - \eta_0} \quad (6.11)$$

where ϕ is the volume fraction, η^* is the effective viscosity, η_s is the viscosity of the spheres and η_0 is the ambient fluid. Hsueh and Wei (2009) provided some additional formulae to enable a quantitative comparison of their results such as:

$$\eta^* = \eta_0 \left[\frac{2\eta_s + 3\eta_0 + 3\phi(\eta_s - \eta_0)}{2\eta_s + 3\eta_0 - 2\phi(\eta_s - \eta_0)} \right] \quad (6.12)$$

which was similar to the expression derived by Bedeaux et al. (1983), Hashim and Shtrikman (1963), and this equation is used as the upper bound solution for two phase flows with small ϕ and $\eta_s < \eta_0$, and as the lower bound solution for $\eta_s > \eta_0$.

$$\eta^* = \eta_s \left[\frac{5\eta_s - 3\phi(\eta_0 - \eta_s)}{5\eta_s + 2\phi(\eta_0 - \eta_s)} \right] \quad (6.13)$$

which was similar to the equation of Hashim and Shtrikman (1963) and this equation is used as the upper bound solution for incompressible composites with $\eta_s > \eta_0$, and as the lower bound solution for $\eta_s < \eta_0$.

$$\phi = 1 - \left(\frac{\eta_0}{\eta^*} \right)^{2/5} \left(\frac{2.5\eta_s + \eta_0}{2.5\eta_s + \eta^*} \right)^{3/5} \quad (6.14)$$

which was equivalent to the equation of Phan-Thien and Pham (1997) for emulsions with small capillary numbers.

A domain consisting of $123[l_u^2]$ was used with a droplet radius $R = 18[l_u]$ for studying the relative viscosity of a two-phase incompressible suspension with deformable spherical droplets. Assuming a unity thickness the volume fractions of 2, 4 and 6 suspended droplets were $\phi = 0.135$, $\phi = 0.270$ and $\phi = 0.405$, respectively. Since the majority of the presented equations (14-18) were applicable to suspensions characterized by a small capillary number, an interfacial tension parameter $\alpha = 4.0 \times 10^{-4}$, and the relaxation times $\tau_o = 0.57$ and $\tau_s = 1.21$, yielding a viscosity ratio $\lambda_{s/o} = 10$, were used to maintain a capillary number $Ca \approx 0.01$. Shear rate $\dot{\gamma} = 9.75 \times 10^{-6} [ts^{-1}]$, density $\rho = 1.0 [mu/lu^2]$ and $c_m^* = 1$ were used in the simulation. The initial separating distance between the neighboring droplets was $d_m = 4[l_u]$. This allowed in addition to the compressional components of the shear flow, the droplets interfaces to come to a proximity which triggered the short-range interactions.

The relative viscosity calculated by Eq. (6.9) from the proposed model was compared with the normalized effective viscosity of Eq. (6.11) to Eq. (6.14) and the results are presented in Fig 6.7 at dimensionless time step $\dot{\gamma}t = 0.39$.

It is evident from the graphs of Fig 6.7 that the proposed model numerical results were in excellent agreement with the analytical solution of Hsueh and Wei (2009) and comparable to Hashim and Shtrikman (1963) lower bound solution. The deviation of the solution from the results of Phan-Thien and Pham (1997) could be due to the fact that Eq. (6.14) was derived for droplets which remained spherical in suspensions characterized by very small capillary numbers.

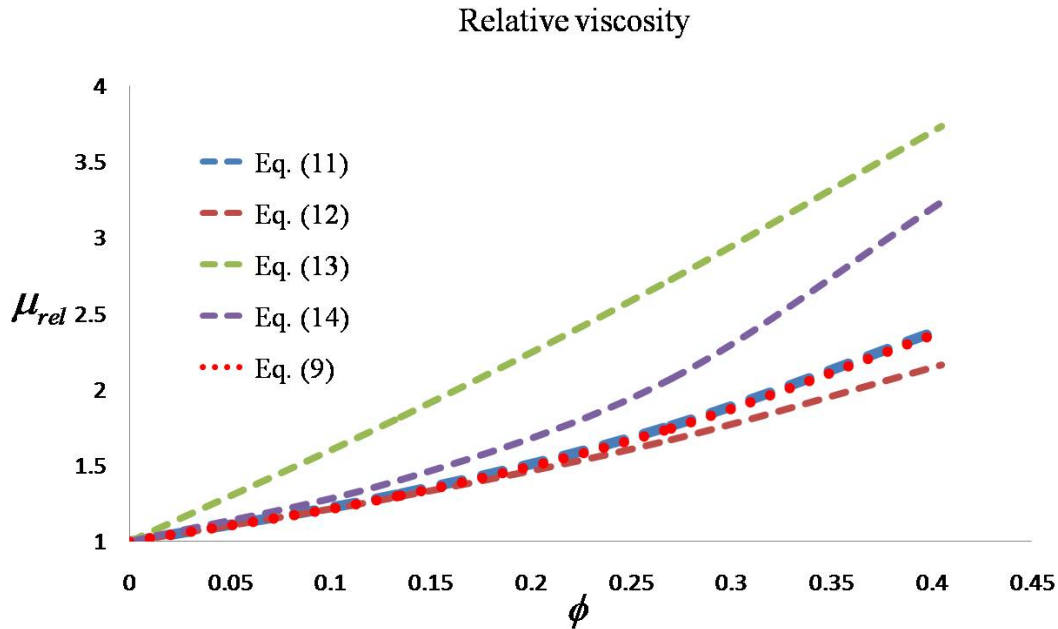


Fig 6.7 Effective viscosity of a binary fluid suspension calculated with respect to the volume fraction of the dispersed phase by Eq. (6.11) to Eq. (6.14) and by the numerical results of the proposed model Eq. (6.9). The insets are for the phase field contours.

Capillary number effects

The domain, the fluids properties and the flow conditions from subsection 3.4 were used to study the effects of the capillary number on the relative viscosity of a droplet-based binary mixture. Two volume fractions $\phi = 0.270$ and $\phi = 0.405$ were used in the simulation. The capillary number was changed in the range $0.01 \leq Ca \leq 0.4$ by varying the interfacial tension and maintaining the shear rate. The calculation of the relative viscosity was done at the dimensionless time step $\dot{\gamma}t = 0.39$. The results are presented in Fig 6.8.

The graphs of Fig 6.8 show a shear thinning behavior, since the effective viscosity diminished with the increase of the capillary number.

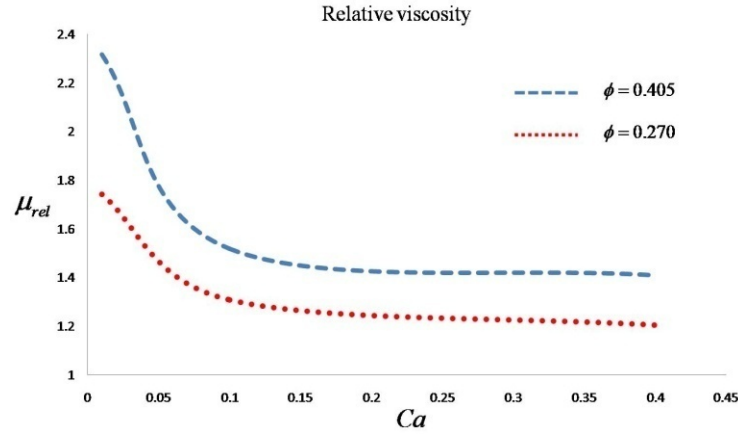


Fig 6.8 Effects of the capillary number on the relative viscosity of a binary mixture for two volume fractions $\phi = 0.270$ and $\phi = 0.405$, constant shear rate $\dot{\gamma} = 9.75 \times 10^{-6} [ts^{-1}]$ and variable interfacial tension at dimensionless time step $\dot{\gamma}t = 0.39$.

Surfactant coverage effects

The effects of the surfactant coverage on the rheology of an immiscible mixture were studied using droplet volume fractions $\phi = 0.135$ and $\phi = 0.270$ in the domain, fluid properties and flow conditions which were described in the previous sections. The Langmuir nonlinear equation of state Eq. (5.20) was used in this simulation with surfactant elasticity $E_0 = 0.5$. The saturation surfactant concentration was calculated and had a value $\Gamma_\infty = 6.0 \times 10^{-4} [lmol/lu^2]$ (lattice mole per lattice square). This allowed the selection of the initial surfactant concentration needed for testing cases in which the surfactant coverage was varied within the range $0 \leq C_{in} \leq 0.4$. The surface Péclet number was set to $Pe_s = 10$. The graphs in Fig 6.9 (A) show the role of surfactant coverage on the rheological behavior of the immiscible mixture, since a reduction in the relative viscosity is observed with the increase in the surfactant coverage.

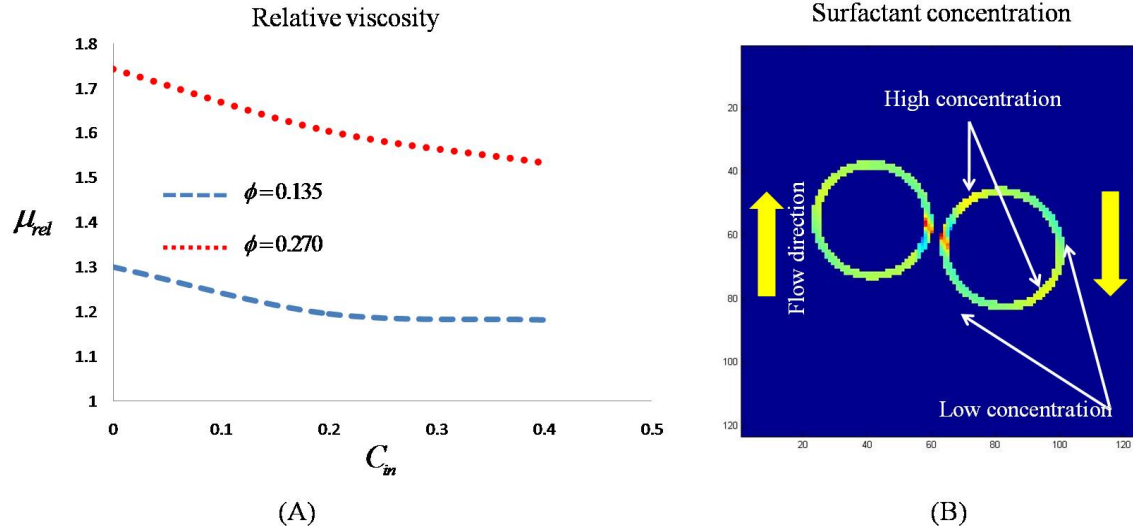


Fig 6.9 Effects of the surfactant surface coverage on the relative viscosity of a droplet based immiscible mixture. The capillary number is $Ca = 0.01$ and the dimensionless time step is $\dot{\gamma}t = 0.39$.

The reason behind such behavior is related to the fact that surfactants in general reduce the interfacial tension of the droplets, thus making them more deformable. The other reason has to do with the convection of the surfactant due to the effects of the interface tangential velocities. This creates Marangoni stress which is highest in the regions with greater surfactant concentration gradients as indicated in Fig 6.9 (B). The high Marangoni stress forces the droplets to align in the direction of the flow (Drumright-Clarke, 2002), thus diminishing their resistance to the flow, which results in a reduction in the relative viscosity of the mixture.

CHAPTER 7

NON-UNIFORM INTERFACIAL TENSION LBM FOR RBC MODELING

This study aims at analyzing the red blood cell (RBC) deformation and velocity while streaming through venules and through capillaries whose diameters are smaller than the RBC size. The characteristics of the RBC shape change and velocity can potentially help in diagnosing diseases. In this work the RBC is considered as a surfactant covered droplet. This is justified by the fact that the cell membrane liquefies under pressure in the capillaries, and this allows the marginalization of its mechanical properties. The RBC membrane is in fact a macro-colloid containing lipid surfactant. When liquefied, it can be considered as a droplet of immiscible hemoglobin covered with lipid surfactant in a plasma surrounding. The local gradient in the surface tension due to non-uniform local interface surfactant distribution is neglected here, and a non-uniform zonal averaged value of surface tension representative of the surfactant bulk zonal concentration is rather implemented. The interplay between the surface tension geometry and the hydrodynamic conditions determines the droplet shape by affecting a change in its Weber number, and influences its velocity. The Gunstensen lattice Boltzmann model for immiscible fluids is used here since it provides independent adjustment of the local surface tension, and allows the use of fluids with viscosity contrast. The proposed concept was used to investigate the dynamic shape change of the RBC while flowing through the microvasculature, and to explore the Fahraeus, and the Fahraeus-Lindqvist effects.

7.1 The heuristic approach for surfactant-covered droplets

The motivation for the use of zonal averaged non-uniform surface tension method stems from the fact that the lipid membrane liquefies at pressure greater than 29 (dyne/cm) as explained by Keller et al. (1998), a condition sought to prevail in the microvasculature. Thus the liquefied lipid bilayer is expected to allow its surfactant molecules to shift in the direction opposite to the flow direction mainly due to convection which is dependent on the tangential surface velocities. Since the number of lipid molecules is constant on the periphery of the RBC and since these molecules are finite by size, the shift comes to a halt when regions of higher surfactant concentration reach their saturation point. Another important factor which prevents any further build-up of the concentration is the Marangoni stress which is expressed as follows:

$$-\nabla_s \sigma_s = -\frac{\partial \sigma_s}{\partial \Gamma} \cdot \nabla_s \Gamma \quad (7.1)$$

where ∇_s is a surface gradient, σ_s is the local surface tension, Γ is the local surfactant concentration. It is convenient to relate the surface tension with the surfactant concentration by the Langmuir surface equation of state expressed as follows:

$$\sigma_s = \sigma_0 + RT\Gamma_\infty \ln(1 - \Gamma/\Gamma_\infty) \quad (7.2)$$

where σ_0 is the surface tension of a clean surface, Γ_∞ is the saturated surfactant surface concentration, R is the gas constant and T is the temperature in Kelvin. Equation (7.1) and Eq. (7.2) yield the following surface tension derivative with respect to the surfactant concentration (Hu and Lips, 2003):

$$\frac{\partial \sigma_s}{\partial \Gamma} = -\frac{RT}{(1 - \Gamma/\Gamma_\infty)} \quad (7.3)$$

Equation (7.3) indicates that an increase in the surfactant surface concentration leads to an increase in the Marangoni stress, which in turn slows the tangential surface velocity and hampers any further convection of surfactant towards the regions of higher concentration. This process prevents the presence of regions with extremely low surface tension and limits the area generation beside the limitations imposed by the contraction of the regions with lower surfactant due to higher surface tension. Eq. (7.2) can be written in the following dimensionless form:

$$\frac{\sigma_s}{\sigma_0} = 1 + E_0 \ln(1 - \Gamma/\Gamma_\infty) \quad (7.4)$$

where $E_0 = RT\Gamma_\infty/\sigma_0$ is the surfactant elasticity which determines the strength of the surfactant effect on the interfacial tension.

In this model an estimated value of $E_0 = 0.2$ was used. A reasonable range for the bulk surfactant concentration ratio of $0.3 \leq \Gamma/\Gamma_\infty \leq 0.7$ was considered in Eq. (7.4) based on a study by Hu and Lips (2003) for some polymer blends. An initial surface tension parameter α_0 from Eq. (2.16) was set such that the droplet deformation index $DI \approx L/D$, was equal to an experimental RBC index, where L, D were the length and the width of the RBC (Hong Jeon et al., 2006). An initial surfactant concentration ratio $\Gamma_i/\Gamma_\infty = 0.7$ was used with the assumption that the lipid bilayer cannot be fully saturated throughout the RBC membrane as stated by Braasch (1971) regarding the radio-autography results. For simplicity the interface of the droplet was then divided into two adjustable regions: frontal region with lower surfactant concentration and backside region with higher concentration as shown in Fig 7.1, such that the initial total surfactant mass was conserved on the droplet interface:

$$\frac{\Gamma_b}{\Gamma_\infty} N_b + \frac{\Gamma_f}{\Gamma_\infty} N_f = \frac{\Gamma_i}{\Gamma_\infty} N_T \quad (7.5)$$

$$\frac{\Gamma_f}{\Gamma_\infty} \leq \frac{\Gamma_b}{\Gamma_\infty} < 1$$

where N_b, N_f, N_T are the number of interfacial nodes in the back, front and total regions respectively. $\Gamma_f, \Gamma_b, \Gamma_i$ are the frontal, backside and initial surfactant concentration. The zonal surface tension parameters of the model had to obey the following equation:

$$\frac{\alpha_k}{\alpha_0} \approx \frac{\sigma_k}{\sigma_0} = 1 + E_0 \ln(1 - \Gamma_k / \Gamma_\infty) \quad (7.6)$$

where $k = f, b$ refer to the frontal and backside regions respectively.

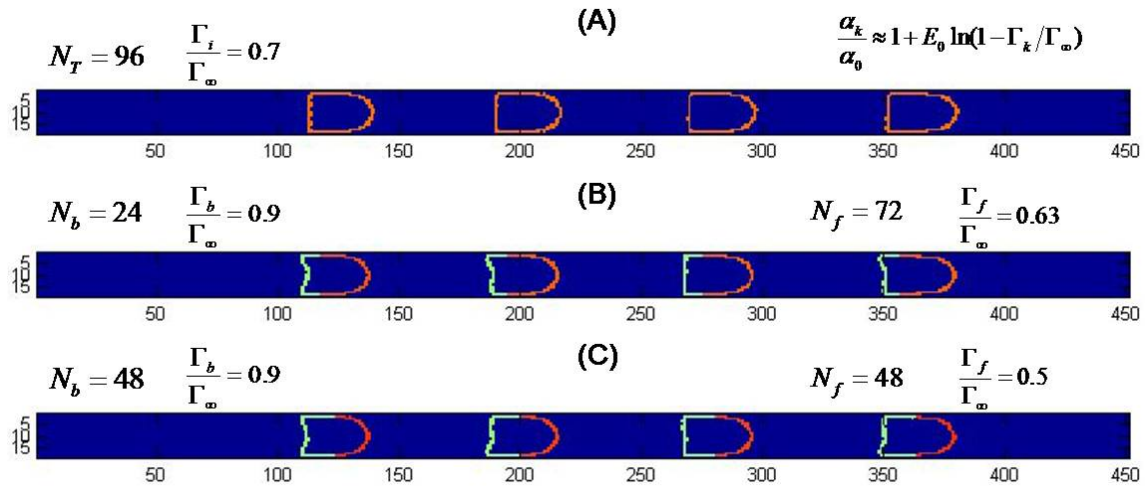


Fig 7.1 Illustrates the adjustable zonal division of the interface with regions of higher (frontal) and lower (backside) interfacial tension. The darker contours show greater surface tension parameter α from Eq. (2.16). (A) Shows homogeneous α value, (B) quarter of the interface had lower α value; (C) the interface was shared equally between high and low values of α .

A viscosity ratio $\mu_h / \mu_p = 7$ was used throughout this model which is an approximation of the ratio of hemoglobin to plasma. Preferential wetting was given to the suspending fluid which was treated as hydrophilic, contrary to the droplets which were hydrophobic.

7.2 Simulation results and discussion

Surface Tension Effects on a Single File Flow RBCs Shape and Velocity

To calibrate the model data were extracted from the experimental work of Hong Jeong et al. (2006) which indicated RBC deformation index $DI = 1.55$ and velocity $V = 1.8 \text{ mm/s}$ inside the capillary of a rat mesentery. Assuming that blood density at normal temperature is $\rho = 1.05 \text{ g/cm}^3$ as was stated by Nakano et al. (2005) and that the velocity of the RBCs is representative of the average blood velocity in the capillary, then the estimated blood viscosity is $\mu = 2.35 \text{ cP}$ and the average Reynolds number is $Re \approx 0.0055$ for a random capillary size.

A domain of 19×450 lattice sites was selected for the simulation of four droplets where all variables were measured in lattice units. The relaxation times were chosen as $\tau_p = 0.602$; $\tau_h = 1.219$; $\tau_{eff} = 0.908$ for the suspending, the suspended fluid and the interface as per Eq. (2.15), respectively. This produced the right viscosity ratio between the two fluids and an apparent kinetic viscosity $\nu_{app} \approx 0.08$ which was calculated based on the density fraction of the red and blue fluids. A density $\rho = 1.05$ was used for both fluids in the model. The average velocity of the bulk fluid was calculated using the known experimental value of the Reynolds number $Re = V_{av} 2h / \nu_{app} \approx 0.0055$, where h was half the channel width. This led to an average velocity $V_{av} \approx 2.5 \times 10^{-5}$ from which the source term was derived as follows (Sukop and Thorne, 2006):

$$F = \frac{2\rho\nu_{app}V_{av}}{h^2} = 5.8 \times 10^{-8} \quad (7.7)$$

The source term in Eq. (2.20) produced the right undisturbed average velocity of the bulk fluid, but since the droplets caused little resistance to the flow, an increase of the source term was deemed necessary, thus a value of $F = 7.8 \times 10^{-8}$ was found by trial to produce the needed average velocity. To maintain a deformation index $DI \approx 1.55$ and the calculated RBC average velocity, the following value for the surface parameter was found by trial $\alpha_0 \approx 1.5 \times 10^{-7}$ as shown in Fig 7.2 (A). Periodic boundary conditions were applied at the inlet and outlet boundaries, and bounce-back conditions at the upper and lower walls. After determining the optimum surface tension parameter α_0 , the zonal averaged non-uniform method with values calculated by Eq. (7.5) and Eq. (7.6) was used in two cases where a lower surface tension parameter value covered about quarter of the interface in one case and half of the interface in the other. The influence of the non-uniform surface tension was more noticeable on the droplets shape through the appearance of tails due to the lower surface tension at the backside and the influence of the shear stresses which were higher near the walls. A velocity drop was also witnessed in case (B) and case (C). This could be due to a relatively higher surface tension parameter resulting from Eq. (26) and Eq. (7.6) in the frontal region which led to a slightly lower droplet average velocity. In the subsequent cases the surfactant concentration distribution of case (B) will be used as a reference.

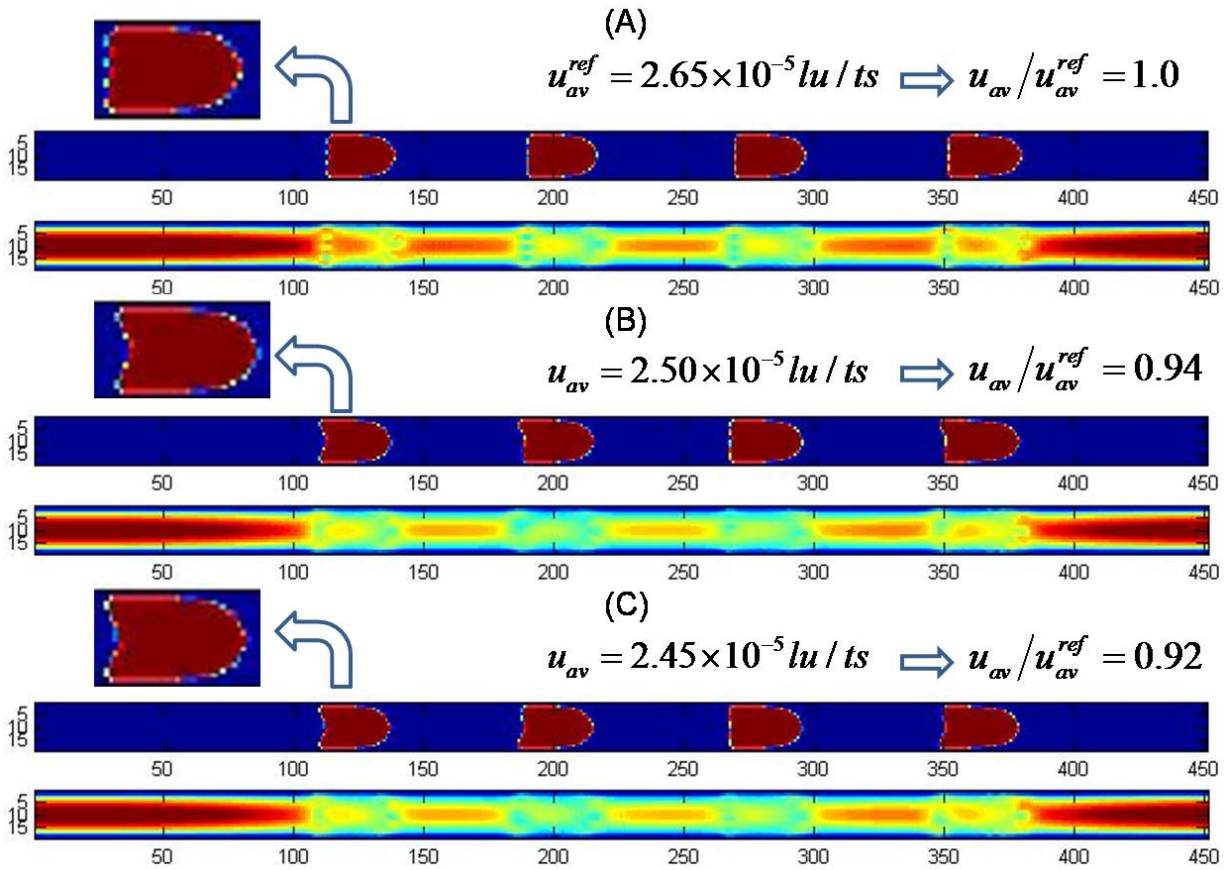


Fig 7.2 Phase field and horizontal velocity contours for four droplets streaming in a narrow vessel with homogeneous surface tension parameter (A), and with zonal averaged non-isotropic surface tension parameter whose values were explained in Fig. 7.1 for insets (B) and (C).

More simulations were performed using the same domain and flow conditions, but the surface tension parameter α_0 was varied in each run. The intention was to investigate the range of the surface tension parameters responsible for slowing down the droplet to about 20%–0% of its nominal velocity and see its effects of the RBC shape.

The mean velocity of the RBC was calculated using the following equation:

$$u_{av} = \frac{1}{A} \iint u_x dx dy \quad (7.8)$$

where A is the total area of the RBCs and the deformation index was computed by the following formula:

$$DI = \frac{(a-b)}{(a+b)} \quad (7.9)$$

where a, b are the major and minor axis of the droplets respectively. Fig 7.3 shows the phase field and velocity contours for four runs where the surface tension parameter was varied $1.5 \times 10^{-7} \leq \alpha_0 \leq 1.05 \times 10^{-6}$ by an equal step.

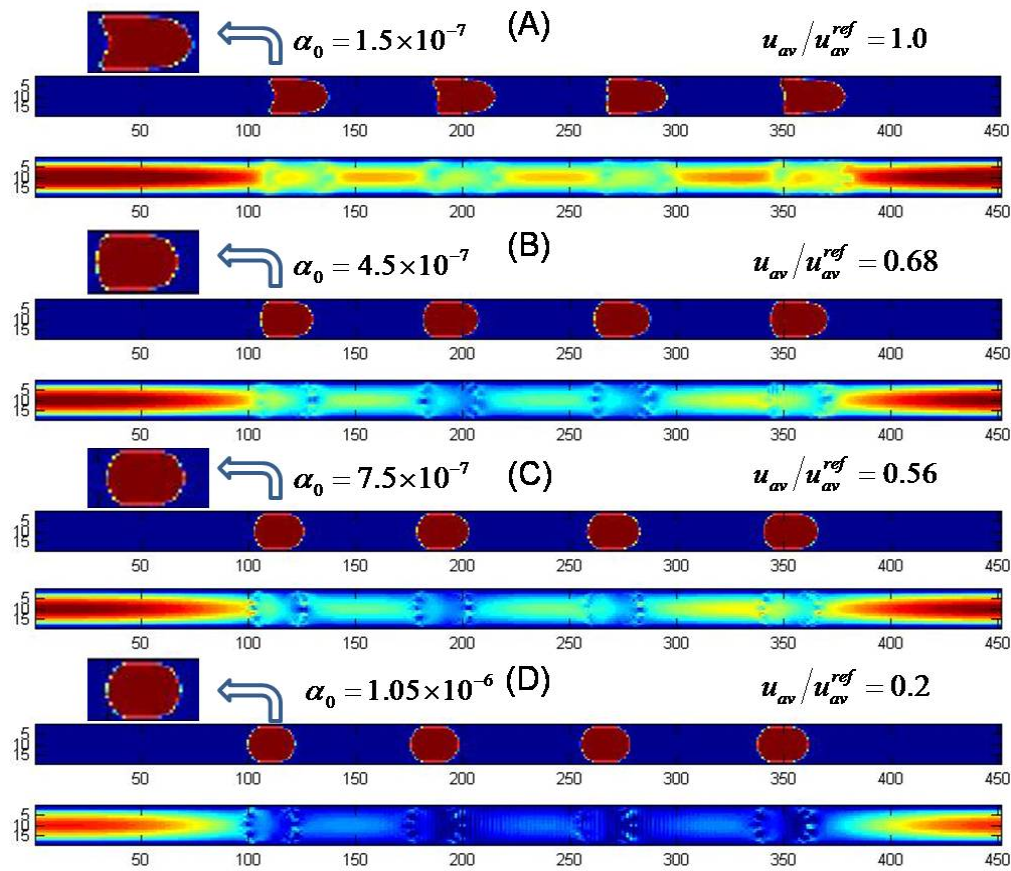


Fig 7.3 Phase field contours and their respective horizontal velocity contours for surface tension parameters $1.5 \times 10^{-7} \leq \alpha_0 \leq 1.05 \times 10^{-6}$ by a step of $\delta_{\alpha_0} = 3.0 \times 10^{-7}$.

The normalized average velocities of the four cases in which the reference case velocity (A) was used in the denominator and the DI were plotted in Fig 7.4. A general trend of increasing velocity and DI is observed with decreasing surface tension parameter. It can be seen from Fig 7.4 that the surface tension parameter had to be raised seven times with respect to the reference parameter in order to reduce the droplet velocity up to 20% of its nominal value and the DI by 50% .

Driessen et al. (1980) tested the effect of injecting hardened RBCs inside the rat mesentery. A decrease of the RBC velocity up to $(71.1 \pm 19.1)\%$ was observed when RBCs treated with 0.5 mmol.L^{-1} diamide were placed in the rat capillaries during the exchange period and to $(8.3 \pm 15.1)\%$ during the hypo-tension period. When 1.5 mmol.L^{-1} diamide was used the velocity dropped to $(86 \pm 24)\%$ during the exchange period and to $(2.1 \pm 6.1)\%$ during the hypo-tension period.

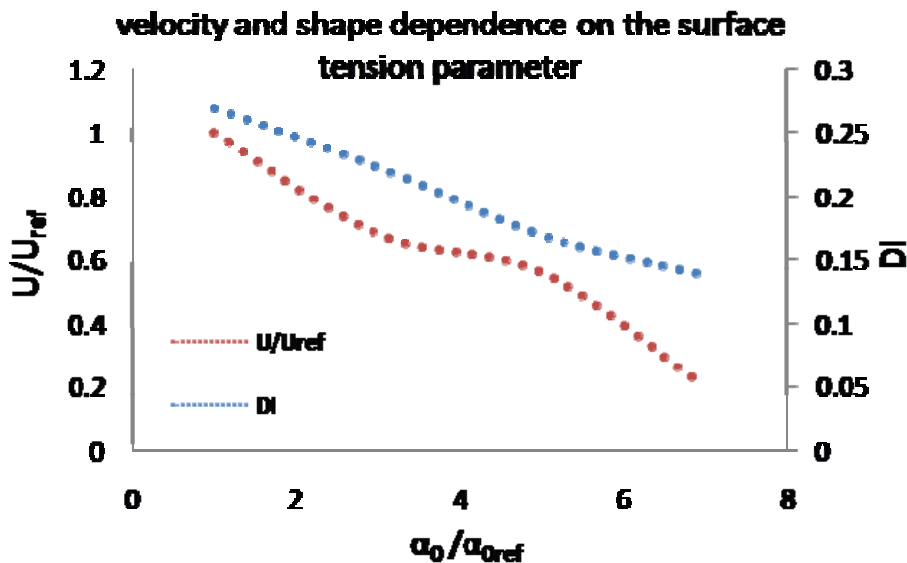


Fig 7.4 Droplet velocity and DI dependence on the surface tension parameter.

It is noticed from Fig 7.4 that for $4.5 \times 10^{-7} \leq \alpha_0 \leq 7.5 \times 10^{-7}$ the normalized velocity curve had a gentle slope and the decrease in velocity was up to 65% , which agrees qualitatively with the experimental trend. This could pave the way for the potential of qualitatively correlating the model results with some experimental data such as the results of Driessen et al. (1980) if more details were available.

RBC Deformability

The role of the endothelial surface layer on the RBC deformability, flow resistivity, and lower tube hematocrit, was studied by (Secomb et al., 1998; Secomb et al., 2001). Special attention was given to the exclusion of the RBC from the capillary walls. The endothelial cell creates a higher level of flow resistance in the microvasculature compared to glass tubes used in in-vitro experiments.

A domain consisting of 160x24 lattice units was used to model single RBC flowing in a capillary of 6 μm diameter. The results of this simulation were expressed in physical values to enable a comparison with the results of Secomb et al. (2001). The reference shape, before applying the non-uniform surface tension method, was assumed to be a sphere of 6 μm diameter as stated by Braasch (1971). The source term was varied in order to achieve droplet velocities ranging from 500 $\mu\text{m}/\text{s}$ to 3,700 $\mu\text{m}/\text{s}$ using Eq. (28). In the proposed model velocities below 500 $\mu\text{m}/\text{s}$ were not used. This was to avoid lattice pinning, which originates from the Gunstensen method for the segregation step at very low velocities (D'Ortona et al., 1995). The surface tension parameters used in this simulation were the same as the reference case and were based on values derived from Eq. (7.5) and Eq. (7.6). The selection ensured a good control over the shape of the RBC. The gap width between the RBC and the wall

was measured in the same manner used by Secomb et al. (1998). The gap was considered as the average width along the whole length of the cell, where the angle between the tangent to the curvature of the cell and the vessel wall was less than 11 degrees as shown in Fig 7.5.

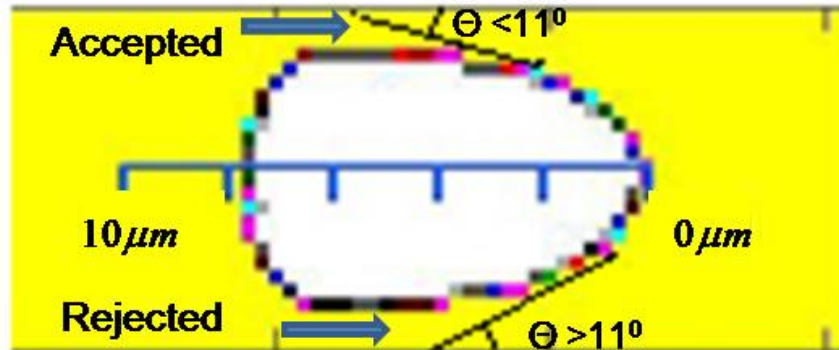


Fig 7.5 Criteria for accepting or rejecting the gap measurement along the length of the RBC used for calculating the average width. For $\theta < 11$ degree the record is taken otherwise it is rejected.

Fig 7.6 shows the droplet-wall gap width variation with respect to changing the velocity. The results obtained from the proposed model were compared to the results of Secomb et al. (2001). The upper higher graph represents the model in which Secomb considered the role of the endothelial surface layer, and the lower graph corresponded to the model in which he disregarded that role. It is evident that the bounce-back condition in the present model did not fully recover the effects of the endothelial surface layer on the RBC exclusion from the wall, but it rather produced reasonable results.

The droplet shape change due to the increase in its velocity is shown in Fig 7.7. This was done by measuring the deformation index as per Eq. (7.9). The same graph shows also the droplet steady state length and gap. A trend of increasing gap, length, and DI is associated with an increase in the droplet velocity.

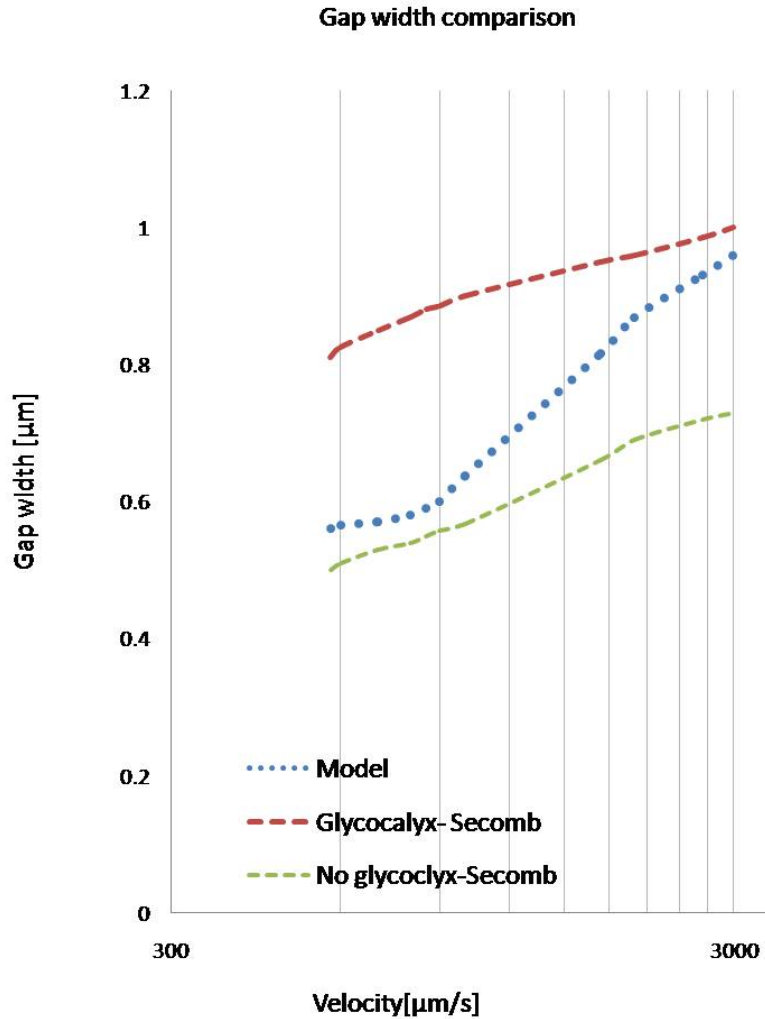


Fig 7.6 Droplet-wall gap width comparison of the proposed model with the data generated from Secomb et al. (2001). (Glycocalyx indicates that the endothelial cell layer was considered in Secomb's model and no glycoclyx indicates otherwise).

In the proposed model a relatively higher velocity was required to achieve a droplet elongation to about $8\mu\text{m}$ as shown in Fig 7.7. This was due to a smaller initial reference shape. The elongation of the droplet was compensated by a greater droplet-wall gap width.

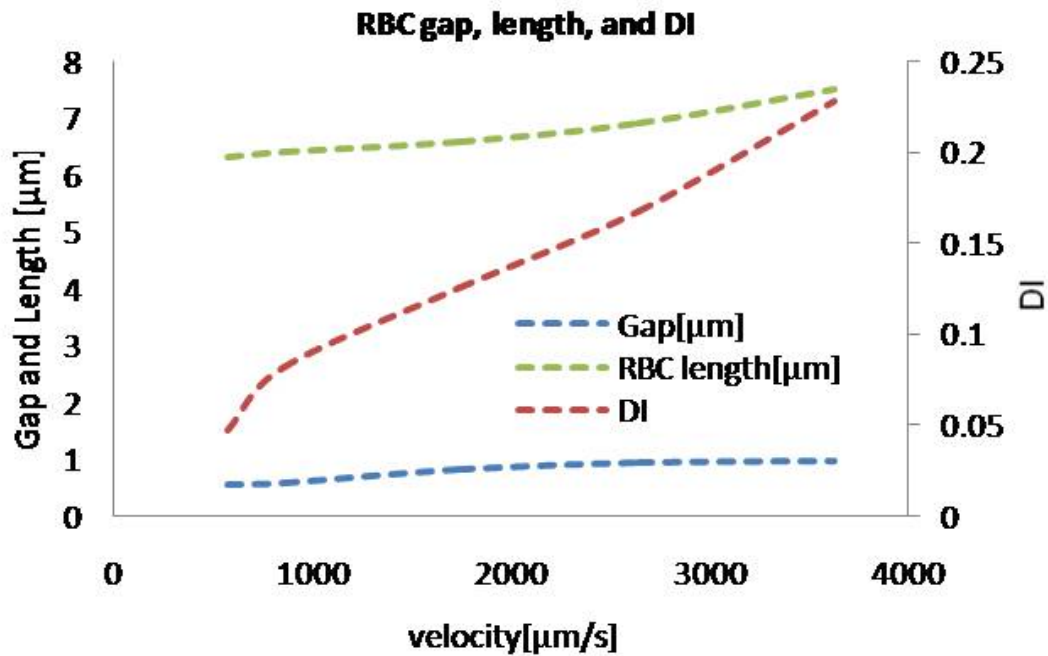


Fig 7.7 Droplet-wall gap, DI, and length calculate with respect to the droplet velocity.

It is reasonable to assume that the deformation was caused mainly by the higher viscous stress near the walls since in the present model the droplet was not allowed to wet the walls. In a straight section of the microvasculature, the RBC tends to form a bullet shape when flowing at its normal velocity as shown in Fig 7.8. This is due to the Poiseuille nature of the flow, which enables the forehead of the RBC to have higher momentum, meanwhile lower momentum prevails at the upper and lower sides because of the retardation caused by the viscous stresses. This results in an exclusion of the RBC from the walls and leads to a considerable reduction of the viscous stresses, and thus to the vanishing of its parachute since the surface tension effects overcame the shear stress effects.

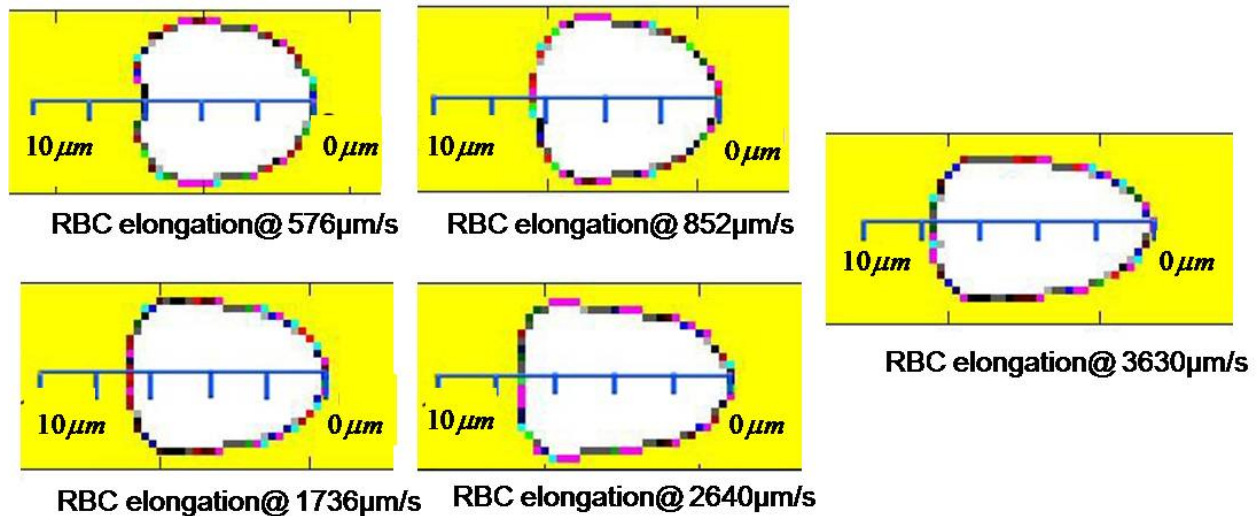


Fig 7.8 Dependence of the wall-droplet gap width on the velocity. The gap increased with increasing the velocity, and the droplet elongated while distancing itself from the wall.

The Fahraeus Effect

The Fahraeus effect describes a blood related phenomenon which occurs in small tubes. It was proven experimentally by Fahraeus that the tube hematocrit H_T is less than the discharge hematocrit H_D . This happens when the RBC mean velocity V_{rbc} is higher than the mean blood velocity \bar{V} . The Fahraeus effect is described by the following equation (Sun and Munn, 2005):

$$\frac{H_T}{H_D} = \frac{\bar{V}}{V_{rbc}} \quad (7.10)$$

Results from the simulations of section 3.3, were revisited to analyze the effect of the RBC velocity on the tube hematocrit and was shown in Fig 7.9. A comparison with the results of Secomb et al. (2001) showed that the model output was closer to Secomb's no glycocalyx model, which disregarded the endothelial surface layer effects. The reason for this behavior could be due to the sensitivity of the present model to the

near-wall viscous effects. This resulted in a relatively lower droplet mean velocity, hence a higher value of the Fahraeus effect. With the increase in velocity, the droplet was excluded from the wall. This reduced the shear stresses and the value of the Fahraeus effect.

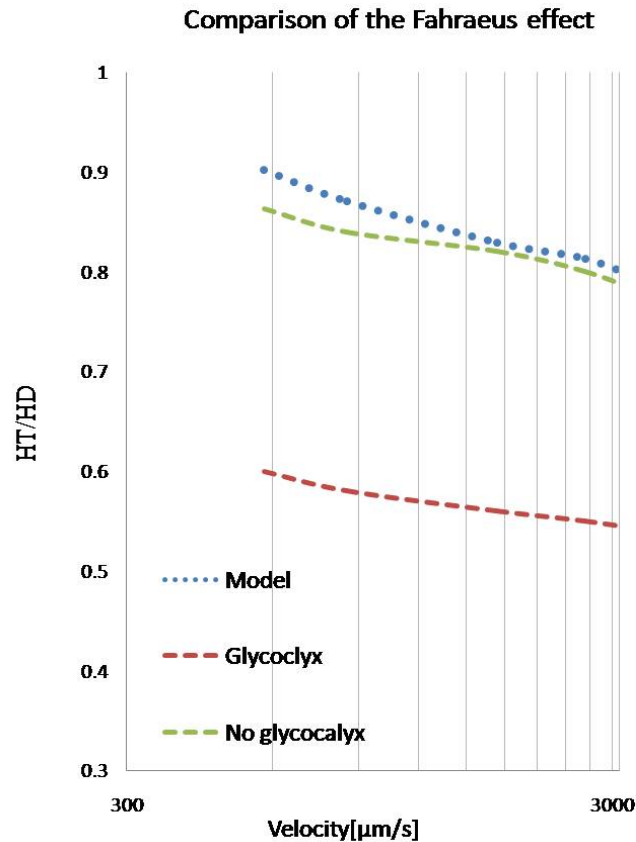


Fig 7.9 Decrease in tube hematocrit with respect to discharged hematocrit due to an increase in RBC velocity, and a comparison with Secomb results (Secomb et al., 2001).

To check the influence of varying the blood hematocrit in a narrow vessel on the Fahraeus effect, a 285×41 lattice sites were used for three runs with different number of droplets placed in the domain as shown in Fig 7.10. This was to simulate $20 \mu\text{m}$ diameter tube experiment, whose results were presented by Sun and Munn (2005).

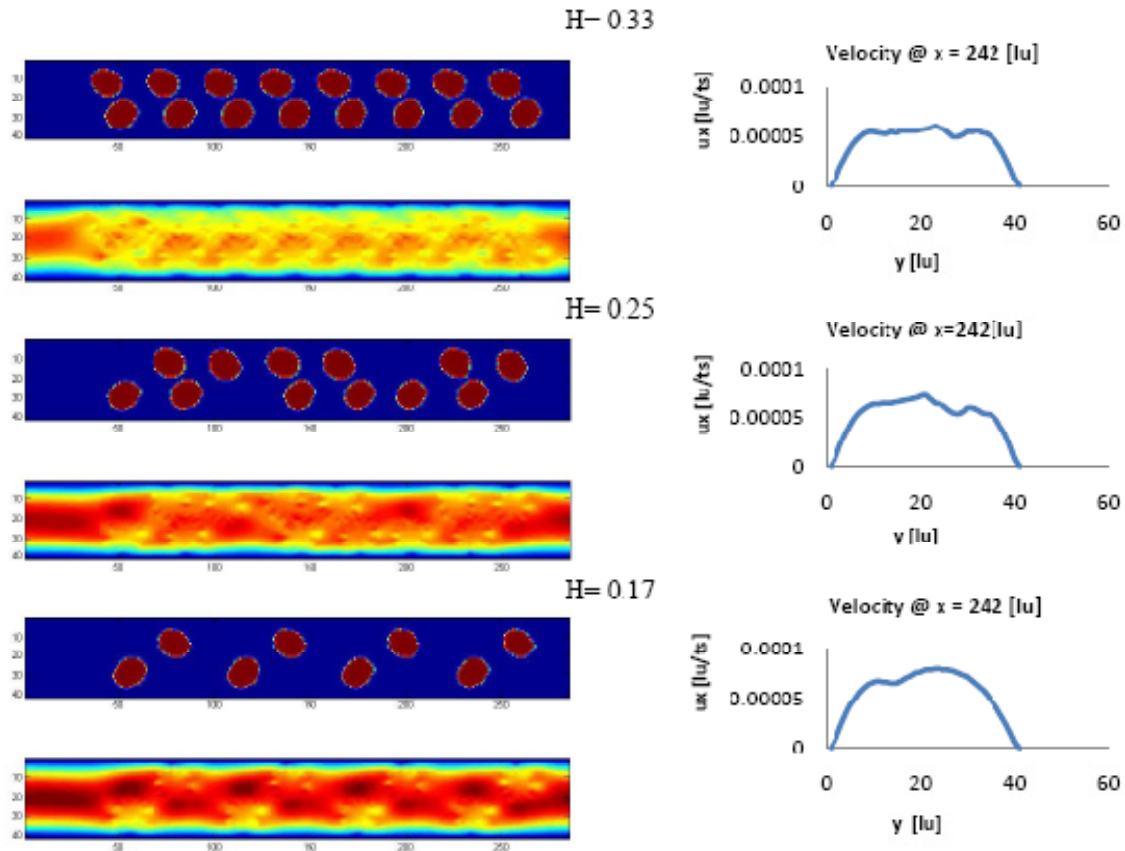


Fig 7.10 Left-phase field contours and horizontal velocity profile for 285x41 lattice sites and 0.17, 0.25 and 0.33 discharge hematocrit. Right-horizontal velocity profile measured at the middle of the domain.

Periodic conditions were applied at the inlet and outlet boundaries and mixed boundary condition at the top and bottom walls. This is a special boundary condition consisting of a combination of the full bounce-back, and the specular-reflection boundary condition. More details on this boundary condition are provided by Shirani and Jafari (2007). The mixed boundary condition was used because the results of Sun and Munn (2005) were compared with in vitro experimental data. The results of the three simulations which were performed with discharge hematocrit 0.17, 0.25 and 0.33, respectively, are presented in Fig 7.11. The average Reynolds number was $Re \approx 0.025$

which is a representative value for blood flow in the venules. The mean droplet velocity was calculated by Eq. (7.8). The Fahraeus effect was evaluated using Eq. (7.10). A reflection coefficient of 0.7 was used for this simulation.

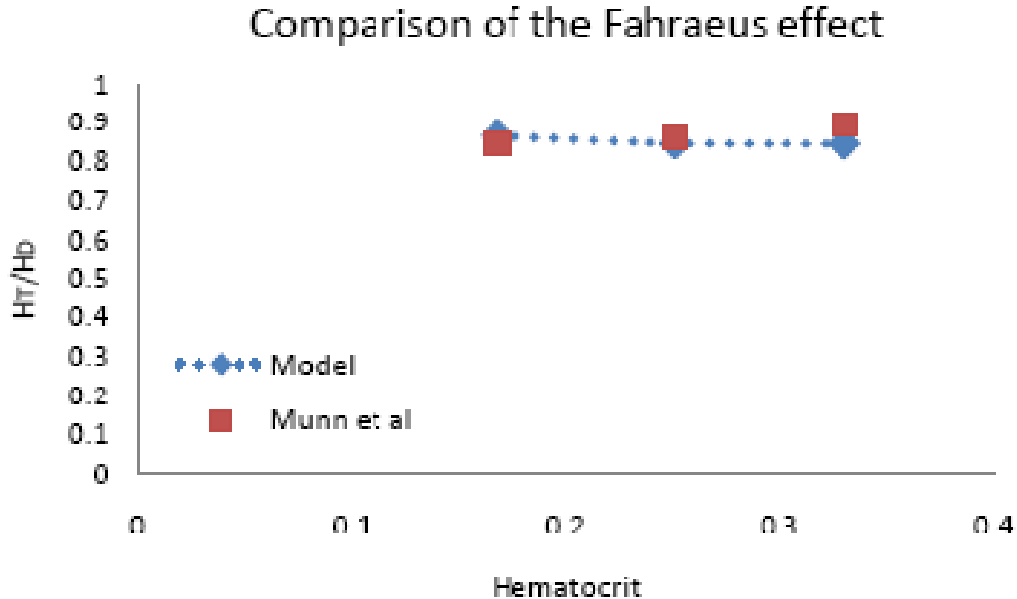


Fig 7.11 The graph represents the dependence of the Fahraeus effect on the discharge hematocrit. Comparison of the model results with the results of Sun and Munn (2005).

The Fahraeus-Lindqvist Effect

The Fahraeus-Lindqvist effect predicts a decrease in the apparent viscosity of blood in a long narrow vessel of diameter ranging from 7 μm to 200 μm . This is due to the presence of a cell-free layer, referred to as plasma-skimming layer near the wall. In the absence of gravitational effects and under shear or parabolic flow it is known that when neutrally buoyant droplets (Legendre and Magnaudet, 1998) or vesicles (Seifert, 1999) are in proximity to a channel walls, they tend to migrate towards the center due to a hydrodynamic shear lift.

With 16 lattice units for the RBC diameter, a 57×240 lattice squares domain was used to investigate the model capability of reproducing a plasma-skimming layer based on the shear lift phenomenon. Eight out of twelve droplets were put initially on the walls. A Reynolds number $Re \approx 0.05$ was used for this simulation. Periodic conditions were applied at the inlet and outlet boundaries to create a resemblance of a long tube and bounce-back at the upper and lower walls to impose zero velocity on the wall as described in the theory (Chandran et al., 2006).

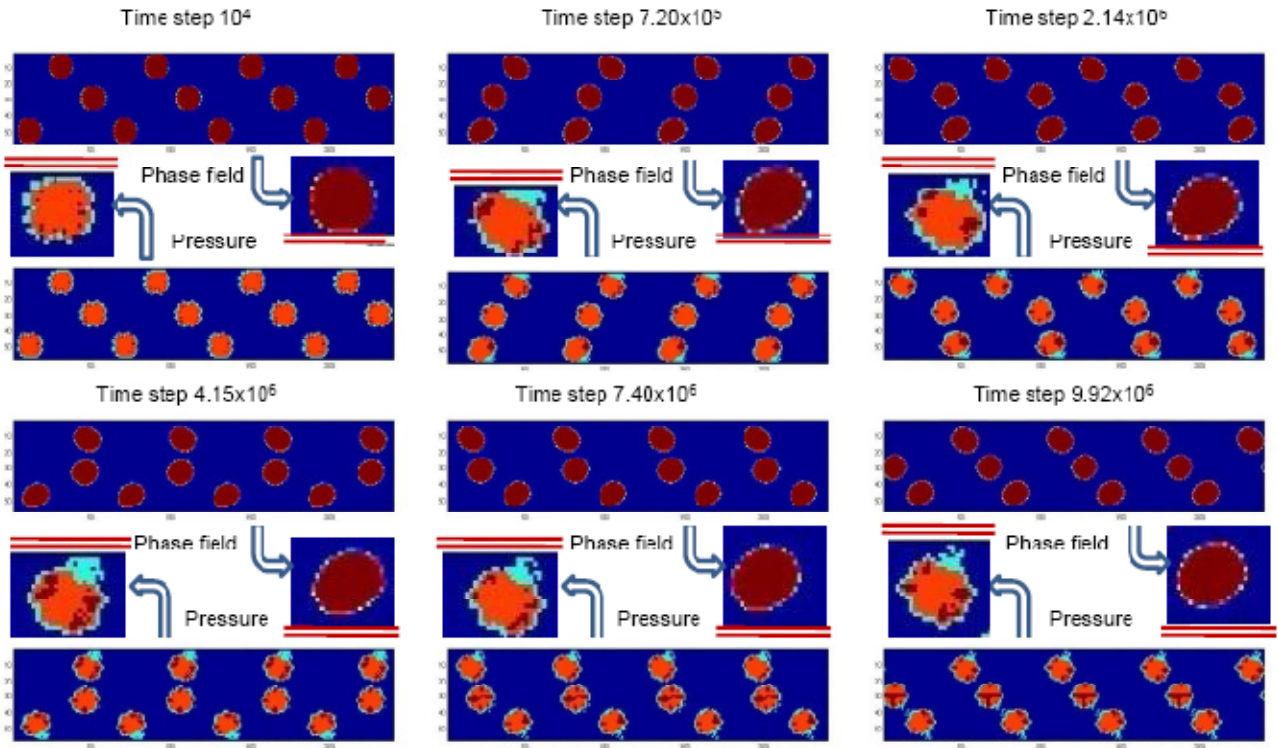


Fig 7.12 Phase field contours and pressure contours for six different time steps. The pressure contours show a pressure difference between regions below and above the wall-side droplets. The phase field contours show the axial migration of the near-wall droplets.

This simulation clearly demonstrated that the near-wall droplets tilted due to the viscous effects of the surrounding fluid, and migrated toward the center as shown in the

phase field contour insets of Fig 7.12. The pressure contour insets of Fig 7.12 show a consistent pressure difference in the regions below and the regions above the droplets. This pressure difference, the droplet tilt, and its elongation are the major contributors to the creation of the lift force.

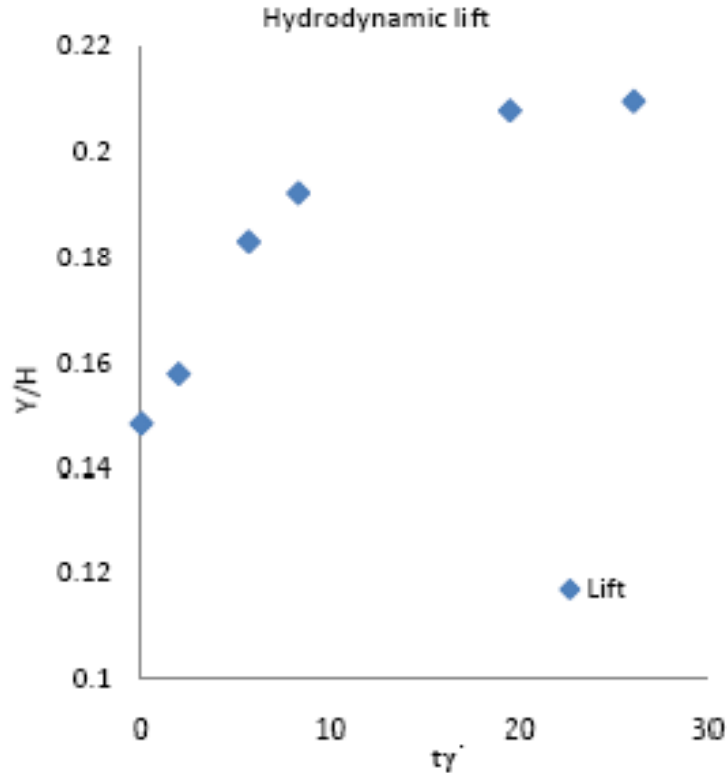


Fig 7.13 Graph representing the axial migration of the near-walls droplets. Normalized displacement of the droplet mass center versus the corresponding time step multiplied by the shear rate of the mid location between the wall and the center of the channel.

To trace the near-wall droplets mass center displacement in the vertical direction due to the shear lift, the normalized y coordinate by the channel width Y/H was plotted versus dimensionless time steps which were defined as ty' where t was the time in lattice units, and for convenience the shear strain rate was taken with respect to the height $H/4$ since in parabolic flows this rate varies with the coordinate of the location of

interest in the vertical direction. This led to the following equation for the shear strain rate:

$$\dot{\gamma} = \frac{2U_0}{H} \quad (7.11)$$

where U_0 is the undisturbed centerline fluid input velocity. The droplets reached an equilibrium position at 21% of the channel height. The result presented in Fig 7.13 is indicative of the joint influence of the shear lift and the effect of the higher velocity droplets placed in the center of the channel, which halted the axial migration when the droplets came into close proximity.

CHAPTER 10

CONCLUSION AND RECOMMENDATIONS

10.1 Conclusion

This research introduced three novel modules to the lattice Boltzmann method: the migrating multi-block which improves the interface resolution and accelerates the LBM solution, the hybrid module which incorporates the surfactants effects on the interface of the mixture and the suppression of coalescence module which facilitates the study of the rheology of emulsions. The combination of these modules provides a convenient tool for the study of the colloidal morphology and rheology. A heuristic surfactant-covered droplet approach was also used for studying the red blood cell deformability in the microvasculature. Summary of each of the studies is presented below.

a. Migrating multi-block schemes

The migrating multi-block concept was introduced and implemented on the single phase, multiphase and multi-component LBM models. The module was tested on asymmetrically placed cylinder in a channel in 2D geometry, which results for the Strouhal number, the lift and the drag coefficients were in good agreement with benchmark published data. The shear lift of a neutrally buoyant droplet was studied. The analysis of the equilibrium distance from the wall matched well with other numerical results. The buoyancy of bubbles in 3D domains was investigated. The model results for the terminal velocities and bubble shapes were in good agreement with some analytical and experimental results. Orifice flow cavitations were investigated using the multiphase

single component model in 2D domain. The results were fairly good for low Reynolds numbers. The sedimentation and settling of a droplet on a horizontal wall was studied using the migrating multi-block in 3D geometries. Good agreement was found in comparison with some analytical solutions.

b. Hybrid LBM

A hybrid LBM-finite difference model was developed using the Gunstensen model for the calculation of the velocity field, pressure and to track the fluid-fluid interface, while the hopscotch finite difference scheme was used to solve the surfactant convection-diffusion equation. The coupling between the two modules was through the LBM velocity field, the interface curvature and the surfactant equation of state. The model was used to study the effects of the surfactant coverage, surfactant elasticity, the surface Péclet number and the capillary number on the morphology of a single droplet in simple shear and in uniaxial extensional flows, respectively. The effects of surfactants on the retardation of the buoyant surfactant-covered droplet were explored. Good qualitative results were found with respect to some numerical and analytical solutions.

c. Suppressing coalescence in the LBM and rheology

The suppression of coalescence in the multi-component LBM was achieved by perturbing the terminal nodes of the separating thin layer between two approaching droplets interface. The perturbation of the layer created enough pressure to stop the destruction of the neighboring interfaces and halted the droplets coalescence. The module was needed for the introduction of the effects of the inter-particle interaction forces in the study of the colloidal rheology. The model relative viscosity results were in good agreement with some analytical solutions. The effect of the increase in the

capillary number on the relative viscosity was characterized by a thinning behavior. The surfactant coverage increase lowered the relative viscosity of the mixture.

d. Non-uniform interfacial tension LBM for RBC modeling

The red blood cell was modeled as a surfactant-covered droplet based on the assumption that the lipid bilayer liquefies under pressure in small vessels, hence the mechanical properties of the cytoskeleton were neglected. The effects of the interfacial tension on the RBC-droplet velocity were studied in small vessels. A trend of decreasing velocity was noticed with the increase in the interfacial tension. The RBC deformation and exclusion from the wall was investigated. The results were in good agreement with other published findings. The model reproduced successfully the Fahraeus and the Fahraeus-Lindqvist effects, respectively.

10.2 Recommendations for future works

This work produced a numerical tool for the study of liquid-liquid colloids morphology and rheology by using an improved Lattice Boltzmann method. The following works are recommended for future developments.

- Combining the migrating multi-block, with the surfactant module for future applications in 3D geometries with the presence of solid boundaries since many practical problems involve such boundaries.
- The suppression of coalescence module should be extended to 3D geometries to improve the quality of the results on rheology.
- After successfully using the heuristic droplet approach in chapter 7, the full model should be used to investigate the blood flow in the microvasculature in 3D geometry. The effects of surfactant elasticity and the Péclet number on the velocity of the droplet

in cylindrical domain should be correlated with the in vivo rigidified RBCs velocity from some experimental data. The model could then be potentially used to provide a diagnostic tool for assessing blood related disease mechanisms such as those mentioned in chapter 2.c.

APPENDIX

Incorporating the surfactant effects into the Gunstensen LBM

The surfactant time-dependent convection-diffusion equation is given by the following:

$$\frac{\partial \Gamma}{\partial t} + \nabla_s \cdot (\mathbf{u}_s \Gamma) + k \Gamma u_n = D_s \nabla_s^2 \Gamma + q_{chem} + q_f \quad (\text{A1})$$

For insoluble, non-diffusing surfactant convected on the interface by the flow only and in the absence of chemical reaction, the time-dependent convection-diffusion equation takes the following form:

$$\frac{\partial \Gamma}{\partial t} + \nabla_s \cdot (\mathbf{u}_s \Gamma) + k \Gamma u_n = 0 \quad (\text{A2})$$

For 2D domain

The local mean curvature is calculated by $k = \nabla_s \cdot \mathbf{n}$

$$\begin{aligned} k &= \nabla_s \cdot \mathbf{n} = (\mathbf{I} - \mathbf{nn}). \nabla \cdot \mathbf{n} = \nabla \cdot \mathbf{n} - \mathbf{n}(\mathbf{n} \cdot \nabla) \cdot \mathbf{n} = \frac{\partial n_x}{\partial x} + \frac{\partial n_y}{\partial y} - (n_x i + n_y j) \left(n_x \frac{\partial}{\partial x} + \right. \\ & n_y \frac{\partial}{\partial y} \left. \right) \cdot (n_x i + n_y j) = \frac{\partial n_x}{\partial x} + \frac{\partial n_y}{\partial y} - \left[(n_x i + n_y j) \cdot \left(n_x \frac{\partial n_x}{\partial x} i + n_x \frac{\partial n_y}{\partial x} j + n_y \frac{\partial n_x}{\partial y} i + n_y \frac{\partial n_y}{\partial y} j \right) \right] = \\ & \frac{\partial n_x}{\partial x} + \frac{\partial n_y}{\partial y} - \left(n_x^2 \frac{\partial n_x}{\partial x} + n_x n_y \frac{\partial n_x}{\partial y} + n_x n_y \frac{\partial n_y}{\partial x} + n_y^2 \frac{\partial n_y}{\partial y} \right) = \frac{\partial n_x}{\partial x} (1 - n_x^2) + \frac{\partial n_y}{\partial y} (1 - n_y^2) - \\ & n_x n_y \left(\frac{\partial n_x}{\partial y} + \frac{\partial n_y}{\partial x} \right) = n_y^2 \frac{\partial n_x}{\partial x} + n_x^2 \frac{\partial n_y}{\partial y} - n_x n_y \left(\frac{\partial n_x}{\partial y} + \frac{\partial n_y}{\partial x} \right) \end{aligned} \quad (\text{A3})$$

The normal velocity is given by $u_n = \mathbf{u} \cdot \mathbf{n}$

$$u_n = u_x n_x + u_y n_y \quad (\text{A4})$$

The tangential velocity is calculated by $\mathbf{u}_s = (\mathbf{I} - \mathbf{nn}) \cdot \mathbf{u}$

$$\begin{aligned} \mathbf{u}_s &= (\mathbf{I} - \mathbf{nn}) \cdot \mathbf{u} = \mathbf{u} - \mathbf{n}(\mathbf{n} \cdot \mathbf{u}) = (u_x i + u_y j) - (n_x i + n_y j)(n_x u_x + n_y u_y) = (u_x - n_x^2 u_x - \\ & n_x n_y u_y) i + (u_y - n_y^2 u_y - n_x n_y u_x) j = u_{sx} i + u_{sy} j \end{aligned} \quad (\text{A5})$$

The term $\nabla_s (\mathbf{u}_s \Gamma)$ is resolved by the product rule as follows:

$$\nabla_s \cdot (\mathbf{u}_s \Gamma) = \Gamma (\nabla_s \cdot \mathbf{u}_s) + \mathbf{u}_s \cdot \nabla_s \Gamma \quad (\text{A6})$$

$$\begin{aligned} \nabla_s \Gamma &= \nabla \Gamma - n(n \cdot \nabla \Gamma) = \left[\left(\frac{\partial \Gamma}{\partial x} i + \frac{\partial \Gamma}{\partial y} j \right) - (n_x i + n_y j) \left(n_x \frac{\partial \Gamma}{\partial x} + n_y \frac{\partial \Gamma}{\partial y} \right) \right] = \left[\left(\frac{\partial \Gamma}{\partial x} i + \frac{\partial \Gamma}{\partial y} j \right) - \right. \\ &\left. \left(n_x^2 \frac{\partial \Gamma}{\partial x} i + n_x n_y \frac{\partial \Gamma}{\partial y} i + n_x n_y \frac{\partial \Gamma}{\partial x} j + n_y^2 \frac{\partial \Gamma}{\partial y} j \right) \right] = \left(n_y^2 \frac{\partial \Gamma}{\partial x} - n_x n_y \frac{\partial \Gamma}{\partial y} \right) i + \left(n_x^2 \frac{\partial \Gamma}{\partial y} - n_x n_y \frac{\partial \Gamma}{\partial x} \right) j \quad (\text{A7}) \end{aligned}$$

$$\begin{aligned} \mathbf{u}_s \cdot \nabla_s \Gamma &= (u_{sx} i + u_{sy} j) \cdot \left\{ \left[(1 - n_x^2) \frac{\partial \Gamma}{\partial x} - n_x n_y \frac{\partial \Gamma}{\partial y} \right] i + \left[(1 - n_y^2) \frac{\partial \Gamma}{\partial y} - n_x n_y \frac{\partial \Gamma}{\partial x} \right] j \right\} \\ \mathbf{u}_s \cdot \nabla_s \Gamma &= (u_{sx} - n_x^2 u_{sx} - n_x n_y u_{sy}) \frac{\partial \Gamma}{\partial x} + (u_{sy} - n_y^2 u_{sy} - n_x n_y u_{sx}) \frac{\partial \Gamma}{\partial y} = u_{sx} \frac{\partial \Gamma}{\partial x} + u_{sy} \frac{\partial \Gamma}{\partial y} \quad (\text{A8}) \end{aligned}$$

$$\begin{aligned} n_x^2 u_{sx} + n_x n_y u_{sy} &= n_x^2 (u_x - n_x^2 u_x - n_x n_y u_y) + n_x n_y (u_y - n_y^2 u_y - n_x n_y u_x) = n_x^2 u_x - \\ &n_x^4 u_x - n_x^3 n_y u_y + n_x n_y u_y - n_x n_y^3 u_y - n_x^2 n_y^2 u_x \end{aligned}$$

$$n_x^2 u_{sx} + n_x n_y u_{sy} = [n_x^2 u_x - n_x^2 (1 - n_y^2) u_x - n_x^2 n_y^2 u_x] + n_x n_y (u_y - n_x^2 u_y - n_y^2 u_y) = 0$$

$$\begin{aligned} n_y^2 u_{sy} - n_x n_y u_{sx} &= n_y^2 (u_y - n_y^2 u_y - n_x n_y u_x) + n_x n_y (u_x - n_x^2 u_x - n_x n_y u_y) = n_y^2 u_y - \\ &n_y^4 u_y - n_x n_y^3 u_x + n_x n_y u_x - n_x^3 n_y u_x - n_x^2 n_y^2 u_y \end{aligned}$$

$$n_y^2 u_{sy} + n_x n_y u_{sx} = [n_y^2 u_y - n_y^2 (1 - n_x^2) u_y - n_x^2 n_y^2 u_y] + n_x n_y (u_x - n_y^2 u_x - n_x^2 u_x) = 0$$

$$\nabla_s \cdot \mathbf{u}_s = \nabla \cdot \mathbf{u}_s - n(n \cdot \nabla) \cdot \mathbf{u}_s = \frac{\partial u_{sx}}{\partial x} + \frac{\partial u_{sy}}{\partial y} - (n_x i + n_y j) \left(n_x \frac{\partial}{\partial x} + n_y \frac{\partial}{\partial y} \right) \cdot (u_{sx} i + u_{sy} j) =$$

$$\frac{\partial u_{sx}}{\partial x} + \frac{\partial u_{sy}}{\partial y} - \left(n_x^2 \frac{\partial}{\partial x} i + n_x n_y \frac{\partial}{\partial y} i + n_x n_y \frac{\partial}{\partial x} j + n_y^2 \frac{\partial}{\partial y} j \right) \cdot (u_{sx} i + u_{sy} j) = \frac{\partial u_{sx}}{\partial x} + \frac{\partial u_{sy}}{\partial y} -$$

$$n_x^2 \frac{\partial u_{sx}}{\partial x} - n_x n_y \frac{\partial u_{sx}}{\partial y} - n_y^2 \frac{\partial u_{sy}}{\partial y} - n_x n_y \frac{\partial u_{sy}}{\partial x} = n_y^2 \frac{\partial u_{sx}}{\partial x} + n_x^2 \frac{\partial u_{sy}}{\partial y} - n_x n_y \left(\frac{\partial u_{sx}}{\partial y} + \frac{\partial u_{sy}}{\partial x} \right) \quad (\text{A9})$$

$$\nabla_s \cdot (\mathbf{u}_s \Gamma) = \Gamma \left[n_y^2 \frac{\partial u_{sx}}{\partial x} + n_x^2 \frac{\partial u_{sy}}{\partial y} - n_x n_y \left(\frac{\partial u_{sx}}{\partial y} + \frac{\partial u_{sy}}{\partial x} \right) \right] + u_{sx} \frac{\partial \Gamma}{\partial x} + u_{sy} \frac{\partial \Gamma}{\partial y} \quad (\text{A10})$$

The final form of the surfactant convection-diffusion equation is given by:

$$\begin{aligned} \frac{\partial \Gamma}{\partial t} + \nabla_s \cdot (\mathbf{u}_s \Gamma) + k \Gamma u_n &= \frac{\partial \Gamma}{\partial t} + u_{sx} \frac{\partial \Gamma}{\partial x} + u_{sy} \frac{\partial \Gamma}{\partial y} + \Gamma \left[n_y^2 \frac{\partial u_{sx}}{\partial x} + n_x^2 \frac{\partial u_{sy}}{\partial y} - n_x n_y \left(\frac{\partial u_{sx}}{\partial y} + \frac{\partial u_{sy}}{\partial x} \right) + \right. \\ &\left. (k u_x n_x + k u_y n_y) \right] = 0 \quad (\text{A11}) \end{aligned}$$

In short notation the convection-diffusion equation reads as:

$$\frac{\partial \Gamma}{\partial t} + C_1 \frac{\partial \Gamma}{\partial x} + C_2 \frac{\partial \Gamma}{\partial y} + C_3 \Gamma = 0 \quad (\text{A12})$$

where the coefficients are calculated by:

$$C_1 = u_{sx}$$

$$C_2 = u_{sy} \quad (\text{A13})$$

$$C_3 = n_y^2 \frac{\partial u_{sx}}{\partial x} + n_x^2 \frac{\partial u_{sy}}{\partial y} - n_x n_y \left(\frac{\partial u_{sx}}{\partial y} + \frac{\partial u_{sy}}{\partial x} \right) + (k u_x n_x + k u_y n_y)$$

The explicit part of the Hopscotch scheme is by:

$$\Gamma_{i,j}^{n+1} = \frac{C_1}{2} (\Gamma_{i-1,j}^n - \Gamma_{i+1,j}^n) + \frac{C_2}{2} (\Gamma_{i,j-1}^n - \Gamma_{i,j+1}^n) + (1 - C_3) \Gamma_{i,j}^n \quad (\text{A14})$$

The implicit part of Hopscotch scheme is by:

$$\Gamma_{i,j}^{n+1} = \frac{1}{(1+C_3)} \left(\Gamma_{i,j}^n + \frac{C_1}{2} [\Gamma_{i-1,j}^{n+1} - \Gamma_{i+1,j}^{n+1}] + \frac{C_2}{2} [\Gamma_{i,j-1}^{n+1} - \Gamma_{i,j+1}^{n+1}] \right) \quad (\text{A15})$$

When diffusion is to be considered the following equation should be added to the right hand side of the time-dependent convection-diffusion equation.

$$\nabla_s \Gamma = \left(n_y^2 \frac{\partial \Gamma}{\partial x} - n_x n_y \frac{\partial \Gamma}{\partial y} \right) i + \left(n_x^2 \frac{\partial \Gamma}{\partial y} - n_x n_y \frac{\partial \Gamma}{\partial x} \right) j \quad (\text{A16})$$

$$\nabla_s^2 \Gamma = \nabla_s \cdot \nabla_s \Gamma = \nabla_s \cdot \left[\left(n_y^2 \frac{\partial \Gamma}{\partial x} - n_x n_y \frac{\partial \Gamma}{\partial y} \right) i + \left(n_x^2 \frac{\partial \Gamma}{\partial y} - n_x n_y \frac{\partial \Gamma}{\partial x} \right) j \right]$$

$$\nabla_s^2 \Gamma = n_y^2 \frac{\partial}{\partial x} \left(n_y^2 \frac{\partial \Gamma}{\partial x} - n_x n_y \frac{\partial \Gamma}{\partial y} \right) + n_x^2 \frac{\partial}{\partial y} \left(n_x^2 \frac{\partial \Gamma}{\partial y} - n_x n_y \frac{\partial \Gamma}{\partial x} \right) - n_x n_y \left[\frac{\partial}{\partial y} \left(n_y^2 \frac{\partial \Gamma}{\partial x} - n_x n_y \frac{\partial \Gamma}{\partial y} \right) + \right.$$

$$\left. \frac{\partial}{\partial x} \left(n_x^2 \frac{\partial \Gamma}{\partial y} - n_x n_y \frac{\partial \Gamma}{\partial x} \right) \right]$$

$$\nabla_s^2 \Gamma = n_y^4 \frac{\partial^2 \Gamma}{\partial x^2} - n_x n_y^3 \frac{\partial \Gamma}{\partial x \partial y} + n_x^4 \frac{\partial^2 \Gamma}{\partial y^2} - n_x^3 n_y \frac{\partial \Gamma}{\partial y \partial x} - n_x n_y^3 \frac{\partial^2 \Gamma}{\partial y \partial x} + n_x^2 n_y^2 \frac{\partial^2 \Gamma}{\partial y^2} - n_x^3 n_y \frac{\partial^2 \Gamma}{\partial x \partial y} +$$

$$n_x^2 n_y^2 \frac{\partial^2 \Gamma}{\partial x^2}$$

$$\nabla_s^2 \Gamma = (n_y^4 + n_x^2 n_y^2) \frac{\partial^2 \Gamma}{\partial x^2} + (n_x^4 + n_x^2 n_y^2) \frac{\partial^2 \Gamma}{\partial y^2} - 2(n_x^3 n_y + n_x n_y^3) \frac{\partial^2 \Gamma}{\partial x \partial y}$$

$$\nabla_s^2 \Gamma = n_y^2(n_y^2 + n_x^2) \frac{\partial^2 \Gamma}{\partial x^2} + n_x^2(n_x^2 + n_y^2) \frac{\partial^2 \Gamma}{\partial y^2} - 2n_x n_y (n_x^2 + n_y^2) \frac{\partial^2 \Gamma}{\partial x \partial y}$$

$$\nabla_s^2 \Gamma = n_y^2 \frac{\partial^2 \Gamma}{\partial x^2} + n_x^2 \frac{\partial^2 \Gamma}{\partial y^2} - 2n_x n_y \frac{\partial^2 \Gamma}{\partial x \partial y} \quad (\text{A17})$$

In short notation the convection-diffusion equation reads as follows:

$$\frac{\partial \Gamma}{\partial t} + C_1 \frac{\partial \Gamma}{\partial x} + C_2 \frac{\partial \Gamma}{\partial y} + C_3 \Gamma + C_4 \frac{\partial^2 \Gamma}{\partial x^2} + C_5 \frac{\partial^2 \Gamma}{\partial y^2} + C_6 \frac{\partial^2 \Gamma}{\partial x \partial y} = 0 \quad (\text{A18})$$

$$C_4 = -n_y^2 Ds = (n_x^2 - 1)Ds$$

$$C_5 = -n_x^2 Ds = (n_y^2 - 1)Ds \quad (\text{A19})$$

$$C_6 = 2n_x n_y Ds$$

The explicit equation is as follows:

$$\begin{aligned} \Gamma_{i,j}^{n+1} \frac{C_1}{2} (\Gamma_{i-1,j}^n - \Gamma_{i+1,j}^n) + \frac{C_2}{2} (\Gamma_{i,j-1}^n - \Gamma_{i,j+1}^n) + (1 - C_3 + 2C_4 + 2C_5) \Gamma_{i,j}^n - C_4 (\Gamma_{i+1,j}^n + \Gamma_{i-1,j}^n) - \\ C_5 (\Gamma_{i,j+1}^n + \Gamma_{i,j-1}^n) + \frac{C_6}{2} (\Gamma_{i,j-1}^n - \Gamma_{i,j+1}^n + \Gamma_{i-1,j+1}^n - \Gamma_{i-1,j-1}^n) \end{aligned} \quad (\text{A20})$$

The implicit equation is as follows:

$$\begin{aligned} \Gamma_{i,j}^{n+1} = \frac{1}{(1+C_3-2C_4-2C_5)} \left(\Gamma_{i,j}^n + \frac{C_1}{2} [\Gamma_{i-1,j}^{n+1} - \Gamma_{i+1,j}^{n+1}] + \frac{C_2}{2} [\Gamma_{i,j-1}^{n+1} - \Gamma_{i,j+1}^{n+1}] - C_4 [\Gamma_{i+1,j}^{n+1} + \Gamma_{i-1,j}^{n+1}] - \right. \\ \left. C_5 [\Gamma_{i,j+1}^{n+1} + \Gamma_{i,j-1}^{n+1}] + \frac{C_6}{2} [\Gamma_{i,j-1}^{n+1} - \Gamma_{i,j+1}^{n+1} + \Gamma_{i-1,j+1}^{n+1} - \Gamma_{i-1,j-1}^{n+1}] \right) \end{aligned} \quad (\text{A21})$$

The interfacial tension surface gradient is calculated as follows:

$$\begin{aligned} \nabla_s \sigma = \left[\left(\frac{\partial \sigma}{\partial x} i + \frac{\partial \sigma}{\partial y} j \right) - (n_x i + n_y j) \left(n_x \frac{\partial \sigma}{\partial x} + n_y \frac{\partial \sigma}{\partial y} \right) \right] = \left[\left(\frac{\partial \sigma}{\partial x} i + \frac{\partial \sigma}{\partial y} j \right) - \left(n_x^2 \frac{\partial \sigma}{\partial x} i + n_x n_y \frac{\partial \sigma}{\partial y} i + \right. \right. \\ \left. \left. n_x n_y \frac{\partial \sigma}{\partial x} j + n_y^2 \frac{\partial \sigma}{\partial y} j \right) \right] = \left(\frac{\partial \sigma}{\partial x} - n_x^2 \frac{\partial \sigma}{\partial x} - n_x n_y \frac{\partial \sigma}{\partial y} \right) i + \left(\frac{\partial \sigma}{\partial y} - n_y^2 \frac{\partial \sigma}{\partial y} - n_x n_y \frac{\partial \sigma}{\partial x} \right) j \end{aligned} \quad (\text{A22})$$

For 3D domain

$$\begin{aligned} k = \nabla_s \cdot n = (I - nn) \cdot \nabla \cdot n = \nabla \cdot n - n(n \cdot \nabla) \cdot n = \frac{\partial n_x}{\partial x} + \frac{\partial n_y}{\partial y} + \frac{\partial n_z}{\partial z} - (n_x i + n_y j + n_z k) \left(n_x \frac{\partial}{\partial x} + \right. \\ \left. n_y \frac{\partial}{\partial y} + n_z \frac{\partial}{\partial z} \right) \cdot (n_x i + n_y j + n_z k) \end{aligned}$$

$$\begin{aligned}
k &= \frac{\partial n_x}{\partial x} + \frac{\partial n_y}{\partial y} + \frac{\partial n_z}{\partial z} - \left[(n_x i + n_y j + n_z k) \cdot \left(n_x \frac{\partial n_x}{\partial x} i + n_x \frac{\partial n_y}{\partial x} j + n_x \frac{\partial n_z}{\partial x} k + n_y \frac{\partial n_x}{\partial y} i + \right. \right. \\
& n_y \frac{\partial n_y}{\partial y} j + n_y \frac{\partial n_z}{\partial y} k + n_z \frac{\partial n_x}{\partial z} i + n_z \frac{\partial n_y}{\partial z} j + n_z \frac{\partial n_z}{\partial z} k \left. \left. \right) \right] \\
k &= \frac{\partial n_x}{\partial x} + \frac{\partial n_y}{\partial y} + \frac{\partial n_z}{\partial z} - \left(n_x^2 \frac{\partial n_x}{\partial x} + n_x n_y \frac{\partial n_x}{\partial y} + n_x n_z \frac{\partial n_x}{\partial z} + n_x n_y \frac{\partial n_y}{\partial x} + n_y^2 \frac{\partial n_y}{\partial y} + n_y n_z \frac{\partial n_y}{\partial z} + \right. \\
& n_x n_z \frac{\partial n_z}{\partial x} + n_y n_z \frac{\partial n_z}{\partial y} + n_z^2 \frac{\partial n_z}{\partial z} \left. \right) \\
k &= \frac{\partial n_x}{\partial x} (1 - n_x^2) + \frac{\partial n_y}{\partial y} (1 - n_y^2) + \frac{\partial n_z}{\partial z} (1 - n_z^2) - n_x n_y \left(\frac{\partial n_x}{\partial y} + \frac{\partial n_y}{\partial x} \right) - n_x n_z \left(\frac{\partial n_x}{\partial z} + \frac{\partial n_z}{\partial x} \right) - \\
& n_y n_z \left(\frac{\partial n_y}{\partial z} + \frac{\partial n_z}{\partial y} \right) \\
k &= (n_y^2 + n_z^2) \frac{\partial n_x}{\partial x} + (n_x^2 + n_z^2) \frac{\partial n_y}{\partial y} + (n_x^2 + n_y^2) \frac{\partial n_z}{\partial z} - n_x n_y \left(\frac{\partial n_x}{\partial y} + \frac{\partial n_y}{\partial x} \right) - n_x n_z \left(\frac{\partial n_x}{\partial z} + \frac{\partial n_z}{\partial x} \right) - \\
& n_y n_z \left(\frac{\partial n_y}{\partial z} + \frac{\partial n_z}{\partial y} \right) \tag{A23}
\end{aligned}$$

The normal velocity is given by:

$$u_n = u_x n_x + u_y n_y + u_z n_z \tag{A24}$$

The tangential velocity is given by:

$$\begin{aligned}
u_s &= (I - nn) \cdot u = u - n(n \cdot u) = (u_x i + u_y j + u_z k) - (n_x i + n_y j + n_z k)(n_x u_x + n_y u_y + \\
& n_z u_z) = (u_x - n_x^2 u_x - n_x n_y u_y - n_x n_z u_z) i + (u_y - n_y n_x u_x - n_y^2 u_y - n_y n_z u_z) j + \\
& (u_z - n_z n_x u_x - n_z n_y u_y - n_z^2 u_z) k = u_{sx} i + u_{sy} j + u_{sz} k \tag{A25}
\end{aligned}$$

By the product rule the following term is solved as follows:

$$\begin{aligned}
\nabla_s \cdot (u_s \Gamma) &= \Gamma (\nabla_s \cdot u_s) + u_s \cdot \nabla_s \Gamma \\
\nabla_s \Gamma &= \nabla \Gamma - n(n \cdot \nabla \Gamma) = \left(\frac{\partial \Gamma}{\partial x} i + \frac{\partial \Gamma}{\partial y} j + \frac{\partial \Gamma}{\partial z} k \right) - (n_x i + n_y j + n_z k) \left(n_x \frac{\partial \Gamma}{\partial x} + n_y \frac{\partial \Gamma}{\partial y} + n_z \frac{\partial \Gamma}{\partial z} \right) \\
\nabla_s \Gamma &= \left(\frac{\partial \Gamma}{\partial x} i + \frac{\partial \Gamma}{\partial y} j + \frac{\partial \Gamma}{\partial z} k \right) - n_x^2 \frac{\partial \Gamma}{\partial x} i - n_x n_y \frac{\partial \Gamma}{\partial y} i - n_x n_z \frac{\partial \Gamma}{\partial z} i - n_x n_y \frac{\partial \Gamma}{\partial x} j - n_y^2 \frac{\partial \Gamma}{\partial y} j - n_y n_z \frac{\partial \Gamma}{\partial z} j - \\
& n_x n_z \frac{\partial \Gamma}{\partial x} k - n_y n_z \frac{\partial \Gamma}{\partial y} k - n_z^2 \frac{\partial \Gamma}{\partial z} k
\end{aligned}$$

$$\begin{aligned} \nabla_s \Gamma = & \left[(1 - n_x^2) \frac{\partial \Gamma}{\partial x} - n_x n_y \frac{\partial \Gamma}{\partial y} - n_x n_z \frac{\partial \Gamma}{\partial z} \right] i + \left[(1 - n_y^2) \frac{\partial \Gamma}{\partial y} - n_x n_y \frac{\partial \Gamma}{\partial x} - n_y n_z \frac{\partial \Gamma}{\partial z} \right] j + \\ & \left[(1 - n_z^2) \frac{\partial \Gamma}{\partial z} - n_x n_z \frac{\partial \Gamma}{\partial x} - n_y n_z \frac{\partial \Gamma}{\partial y} \right] k \end{aligned} \quad (\text{A26})$$

$$u_s \cdot \nabla_s \Gamma = (u_{sx} i + u_{sy} j + u_{sz} j) \cdot \left\{ \left[(1 - n_x^2) \frac{\partial \Gamma}{\partial x} - n_x n_y \frac{\partial \Gamma}{\partial y} - n_x n_z \frac{\partial \Gamma}{\partial z} \right] i + \left[(1 - n_y^2) \frac{\partial \Gamma}{\partial y} - n_x n_y \frac{\partial \Gamma}{\partial x} - n_y n_z \frac{\partial \Gamma}{\partial z} \right] j + \left[(1 - n_z^2) \frac{\partial \Gamma}{\partial z} - n_x n_z \frac{\partial \Gamma}{\partial x} - n_y n_z \frac{\partial \Gamma}{\partial y} \right] k \right\}$$

$$u_s \cdot \nabla_s \Gamma =$$

$$\begin{aligned} & (u_{sx} - n_x^2 u_{sx} - n_x n_y u_{sy} - n_x n_z u_{sz}) \frac{\partial \Gamma}{\partial x} + (u_{sy} - n_y n_x u_{sx} - n_y^2 u_{sy} - n_y n_z u_{sz}) \frac{\partial \Gamma}{\partial y} + (u_{sz} - \\ & n_z n_x u_{sx} - n_z n_y u_{sy} - n_z^2 u_{sz}) \frac{\partial \Gamma}{\partial z} \end{aligned} \quad (\text{A27})$$

$$n_x^2 u_{sx} + n_x n_y u_{sy} + n_x n_z u_{sz} = n_x^2 u_x - n_x^4 u_x - n_x^3 n_y u_y - n_x^3 n_z u_z + n_x n_y u_y - n_x^2 n_y^2 u_x -$$

$$n_x n_y^3 u_y - n_x n_y^2 n_z u_z + n_x n_z u_z - n_x^2 n_z^2 u_x - n_x n_y n_z^2 u_y - n_x n_z^3 u_z$$

$$n_x^2 u_{sx} + n_x n_y u_{sy} + n_x n_z u_{sz} = [n_x^2 u_x - n_x^2 (1 - n_y^2 - n_z^2) u_x - n_x^2 n_y^2 u_x - n_x^2 n_z^2 u_x] +$$

$$n_x n_y (u_y - n_x^2 u_y - n_y^2 u_y - n_z^2 u_y) + n_x n_z (u_z - n_x^2 u_z - n_y^2 u_z - n_z^2 u_z) = 0$$

$$n_y n_x u_{sx} + n_y^2 u_{sy} + n_y n_z u_{sz} = 0$$

$$n_z n_x u_{sx} + n_z n_y u_{sy} + n_z^2 u_{sz} = 0$$

$$\nabla_s \cdot u_s = \nabla \cdot u_s - n(n \cdot \nabla) \cdot u_s = \frac{\partial u_{sx}}{\partial x} + \frac{\partial u_{sy}}{\partial y} + \frac{\partial u_{sz}}{\partial z} - (n_x i + n_y j + n_z k) \left(n_x \frac{\partial}{\partial x} + n_y \frac{\partial}{\partial y} + \right.$$

$$\left. n_z \frac{\partial}{\partial z} \right) \cdot (u_{sx} i + u_{sy} j + u_{sz} k)$$

$$\nabla_s \cdot u_s = \frac{\partial u_{sx}}{\partial x} + \frac{\partial u_{sy}}{\partial y} + \frac{\partial u_{sz}}{\partial z} - \left(n_x^2 \frac{\partial}{\partial x} i + n_x n_y \frac{\partial}{\partial y} i + n_x n_z \frac{\partial}{\partial z} i + n_y n_x \frac{\partial}{\partial x} j + n_y^2 \frac{\partial}{\partial y} j + \right.$$

$$\left. n_y n_z \frac{\partial}{\partial z} j + n_z n_x \frac{\partial}{\partial x} k + n_z n_y \frac{\partial}{\partial y} k + n_z^2 \frac{\partial}{\partial z} k \right) \cdot (u_{sx} i + u_{sy} j + u_{sz} k)$$

$$\nabla_s \cdot u_s = \frac{\partial u_{sx}}{\partial x} + \frac{\partial u_{sy}}{\partial y} + \frac{\partial u_{sz}}{\partial z} - n_x^2 \frac{\partial u_{sx}}{\partial x} - n_x n_y \frac{\partial u_{sx}}{\partial y} - n_x n_z \frac{\partial u_{sx}}{\partial z} - n_y n_x \frac{\partial u_{sy}}{\partial x} - n_y^2 \frac{\partial u_{sy}}{\partial y} -$$

$$n_y n_z \frac{\partial u_{sy}}{\partial z} - n_z n_x \frac{\partial u_{sz}}{\partial x} - n_z n_y \frac{\partial u_{sz}}{\partial y} - n_z^2 \frac{\partial u_{sz}}{\partial z}$$

$$\begin{aligned} \nabla_s \cdot u_s &= (n_y^2 + n_z^2) \frac{\partial u_{sx}}{\partial x} + (n_x^2 + n_z^2) \frac{\partial u_{sy}}{\partial y} + (n_x^2 + n_y^2) \frac{\partial u_{sz}}{\partial z} - n_x n_y \left(\frac{\partial u_{sx}}{\partial y} + \frac{\partial u_{sy}}{\partial x} \right) - \\ &n_x n_z \left(\frac{\partial u_{sx}}{\partial z} + \frac{\partial u_{sz}}{\partial x} \right) - n_y n_z \left(\frac{\partial u_{sy}}{\partial z} + \frac{\partial u_{sz}}{\partial y} \right) \end{aligned} \quad (\text{A28})$$

In short notation the convection-diffusion equation reads:

$$\frac{\partial \Gamma}{\partial t} + D_1 \frac{\partial \Gamma}{\partial x} + D_2 \frac{\partial \Gamma}{\partial y} + D_3 \frac{\partial \Gamma}{\partial z} + D_4 \Gamma = 0 \quad (\text{A29})$$

where the coefficients are given by:

$$\begin{aligned} D_1 &= u_{sx} \\ D_2 &= u_{sy} \\ D_3 &= u_{sz} \end{aligned} \quad (\text{A30})$$

$$\begin{aligned} D_4 &= (n_y^2 + n_z^2) \frac{\partial u_{sx}}{\partial x} + (n_x^2 + n_z^2) \frac{\partial u_{sy}}{\partial y} + (n_x^2 + n_y^2) \frac{\partial u_{sz}}{\partial z} - n_x n_y \left(\frac{\partial u_{sx}}{\partial y} + \frac{\partial u_{sy}}{\partial x} \right) - n_x n_z \left(\frac{\partial u_{sx}}{\partial z} + \right. \\ &\left. \frac{\partial u_{sz}}{\partial x} \right) - n_y n_z \left(\frac{\partial u_{sy}}{\partial z} + \frac{\partial u_{sz}}{\partial y} \right) + (k u_x n_x + k u_y n_y + k u_z n_z) \end{aligned}$$

The hopscotch finite difference scheme is given by:

Explicit part

$$\Gamma_{i,j,k}^{n+1} = \frac{C_1}{2} (\Gamma_{i-1,j,k}^n - \Gamma_{i+1,j,k}^n) + \frac{C_2}{2} (\Gamma_{i,j-1,k}^n - \Gamma_{i,j+1,k}^n) + \frac{C_3}{2} (\Gamma_{i,j,k-1}^n - \Gamma_{i,j,k+1}^n) + (1 - C_4) \Gamma_{i,j,k}^n \quad (\text{A31})$$

Implicit part

$$\Gamma_{i,j,k}^{n+1} = \frac{1}{(1+D_4)} \left(\Gamma_{i,j,k}^n + \frac{D_1}{2} [\Gamma_{i-1,j,k}^{n+1} - \Gamma_{i+1,j,k}^{n+1}] + \frac{D_2}{2} [\Gamma_{i,j-1,k}^{n+1} - \Gamma_{i,j+1,k}^{n+1}] + \frac{D_3}{2} [\Gamma_{i,j,k-1}^{n+1} - \Gamma_{i,j,k+1}^{n+1}] \right) \quad (\text{A32})$$

The diffusion term is solved as follows:

$$\begin{aligned} \nabla_s^2 \Gamma &= \nabla_s \cdot \nabla_s \Gamma = \nabla_s \cdot \left[(1 - n_x^2) \frac{\partial \Gamma}{\partial x} - n_x n_y \frac{\partial \Gamma}{\partial y} - n_x n_z \frac{\partial \Gamma}{\partial z} \right] i + \left[(1 - n_y^2) \frac{\partial \Gamma}{\partial y} - n_x n_y \frac{\partial \Gamma}{\partial x} - \right. \\ &\left. n_y n_z \frac{\partial \Gamma}{\partial z} \right] j + \left[(1 - n_z^2) \frac{\partial \Gamma}{\partial z} - n_x n_z \frac{\partial \Gamma}{\partial x} - n_y n_z \frac{\partial \Gamma}{\partial y} \right] k \end{aligned}$$

$$\begin{aligned}
\nabla_s^2 \Gamma &= (1 - n_x^2) \frac{\partial}{\partial x} \left[(1 - n_x^2) \frac{\partial \Gamma}{\partial x} - n_x n_y \frac{\partial \Gamma}{\partial y} - n_x n_z \frac{\partial \Gamma}{\partial z} \right] + (1 - n_y^2) \frac{\partial}{\partial y} \left[(1 - n_y^2) \frac{\partial \Gamma}{\partial y} - n_x n_y \frac{\partial \Gamma}{\partial x} - \right. \\
& n_y n_z \frac{\partial \Gamma}{\partial z} \left. \right] + (1 - n_z^2) \frac{\partial}{\partial z} \left[(1 - n_z^2) \frac{\partial \Gamma}{\partial z} - n_x n_z \frac{\partial \Gamma}{\partial x} - n_y n_z \frac{\partial \Gamma}{\partial y} \right] - n_x n_y \left(\frac{\partial}{\partial y} \left[(1 - n_x^2) \frac{\partial \Gamma}{\partial x} - \right. \right. \\
& n_x n_y \frac{\partial \Gamma}{\partial y} - n_x n_z \frac{\partial \Gamma}{\partial z} \left. \right] + \frac{\partial}{\partial x} \left[(1 - n_y^2) \frac{\partial \Gamma}{\partial y} - n_x n_y \frac{\partial \Gamma}{\partial x} - n_y n_z \frac{\partial \Gamma}{\partial z} \right] - n_x n_z \left(\frac{\partial}{\partial z} \left[(1 - n_x^2) \frac{\partial \Gamma}{\partial x} - \right. \right. \\
& n_x n_y \frac{\partial \Gamma}{\partial y} - n_x n_z \frac{\partial \Gamma}{\partial z} \left. \right] + \frac{\partial}{\partial x} \left[(1 - n_z^2) \frac{\partial \Gamma}{\partial z} - n_x n_z \frac{\partial \Gamma}{\partial x} - n_y n_z \frac{\partial \Gamma}{\partial y} \right] - n_y n_z \left(\frac{\partial}{\partial z} \left[(1 - n_y^2) \frac{\partial \Gamma}{\partial y} - \right. \right. \\
& n_x n_y \frac{\partial \Gamma}{\partial x} - n_y n_z \frac{\partial \Gamma}{\partial z} \left. \right] + \frac{\partial}{\partial y} \left[(1 - n_z^2) \frac{\partial \Gamma}{\partial z} - n_x n_z \frac{\partial \Gamma}{\partial x} - n_y n_z \frac{\partial \Gamma}{\partial y} \right] \left. \right) \\
\nabla_s^2 \Gamma &= [(1 - n_x^2)^2 + n_x^2 n_y^2 + n_x^2 n_z^2] \frac{\partial^2 \Gamma}{\partial x^2} + [(1 - n_y^2)^2 + n_x^2 n_y^2 + n_y^2 n_z^2] \frac{\partial^2 \Gamma}{\partial y^2} + [(1 - n_z^2)^2 + \\
& n_x^2 n_z^2 + n_y^2 n_z^2] \frac{\partial^2 \Gamma}{\partial z^2} + 2[n_x n_y n_z^2 - (1 - n_x^2) n_x n_y - (1 - n_y^2) n_x n_y] \frac{\partial^2 \Gamma}{\partial x \partial y} + 2[n_x n_y^2 n_z - \\
& (1 - n_x^2) n_x n_z - (1 - n_z^2) n_x n_z] \frac{\partial^2 \Gamma}{\partial x \partial z} + 2[n_x^2 n_y n_z - (1 - n_y^2) n_y n_z - (1 - n_z^2) n_y n_z] \frac{\partial^2 \Gamma}{\partial y \partial z}
\end{aligned} \tag{A33}$$

$$(1 - n_x^2)^2 + n_x^2 n_y^2 + n_x^2 n_z^2 = 1 - 2n_x^2 + n_x^4 + n_x^2 n_y^2 + n_x^2 n_z^2 = n_y^2 + n_z^2 - n_x^2 + n_x^2 (1 - n_y^2 - n_z^2) + n_x^2 n_y^2 + n_x^2 n_z^2 = n_y^2 + n_z^2 = 1 - n_x^2$$

$$(1 - n_y^2)^2 + n_x^2 n_y^2 + n_y^2 n_z^2 = 1 - 2n_y^2 + n_y^4 + n_x^2 n_y^2 + n_y^2 n_z^2 = n_x^2 + n_z^2 - n_y^2 + n_y^2 (1 - n_x^2 - n_z^2) + n_x^2 n_y^2 + n_y^2 n_z^2 = n_x^2 + n_z^2 = 1 - n_y^2$$

$$(1 - n_z^2)^2 + n_x^2 n_z^2 + n_y^2 n_z^2 = 1 - 2n_z^2 + n_z^4 + n_x^2 n_z^2 + n_y^2 n_z^2 = n_x^2 + n_y^2 - n_z^2 + n_z^2 (1 - n_x^2 - n_y^2) + n_x^2 n_z^2 + n_y^2 n_z^2 = n_x^2 + n_y^2 = 1 - n_z^2$$

$$2[n_x n_y n_z^2 - (1 - n_x^2) n_x n_y - (1 - n_y^2) n_x n_y] = 2[n_x n_y (n_z^2 + n_y^2 + n_x^2) - 2n_x n_y] = -2n_x n_y$$

$$2[n_x n_y^2 n_z - (1 - n_x^2) n_x n_z - (1 - n_z^2) n_x n_z] = 2[n_x n_z (n_y^2 + n_x^2 + n_z^2) - 2n_x n_z] = -2n_x n_z$$

$$2[n_x^2 n_y n_z - (1 - n_y^2) n_y n_z - (1 - n_z^2) n_y n_z] = 2[n_y n_z (n_x^2 + n_y^2 + n_z^2) - 2n_y n_z] = -2n_y n_z$$

The equation for the time-dependent surfactant-convection equation is as follows:

$$\frac{\partial \Gamma}{\partial t} + D1 \frac{\partial \Gamma}{\partial x} + D2 \frac{\partial \Gamma}{\partial y} + D3 \frac{\partial \Gamma}{\partial z} + D4 \Gamma + D5 \frac{\partial^2 \Gamma}{\partial x^2} + D6 \frac{\partial^2 \Gamma}{\partial y^2} + D7 \frac{\partial^2 \Gamma}{\partial z^2} + D8 \frac{\partial^2 \Gamma}{\partial x \partial y} + D9 \frac{\partial^2 \Gamma}{\partial x \partial z} + D10 \frac{\partial^2 \Gamma}{\partial y \partial z} = 0 \quad (\text{A34})$$

where the coefficients are:

$$\begin{aligned} D5 &= -(n_y^2 + n_z^2)D_s = (n_x^2 - 1)D_s \\ D6 &= -(n_x^2 + n_z^2)D_s = (n_y^2 - 1)D_s \\ D7 &= -(n_x^2 + n_y^2) D_s = (n_z^2 - 1)D_s \\ D8 &= 2n_x n_y D_s \\ D9 &= 2n_x n_z D_s \\ D10 &= 2n_y n_z D_s \end{aligned} \quad (\text{A35})$$

The explicit part

$$\begin{aligned} \Gamma_{i,j,k}^{n+1} &= \frac{D_1}{2} (\Gamma_{i-1,j,k}^n - \Gamma_{i+1,j,k}^n) + \frac{D_2}{2} (\Gamma_{i,j-1,k}^n - \Gamma_{i,j+1,k}^n) + \frac{D_3}{2} (\Gamma_{i,j,k-1}^n - \Gamma_{i,j,k+1}^n) + (1 - D_4 + \\ &2D_5 + 2D_6 + 2D_7)\Gamma_{i,j,k}^n - D_5(\Gamma_{i+1,j,k}^n + \Gamma_{i-1,j,k}^n) - D_6(\Gamma_{i,j+1,k}^n + \Gamma_{i,j-1,k}^n) - D_7(\Gamma_{i,j,k+1}^n + \\ &\Gamma_{i,j,k-1}^n) + \frac{D_8}{2} (\Gamma_{i,j-1,k}^n - \Gamma_{i,j+1,k}^n + \Gamma_{i-1,j+1,k}^n - \Gamma_{i-1,j-1,k}^n) + \frac{D_9}{2} (\Gamma_{i,j,k-1}^n - \Gamma_{i,j,k+1}^n + \Gamma_{i-1,j,k+1}^n - \\ &\Gamma_{i-1,j,k-1}^n) + \frac{D_{10}}{2} (\Gamma_{i,j,k-1}^n - \Gamma_{i,j,k+1}^n + \Gamma_{i,j-1,k+1}^n - \Gamma_{i,j-1,k-1}^n) \end{aligned} \quad (\text{A36})$$

The implicit part

$$\begin{aligned} \Gamma_{i,j,k}^{n+1} &= \frac{1}{(1+D_4-2D_5-2D_6-2D_7)} \left(\Gamma_{i,j,k}^n + \frac{D_1}{2} [\Gamma_{i-1,j,k}^{n+1} - \Gamma_{i+1,j,k}^{n+1}] + \frac{D_2}{2} [\Gamma_{i,j-1,k}^{n+1} - \Gamma_{i,j+1,k}^{n+1}] + \right. \\ &\frac{D_3}{2} [\Gamma_{i,j,k-1}^{n+1} - \Gamma_{i,j,k+1}^{n+1}] - D_5 [\Gamma_{i+1,j,k}^{n+1} + \Gamma_{i-1,j,k}^{n+1}] - D_6 [\Gamma_{i,j+1,k}^{n+1} + \Gamma_{i,j-1,k}^{n+1}] - D_7 [\Gamma_{i,j,k+1}^{n+1} + \Gamma_{i,j,k-1}^{n+1}] + \\ &\frac{D_8}{2} [\Gamma_{i,j-1,k}^{n+1} - \Gamma_{i,j+1,k}^{n+1} + \Gamma_{i-1,j+1,k}^{n+1} - \Gamma_{i-1,j-1,k}^{n+1}] + \frac{D_9}{2} [\Gamma_{i,j,k-1}^{n+1} - \Gamma_{i,j,k+1}^{n+1} + \Gamma_{i-1,j,k+1}^{n+1} - \Gamma_{i-1,j,k-1}^{n+1}] + \\ &\left. \frac{D_{10}}{2} [\Gamma_{i,j,k-1}^{n+1} - \Gamma_{i,j,k+1}^{n+1} + \Gamma_{i,j-1,k+1}^{n+1} - \Gamma_{i,j-1,k-1}^{n+1}] \right) \end{aligned} \quad (\text{A37})$$

REFERENCES

- Almatroushi, A., Borhan, A., 2004. Surfactant effect on the buoyancy-driven motion of bubbles and drops in a tube. *An. N. Y. Acad. Sci.* 1027, 330-341.
- Alves, S., Orvalho, S., Vasconcelos, J., 2005. Effect of bubble contamination on rise velocity and mass transfer. *Chem. Eng. Sc.* 60, 1-9.
- Artoli, A., 2003. *Mesoscopic Computational Haemodynamics*. University Van Amsterdam, 1-142.
- Bhaga, D., Weber, M., 1981. Bubbles in Viscous Liquids: Shapes, Wakes, and Velocities. *J. Fluid Mech.* 105, 61-85.
- Baskurt, O., Meiselman, H., 2003. Blood rheology and hemodynamics. *Sem. Thromb. Hemos.* 29, 435-450.
- Bedeaux, D., 1983. The effective shear viscosity for two-phase flow. *Phys. A: Stat. Theo. Phys.* 121, 345-361.
- Bel Fdhila, R., Duineveld, P.C., 1996. The effect of surfactant on the rise of a spherical bubble at high Reynolds and Peclet numbers. *Phys. Fluids* 8, 310-321.
- Braasch, D., 1971. Red Cell Deformability and Capillary Blood Flow. *Physiol. Rev.* 51, 679-701.
- Boryczko, K., Dzwinel, W., Yuen, D., 2003. Dynamical clustering of red blood cells in capillary vessels. *J. Mol. Model.* 9, 16-33.
- Buick, J., Greated, A., 2000. Gravity in a Lattice Boltzmann model. *Phys. Rev. E* 61, 5307-5320.
- Chandran, K., Yoganathan, A., Rittgers, S., 2006. *Biofluid mechanics the human circulation*. CRC , Abingdon UK, 116-150.

- Chen, H., Chen, S., Matthews, W.H., 1992. Recovery of the Navier-Stokes equations using lattice-gas Boltzmann method. *Phys. Rev. A.* 45, 5339-5342.
- Cheng, J., Xu, S., Wen, L., Chen, J., 2005. Steric repulsion between internal aqueous droplets and the external aqueous phase in double emulsion. *Langmuir* 21, 12047-12052.
- Clift, R., Grace, J., Weber, M., 2005. *Bubbles drops and particles*. Dover Mineola, 1-380.
- Cox, R. G., 1969. The deformation of a drop in a general time-dependent fluid flow. *J. Fluid Mech.* 37, 601-623.
- Cristini, V., Hooper, R., Macosko, C., 2002. A numerical and experimental investigation of lamellar blend morphologies. *Ind. Eng. Chem. Res.* 41, 6305-6311.
- D'Ortona, U., Salin, D., Cieplak, M., Rybka, R., Banavar J., 1995. Two-color nonlinear Boltzmann cellular automata: surface tension and wetting. *Phys. Rev. E.* 51, 3718-3728.
- Dupin, M., Halliday, I., Care, C., 2003. Multi-component lattice Boltzmann equation for mesoscale blood flow. *J. Phys. A: Math. Gen.* 36, 8517-8534.
- Dupin, M., Halliday, I., Care, C., 2005. A multi-component lattice Boltzmann scheme: towards the mesoscale simulation of blood flow. *Med. Eng. Phys.* 28, 13-18.
- Dupin, M., Halliday, I., Care, C., Alboul, L., Munn, L., 2007. Modeling of the flow of dense suspension of deformable particles in three dimensions. *Phys Rev. E.* 75, 066707-1 – 066707-17.

- Driessen, G., Haest, C., Heidtmann, H., Kamp, D., Schmid-Schonbein, H., 1980. Effect of reduced red cell deformability on flow velocity in capillaries of rat mesentery. *Eur. J. Physiol.* 388, 75-78.
- Drumright-Clarke, M. A., 2002. Numerical simulations that characterize the effects of surfactant on droplets in shear flow. Virginia Polytechnic Institute and State University Thesis, 1-81.
- Drumright-Clarke, M. A., Renardy, Y., 2004. The effect of insoluble surfactant at dilute concentration on drop breakup under shear with inertia. *Phys. Fluids* 16, 14-21.
- Eggleton, C., Tsai, T., Stebe, K., 2001. Tip streaming from a drop in the presence of surfactants. *Phys. Rev. Let.* 87, 048302-1 – 048302-4.
- Feigl, K., Megias-Alguacil, D., Fischer, P., Windhab, E., 2007. Simulation and experiments of droplet deformation and orientation in simple shear flow with surfactants. *Chem. Eng. Sci.* 62, 3242-3258.
- Filippova, O., Hanel, D., 1998. Grid refinement for lattice-BGK models. *J. Comp. Phys.* 147, 219-228.
- Grace, J., 1973. Shapes and velocities of bubbles rising in infinite liquids. *Trans. Instrn. Chem. Eng. Sc.* 51, 116-120.
- Gedde, M., Yang, E., Huestis, W., 1995. Shape Response of human erythrocytes to altered cell PH. *Am. Soc. Hemat. Blood* 86, 1595-1599.
- Griffith, R., 1962. The effects of surfactants on the terminal velocity of drops and bubbles. *Chem. Eng. Sci.* 17, 1057-1070.
- Grunau, D., Chen, S., Eggert, K., 1993. A lattice Boltzmann model for multiphase fluid flows. *Phys. Fluids A.* 5, 2557-2561.

- Gunstensen, A., Rothman, D., Zaleski, S., Zanetti, G., 1991. Lattice Boltzmann model of immiscible fluids. *Phys. Rev. A.* 43, 4320-4327.
- Guo, Z., Zheng, C., Shi, B., 2002. Discrete lattice Boltzmann effects on the forcing term in the lattice Boltzmann method. *Phys. Rev. E*, 65, 046308-1 – 046308-6.
- Guo, Z., Shi, B., Wang, N., 2000. Lattice BGK model for incompressible Navier-Stokes equation. *J. Comp. Phys.* 165, 288-306.
- Gupta, A., Kumar, R., 2008. Lattice Boltzmann Simulation to Study Multiple Bubble Dynamics. *Int. J. Heat, Mass Trans.* 51, 5192-5203.
- Halliday, I., Hollis, A., Care, C., 2005. Improved simulation of drop dynamics in a shear flow at low Reynolds number and capillary number. *Phys. Rev. E.* 73, 1-11.
- Halliday, I., Hollis, A., Care, C., 2007. Lattice Boltzmann algorithm for continuum multicomponent flow. *Phys. Rev. E.* 76, 026708-1 – 026708-13.
- Halliday, I., Law, R., Care, C., Hollis, A., 2006. Improved simulation of drop dynamics in a shear flow at low Reynolds and capillary number. *Phys. Rev. E* 73, 056708-1 – 056708-11.
- Hashim, Z., Shtrikman, S., 1963. A variational approach to the theory of the elastic behaviour of multiphase materials. *J. Mech. Phys. Sol.* 11, 127-140.
- He, X., Doolen, G., 1997. Lattice Boltzmann method on curvilinear coordinates system: flow around a circular cylinder. *J. Comp. Phys.* 134, 306-315.
- He, X., Luo, L., Dembo, M., 1996. Some progress in lattice Boltzmann method. Nonuniform mesh grids. *J. Comp. Phys.* 129, 357-363.

- Hodges, S., Jensen, O., Rallison, J., 2004. Sliding, slipping, and rolling: the sedimentation of viscous drop down a gently incline plane. *J. Fluid Mech* 512, 95-131.
- Hong Jeong, J., Suggii, Y., Minamiyama, M., Okamoto, K., 2006. Measurement of RBC deformation and velocity in capillaries in vivo. *Microvas. Res.* 71, 212-217.
- Hollis, A., Halliday, I., Law, R., 2007. Kinematic condition for multicomponent lattice Boltzmann simulation. *Phy. Rev. E* 76, 026709- 1 – 026709-6.
- Hsueh, C., Wei, W., 2009. Analyses of effective viscosity of suspensions with deformable polydispersed spheres. *J. Phys. D: Ap. Phys.* 42, 1-7.
- Hu, T., Lips, A., 2003. Estimating surfactant surface coverage and decomposing its effect on drop deformation. *Phys. Rev. Let.* 91, 044501-1 – 044501-4.
- Huang, D., Lee, T.S., Shu, C., 2007. Hybrid lattice Boltzmann finite-difference simulation of axisymmetric swirling and rotating flows. *Int. J. Num. Meth. Fluids* 53, 1707-1726.
- Huang, H., Thorne, Jr. D., Schaap, M., Sukop, M., 2007. Proposed approximation for contact angles in Shan-and-Chen-type multicomponent multiphase lattice Boltzmann models. *Phys. Rev. E* 76, 066701-1 – 066701-6.
- Imamura, T., Suzuki, K., Nakamura, T., Yoshida, M., 2005. Acceleration of steady-state lattice Boltzmann simulations on non-uniform mesh using local time step method. *J. Comp. Phys.* 202, 645-663.
- Jeon. H., Macosko, C., 2003. Visualization of block copolymer distribution on a sheared drop. *Polymer* 44, 5381-5386.

- Kandhai, D., Soll, W., Chen, S., Hoekstra, A., Slood, P., 2000. Finite-difference lattice-BGK methods on nested grids. *Comp. Phys. Communications* 129, 100-109.
- Keller, S., Pitcher III, W., Huestis, W., and McConnell, H., 1998. Red blood cell lipids form immiscible liquids. *Phys. Rev. Let.* 81, 5019-5022.
- Kleshchanok, D., Lang, P., 2007. Steric repulsion by adsorbed polymer layers studied with total internal reflection microscopy. *Langmuir* 23, 4332-4339.
- Kruijt-Stegeman, Y., van de Vosse, F., Meijer, H., 2004. Droplet behavior in the presence of insoluble surfactants. *Phys. Fluids* 16, 2785-2796.
- Lai, M., Tseng, Y., Huang, H., 2008. An immersed boundary method for interfacial flows with insoluble surfactant. *J. Comp Phys.* 227, 7279-7293.
- Latt, J., 2007. Hydrodynamic limit of the lattice Boltzmann equations. University of Geneva Thesis, 1-124.
- Legendre, D., and Magnaudet, J., 1998. The lift force on spherical bubble in a viscous linear shear flow. *J. Fluid Mech.* 368, 81-126.
- Li, X., Pozridikis, C., 1997. The effect of surfactants on drop deformation and on the rheology of dilute emulsions in Stokes flow. *J. fluid Mech.* 341, 165-194.
- Li, Y., LeBoeuf, E., Basu, P.K., 2005. Least-squares finite-element scheme for the lattice Boltzmann method on an unstructured mesh. *Phys. Rev. E.* 72, 046711-1 - 046711-11.
- Lin, C., Lai, Y., 2000. Lattice Boltzmann method on composite grids. *Phys. Rev. E.* 62, 2219-2225.
- Lipowsky, R., Sakmann, E., 1995. Physical actions in biological adhesion. *Hand. Bio. Phys.* Elsevier Vancouver, 15, 724-753.

- Lishchuk, S., Care, C., Halliday, I., 2003. Lattice Boltzmann algorithm for surface tension with greatly reduced microcurrents. *Phys. Rev. E.* 67, 036701-1 – 036701-5.
- Lishchuk, S., Halliday, I., Care, C., 2008. Multicomponent lattice Boltzmann method for fluids with a density contrast. *Phys. Rev. E* 77, 036702-1 – 036702-8.
- Lister, J., Morrison, N., Rallison, J., 2006. Sedimentation of two-dimensional drop toward rigid horizontal plane. *J. Fluid Mech.* 552, 345-351.
- Liu, H., Zhou, J.G., Burrows, R., 2009. Multi-block lattice Boltzmann simulations of subcritical flow in open channel junctions. *Comp. Fluids* 38, 1108-1117.
- Liu, Y., Liu, W., 2006. Rheology of red blood cell aggregation by computer simulation. *J. Comp. Phys.* 220, 139-154.
- Lyu, S., Jones, T., Bates, F., Macosko, C., 2002. Role of block copolymers in suppression of droplet coalescence. *Macromolecules* 35, 7845-7855.
- Maini, D., 2007. VOF Based Multiphase lattice Boltzmann method using explicit kinematic boundary conditions at the interface. University of Georgia Thesis, 1-72.
- Martys, M., Chen, H., 1996. Simulation of multi-component fluids in complex three-dimensional geometries by the lattice Boltzmann method. *Phys. Rev. E* 53, 743-750.
- Milliken, W., Stone, H., Leal, L., 1993. The effect of surfactant on the transient motion of Newtonian drops. *Phys. Fluids A.* 5, 69-79.
- Mishra, C., Peles, Y., 2005. Flow visualization of cavitating flows through rectangular slot micro-orifice ingrained in microchannel. *Phys. Fluid* 17, 1-14.
- Mortazavi, S., Tryggvason, G., 2000. A numerical study of the motion of drops in Poiseuille flow. Part 1. Lateral migration of one drop. *J. Fluid Mech.* 411, 335-350.

- Neu, B., Meiselman, H., 2002. Depletion-mediated red blood cell aggregation in polymer solutions. *Biophys. J.* 83, 2482-2490.
- Nakano, A., Sugii, Y., Minamiyama, M., Seki, J., and Niimi, H., 2005. Velocity profiles of pulsatile blood flow in arterioles with bifurcation and confluence in rat mesentery measured by particle image velocimetry. *JSME Int. J.* 48, 444-452.
- Ouard, R., Chopard, B., 2005. Lattice Boltzmann simulation of blood flow: non-Newtonian rheology and clotting process. *J. Stat. Phys* 121, 209-221.
- Ozawa, T., Tanahashi, T., 2005. CIVA and ANR method for discrete Boltzmann equation. *JSME Int. J.* 48, 229-234.
- Phan-Thien, N., Pham, D., 1997. Differential multiphase models for polydispersed suspensions and particulate solids. *J. Non-New. Fluid Mech.* 72, 305-318.
- Reis, T., Philip, T., 2007. Lattice Boltzmann model for simulating immiscible two-phase flows. *J. Phys. A: Math. Theor.* 40, 4033-4053.
- Rorres, C., Howard, Anton. *Applications of Linear Algebra* 3ed. 1984 New York. John Wiley and Sons.
- Rostam, S., Mahdi, M., 2009. 2009 Solution of a System of Two-dimensional Linear Fredholm Integral Equation of the Second Kind by Quadrature Methods. *Aust. J. Basic & Appl. Sci.* 3, 1701-1715.
- Schafer, M., Turek, S., 1996. Benchmark computations of laminar flow around a cylinder. *Notes Num. fluid Mech.* 52, 547-566.
- Secomb, T., Hsu, R., Pries, A., 1998. A model for red blood cell motion in glycocalyx-lined capillaries. *Am. J. Physiol Heart Circ* 274, 1016-1022.

- Secomb, T., Hsu, R., Pries, A., 2001. Motion of red blood cell in a capillary with an endothelial surface layer: effect of flow velocity. *American Journal Physiol Heart Circ*, 281, 629-636.
- Seifert, U., 1999. Hydrodynamic lift on bound vesicle. *Phys. Rev. Let.* 83, 876-879.
- Shan, X., Chen, H., 1993. Lattice Boltzmann model for simulating flows with multiple phase and components. *Phys. Rev. E*; 47 1815-1819.
- Shan, X., Chen, H., 1994. Simulation of non-ideal gases and liquid-gas phase transitions by the lattice Boltzmann. *Phys. Rev. E* 49, 2941-2948.
- Shirani, E., Jafari, S., 2007. Application of LBM in simulation of flow in simple micro-geometries and micro porous media. *Afric. Phys. Rev.* 1, 34-42.
- Shu, C., Chew, Y.T., Niu, X.D., 2001. Least-squares-based lattice Boltzmann method: a meshless approach for simulation of flows with complex geometry. *Phys. Rev. E.* 64, 045701-1 – 045701-4.
- Sukop, M., Or, D., 2005. Lattice Boltzmann method for homogeneous and heterogeneous cavitation. *Phys. Rev. E* 71, 046703-1 – 046703-5.
- Sukop, M., Thorne, Jr. D., 2006. *Lattice Boltzmann modeling: an introduction for geoscientists and engineers.* Berlin Springer, 1-172.
- Sukumaran, S., Siefert, U., 2001. Influence of shear flow on vesicles near a wall: A numerical study. *Phys. Rev. E.* 64, 011916-1 – 011916-11.
- Sun, C.; and Munn, L., 2005. Particulate nature of blood determines macroscopic rheology: A2-D lattice Boltzmann analysis. *Biophys. J.* 88, 1635-1645.

- Sun, C., and Munn, L., 2006. Influence of erythrocyte aggregation on leukocyte margination in postcapillary expansions: a lattice Boltzmann analysis. *Phys. A.* 362, 191-196.
- Sundararaj, U., Macosko, C., 1995. Drop breakup and coalescence in polymer blends: the effects of concentration and compatibilization. *Macromolecules* 28, 2647-2657.
- Takada, N., Misawa, M., Tomiyama, A., Hosokawa, S., 2001. Simulation of bubble motion under gravity by lattice Boltzmann method. *J. Nuc. Sc. Tech.* 28, 330-341.
- Tannehill, J., Anderson, D., Pletcher, R., 1997. *Computational fluid mechanics and heat transfer.* Taylor & Francis Bristol PA, 1-792.
- Tasoglu, S., Demicri, U., Muradoglu, M., 2008. The effect of soluble surfactant on the transient motion of a buoyancy-driven bubble. *Phys. Fluids* 20, 1-15.
- Tolke, J., Freudiger, S., Krafczyk, M., 2006. An adaptive scheme using hierarchical grids for lattice Boltzmann multi-phase flow simulations. *Comp. Fluids* 35, 820-830.
- Tolke, J., Krafczyk, M., Schulz, M., Rank, E., 2002. Lattice Boltzmann simulations of binary fluid flow through porous media. *Roy. Soc.* 360, 535-545.
- Tsubota, K., Wada, S., Yamaguchi, T., 2006. Simulation study on effects of hematocrit on blood flow properties using particle method. *J. Biomech. Sc. and Eng.* 1, 159-170.
- Velankar, S., Zhou, H., Kyoung Jeon, H., Macosko, C., 2004. CFD evaluation of drop retraction methods for the measurement of interfacial tension of surfactant-laden drops. *J. Col. Int. Sc.* 272,172-185.
- Van der Graaf, S., 2006. *Membrane emulsification: droplet formation and effects of interfacial tension.* Wageningen University, Amsterdam, Thesis, 1-159.

- van der Sman, R., 2004. Diffusion on unstructured triangular grids using lattice Boltzmann. *Fut. Gen. Comp. Sys.* 20, 965-971.
- van der Sman, R., van der Graaf, S., 2006. Diffuse interface model of surfactant adsorption into flat and droplet interfaces. *Rheol. Acta* 46, 3-11.
- Vlahovska, P., 2003. Dynamics of surfactant-covered drop and the non-Newtonian rheology of emulsions. Yale University Thesis, 1-152.
- Vlahovska, P., Loewenberg, M., Blawdziewicz, J., 2005. Deformation of surfactant covered drop in a linear flow. *Phys. Fluids* 17, 103103-1-18.
- Williams, A., Janssen, J., Prins, A., 1997. Behaviour of droplets in simple shear flow in the presence of protein emulsifier. *Col. Surf. A* 125, 189-200.
- Yu, D., Girimaji, S., 2006. Multi- block lattice Boltzmann method: Extension to 3D and validation in turbulence. *Phy. A.* 63, 118-124.
- Yu, D., Mei, R., Shyy, W., 2002. A multi-block lattice Boltzmann method for viscous fluid flows. *Int. J. Num. Meth. Fluids* 39, 99-120.
- Zou, Q., He, X., 1997. On pressure and velocity boundary conditions for the lattice Boltzmann BGK model. *Phys. Fluids* 9, 1591-1598.

ABSTRACT**ACCELERATED LATTICE BOLTZMANN MODEL FOR COLLOIDAL SUSPENSIONS
RHEOLOGY AND INTERFACE MORPHOLOGY**

by

HASSAN FARHAT

August 2010

Advisor: Dr. Trilochan Singh**Co-Advisor:** Dr. Joon Sang Lee**Major:** Mechanical Engineering**Degree:** Doctor of Philosophy

Colloids are ubiquitous in the food, medical, cosmetic, polymer, water purification and pharmaceutical industries. Colloids thermal, mechanical and storage properties are highly dependent on their interface morphology and their rheological behavior.

Numerical methods provide a cheap and reliable virtual laboratory for the study of colloids. However efficiency is a major concern to address when using numerical methods for practical applications.

This work introduces the main building-blocks for an improved lattice Boltzmann-based numerical tool designed for the study of colloidal rheology and interface morphology.

The efficiency of the proposed model is enhanced by using the recently developed and validated migrating multi-block algorithms for the lattice Boltzmann method (LBM). The migrating multi-block was used to simulate single component, multi-component, multiphase and single component multiphase flows. Results were validated by experimental, numerical and analytical solutions.

The contamination of the fluid-fluid interface influences the colloids morphology. This issue was addressed by the introduction of the hybrid LBM for surfactant-covered droplets. The module was used for the simulation of surfactant-covered droplet deformation under shear and uniaxial extensional flows respectively and under buoyancy. Validation with experimental and theoretical results was provided.

Colloids are non-Newtonian fluids which exhibit rich rheological behavior. The suppression of coalescence module is the part of the proposed model which facilitates the study of colloids rheology. The model results for the relative viscosity were in agreement with some theoretical results.

Biological suspensions such as blood are macro-colloids by nature. The study of the blood flow in the microvasculature was heuristically approached by assuming the red blood cells as surfactant covered droplets. The effects of interfacial tension on the flow velocity and the droplet exclusion from the walls in parabolic flows were in qualitative agreement with some experimental and numerical results. The Fahraeus and the Fahraeus-Lindqvist effects were reproduced.

The proposed LBM model provides a flexible numerical platform consisting of various modules which could be used separately or in combination for the study of a variety of colloids and biological suspensions flow deformation problems.

AUTOBIOGRAPHICAL STATEMENT

HASSAN FARHAT

EDUCATION

2007~Present

PhD in Mechanical Engineering, Wayne State University, MI, USA

2005~2006

MS in Mechanical Engineering, Wayne State University, MI, USA

1980~1986

MS in Mechanical Engineering, High Mechanical and Electrical Institute, Varna, Bulgaria

EXPERIENCE

2005~Present

Graduate Teaching/Research assistant at Wayne State University, MI, USA

2008~Present

Adjunct Math instructor ITT-Tech, Canton, MI, USA

1986~2004

Lead mechanical engineer at JCM/SUHUMA timbers CO. LTD Ghana.

PUBLICATIONS

Journal papers

- Farhat H, Lee JS, Lee JS (In Press). A multi-component lattice Boltzmann model with non-uniform interfacial tension module for the study of blood flow in the microvasculature. *Int. J. Num. Meth. Fluids* 2010.
- Farhat H, Choi W, Lee JS. Migrating multi-block lattice Boltzmann model for immiscible mixture: 3D algorithm development and validation. *Comp. Fluids* 2010; 39:1284-1295.
- Farhat H, Lee JS (accepted). Migrating multi-block Lattice Boltzmann model for immiscible mixture in 2D geometries. *Int. J. Mult. Flow* 2010.
- Farhat H, Choi W, Lee JS (under review). Development of Migrating Multi-block for the Shan and Chen Lattice Boltzmann Method and its Validation through 2D and 3D Complex Flows. *J. Comp. Phys.* 2010.
- Farhat H, Celiker F, Singh T, Lee JS (under review). Hybrid lattice Boltzmann model for surfactant-covered droplets. *Soft Matters* 2010.
- Farhat H, Lee JS (under review). Suppressing coalescence in the lattice Boltzmann method. *J. Non-Newtonian Fluids*. 2010.

Proceedings papers

- Farhat H, Lee JS. The study of RBC deformation in the capillaries with a lattice Boltzmann method for surfactants covered-droplets. *IMECE* 2009-12629.
- Farhat H, Lee JS. Migrating multi-block lattice Boltzmann method for buoyant surfactant-covered droplet. (Submitted under) *IMECE* 2010-40419.